Investigation of the magnetic and magnetocaloric properties of complex lanthanide oxides

Paromita Mukherjee

Department of Physics
University of Cambridge

This dissertation is submitted for the degree of
Doctor of Philosophy

King's College April 2018

This thesis is dedicated to my parents.

Declaration

I hereby declare that except where specific reference is made to the work of others, the contents of this dissertation are original and have not been submitted in whole or in part for consideration for any other degree or qualification in the University of Cambridge, or any other university. This dissertation is my own work and contains nothing which is the outcome of work done in collaboration, except as specified in the text and Acknowledgements. This dissertation contains fewer than 60,000 words including abstract, tables, footnotes and appendices. Some of the work described herein has been published as follows:

Chapter 3 is an expanded version of:

P. Mukherjee, A. C. Sackville Hamilton, H. F. J. Glass, S. E. Dutton, Sensitivity of magnetic properties to chemical pressure in lanthanide garnets $Ln_3A_2X_3O_{12}$, Ln = Gd, Tb, Dy, Ho, A = Ga, Sc, In, Te, X = Ga, Al, Li, Journal of Physics: Condensed Matter **29**, 405808 (2017).

Chapter 4 contains material from:

P. Mukherjee, S. E. Dutton, Enhanced magnetocaloric effect from Cr substitution in Ising lanthanide gallium garnets $Ln_3CrGa_4O_{12}$ (Ln = Tb, Dy, Ho), Advanced Functional Materials **27**, 1701950 (2017).

P. Mukherjee, H. F. J. Glass, E. Suard, and S. E. Dutton, Relieving the frustration through Mn^{3+} substitution in holmium gallium garnet, Physical Review B **96**, 140412(R) (2017).

Chapter 5 contains material from:

P. Mukherjee, Y. Wu, G. I. Lampronti, and S. E. Dutton, Magnetic properties of monoclinic lanthanide orthoborates, $LnBO_3$, Ln = Gd, Tb, Dy, Ho, Er, Yb, Materials Research Bulletin **98**, 173 (2018).

Chapter 6 contains material from:

P. Mukherjee, E. Suard, S. E. Dutton, Magnetic properties of monoclinic lanthanide metaborates, $Ln(BO_2)_3$, Ln = Pr, Nd, Gd, Tb, Journal of Physics: Condensed Matter **29**, 405807 (2017).

Paromita Mukherjee
April 2018

Acknowledgements

I am very grateful to my supervisor Dr. Siân E. Dutton for giving me the opportunity to work in her group for my PhD. This work would not have been possible without her continuous support and guidance in all aspects of research. I am very thankful for her invaluable mentorship and for giving me the freedom to pursue my research interests.

I thank all members of the Dutton group, past and present, for being such amazing colleagues and friends: Adrien Amigues, Hugh Glass and Hajime Shinohara who welcomed me into the group as well as Jack Hodkinson, Joshua Lewis and Dr. Joseph Paddison for all their friendly advice and making the office a wonderful place to work in. Many thanks to members of the Quantum Matter group for all the friendly discussions, help and encouragement: Philip Brown, Konstantin Semeniuk, Jiasheng Chen, Matthew Coak, Yu-Te Hsu, Mate Hartstein, Sophia Taylor, Hsu Liu and others. I am also very thankful to Dr. Patricia Alireza, Dr. Siddharth Saxena, Dr. Michael Carpenter and Dr. Nalin Patel for their guidance.

Thanks to Doug Astill for his help with the SQUID and to Adam Brown and Dr. Oleg Ignatchik for their assistance with measurements on the new SQUID and PPMS.

I am indebted to Dr. Emmanuelle Suard, ILL and Dr. Pascal Manuel, ISIS for their patience and guidance in all aspects of neutron diffraction experiments from proposal writing to data analysis. Thanks to Hugh Glass, Jack Hodkinson and Joshua Lewis for their support during the various neutron experiments. I thank Dr. Giulio Lampronti, Department of Earth Sciences, Cambridge for collecting X-Ray diffraction data on the lanthanide orthoborates discussed in this thesis. Thanks also to Yutian Wu and Alice Sackville Hamilton for preliminary work on the lanthanide orthoborates and lanthanide garnets respectively prior to my PhD.

I thank the Winton Programme for the Physics of Sustainability for my PhD funding.

My mentors, friends and family at home have been a huge source of strength and inspiration. I thank all my teachers from school, college and university. Thanks to my friends for their good wishes and support, especially Anwesha Sengupta, Prianthi Roy, Jahnavi Jha, Sreya Banerjee, Amartya Mitra and Soumi De. Also to my relatives, well-wishers and family friends. I thank my mother Sumita Mukherjee and father Pradeep Kumar Mukherjee for their unwavering love, support and faith in me.

Many thanks to Jack Hodkinson, Amartya Mitra and Philip Brown for their help and advice on writing the thesis in LaTeX and to Dr. Joseph Paddison, Philip Brown, Jack Hodkinson, Joshua Lewis, Alexander Hickey, Keiron Murphy for proofreading thesis chapters.

Abstract

Complex lanthanide oxide systems are known to host novel phases of matter, while also providing functionality for practical applications. In this dissertation, the structural, magnetic and magnetocaloric properties of three families of lanthanide oxides have been studied with the dual aims of investigating the magnetic behaviour and identifying promising magnetic refrigerants for cooling to temperatures currently accessible using non-renewable liquid He.

The thesis presents a two-part study of the magnetic and magnetocaloric properties of the geometrically frustrated lanthanide garnets, where the magnetic Ln^{3+} form corner-sharing triangles. First, the family of garnets $Ln_3A_2X_3O_{12}$, Ln = Gd, Tb, Dy, Ho, A = Ga, Sc, In, Te, X = Ga, Al, Li are investigated. Changes to the single-ion anisotropy of the magnetic ion as well as variations in the chemical pressure radically alters the nature of magnetic ordering, the degree of frustration and the magnetocaloric performance. In the second part, the garnets $Ln_3A\mathrm{Ga}_4O_{12}$, Ln = Gd, Tb, Dy, Ho, A = Cr, Mn, are studied. Introducing additional spins significantly reduces the frustration in the garnet lattice. Low temperature powder neutron diffraction of $Ho_3MnGa_4O_{12}$ reveals concomitant ordering of Ho^{3+} and Mn^{3+} moments below the ordering temperature, $T_N = 5.8$ K. The magnetocaloric performance of $Ln_3CrGa_4O_{12}$, Ln = Gd, Dy, Ho, greatly surpasses that of the parent $Ln_3Ga_5O_{12}$ at $T = 2$ K.

The final results chapters in the thesis describe the magnetism and magnetocaloric effect in the lanthanide orthoborates, $LnBO_3$, Ln = Eu, Gd, Tb, Dy, Ho, Er, Yb and the lanthanide metaborates, $Ln(BO_2)_3$, Ln = Pr, Nd, Gd, Tb. The magnetic Ln^{3+} form slightly distorted edge-sharing triangular layers in $LnBO_3$. Unique magnetic features are observed, including short-range ordering and spin reorientation transitions depending on the single-ion anisotropy of the Ln^{3+}. The $LnBO_3$ are also efficient magnetocalorics in the liquid helium temperature range. The lanthanide metaborates contain one-dimensional chains of magnetic lanthanide ions. Bulk magnetic measurements show features consistent with low-dimensional magnetism, such as magnetisation plateaux at one-third of the saturation magnetisation for $Nd(BO_2)_3$ and $Tb(BO_2)_3$ in a field of 14 T.

This thesis provides insight into the fundamental magnetic properties of complex lanthanide oxide systems and also demonstrates strategies for identifying new magnetocaloric materials: both through chemical control of the structure of well-known magnetocalorics and by studying materials that have not been explored previously. The results pave the way for further in-depth investigations and finding new magnetic coolants based on complex lanthanide oxide systems.

Table of contents

Chapter 1

Introduction

The history of magnetism begins in ancient times, when people found that lodestones attracted iron. Rapid advancements were made in the 1800s when the relationship between electricity and magnetism was explored in depth. This finally culminated in Maxwell's equations that unified electricity, magnetism and optics giving the first unified theory of physics: that of electromagnetism. Another ground-breaking achievement came with the advancement of relativistic quantum mechanics in the early 1900s and the discovery of spin, a property intrinsic to every elementary particle. Magnetism continues to be an active field of fundamental research while also finding widespread practical applications, from existing technologies like motors and hard disk drives to technologies of the future such as spintronics and skyrmionic memory storage devices. A more in-depth review of the history and advances in magnetism can be found in [1].

This thesis explores the fundamental magnetic properties of three families of complex lanthanide oxides, where the connectivity of the magnetic lanthanide (Ln^{3+}) ions is geometrically frustrated. In geometrically frustrated magnetic materials, the underlying geometry of the structure prevents all the pairwise interactions between magnetic spins from being satisfied simultaneously. The system fluctuates between degenerate ground states, leading to emergent states of matter with exotic behaviour such as the magnetic analogues of ice and liquids [2]. The ground state selected by a geometrically frustrated system is fragile and sensitive to the slightest structural perturbations. Thus, the system may be driven to a different ground state through chemical substitution. In this thesis, a comprehensive study of the impact of chemical substitution on a known family of frustrated lanthanide oxides, the lanthanide garnets, is presented for the first time. The magnetic properties of two families of lanthanide borates with frustrated lattices, which had not been explored previously, is also discussed.

Another key research theme explored in this thesis is examining the performance of these complex lanthanide oxides as solid state magnetic refrigerants at low temperatures, $T \geq 2$ K. Due to the increasing scarcity and cost of liquid helium, sustainable alternatives for cooling to low temperatures need to be explored: one such technique is magnetic refrigeration. The materials studied in this thesis have very low transition temperatures (which determines the cooling limit) and high magnetic moments (which determines the efficiency of the refrigeration cycle) and so, are ideal candidates for magnetic refrigeration in the liquid helium temperature regime.

This chapter presents a general introduction to the thesis; the materials are introduced in the respective results chapters. The chapter begins with an introduction to the fundamentals of magnetism; a more complete description can be found elsewhere, such as in [3, 4]. This is followed by discussions on geometrical frustration and low temperature magnetic refrigeration, which are concepts key to the materials discussed in this thesis. The chapter concludes with a brief overview of the subsequent chapters in this dissertation.

1.1 Magnetic moments in atoms

In classical electromagnetism, a quantity called magnetic moment can be defined as follows: For a loop of infinitesmally small area $\mathbf{d}A$ carrying current I, the magnetic moment, μ is given by

$$\mu = \int \mathbf{d}\mu = \int I\mathbf{d}A \tag{1.1}$$

This entity is equivalent to a magnetic dipole [5].

A current loop and the corresponding magnetic moment is due to the motion of one or more electrically charged particles. In atoms, the orbital motion of electrons is associated with an orbital magnetic moment, μ_L, and an orbital angular momentum, L. In the quantum mechanical description, $\hat{\mu_L}$ and $\hat{L}$ are defined as operators and are related as follows:

$$\hat{\mu_L} = \frac{-e}{2m_e}\hat{L} \tag{1.2}$$

where e is the magnitude of electronic charge and m_e is the mass of an electron. In the quantum mechanical theory of angular momentum, $\hat{L^2}$ and one of the three components of the angular momentum operator, conventionally the z component, $\hat{L_z}$, commute and provide a complete description of the angular momentum of a particle [6]. $\hat{L^2}$ has an eigenvalue given by:

$$\hat{L^2} = l(l+1)\hbar^2 \tag{1.3}$$

where l is the angular momentum quantum number. $\hat{L_z}$ has an eigenvalue given by:

$$\hat{L_z} = m_l\hbar \tag{1.4}$$

where m_l is the magnetic quantum number ranging from $-l$ to $+l$. The unit of magnetic moment for atoms is named the Bohr magneton, μ_B, and is defined as:

$$\mu_B = \frac{e\hbar}{2m_e} \tag{1.5}$$

Therefore the magnitude of the orbital magnetic moment, μ_L, is given by:

$$\mu_L = g_L L = g_L\sqrt{l(l+1)}\mu_B \tag{1.6}$$

where $g_L = 1$ for an infinitely massive nucleus and is defined as the orbital g factor for an electron. For a finite mass nucleus, $g_L = 1 - \frac{1}{M}$, where M is the ratio of the nuclear mass to the electron mass [7].

There is another source of magnetic moment for all elementary particles: the spin S. Contrary to the classical picture for a current loop for the orbital angular momentum, spin has a purely quantum mechanical description and is intrinsic to all elementary particles, like mass. Analogous to $\hat{L}$, $\hat{S}$ is given by

$$\hat{S}^2 = s(s+1)\hbar^2 \tag{1.7}$$

where s is the spin quantum number. For an electron, $s = \frac{1}{2}$. The z component of $\hat{S}$, $\hat{S_z}$, has an eigenvalue:

$$\hat{S_z} = m_s\hbar \tag{1.8}$$

where m_s has values ranging from $-s$ to $+s$. For an electron, the magnitude of the spin magnetic moment, μ_S, is related to the spin angular momentum, S, by the following equation:

$$\mu_S = g_S S = g_S\sqrt{s(s+1)}\mu_B \tag{1.9}$$

where g_S is the spin g factor for an electron. From Dirac's theory of relativistic quantum mechanics, $g_S = 2$. However, from later developments in quantum electrodynamics, it was shown that g_S can be expressed as a power series in α (where $\alpha = \frac{e^2}{4\pi\varepsilon_0\hbar c} = \frac{1}{137.04}$ is the fine structure constant) and the actual value is 2.0023.... This is owing to the fact that electromagnetic interactions originate from the action of virtual photons that are emitted and reabsorbed by electrons: the successive terms in the power series indicate the contributions of increasing number of formation and annihilation of virtual photons. In this thesis, the approximation $g_S = 2$ is used for simplicity.

For a many-electron atom with no spin-orbit coupling, the total orbital angular momentum **L** is the vector sum of the individual orbital angular momenta (here the bold type indicates a vector operator):

$$\mathbf{L} = \sum_i l(i) \tag{1.10}$$

The magnitude of **L** is given by

$$|\mathbf{L}| = \sqrt{L(L+1)}\hbar \tag{1.11}$$

The z component, L_z, has the magnitude $M_L\hbar$ where M_L, the auxiliary or magnetic quantum number, is given by:

$$M_L = \sum_i m_l(i) \tag{1.12}$$

M_L ranges from $-L$ to $+L$, that is, each L state has a degeneracy of $(2L+1)$. Similarly in the absence of spin-orbit coupling, the total spin angular momentum, **S**, is defined as:

$$\mathbf{S} = \sum_i s(i) \tag{1.13}$$

and has the magnitude:

$$|\mathbf{S}| = \sqrt{S(S+1)}\hbar \tag{1.14}$$

S_z has the magnitude $M_S\hbar$ where M_S is given by:

$$M_S = \sum_i m_s(i) \tag{1.15}$$

M_S ranges from $-S$ to $+S$, with each S state having $(2S+1)$ degeneracy. Now in a many-electron atom, the spin-orbit interaction, which is the interaction between the spin and orbital components of the electronic wavefunction must also be considered. Then, **L** and **S** are no longer conserved and instead the total angular momentum, **J**, is conserved. **J** is given by:

$$\mathbf{J} = \mathbf{L} + \mathbf{S} \tag{1.16}$$

and has the magnitude:

$$|\mathbf{J}| = \sqrt{J(J+1)}\hbar \tag{1.17}$$

J has allowed values in the range $|L-S|$ to $L+S$. The z component, J_Z, has magnitude $M_J\hbar$ where

$$M_J = M_L + M_S = \sum_i m_j(i) \tag{1.18}$$

M_J ranges from $-J$ to $+J$; thus each J state is $(2J+1)$ degenerate. Therefore the relation $\sum_J(2J+1) = (2L+1)(2S+1)$ is always valid.

The general expression for the magnitude of $\boldsymbol{\mu}$, μ_{eff}, can be written in a manner analogous to the orbital magnetic moment and spin magnetic moment as:

$$\mu_{eff} = g_J\sqrt{J(J+1)}\mu_B \tag{1.19}$$

The Landé g factor for the total angular momentum, g_J, is given by the expression:

$$g_J = \frac{3}{2} + \frac{S(S+1)-L(L+1)}{2J(J+1)} \tag{1.20}$$

The values of L, S and J are obtained following Pauli's exclusion principle and Hund's rules. Pauli's exclusion principle for electrons in atoms can be stated as 'No two electrons in a multi-electron atom can have the same values for all four quantum numbers'. Here, the four quantum numbers referred to are: n, the principal quantum number, l, the angular momentum quantum number, m_l, the magnetic quantum number, and m_s, the spin quantum number. Pauli's exclusion principle implies that electrons in an atom occupy distinct quantised orbitals with at most two electrons per orbital.

Hund's rules can be stated as [3]:

(a) The lowest energy state for an atom is that for which the total spin quantum number, S is maximised. This minimises the Coulomb repulsion energy in accordance with the Pauli exclusion principle.

(b) For the energy state determined by the first rule, maximise L. Once again, this minimises the Coulomb repulsion energy since electrons rotating in orbits in the same direction may 'avoid' each other more effectively.

(c) J is given by $|L-S|$ for less than half-filled shells and by $L+S$ for shells that are more than half-filled. This minimises the spin-orbit energy.

The values of L, S and J can also be used to summarise the ground state using a term symbol ${}^{2S+1}L_J$. Here, $2S+1$ denotes the spin multiplicity and L is represented by a letter according to the sequence given in Table 1.1. It must be noted that Hund's rules only lead to a prediction of the ground state J manifold and do not yield any information about the excited states or

Table 1.1 L values and corresponding letters in the term symbol $^{2S+1}L_J$.

L	0	1	2	3	4	5	6	...
	S	P	D	F	G	H	I	...

Table 1.2 Magnetic ground states for some Ln^{3+} ions using Hund's rules. The values of S, L, J, g_J, $\mu_{eff}/\mu_B = g_J\sqrt{J(J+1)}$ and $\Delta S_{max} = R\ln(2J+1)$ are listed for the ground state.

Ion	Shell	S	L	J	g_J	μ_{eff} (μ_B)	ΔS_{max} (J K^{-1} mol^{-1})
Pr^{3+}	$4f^2$	1	5	4	0.80	3.58	18.27
Nd^{3+}	$4f^3$	1.5	6	4.5	0.73	3.62	19.14
Eu^{3+}	$4f^6$	3	3	0	0.00	0.00	0.00
Gd^{3+}	$4f^7$	3.5	0	3.5	2.00	7.94	17.29
Tb^{3+}	$4f^8$	3	3	6	1.50	9.72	21.32
Dy^{3+}	$4f^9$	2.5	5	7.5	1.33	10.65	23.05
Ho^{3+}	$4f^{10}$	2	6	8	1.25	10.61	23.56
Er^{3+}	$4f^{11}$	1.5	6	7.5	1.20	9.58	23.05
Yb^{3+}	$4f^{13}$	0.5	3	3.5	1.14	4.54	17.29

how close they are to the ground state. This thesis focuses on magnetism arising from rare earth ions, Ln^{3+}, which obey Hund's rules very well. However, Hund's third rule is violated for certain transition metal ions, as will be explained in a later section.

The values of orbital angular momentum L, spin angular momentum S and total angular momentum J for the Ln^{3+} ions can be used to calculate the g factor and the theoretical magnetic moment. These values are compiled in Table 1.2 for some magnetic Ln^{3+} [3].

1.2 Bulk magnetism: isolated moments

Having defined the different aspects of magnetic moments in atoms, an overview of commonly observed magnetic behaviour in bulk magnetic materials is presented. It will be noted here that although the discussion is for atoms, these considerations apply equally well to ions, such as the magnetic lanthanide ions that are the focus of this thesis [3, 4]. In this section the phenomena involving isolated, non-interacting magnetic moments are discussed.

1.2.1 Magnetic susceptibility

A bulk magnetic material contains of a large number of atoms with magnetic moments. The magnetisation, **M**, is defined as the magnetic moment per unit volume. In free space, when the magnetisation is zero, the magnetic field is defined by **B** and **H** which are related by $\mathbf{B} = \mu_0\mathbf{H}$ where $\mu_0 = 4\pi \times 10^{-7}$ H m^{-1} is the permeability of free space. The magnetic susceptibility, χ, is defined by the relation:

$$\chi = \frac{dM}{dH} \tag{1.21}$$

Typically the isothermal magnetisation, $M(H)$, curves are linear in very low magnetic fields and the susceptibility χ can be approximated by the formula:

$$\chi = \frac{M}{H} \tag{1.22}$$

1.2.2 Diamagnetism

This phenomenon is seen in all materials and is characterised by a negative value of the magnetisation and the magnetic susceptibility. It can be qualitatively explained by Lenz's law of electromagnetic induction, although the origins are purely quantum mechanical. When an external magnetic field is applied, the electronic orbits cross the field and hence experience an electromotive force associated with the change in flux. As per Lenz's law, the resulting current (and hence magnetisation) opposes the cause, that is, the direction of the initial applied field. The diamagnetic susceptibility is usually independent of temperature and decreases linearly with increase in applied magnetic field. The diamagnetic susceptibility, χ_{dia} can be calculated using Pascal's constants [8] for a specific material. However, usually it is several orders of magnitude smaller than the paramagnetic susceptibility and can be neglected. It is the dominant contribution to the susceptibility for closed-shell species which have no paramagnetic moment.

1.2.3 Paramagnetism

Paramagnetism is observed in materials that contain atoms having net magnetic moments due to unpaired electrons. For an ideal paramagnet, in the absence of an applied magnetic field, the magnetic moments are oriented randomly due to thermal fluctuations. When an external magnetic field is applied, the magnetic moments attempt to align parallel to the direction of the magnetic field. This gives rise to a positive magnetic susceptibility. An increase in magnetic field will align the spins whereas an increase in temperature will increase the random fluctuations. Therefore the magnetisation is expected to be a function of the ratio of B/T where B is the magnetic field and T is the temperature. In a semiclassical treatment, the quantisation of magnetic moments is neglected and the angular momentum levels are assumed to be continuous ($J = \infty$). In this case, the magnetisation is given by:

$$M = M_{sat} L(y) \tag{1.23}$$

where $L(y) = \coth y - 1/y$ is the Langevin function, $M_{sat} = N_A \mu_{eff}$ is the saturation magnetisation, when all the magnetic moments are aligned parallel to the field, and $y = \mu_{eff} B/k_B T$. The susceptibility, χ_{para}, obeys Curie's law and is given by:

$$\chi_{para} = \frac{C}{T} \tag{1.24}$$

where C is the Curie constant given by

$$C = \frac{N_A \mu_{eff}^2}{3k_B} \tag{1.25}$$

The magnetic moment can be determined from the Curie constant as:

$$\mu_{eff} = \sqrt{\frac{3k_B C}{N_A}} \tag{1.26}$$

In the quantum mechanical description, J can only take discrete values (integer or a half-integer). Then the magnetisation is given as:

$$M = M_{sat} B_J(y) \tag{1.27}$$

where the saturation magnetisation, M_{sat}, is given by:

$$M_{sat} = g_J J \mu_B \tag{1.28}$$

y is defined as:

$$y = \frac{g_J J \mu_B B}{k_B T} \tag{1.29}$$

and $B_J(y)$ is the Brillouin function defined as:

$$B_J(y) = \frac{2J+1}{2J} \coth \frac{2J+1}{2J} y - \frac{1}{2J} \coth \frac{y}{2J} \tag{1.30}$$

For small y (high temperatures and/or low magnetic fields), $B_J(y)$ can be approximated as:

$$B_J(y) = \frac{(J+1)y}{3J} + O(y^3) \tag{1.31}$$

Neglecting the second term, the magnetic susceptibility is given by

$$\chi_{para} = \frac{N_A g_J^2 J(J+1)\mu_B^2}{3k_B T} = \frac{N_A \mu_{eff}^2}{3k_B T} \tag{1.32}$$

and hence is same as the classical Curie law. Experimentally the paramagnetic susceptibility can be determined as:

$$\chi_{para} = \chi_{expt} - \chi_{dia} \tag{1.33}$$

where χ_{dia} is the diamagnetic susceptibility and χ_{expt} is the experimentally measured magnetic susceptibility. The experimental measurement of $\chi(T)$ would yield a magnetic moment value, equation (1.26), which can be compared with the theoretical magnetic moment defined by equation (1.19).

From the Curie law, $\chi \propto 1/T$ and hence the graph of $1/\chi$ vs. T is a straight line.

A weak form of paramagnetism called Pauli paramagnetism is observed in metals. This is temperature independent to a first approximation. It arises due to the itinerant electrons that are responsible for conduction in metals. This is not observed for the materials discussed in this thesis.

1.2.4 van Vleck paramagnetism

If the electronic ground state has $J = 0$, there is no paramagnetic effect and hence no paramagnetic susceptibility because the ground state of the system does not change on application of an external magnetic field. However this statement is only valid in the limit of first order perturbation theory. In second order perturbation theory, admixture of excited states is considered for which $J \neq 0$. In this case the magnetic susceptibility is given by:

$$\chi = 2N_A \sum_n \frac{|<0|(L_z + gS_z)|n>|^2}{E_n - E_0} \mu_B^2 + \chi_{dia} \tag{1.34}$$

where E_n and E_0 are the energies of the nth excited state and ground state respectively. The first term in equation (1.34) is positive and is referred to as the van Vleck paramagnetic susceptibility while the second term is the diamagnetic susceptibility which is negative. van Vleck paramagnetism is similar to diamagnetism in that it is a small effect and is temperature independent. It is important for rare-earth ions like Sm^{3+} and Eu^{3+} where the theoretical magnetic moment is close to or exactly zero and admixture of ground state and excited states need to be considered to model the magnetic susceptibility effectively [3].

1.2.5 Magnetic entropy

For an ideal paramagnet containing N_A independent magnetic moments per mole, in the absence of a magnetic field, the magnetic moments are subject to thermal fluctuations and have random orientations. This is a state of complete disorder and the resultant magnetisation is zero. In an applied magnetic field, the magnetic moments would align, resulting in a net magnetisation and this would reduce the random fluctuations of the moments. This can be quantified in terms of entropy. The general definition of entropy, S, which is a measure of 'disorder', is given by:

$$S = k_B \ln \omega \tag{1.35}$$

where ω is the number of microstates of the system. At very high temperatures, in the absence of magnetic field, the thermal energy $k_B T$ is sufficiently large that the system is totally disordered. m_J can take $(2J+1)$ values and so the total possible number of microstates are $\omega = (2J+1)^{N_A}$. Hence, the entropy becomes:

$$S = N_A k_B \ln(2J+1) = R \ln(2J+1) \tag{1.36}$$

The magnetisation is a function of B/T so that on applying a magnetic field and at low temperatures, the moments align with the field. At sufficiently low temperatures, all the magnetic moments align parallel with the field and there is only one possible microstate such that $\omega = 1$ and S = 0. Thus the maximum change in magnetic entropy that can be theoretically extracted, ΔS_{max}, in units of $\mathrm{J\,K^{-1}\,mol^{-1}}$, is given by:

$$\Delta S_{max} = R \ln(2J+1) \tag{1.37}$$

For the case with effective $J = 1/2$ (as is observed in many complex lanthanide oxides at low temperatures), ΔS_{max} is given by:

$$\Delta S_{max} = R \ln 2 \tag{1.38}$$

The ΔS_{max} values for some magnetic Ln^{3+} according to equation (1.37) are given in Table 1.2.

1.3 Crystal fields and magnetic interactions

The impact of the local crystal environment and interactions between magnetic moments is described in this section.

1.3.1 Crystal fields

In an actual crystal, the magnetic ions are not isolated but are coordinated via ligands. The crystal field can be defined as an electric field due to the neighbouring ions in a crystal. The neighbouring orbitals are modelled as negative point charges; in a more sophisticated analysis, the overlap between the orbitals of the central magnetic ion and the orbitals of neighbouring ions is considered. The nature of the crystal field for a magnetic ion is completely dependent on the symmetry of the local environment as the electrostatic repulsion between the electrons of the ligand and magnetic ion is dependent on the spatial distribution of the electrons and hence the orbitals. With the exception of s orbitals, the local environment is not spherically symmetric so different orbitals behave differently. The charge of the magnetic ion, the nature of the ligand and the coordination geometry all play an important role in determining the crystal field levels. For example, octahedral or tetrahedral environments for $3d$ transition metal ions produce different crystal field splittings.

For $3d$ transition metal ions, the crystal field effect is much stronger than the spin-orbit interaction and so Hund's third rule is not obeyed. In such systems, a ground state usually has $L = 0$ and so $J = S$ and $g_J = 2$. Therefore the magnetic moment is usually given by:

$$\mu_{eff,TM} = 2\sqrt{S(S+1)}\mu_B \tag{1.39}$$

This effect is known as orbital quenching because the orbital moment is effectively quenched. For higher transition metal ions, ($4d$ and $5d$) the situation is complex because the spin-orbit interaction and the crystal field effects are of comparable magnitude. For the $4f$ rare earth ions, the delocalisation of the orbitals from the nucleus is much less as they lie beneath the $5s$ and $5p$ shells and so crystal field interactions are weaker than the spin-orbit interactions. Therefore Hund's third rule is obeyed.

Another consequence of the crystal field is that if it causes a sufficiently large splitting of the energy levels, the pairing energy of spins might be lower than the energy separation between the crystal field levels. In such a case, it is energetically favourable to violate Hund's first rule and pair up spins in the lower crystal field levels, known as a 'low spin' state. If the energy separation between crystal field levels is lower than the pairing energy, a 'high spin' state is favoured. This is observed in materials containing $3d$ transition metal ions. For example, both 'high spin' and 'low spin' states are possible for Mn^{2+}, Fe^{3+} or Co^{2+} in octahedral environments [3, 9]

The final important consequence of crystal field effects is to generate a single-ion anisotropy for the magnetic ion such that the spins locally prefer to orient along specific directions. In axial environments, the effect of the crystal electric field on the orientations of the spins may be modelled using a term in the Hamiltonian given by:

$$H_{CF} = -\Delta \sum_i (\mathbf{S}_i \cdot \mathbf{z}_i)^2 \tag{1.40}$$

where $\mathbf{z}_i$ is a local axis along which the spins $\mathbf{S}_i$ may align and Δ is defined as the single-ion anisotropy constant. If $\Delta > 0$, spins prefer to align along $\mathbf{z}_i$: this is referred to as ‘easy-axis’ anisotropy. On the other hand, if $\Delta < 0$, spins prefer to align perpendicular to $\mathbf{z}_i$: this is referred to as ‘easy-plane’ anisotropy.

For the complex lanthanide oxides considered in this thesis, the magnetic ions are the $4f$ rare-earth ions and therefore Hund’s rules are obeyed. The crystal field arises from the interactions between the $4f$ orbitals of the magnetic Ln^{3+} and the $2p$ orbitals of O^{2-}. The $4f$ orbitals have highly anisotropic distributions and so the crystal field will cause splitting of the J multiplet energies into $(2J+1)$ levels. *A priori* calculations of the crystal field levels for $4f$ rare earth ions can be extremely complex and they are mainly determined from experiments such as inelastic neutron scattering for a specific sample. However, some general comments can be made. Firstly, the interactions of the f orbital distribution with the crystal field can give rise to substantial single-ion anisotropies of the magnetic Ln^{3+}. Secondly, Kramers’ degeneracy theorem states that for all systems with time-reversal symmetry and half-integer total spin, every energy level is at least doubly degenerate [10]. This implies that for magnetic Ln^{3+} with half-integral values of J (such as Dy^{3+}, Er^{3+}), known as Kramers ions, all crystal field levels are at least doubly degenerate irrespective of the point symmetry of the crystallographic site where the magnetic ion is situated. On the contrary, for non-Kramers ions (such as Tb^{3+}, Ho^{3+}), there is no such constraint and the ground state is determined by the point symmetry of the crystallographic site.

1.3.2 Dipolar interactions

As already discussed, a magnetic moment $\boldsymbol{\mu}$ behaves like a magnetic dipole. Thus a collection of magnetic moments in a solid can be considered to be a system of interacting magnetic dipoles. The energy of interaction between two such magnetic dipoles $\boldsymbol{\mu}_1$ and $\boldsymbol{\mu}_2$ separated by a distance $\boldsymbol{r}$ is given by:

$$E = \frac{\mu_0}{4\pi r^3}[\boldsymbol{\mu}_1 \cdot \boldsymbol{\mu}_2 - \frac{3}{r^2}(\boldsymbol{\mu}_1 \cdot \boldsymbol{r})(\boldsymbol{\mu}_2 \cdot \boldsymbol{r})] \tag{1.41}$$

The dipolar interaction energy depends on the magnitude, separation and the relative alignment of the magnetic moments. However, in order to obtain an order of magnitude approximation, the magnetic dipolar interaction energy, D can be estimated as:

$$D = \frac{\mu_0 \mu_{eff}^2}{4\pi R_{nn}^3} \tag{1.42}$$

where R_{nn} is the nearest neighbour distance between the magnetic ions and μ_{eff} is determined from the Curie constant, equation (1.26).

1.3.3 Exchange interactions

Exchange interactions have a purely quantum mechanical origin. They can be thought of as a manifestation of the fact that the wave functions of identical particles are subject to exchange symmetry, that is, they remain unchanged when two particles are exchanged (symmetric wave function) or change sign when two particles are exchanged (antisymmetric wave function). The former case is true for bosons obeying Bose-Einstein statistics and the latter is true for fermions obeying Fermi-Dirac statistics (a consequence of which is the Pauli exclusion principle). Electrons fall in the latter category and the overall wave function must be antisymmetric. Thus for a symmetric spatial wave function, the spin wave function must be antisymmetric, that is, a singlet state with $S = 0$, while for an antisymmetric spatial wave function, the spin part must be a symmetric triplet state with $S = 1$. The effective Hamiltonian can be written as:

$$\hat{H} = \frac{1}{4}(E_S + 3E_T) - (E_S - E_T)\mathbf{S}_1 \cdot \mathbf{S}_2 \tag{1.43}$$

where E_S and E_T are the energies for the singlet and triplet states. The Hamiltonian is the sum of a constant term, and a spin-dependent term. The exchange constant or exchange integral, J, which indicates the preference for a singlet or a triplet state, is defined by:

$$J = \frac{E_S - E_T}{2} \tag{1.44}$$

So the spin-dependent term in the effective Hamiltonian can be written as:

$$\hat{H}^{spin} = -2J\mathbf{S}_1 \cdot \mathbf{S}_2 \tag{1.45}$$

Generalising to a many-electron system, the Hamiltonian for the Heisenberg model is given by:

$$\hat{H}^{spin} = -\sum_{ij} J_{ij}\mathbf{S}_i \cdot \mathbf{S}_j \tag{1.46}$$

where J_{ij} is the exchange constant between the i^{th} and j^{th} spins and the factor 2 is removed because each pair of spins is included in the sum twice. It is common to take $J_{ij} = J$, a constant for nearest neighbour spins and to be equal to zero otherwise.

Direct exchange

Direct exchange refers to electrons on neighbouring atoms interacting directly via the exchange interaction. However this may not be the true mechanism for exchange interactions in many materials. For example, in the $4f$ rare earth ions, the $4f$ electrons are very strongly localised and are situated close to the nucleus and so there is insufficient direct overlap between the neighbouring orbitals of the magnetic ions. Even in $3d$ transition metals like Fe, Co, Ni, direct exchange cannot explain the observed magnetic properties completely. In most magnetic materials, some indirect exchange interaction mechanism such as superexchange, double exchange or anisotropic exchange (also known as the Dzyaloshinsky-Moriya interaction) must be considered [3].

Superexchange

The exchange mechanism operating in many ionic solids, such as transition metal oxides as well as complex lanthanide oxides (discussed in this thesis) is the superexchange interaction, first proposed by Kramer [11] and later refined by Anderson [12]. Superexchange is defined as the indirect exchange interaction between non-neighbouring magnetic ions that is mediated by a non-magnetic ion situated in between those magnetic ions. Superexchange strongly depends on the degree of overlap of the orbitals and hence on the M-O-M bond angle, where M is the magnetic ion and O is oxygen.

The exchange integral consists of a potential exchange term due to electron repulsion that favours a ferromagnetic ground state, and a kinetic exchange term which favours an antiferromagnetic ground state. In most cases of superexchange, the kinetic term dominates. The antiferromagnetic coupling reduces the energy of the system by allowing electrons to become fully or partially delocalised over the entire structure and subsequently lowering the kinetic energy. In some cases, superexchange can be ferromagnetic but this is typically weaker than the antiferromagnetic superexchange. The nature of the superexchange coupling between d orbitals can usually be explained by a set of empirical rules known as the Goodenough-Kanamori rules [13–15] although there are exceptions such as when spin-orbit coupling becomes significant. It is not possible to directly construct such a simple scheme to rationalise the sign of exchange interactions for $4f$ orbitals, such as the magnetic Ln^{3+} considered in this thesis.

1.3.4 Relative magnitude of dipolar and exchange interactions

Dipolar interactions, D, are determined by the magnitude of magnetic moments and distance between the magnetic moments. Typically D has an order of magnitude of 0.1 - 1 K for magnetic materials. The magnitude of exchange interactions, J, is usually determined by the degree of overlap between orbitals. For $3d$ magnetic ions, J can range between 10 - few 100 K, whereas for more localised $4f$ orbitals, the typical range of J is 1 - 10 K. Therefore, for $3d$ ions, usually $J >> D$ and it is sufficient to consider only exchange interactions for understanding the magnetic properties. However, for $4f$ ions, such as the complex lanthanide oxides discussed in this thesis, J and D are of the same order of magnitude and both need to be considered for understanding the magnetic properties.

1.3.5 Heisenberg, Ising and XY models

In order to understand the magnetic behaviour of bulk solids, one has to also consider the microscopic models of the magnetic interactions. A common general model is the nearest neighbour classical Heisenberg model for which the Hamiltonian is given by:

$$\hat{H} = -\sum_{<ij>} J\mathbf{S}_i \cdot \mathbf{S}_j \tag{1.47}$$

where J is the constant denoting the exchange integral and $< ij >$ represents a sum over nearest neighbours. In a classical model, the spins $\mathbf{S}_i$ are considered to be three-dimensional vectors and the sum can be taken over a lattice of 1, 2 or 3 dimensions. It is important to note the distinction between d, the dimensionality of the lattice where the spins are located, and D, the dimensionality of the spins themselves. For the Heisenberg model, $D = 3$ and d can be 1, 2 or 3. The maximum magnetic entropy associated with Heisenberg spins is given by equation (1.37). In the XY model, the Hamiltonian is the same as equation (1.47) except $D = 2$ so the spins are two-dimensional vectors, confined to a plane. In the Ising model, $D = 1$ and spins are only allowed to point up or down; that is, only the z component of the spin is considered (the choice of z is not unique but this is the convention). The Hamiltonian is given by:

$$\hat{H} = -\sum_{<ij>} JS_i^z S_j^z \tag{1.48}$$

These spins could be arranged on a lattice with d = 1,2 or 3. The maximum magnetic entropy associated with Ising spins with effective $S = 1/2$ is given by equation (1.38).

1.4 Bulk magnetism: interacting moments

Having discussed the importance of the local environment and the main kinds of magnetic interactions, the resultant phenomena in bulk magnetic materials are discussed in this section.

1.4.1 Ferromagnetism

Ferromagnetism refers to the existence of spontaneous magnetisation in the absence of magnetic field, due to exchange interactions. For a ferromagnet in an applied magnetic field, the Hamiltonian is given by:

$$\hat{H} = -\sum_{ij} J_{ij}\mathbf{S}_i \cdot \mathbf{S}_j + g\mu_B \sum_j \mathbf{S}_j \cdot \mathbf{B} \tag{1.49}$$

In the Weiss model of ferromagnetism, a molecular field simulating the effect of magnetic ordering in the system, $\mathbf{B}_{mf} = \lambda\mathbf{M}$ is considered where $\mathbf{M}$ is the magnetisation and λ is the parameter denoting the strength of the molecular field. It can be shown that below a certain temperature T_c, non-zero magnetisation occurs even in the absence of applied magnetic field and this increases with decrease in temperature. The magnetisation is zero for $T \geq T_C$ and non-zero for $T < T_C$. The magnetisation is continuous at $T = T_C$ but the gradient is discontinuous; thus the phase transition from a paramagnetic to ferromagnetic phase is a second order phase transition. The transition temperature, T_c, is called the Curie temperature and is given by:

$$T_C = \frac{g_J\mu_B(J+1)\lambda M_{sat}}{3k_B} = \frac{N_A\lambda\mu_{eff}^2}{3k_B} \tag{1.50}$$

and the molecular field is given by:

$$B_{mf} = \lambda M_s = \frac{3k_B T_C}{g_J\mu_B(J+1)} \tag{1.51}$$

The origin of the molecular field is the exchange interaction, which is an electrostatic effect. The molecular field is a way of simulating the effect of the exchange interaction and the parameter λ can be related to the exchange interaction J_1. If it is assumed that the exchange interaction is only effective over z nearest neighbours of a magnetic ion with a constant value J_1, then:

$$\lambda = \frac{2zJ_1}{N_A g_J^2 \mu_B^2} \tag{1.52}$$

and the Curie-temperature is written as:

$$T_C = \frac{2zJ_1 J(J+1)}{3k_B} \tag{1.53}$$

This equation is valid for most $3d$ ions where the orbital moment is quenched, that is, $L = 0$ so $J = S$. However, for $4f$ ions, which are the main focus of this thesis, $\mathbf{S}$ is not a good quantum number but $\mathbf{J}$ is a good quantum number. Hence the component of $\mathbf{S}$ parallel to $\mathbf{J}$, $(g_J - 1)\mathbf{J}$, is conserved. Therefore λ is given by:

$$\lambda = \frac{2zJ_1 (g_J - 1)^2}{N_A g_J^2 \mu_B^2} \tag{1.54}$$

and the Curie temperature is given by:

$$T_C = \frac{2zJ_1 (g_J - 1)^2}{3k_B} J(J+1) \tag{1.55}$$

When a small magnetic field is applied at $T \geq T_C$, a small magnetisation will be generated. The magnetic susceptibility is then given by:

$$\chi = \frac{C}{T - T_C} \tag{1.56}$$

where C is the Curie constant as defined previously. This is known as the Curie-Weiss law.

1.4.2 Antiferromagnetism

If the exchange interaction J_{ij} in equation (1.49) is negative, the molecular field favours antiparallel alignment of nearest neighbour magnetic moments. In the Weiss model, such antiferromagnetic systems can be modelled as two interpenetrating sublattices, where the moments on one sublattice are antiparallel to the other. The molecular fields are given by $B_{+(-)} = -|\lambda| M_{-(+)}$ where λ is now negative. In the absence of a magnetic field, there is a transition temperature above which the molecular field on each sublattice will disappear. This is the Néel temperature, T_N, defined by:

$$T_N = \frac{g_J \mu_B (J+1)|\lambda| M_{sat}}{3k_B} = \frac{N_A |\lambda| \mu_{eff}^2}{3k_B} \tag{1.57}$$

The two magnetisations of the sublattices will be in opposite directions and hence the net magnetisation, $M_+ + M_-$, would be zero.

Application of a small magnetic field at $T \geq T_N$ results in a magnetic susceptibility:

$$\chi = \frac{C}{T+\theta} \tag{1.58}$$

If only nearest neighbour interactions are considered, $\theta = T_N$, the Néel temperature but usually $T_N < \theta$ as further neighbour interactions also play a role. For an antiferromagnet, T_N can usually vary between $\theta/2$ to $\theta/4$.

1.4.3 General form of magnetic susceptibility

The results of the previous sections are generalised as follows: A Curie-Weiss temperature, θ_{CW}, denoting the temperature scale of the magnetic ordering is defined. In the paramagnetic regime, when $T >> \theta_{CW}$, thermal fluctuations dominate and the reciprocal molar susceptibility obeys the Curie-Weiss law. From the $\frac{1}{\chi}$ vs T curve, a fit to the Curie-Weiss law can be carried out at high temperatures:

$$\frac{1}{\chi} = \frac{T-\theta_{CW}}{C} \tag{1.59}$$

The magnetic moment and the dipolar interactions can be calculated from C using equation (1.26) and equation (1.42). If θ_{CW} is negative, it denotes antiferromagnetic exchange interactions whereas if it is positive, it denotes ferromagnetic exchange interactions. A schematic of the susceptibility and reciprocal susceptibility for a typical paramagnet, ferromagnet and antiferromagnet is shown in Figure 1.1.

For the complex lanthanide oxides discussed in this thesis, nearest neighbour interactions between the Ln^{3+} ions are expected to be superexchange interactions mediated by oxygen ligands. An order of magnitude approximation for the nearest neighbour exchange interaction energy, J_1, for the Ln^{3+} can be obtained from the Curie-Weiss temperature using the mean-field theory approximation (this assumes that further neighbour interactions can be neglected compared to nearest neighbour interactions) [17]:

$$J_1 = J_{nn}S(S+1) = \frac{3k_B\theta_{CW}}{2n} \tag{1.60}$$

where n is the number of nearest neighbour Ln^{3+} surrounding one Ln^{3+} ion and J_{nn} is the scale of the interaction.

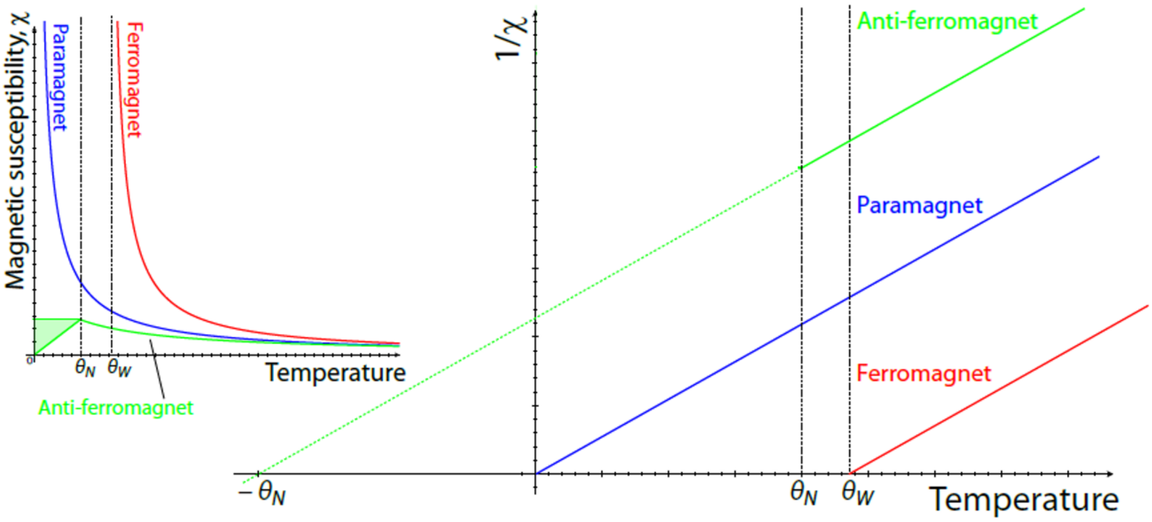

Figure 1.1 Magnetic susceptibility, χ, and the reciprocal susceptibility, χ^{-1}, as a function of temperature for different kinds of magnetic materials. The y intercept for the $\chi^{-1}(T)$ graph is $T = 0$ for a paramagnet, $T = \theta_W > 0$ for a ferromagnet and $T = \theta_N < 0$ for an antiferromagnetic material. Image taken from [16].

1.4.4 Ferrimagnetism

In the Weiss model for an antiferromagnet, the magnetisation of the two sublattices are assumed to be equal and opposite in sign. However there may be cases where although the magnetisation is of opposite sign, the two sublattices are not equivalent and so the magnetisations will not cancel out. This means the material will have a net spontaneous magnetisation, although weaker than a ferromagnet. This phenomenon is known as ferrimagnetism.

As the molecular field on the two sublattices is different, the spontaneous magnetisation has a complicated temperature dependence. Sometimes one sublattice magnetisation dominates at lower temperatures whereas the other takes precedence at higher temperatures; in such cases the magnetisation can be zero and change sign at an intermediate temperature known as the compensation temperature, T_{comp}. The magnetic susceptibility of a ferrimagnet also has a more complex temperature dependence than the Curie-Weiss law. The ferrimagnetic Curie temperature, $T_{C,ferri}$ is given by:

$$T_{c,ferri} = \mu\sqrt{C_A C_B} \tag{1.61}$$

where C_A and C_B are the individual Curie constants for the ions on the two magnetic sublattices, denoted by A and B respectively and μ is the strength of antiparallel interaction between A and B sites. The material is ferrimagnetic for $T < T_{C,ferri}$ and paramagnetic for

$T >> T_{C,ferri}$. The magnetic susceptibility for $T > T_{C,ferri}$ is given by [4]:

$$\chi = \frac{(C_A + C_B)T - 2\mu C_A C_B}{T^2 - T^2_{C,ferri}} \tag{1.62}$$

The curvature in the plot of the inverse susceptibility as a function of temperature is a characteristic feature of a ferrimagnet.

1.4.5 Field-induced magnetic transitions

In an antiferromagnet, as the field is gradually increased, the nature of the field-induced transitions depends on the direction of the applied field relative to the initial direction of the magnetisation of the sublattice. Such transitions are generally known as metamagnetic transitions and can be first or second-order depending on the magnetocrystalline anisotropy. Bulk magnetic materials exhibiting field-induced transitions can be classified as isotropic or weakly anisotropic and highly anisotropic. Field-induced transitions in the first class of materials typically involve rotations of spins whereas in the highly anisotropic materials, they involve simple reversal of spin directions.

The first kind are often referred to as spin-flop transitions. When the applied magnetic field is parallel to the initial sublattice magnetisations, the system remains in the antiferromagnetic phase at low fields but at a critical field, $B_{spin-flop}$, the spins suddenly rotate into a different configuration, with the moments canted away from the easy axis. This is a first-order transition to the spin-flop phase. After this , as the field is increased further, there is a second-order transition where the canting of the spins goes continuously to zero until the magnetic moments all align with the field [3, 18]. However for strongly anisotropic materials, the anisotropy prevents any rotation of the spins. The field-induced transitions in such cases are called spin-flip transitions, where the magnetisation of one sublattice abruptly reverses for a critical value of the magnetic field, $B_{spin-flip}$, and the system transitions into a ferromagnetic state. It is characterised by a first-order transition from a state with low magnetisation to a state with high magnetisation on application of a small magnetic field at low temperatures [3, 18].

1.4.6 Spin glasses

A spin glass is a disordered magnetic system, usually with competing magnetic interactions (e.g. ferromagnetic and antiferromagnetic), where there is random but cooperative freezing of spins at a particular temperature, T_f. A spin glass is paramagnetic well above T_f. However, below T_f, it exists in a metastable state with the spins frozen into a random arrangement, distinct from usual long-range order. It is metastable because the stable configuration that the spins are frozen into is distinct from the minimum energy state. Spin glasses are often found in systems where there is random site dilution or other forms of site disorder (such as CuMn [19] or AuFe alloys [20]) as well as systems in which there is bond randomness (such as URh_2Ge_2 [21] and $Fe_{1-x}Mn_xTiO_3$ [22]). Key experimental signatures of a spin glass include a) deviation in the zero-field cooled (ZFC) and field-cooled (FC) DC magnetic susceptibility below the freezing temperature and b) slow dynamics at temperatures below T_f, manifested as long relaxation times in the measurement of the AC susceptibility. More comprehensive reviews of examples and properties of spin glasses can be found in [23–26]. Recent studies have proposed different categories of magnetic glassy materials based on non-equilibrium relaxation dynamics [27, 28]. One such state is a spin jam, where the glassy state is induced by quantum fluctuations in a frustrated magnet like $SrCr_{9p}Ga_{12-9p}O_{19}$ [29, 30] (the concept of geometrical frustration will be elaborated in the next section).

1.5 Geometrically frustrated magnets (GFMs)

The concept of frustration was first used for spin glasses [31–33] to denote competing interactions that cannot be minimised simultaneously; for example, in a system with bond randomness, the nearest neighbour interactions vary between $-J_1$ and $+J_1$, leading to frustration. In spin glasses, disorder and frustration exist simultaneously because the disordering in the lattice gives rise to frustrated interactions. However, it is possible to have 'clean' and periodic systems where the structure alone can 'frustrate' the competing interactions. Such materials are said to exhibit geometrical frustration [17]. Figure 1.2 shows the different classes of magnetic materials based on the interplay between disorder and frustration.

Geometrically frustrated lattices are those in which the underlying geometry of the magnetic lattice prevents all the pairwise magnetic interactions from being satisfied simultaneously. The canonical example of geometrical frustration is that of Ising spins coupled by nearest neighbour antiferromagnetic exchange on a triangular lattice, first studied by Wannier in 1950 [34]. Two spin configurations are considered: A square and an equilateral triangular plaquette, both with Ising spins at the vertices coupled by nearest neighbour antiferromagnetic exchange interactions, Figure 1.3. For the square plaquette, each spin can be aligned antiparallel with all its neighbours and hence it is unfrustrated. On a triangular lattice, this is not possible as all the pairwise antiferromagnetic interactions among the three spins cannot be satisfied. Hence this system is frustrated purely because of the incompatibility of the magnetic interactions with the geometry of the magnetic lattice [2].

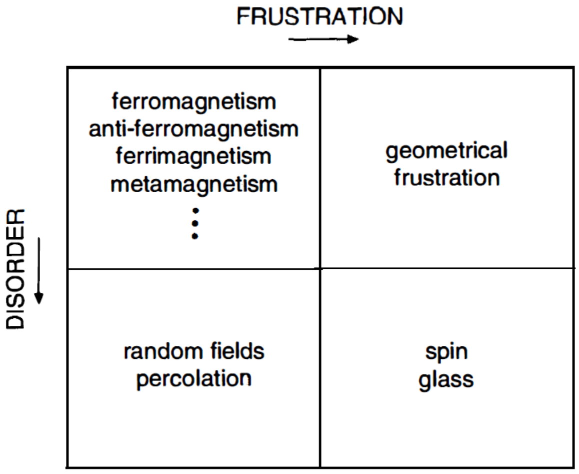

Figure 1.2 Different classes of magnetic materials arising from the interplay between disorder and frustration. Image taken from [17].

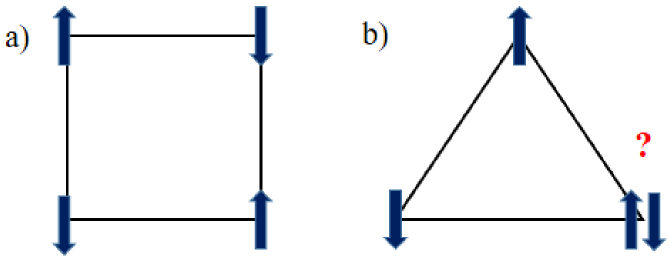

Figure 1.3 Ising spins coupled by antiferromagnetic exchange on a) a square b) an equilateral triangle. Spins are denoted by blue arrows.

Two consequences of this inability to satisfy all the pairwise interactions are a large degeneracy in the number of possible ground states (there is no unique ground state) and a suppression of the magnetic ordering temperature or, in ideal cases, complete absence of long-range ordering. The frustration index, f, for a material is defined as [17]:

$$f = \left| \frac{\theta_{CW}}{T_0} \right| \tag{1.63}$$

where θ_{CW} is the Curie-Weiss temperature and T_0 is the temperature at which any kind of cooperative magnetic ordering sets in. A material is said to be a strongly geometrically frustrated magnet when $f \geq 10$ [17].

Frustrated geometries are not limited to two dimensions or triangular plaquettes. In three dimensions, the tetrahedron consisting of four edge-sharing equilateral triangles is frustrated as only two of the four nearest neighbour antiferromagnetic interactions can

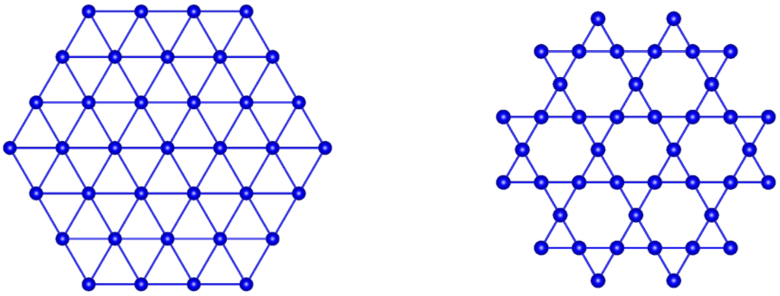

Triangle Kagome

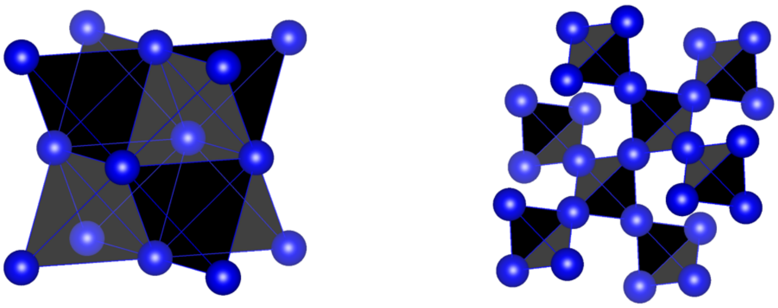

FCC Pyrochlore

Figure 1.4 Common frustrated lattice geometries.

be satisfied simultaneously. The most commonly frustrated lattices consist of triangular or tetrahedral geometries. In two dimensions, frustrated lattices include planes of edge-sharing or corner-sharing equilateral triangles and are referred to as ‘triangular’ and ‘kagome’ lattices respectively. Examples of three-dimensionally frustrated lattices are the fcc lattice (three-dimensional analogue of the triangular lattice) consisting of edge-sharing tetrahedra and the pyrochlore lattice (three-dimensional analogue of the kagome lattice) consisting of corner-sharing tetrahedra. These commonly known frustrated plaquettes are shown in Figure 1.4.

In frustrated systems, a delicate balance among competing interactions determines the ultimate magnetic ground state. Even slight perturbations may cause instabilities and drastically alter the properties of such systems [2]. Depending on the relative magnitude of competing interactions (symmetric and antisymmetric exchange interactions, dipolar interactions, crystal electric field (CEF) effects, lattice distortions), the system may be driven into a long range ordered state, thus relieving the frustration, or remain in a disordered, but dynamical, strongly correlated regime. It is the latter case which leads to exotic states of matter like spin ice or spin liquids [2, 35]. It is interesting to note that the lifting of degeneracy may also proceed through thermal or quantum fluctuations instead of external perturbations, through a process known as ‘order by disorder’ [36–38]. Over the years, the study of frustrated magnetism has

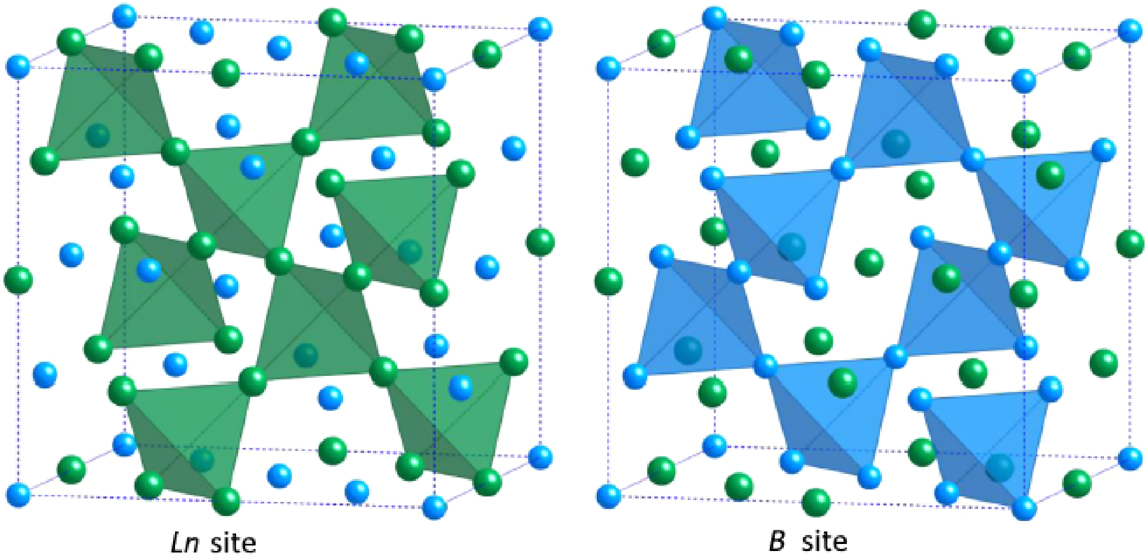

Figure 1.5 The *Ln* (green) and *B* (blue) sublattices forming interpenetrating networks of corner-sharing tetrahedra in the lanthanide pyrochlores. Image taken from [46].

evolved into a vast and rapidly developing field of condensed matter physics with discovery of new frustrated materials, observation of exotic magnetic phenomena and development of novel experimental techniques and theoretical models to study the fundamental magnetic behaviour of these materials. Discussion of such a vast field is beyond the scope of this thesis, and, for a more complete review of frustrated systems, one can refer to [17, 39–43]. Instead, since lanthanide oxides are the subject of investigation in this thesis, the magnetic properties of some frustrated lanthanide oxide families will be discussed briefly.

1.5.1 $Ln_2B_2O_7$

The lanthanide pyrochlores are the most widely investigated family of frustrated lanthanide oxides. They have the general formula $Ln_2B_2O_7$ where *Ln* is a trivalent lanthanide ion and *B* generally is a tetravalent ion which can be magnetic or non-magnetic. The pyrochlores crystallise in a cubic structure where the magnetic Ln^{3+} and the B^{4+} ions lie on two distinct interpenetrating lattices of corner-sharing tetrahedra, Figure 1.5. There are many tetravalent ions that can occupy the *B* site for a particular Ln^{3+}: a more complete review of the possible structural combinations can be found in [44]. There is a wide variety in the observed magnetic properties of the lanthanide pyrochlores depending on the interplay of the exchange interaction, dipolar interaction and single-ion anisotropy of the magnetic Ln^{3+} ion as well as the nature of the ion on the *B* site; an extensive review is presented in [45]. Here some key advances in the field of frustrated magnetism in lanthanide pyrochlores will be mentioned.

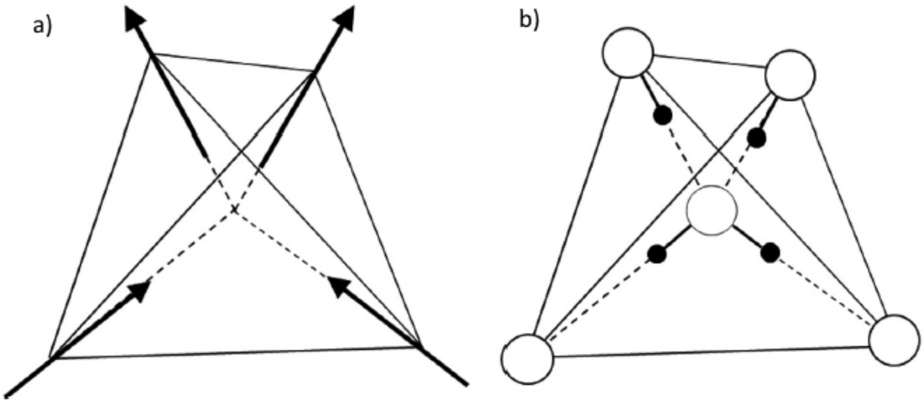

Figure 1.6 Comparison of the local spin constraints obeyed in spin ice and the Bernal-Fowler ice rules: a) Magnetic Ln^{3+} spins on a tetrahedron locally obey the 2-in 2-out rule (spins are denoted by arrows). b) This maps exactly onto the arrangement of hydrogen ions in water ice forming 2 long 2 short O-H bonds (hydrogen ions are denoted by small black spheres and oxygen ions are shown by large white spheres). Image taken from [46].

The Ising antiferromagnet on a pyrochlore lattice was first considered by Anderson [47]. Later Villain showed that the pyrochlore lattice shows strong geometrical frustration for nearest neighbour antiferromagnetic exchange between Heisenberg spins [48]. He also defined the term ‘collective paramagnet’ which is a disordered strongly correlated state of fluctuating spins. Nowadays this is also referred to as a ‘classical spin liquid’. Thus Anderson [47] and Villain [48] predicted the absence of long-range order at non-zero temperatures for Ising and Heisenberg pyrochlore antiferromagnets respectively but experimental realisations of such spin liquid states proved elusive. For Ising systems, due to the cubic symmetry, there is no energetic reason for a global Ising direction being physically meaningful whereas in Heisenberg pyrochlore antiferromagnets such as $Gd_2Ti_2O_7$ and $Gd_2Sn_2O_7$, the dipolar interactions compete with the exchange interactions, driving the system to a long-range ordered state [45, 49, 50]. Perhaps the most significant experimental breakthrough in the study of frustrated pyrochlores came with the discovery of spin ice. In 1997, Harris et. al [51] showed that geometrical frustration was possible for ferromagnetic interactions on a pyrochlore lattice for the material $Ho_2Ti_2O_7$. Neutron scattering experiments showed no long range order down to 0.35 K but short-range ferromagnetic correlations were observed. More remarkably, the spin configurations on individual tetrahedra was shown to exactly map on to the O-H bonds in the hexagonal phase of water ice at ambient pressure. Later Ramirez et. al [52] showed that the value of zero point entropy in another spin ice material $Dy_2Ti_2O_7$ was identical to that obtained by Pauling for water ice [53]. A more comprehensive review of the development of spin ice can be found in [45, 54–56].

$Ln_2B_2O_7$ (Ln = Dy, Ho; B = Ti, Sn, Ge) are known as the classical dipolar spin ices [52, 54, 56–59]. They have large magnetic moments $\approx 10\mu_B$ and the crystalline electric field (CEF) is such that the ground state is an effective $S = 1/2$ doublet at low temperatures. The nearest neighbour interactions are antiferromagnetic but the competing dipolar interactions play a significant role, giving rise to net ferromagnetic interactions. The CEF gives rise to a strong $\langle 111 \rangle$ Ising anisotropy which frustrates the ferromagnetic interactions such that in each tetrahedra, the spins locally obey a '2 in 2 out' constraint (analogous to the Bernal-Fowler ice rules [55]), Figure 1.6, giving rise to a residual entropy at absolute zero. The classical spin ices are examples of the cooperative paramagnet (or classical spin liquid) state proposed by Villain [48] as the spins have short-range correlations (the local constraint being the '2 in 2 out' ice rule) but experience strong fluctuations driven by thermal energy. At sufficiently low temperatures ($\approx$ 1 K), the spins freeze due to the activation barrier between the different ice-rule satisfying ground states [35, 56].

In the spin ices, the net magnetic charge at the centre of each 'tetrahedron' is zero. This local constraint can be mapped to a divergence-free condition of an emergent gauge field; this belongs to a wider class of Coulomb phases [60, 61]. The novelty lies in the fact that if one of the spins flip on a tetrahedra (called a defect), this results in '3 in 1 out' or '1 in 3 out' spin configurations giving rise to a net magnetic charge at the centre of the tetrahedron. Thus the classical dipolar spin ices host magnetic monopole excitations. This was predicted theoretically by Castelnovo et. al [62] and shown experimentally by Fennell et. al [63] and Morris et. al [64]. Bramwell et. al [65] subsequently demonstrated the phenomenon of magnetricity in $Dy_2Ti_2O_7$: they showed that the magnetic charges propagated in this material and generated actual measurable currents. Study of the classical dipolar spin ices have also led to the development of 'artificial spin ice', which has greater implications for practical applications based on these materials [66–68].

If the spin ice state exhibits quantum fluctuations, it could lead to an experimental realisation of a quantum spin liquid state. The term quantum spin liquid was first used by Anderson for describing the ground state of an $S = 1/2$ Heisenberg antiferromagnet on a triangular lattice, which he called a resonating valence bond state [69]. Although Anderson's proposition was not completely correct (the Heisenberg spins can align at 120° leading to Néel order), the search for experimental realisations of quantum spin liquids and resonating valence bond (RVB) states has continued unabated. This is because in quantum spin liquids, the quantum fluctuations of spins (which prevent long-range order) can be phase coherent leading to highly entangled spin states. These can host exotic ground states and non-local fractionalised excitations. More complete reviews of quantum spin liquids can be found in [35, 70–72] but here the discussion will be restricted to quantum spin ice. This is a quantum spin liquid state with gapless photon-like excitations, arising from quantum fluctuations acting on the spin ice states [56, 73]. A detailed review of quantum spin ice can be found in [56] but here the discussion will focus on three candidate materials: $Tb_2Ti_2O_7$, $Yb_2Ti_2O_7$ and $Pr_2Zr_2O_7$.

$Tb_2Ti_2O_7$, which shows dynamic spin fluctuations down to 0.05 K without any magnetic ordering, was the first material for which the term quantum spin ice was used [74]. Since then, the magnetic properties have been studied extensively but the exact nature of the low temperature ground state has remained a matter of debate [75–81]. The complexity has been compounded by the fact that the magnetic properties are highly sample dependent and minute variations in the stoichiometry can drive the system to a long-range ordered state [82]. Similar sample dependence of the properties is observed for $Yb_2Ti_2O_7$ for which several studies have reported features consistent with a quantum spin ice state [83–87] but the magnetic ground state and nature of interactions remains contentious [88–92]. $Pr_2Zr_2O_7$ also shows evidence of quantum spin ice behaviour [93] but further studies of the magnetic ground state and interactions have only recently begun gaining momentum [94–96]. Overall, the presence of a quantum spin ice state in $Tb_2Ti_2O_7$, $Yb_2Ti_2O_7$ and $Pr_2Zr_2O_7$ cannot be ruled out at this stage.

The discussion of the exotic magnetic behaviour in lanthanide pyrochlores will be concluded with two final examples. The first is the appearance of quantum order-by-disorder in the XY pyrochlore $Er_2Ti_2O_7$ [97–101]. In this material, the XY anisotropy and exchange interactions result in an ‘accidental’ degeneracy. Quantum mechanical spin fluctuations break this degeneracy, resulting in a ground state selection by entropic and not energetic considerations and magnetic ordering at $T = 1.2$ K. This is the only known experimental realisation of order by disorder in frustrated pyrochlores. The second example is one that has only recently been reported: the phenomenon of magnetic fragmentation in spin ice. In 2014, Brooks-Bartlett et. al [102] theoretically proposed that in presence of dipolar interactions and for sufficiently high monopole densities, the magnetic moment field in spin ice could fragment into two parts: a divergence-free Coulomb spin liquid and a magnetic monopole crystal with a non-zero divergence. This was experimentally observed for $Nd_2Zr_2O_7$ [61]. Lefrancois et. al demonstrated an alternative route to achieving fragmentation in $Ho_2Ir_2O_7$ where the staggered field from the Ir^{4+} spins competes with the spin ice state resulting in fragmentation at $T \leq 2$ K [103].

1.5.2 $Ln_3A_2Sb_3O_{14}$

The frustrated kagome lattice, consisting of corner-sharing triangles in two dimensions, has been theoretically predicted to host exotic magnetic phases such as the quantum spin liquid state [104–106]. However, for a long time, there were no candidate materials containing magnetic rare-earth ions. One exception were the langasites $Ln_3Ga_5SiO_{14}$, *Ln* = Pr, Nd, consisting of ‘pinched’ kagome planes [107, 108] where the absence of long-range order down to the lowest temperatures has been interpreted as a spin liquid state or a non-magnetic ground state for *Ln* = Pr [109, 110] and as a spin liquid or paramagnetic ground state for *Ln* = Nd [111–113]. However, these materials did not possess structurally perfect kagome lattices.

The breakthrough came with the discovery of the $Ln_3A_2Sb_3O_{14}$ family of materials where *A* = Mg, Zn, Co, Mn [114–118]. These materials crystallise in a rhombohedral structure which is closely related to the $Ln_2B_2O_7$ pyrochlore structure. The pyrochlore structure can be viewed along [111] as Ln_3B and B_3Ln layers consisting of kagome planes of *Ln* and *B* with *B* and *Ln* in non-kagome positions respectively, Figure 1.7a. In contrast to the pyrochlore structure which has magnetic ions connecting its kagome layers, substitution of non-magnetic *A* cations (e.g. *A* = Mg, Zn) in $Ln_3A_2Sb_3O_{14}$ gives rise to fully ordered kagome planes of Ln^{3+} separated by non-magnetic cations, Figure 1.7b. The rare-earth ions lie on an ideal kagome lattice, Figure 1.7c, with $A : Ln$ on the pyrochlore *Ln* site and $A : Sb$ on the pyrochlore *B* site in a ratio 1:3. $Ln_3A_2Sb_3O_{14}$ (*Ln* = Mg, Zn) are the first experimental realisation of an ideal two-dimensional kagome system containing magnetic Ln^{3+} [116, 118]. There is very low *Ln*/*A* site disorder ($\approx$ 1 - 5%) in $Ln_3Mg_2Sb_3O_{14}$ for all *Ln*. The site disorder is low for most $Ln_3Zn_2Sb_3O_{14}$ except for *Ln* = Ho, Er, Yb where there are indications of significant *Ln*/Zn site disorder ($\approx$ 40 - 60%) [119]. Such extreme site disorder destroys the well-separated *Ln* kagome layers, leading to the formation of a three-dimensional cation disordered pyrochlore where *Ln*/Zn are disordered over each cation site [119].

Extensive research into the magnetic properties of $Ln_3Mg_2Sb_3O_{14}$ and $Ln_3Zn_2Sb_3O_{14}$ has begun only recently [118, 119] but already several interesting results have been reported. Two specific cases will be discussed here. The first is the appearance of an all-in all-out order in $Nd_3Mg_2Sb_3O_{14}$ [120]. Heat capacity measurements on this material reported a sharp λ type anomaly at 0.56 K, consistent with a peak in the AC susceptibility [119, 120]. Neutron diffraction measurements below the magnetic transition revealed three-dimensional antiferromagnetic ordering with the moments pointing ‘all-in’ or ‘all-out’ in the kagome triangles. This structure could be visualised as the two-dimensional kagome analogue of the all-in all-out ordering observed in the pyrochlore $Nd_2Sn_2O_7$ [119, 121]. The second case is emergent charge order observed for $Dy_3Mg_2Sb_3O_{14}$ [122]. Heat capacity measurements on $Dy_3Mg_2Sb_3O_{14}$ report a sharp transition at $\approx$ 0.3 K [116, 122] with a zero-point entropy of $\frac{1}{3}\ln\frac{9}{2}\mathrm{R}\ \mathrm{mol}_{\mathrm{Dy}}^{-1}$ while neutron scattering experiments show coexistence of strong magnetic diffuse scattering with Bragg peaks down to the lowest temperatures ($\approx$ 0.05 K). These are

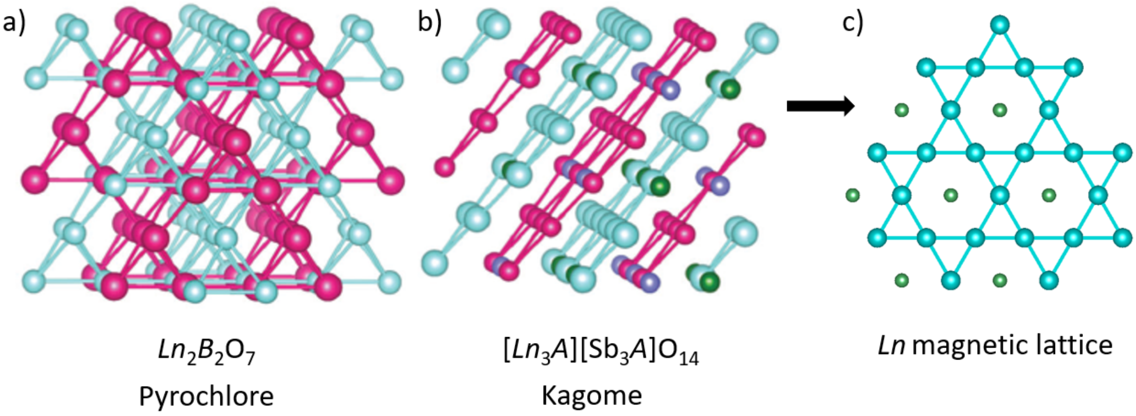

Figure 1.7 Comparison of the cubic pyrochlore $Ln_2B_2O_7$ structure with the rhombohedral kagome $Ln_3A_2Sb_3O_{14}$ structure. a) In $Ln_2B_2O_7$, networks of *Ln* (cyan) and *B* (pink) tetrahedra constitute the pyrochlore structure. b) In $Ln_3A_2Sb_3O_{14}$, substitution of *A* ions (purple, green) leads to the formation of well-separated kagome layers. Oxygens are not shown in both structures for clarity. Image taken from [118]. c) The *Ln* magnetic kagome lattice. Image adopted from [118].

both signatures of an emergent charge ordered state which can be understood as follows: The Dy^{3+} Ising spins point towards or away from the centre of the triangle in the kagome planes. The spins can be considered as two separated + and - magnetic charges and the emergent charge in a triangle is the the algebraic sum over the three charges it contains, Figure 1.8a. In the emergent charge ordered state, the net magnetic charge in a triangle alternates between +1 and -1, Figure 1.8b. However, the three-fold degeneracy of the spin states for each charge remains, meaning that that there is ordering of the emergent charges in the triangle, but not the individual spins. The spins continuously fluctuate between the possible emergent charge ordered microstates, resulting in an average all-in all-out Bragg structure with an effective moment of $\mu_{avg} = \frac{1}{3}\mu_{net}$, Figure 1.8c [122]. The partial spin order in the emergent charge ordered state can also be conceptualised in terms of fragmentation (discussed in the previous section) [102], as the sum of two independent components: the average Bragg structure with non-zero divergence and the divergence-free spin fluctuations [122]. Such fragmentation was reported in artifical kagome spin ice [123] but the observation in a bulk material like $Dy_3Mg_2Sb_3O_{14}$ is quite unique and opens a promising new field of research.

1.5.3 $SrLn_2O_4$

The $SrLn_2O_4$ family of materials crystallise in a orthorhombic structure where the connectivity of the magnetic Ln^{3+} can be visualised as a network of hexagons and triangles [108, 124], Figure 1.9. The frustration arises from the ziglag ladders along the *c* axis that link the

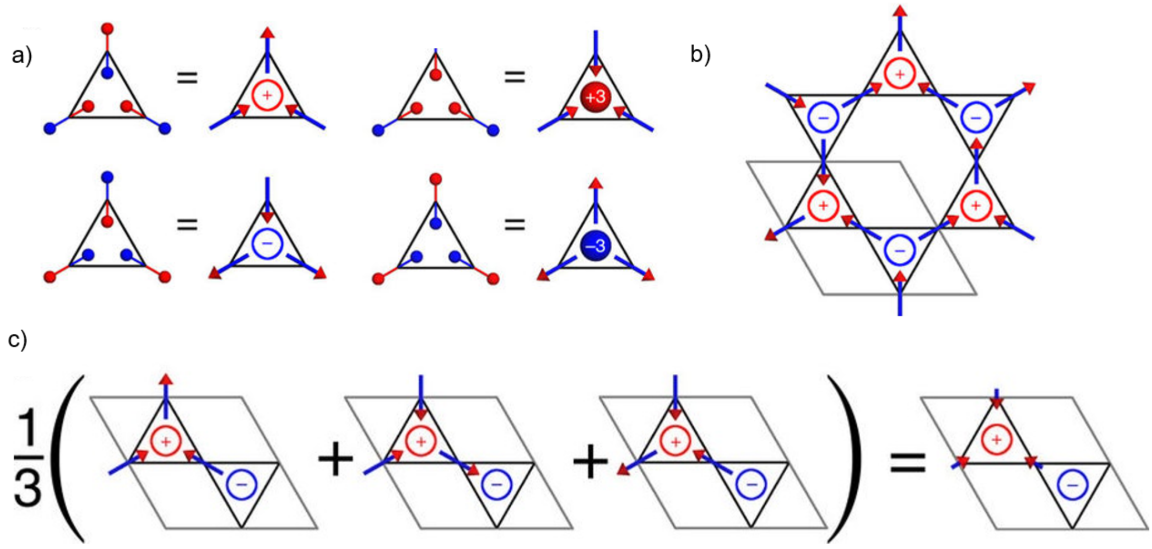

Figure 1.8 Emergent charge order in $Dy_3Mg_2Sb_3O_{14}$: a) The relationship between spin vectors (arrows), magnetic dipoles (connected red and blue spheres) and emergent charge of a triangle (labelled ± or ±3). b) Example of a possible microstate showing emergent charge order. c) Average of the possible microstates results in an all-in all-out Bragg structure with an effective moment of $\mu_{avg} = \frac{1}{3}\mu_{net}$. Image taken from [122].

honeycomb layers, analogous to β-$CaCr_2O_4$ [125, 126]. A brief overview of the magnetic properties will be presented here but a more complete review can be found in [127].

$SrGd_2O_4$ has two magnetic ordering transitions at 0.48 K and 2.73 K; this has been postulated to arise from the interplay between exchange and dipolar interactions [128]. Neutron diffraction experiments on $SrTb_2O_4$ report an incommensurate antiferromagnetic ordering below $T_N = 4.28$ K with partially ordered moments arising from one of the two inequivalent Tb sites [129]. $SrDy_2O_4$ shows no long range magnetic ordering down to 0.02 K and only broad diffuse scattering is observed in neutron diffraction experiments [130, 131]. Muon spectroscopy measurements on $SrDy_2O_4$ have reported features consistent with a spin liquid state [132] but it shows long-range order in applied magnetic field [131, 133]. In $SrEr_2O_4$, long range antiferromagnetic order with $\mathbf{k}$ = (0, 0, 0) and moments pointing along the c axis coexists with short-range order in an incommensurate structure below T_N =0.75 K [134, 135]. Long and short range magnetic order are also found to coexist in $SrYb_2O_4$ [136] below T_N =0.9 K. However, the long-range ordered structure is a $\mathbf{k}$ = (0, 0, 0) non-collinear antiferromagnet with moments in the $a-b$ plane while the short-range ordering has not been analysed in further detail. The case for $SrHo_2O_4$ is rather interesting. Initial studies had reported the coexistence of $\mathbf{k}$ = (0, 0, 0) long range antiferromagnetic order and short range magnetic correlations below T_N =0.68 K [137, 138], similar to that reported for $SrEr_2O_4$ and

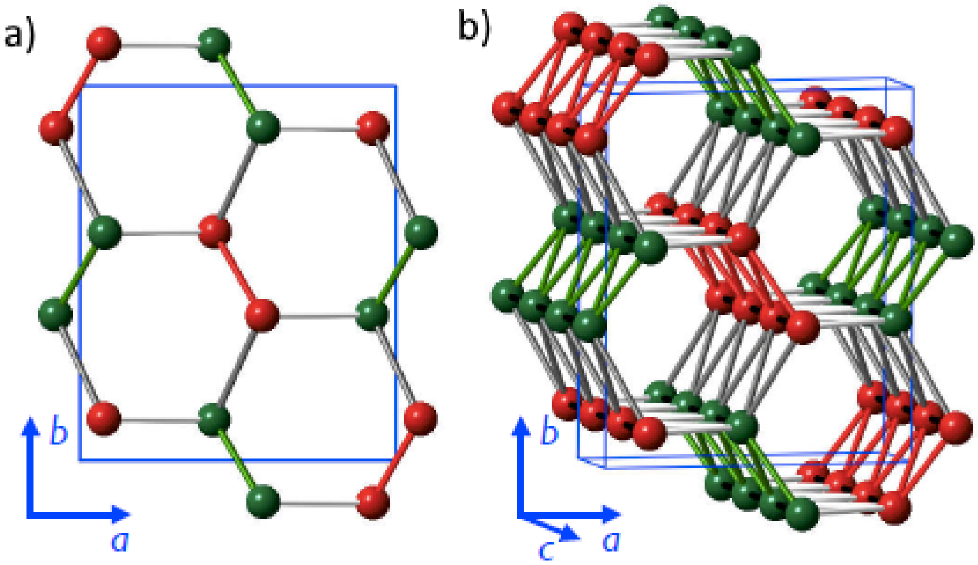

Figure 1.9 Connectivity of Ln^{3+} in $\mathrm{Sr}Ln_2\mathrm{O}_4$ with the two crystallographically inequivalent *Ln* sites shown in red and green: a) Honeycomb-like arrangement of Ln^{3+} along the *c* axis. b) Zigzag ladders along *c* axis giving rise to geometrical frustration. Image taken from [127].

$\mathrm{SrYb_2O_4}$. However later more detailed investigations using neutron scattering experiments on single crystals revealed the unique coexistence of two types of short-range magnetic ordering below 0.7 K: the first type of diffuse magnetic scattering has propagation vector $\mathbf{k} = (0, 0, 0)$ and the second appears as planes of scatttering intensity at $(h\ k\ \pm\frac{1}{2})$ [139].

The $\mathrm{Sr}Ln_2\mathrm{O}_4$ family exhibits a wide variety of magnetic behaviour, similar to the lanthanide pyrochlore and kagome families. Modelling of the magnetic interactions is highly challenging due to the complex three-dimensional frustrated geometry. Determining the precise crystal electric field scheme poses another challenging problem due to the low symmetry of the Ln^{3+} site [127]. Further in-depth investigations of the $\mathrm{Sr}Ln_2\mathrm{O}_4$ family is another continuously evolving field of exploration in research on frustrated magnetism in complex lanthanide oxides.

1.5.4 $\mathrm{Gd_3Ga_5O_{12}}$

Gadolinium gallium garnet (GGG), $\mathrm{Gd_3Ga_5O_{12}}$, was established as a geometrically frustrated magnet as early as the 1980s with a Weiss temperature $\theta_{CW} \approx -2$ K and no magnetic long range ordering down to 0.025 K [140, 141]. In $\mathrm{Gd_3Ga_5O_{12}}$, the magnetic $\mathrm{Gd^{3+}}$ lie at the vertices of corner-sharing triangles, forming a highly frustrated lattice in three dimensions, Figure 1.10. $\mathrm{Gd_3Ga_5O_{12}}$ is a part of a larger family of materials called the lanthanide garnets.

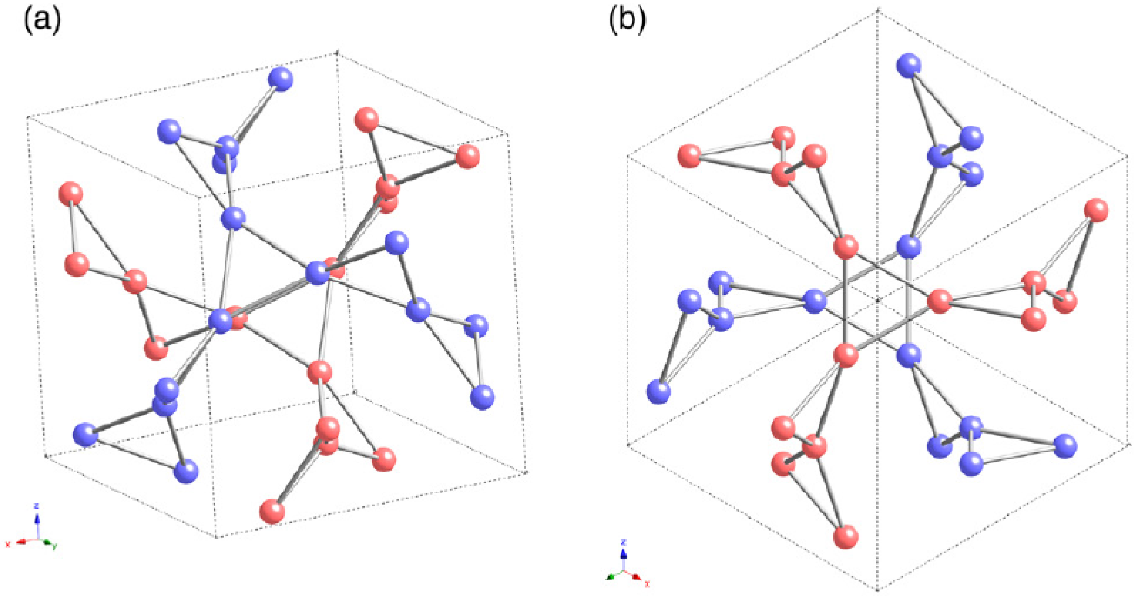

Figure 1.10 Connectivity of Gd^{3+} in $Gd_3Ga_5O_{12}$ forming interpenetrating ten-membered rings of corner-sharing triangles: a) seen along [010]. b) seen along [111]. The Gd^{3+} in the two rings are shown in blue and red. Image taken from [142].

The discussion of the structure and magnetic properties of these materials forms a key component of the results chapters in this thesis and so an in-depth discussion is reserved for Chapters 3 and 4. Here, only the properties of $Gd_3Ga_5O_{12}$ will be discussed.

In $Gd_3Ga_5O_{12}$, a spin liquid state with short range spin fluctuations is observed from 5 K down to $\approx$ 0.14 K below which the spins freeze into a 'glassy state' [143, 144]. However neutron diffraction experiments have shown that although the state below $\approx$ 0.14 K has a longer correlation length, it is more consistent with a mixed spin liquid/solid state, also referred to as a 'spin slush' state [145]. Muon spectroscopy measurements have shown persistent spin fluctuations down to the lowest temperatures, showing absence of static order, although the studies do not agree on the nature of slowing of the spin fluctuations [146, 147]. However, AC susceptibility measurements have reported unconventional glassy behaviour that is more consistent with an ordering transition [148]. Inelastic neutron scattering measurements have reported three gapped dispersionless excitations and coexistence of different timescales corresponding to dimerised short-range antiferromagnetic correlations and cooperative paramagnetism [149]. A recent neutron scattering study on $Gd_3Ga_5O_{12}$ has revealed a hidden non-dipolar order in the spin liquid state. The order is long-ranged with a diverging correlation length, forming multipoles from ten-membered loops of spins and results from the subtle interplay between nearest neighbour antiferromagnetic correlations and local XY anisotropy [150]. Another recent study has shown that doping with $\approx 1\%$ Nd^{3+} in $Gd_3Ga_5O_{12}$ increases the frustration in the lattice [142].

Just as the exact nature of the magnetic ground state of $Gd_3Ga_5O_{12}$ remains elusive, the in-field behaviour poses an equal challenge. An early study of the magnetic phase diagram revealed a strongly anisotropic antiferromagnetic dome with the transition temperature and field range varying with direction of applied field [141]. This was corroborated by a later study which showed that in an applied magnetic field of ≈ 1 T, antiferromagnetic ordering was observed below ≈ 0.38 K [151]. On further investigation, it was reported that in addition to the 'glassy' phase in 0 T and antiferromagnetic 'dome' in fields 0.7 - 1.4 T, there is an intermediate field phase which has characteristics of a spin liquid. The phase boundary between the intermediate field and antiferromagnetic phases was reported to have a distinct minimum at 0.18 K, analogous to the minimum in the melting curve of ^4He [152]. Recent studies have revealed a more complex phase diagram with multiple phase boundaries, competing interactions among spins and emergent loops of trimers and decagons [153]. Another recent investigation has reported the existence of dispersionless spin waves on the ten-membered rings in high magnetic fields above 1.8 T and coexistence of antiferromagnetic and incommensurate order in fields below 1.8 T [154].

It is clear that much remains to be explored about the magnetic ground state and magnetic phase diagram of $Gd_3Ga_5O_{12}$. Very recent studies have begun using alternative experimental techniques to understand the magnetic behaviour. One study has used sound velocity measurements to show that the magnetic field response in $Gd_3Ga_5O_{12}$ is highly anisotropic with two field-induced antiferromagnetic phases in fields parallel to [110] and only one field-induced antiferromagnetic phase in fields parallel to [100]. Additionally they have observed evidence for a spin gap in the excitation spectrum in the spin liquid phase [155]. Another study has investigated the short-range magnetic order in $Gd_3Ga_5O_{12}$ using the spin Seebeck effect, which has been shown to give rise to spin currents. In smaller fields, modulations in the spin Seebeck effect have been shown to be consistent with the field-induced antiferromagnetic ordering while additional modulations are observed in high magnetic fields ≈ 9 T, paving the way for further investigations in the high-field regime of the magnetic phase diagram [156].

1.5.5 $YbMgGaO_4$

In 2015 Li et. al reported the discovery of a quantum spin liquid candidate, $YbMgGaO_4$, which contains perfect triangular layers of magnetic Yb^{3+}, Figure 1.11, with effective $S = 1/2$ and antiferromagnetic exchange between nearest neighbour spins ($\theta_{CW} \approx -4$ K). The compound showed no magnetic long-range ordering or evidence of spin freezing down to 60 mK and zero residual spin entropy, indicating that a possible quantum spin liquid ground

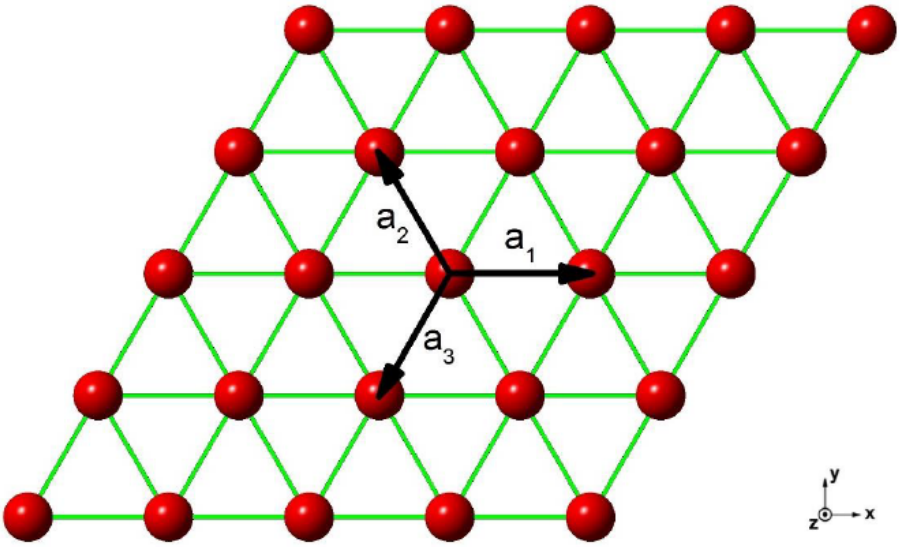

Figure 1.11 Connectivity of Yb^{3+} (red spheres) in $YbMgGaO_4$ forming a triangular lattice in the $a-b$ plane. Image taken from [158].

state had been achieved [157]. Since then, a number of efforts have been made to establish the exact nature of the ground state and the relevant magnetic interactions that play a role in determining the ground state.

Shen et. al [159] reported the presence of diffusive magnetic excitations in inelastic neutron scattering measurements with an upper excitation edge, consistent with a spinon Fermi surface and a U(1) quantum spin liquid state. Muon spin relaxation experiments [160] and theoretical investigations [161, 162] provided further evidence for a gapless U(1) quantum spin liquid ground state in $YbMgGaO_4$. However, a thermal conductivity study reported the absence of any contribution from magnetic excitations and a magnon gap of the fully polarised state in field, which was inconsistent with the spinon Fermi surface hypothesis [163]. Measurements on single crystals of $YbMgGaO_4$ and preliminary theoretical investigations reported highly anisotropic magnetic interactions, dependent on the bond orientations due to the spin-orbit entanglement [164, 165].

Paddison et. al [166] noted that there were other mechanisms for stabilising the quantum spin liquid state such as further neighbour-interactions, entanglement induced by disorder and multiple spin excitations. Inelastic neutron scattering measurements by Paddison et. al showed a continuum of excitations consistent with a quantum spin liquid state. Modelling of the interactions showed that the quantum spin liquid state was stabilised by further neighbour interactions, spin anistropy and the disorder between Mg^{2+}/Ga^{3+} [166]. Separate theoretical studies proposed that chemical disorder in $YbMgGaO_4$ can induce stripe superposition domains that mimic a quantum spin liquid state [167, 168]. Another single crystal inelastic neutron scattering study confirmed the presence of nearest neighbour resonating valence bond correlations [158], consistent with Anderson's initial proposition for a quantum spin liquid state [69]. A very recent investigation has attempted to resolve the exchange interactions in $YbMgGaO_4$ using complementary information from time-domain THz spectroscopy and inelastic neutron scattering measurements in the field polarised state [169]. The study places strong constraints on the ratio of interactions required for a quantum spin liquid state and concludes that alternative mechanisms such as spin liquid mimicry could be possible explanations for the ground state magnetic behaviour of $YbMgGaO_4$. The study of $YbMgGaO_4$ is thus a rapidly evolving field and the question of whether the ground state is a true quantum spin liquid or not remains open to further investigation.

1.6 Low temperature magnetic refrigeration

Having discussed the fundamental magnetic properties of some geometrically frustrated lanthanide oxides, this section will focus on a key practical application of such materials being explored in this thesis: solid state magnetic refrigeration at temperatures close to absolute zero, which is currently achieved using non-renewable liquid heium.

Many areas of fundamental and applied scientific research including spintronics and quantum computing as well as devices such as magnetic resonance imaging (MRI) or computed tomography (CT) scanners and cryogenic sensors (such as those in space detectors) require cooling to low temperatures. This is usually achieved using liquid cryogens such as liquid nitrogen for $T > 80$ K, liquid helium (^{4}He) for $T > 2$ K or a mixture of ^{3}He and ^{4}He for cooling down to 20 mK [170]. However, helium, a by-product obtained during the extraction of natural gas, is a non-renewable source which is gradually becoming scarce and increasingly expensive (the ^{3}He isotope is even less abundant) [171]. This means that sustainable alternatives to cooling using liquid helium must be explored. One such alternative is solid state magnetic cooling using adiabatic demagnetisation refrigerators (ADRs) which are based on the principle of the magnetocaloric effect (MCE) in magnetic materials [172].

The magnetocaloric effect (MCE) is the adiabatic change in temperature of a material on application or removal of an external magnetic field. It is due to the coupling of the magnetic sublattice with the magnetic field, changing the magnetic entropy in the solid. Thus it can be characterised by the isothermal change in magnetic entropy ΔS_m [173]. The MCE was discovered by Weiss and Pickard and later Giaque and MacDougall reached temperatures below 1 K using adiabatic demagnetisation of $Gd_2(SO_4)_2 \cdot 8\,H_2O$ [174]. Figure 1.12 shows a schematic of a magnetic refrigeration cycle using the MCE. During adiabatic demagnetisation, the magnetic entropy of the material increases but as the total entropy

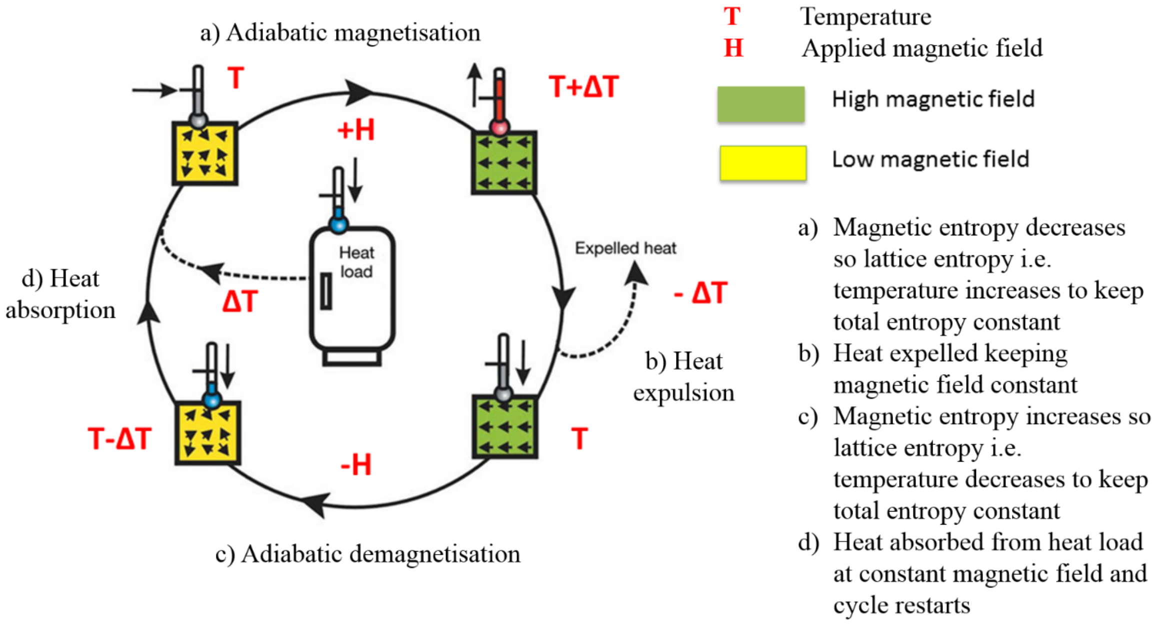

a) Magnetic entropy decreases so lattice entropy i.e. temperature increases to keep total entropy constant
b) Heat expelled keeping magnetic field constant
c) Magnetic entropy increases so lattice entropy i.e. temperature decreases to keep total entropy constant
d) Heat absorbed from heat load at constant magnetic field and cycle restarts

Figure 1.12 Schematic of a magnetic refrigeration cycle using the magnetocaloric effect (MCE). Image adopted from [175].

remains constant, the lattice entropy and hence the temperature decreases. In the final stage, the magnetic refrigerant absorbs heat from the load in a constant magnetic field to reach its original temperature and hence cools the system.

The MCE is measured in terms of the isothermal change in magnetic entropy ΔS_m given by [176]:

$$\Delta S_m = \int_0^{\mu_0 H_{max}} \left(\frac{dM}{dT}\right)_H dH \tag{1.64}$$

As seen from equation (1.64) the MCE will increase when M and (dM/dT) are large. dM/dT would have a maximum at the magnetic ordering temperature when there is a phase transition. Therefore, materials utilised for magnetic refrigeration in the liquid helium temperature range should have a large magnetic moment and order at low temperatures (since the cooling limit is determined by the magnetic ordering temperature, T_0, of the material). A more in-depth review of the magnetocaloric effect can be found in [173]. Reviews of efficient magnetic refrigerant materials in various temperature regimes from room temperature down to temperatures close to absolute zero can be found in [175, 177, 178].

ADRs using dilute paramagnetic salts were used to cool down to temperatures of few mK as early as the 1930s [179–181]. Nowadays, paramagnetic salts commonly used for cooling are cerium magnesium nitrate (CMN), chromium potassium alum (CPA) and ferric ammonium alum (FAA). In these salts, the presence of non-polar water molecules isolates the magnetic ions and suppresses the ordering temperature to the order of a few mK [178]. However, the poor chemical stability of these materials make them less viable for widespread practical applications. A different approach is to use ceramic materials which have geometrically frustrated magnetic lattices [182]. As discussed in a previous section, geometrically frustrated magnets typically show ordering features at $T_0 \approx \theta_{CW}/10$ where θ_{CW} is the Curie-Weiss temperature, thereby suppressing the ordering temperature [17]. In complex lanthanide oxides, the highly localised $4f$ orbitals have weak magnetic interactions, i.e. θ_{CW} is small and so when the magnetic lattice is frustrated, ordering is suppressed to even lower temperatures or completely absent in certain cases. Further, the theoretical magnetic entropy that can be extracted is much higher than in transition metal compounds. Geometrically frustrated materials with Ln^{3+} ions are therefore ideal magnetocaloric materials (MCMs) for cooling to liquid helium temperatures. Another advantage is that the lanthanides are chemically very similar but their magnetic properties vary widely. This leads to the possibility of tuning the chemical composition for optimisation of the MCE [183–185].

The frustrated magnet gadolinium gallium garnet (GGG) (discussed in a previous section) is a well-known MCM for magnetic refrigeration in the liquid helium temperature regime [178]. The absence of long range ordering, high density of magnetic ions, chemical stability and lack of single-ion anisotropy ($L = 0$ for Gd^{3+}) allowing for the full magnetic entropy ($R\ln(2J+1)$ = 17.29 $\mathrm{J\,K^{-1}\,mol_{Gd}^{-1}}$) to be extracted in high magnetic fields makes it an ideal magnetic refrigerant for cooling to temperatures below 20 K [141, 183, 186–188]. An early compilation of possible Gd^{3+} based MCMs is given in [183]. In recent years, several Gd^{3+} containing MCMs with better magnetocaloric performance than GGG at T = 2 K have been reported such as $Gd(HCOO)_3$ [189], $Gd(OH)CO_3$ [190], $GdPO_4$ [191], $Gd(OH)_3$ [192], GdF_3 [193] and recently $K_3Li_3Gd_7(BO_3)_9$ [194]. Of these materials, GdF_3 has been reported to have the maximum MCE in a field of 7 T at T = 2 K, Table 1.3. In addition to the weak exchange and dipolar interactions that suppress magnetic ordering to very low temperatures, the light mass and relatively high densities of the polyanion frameworks lead to high MCE in gravimetric or volumetric units. This opens the possibility of obtaining efficient magnetocaloric materials in other Gd^{3+} containing polyanion frameworks, which will be explored in this thesis.

For all the Gd^{3+} based magnetocaloric materials, the change in magnetic entropy is maximized in fields of 5 T or higher. Such high magnetic fields can only be produced using a superconducting magnet which again requires cooling using liquid helium. In order to eliminate the need for cryogens altogether, one needs to develop materials with high MCE in fields $\leq$ 2 T, attainable using more commonly available permanent magnets. In 1986, Li et. al showed that dysprosium aluminium garnet (DAG), $Dy_3Al_5O_{12}$, isostructural with

Table 1.3 Changes in magnetic entropy at 2 K, 7 T for selected Gd^{3+} based MCMs, data taken from [193] and [194].

Compound	$-\Delta S_m$	
	$\mathrm{J\,kg^{-1}\,K^{-1}}$	$\mathrm{mJ\,cc^{-1}\,K^{-1}}$
$Gd_3Ga_5O_{12}$	38.4	272
$Gd(HCOO)_3$	55.9	216
$Gd(OH)CO_3$	66.4	355
$GdPO_4$	62.0	376
$Gd(OH)_3$	62.0	346
GdF_3	71.6	506
$K_3Li_3Gd_7(BO_3)_9$	56.6	279.2

GGG, was a promising magnetic refrigerant in the temperature range 4.2 - 20 K and had a higher magnetocaloric efficiency than $Gd_3Ga_5O_{12}$ in magnetic fields below 2 T [195]. The higher magnetocaloric effect was attributed to the strongly anisotropic g factor in $Dy_3Al_5O_{12}$ leading to Ising Dy^{3+} spins, which experience larger changes in the magnetic entropy at low fields as compared to $Gd_3Ga_5O_{12}$ which contains isotropic Gd^{3+} spins [178, 184, 195]. In larger magnetic fields, the use of $Gd_3Ga_5O_{12}$ was found to be more advantageous. This is because the crystal electric field in $Dy_3Al_5O_{12}$ leads to an effective $S = 1/2$ doublet, limiting the maximum magnetic entropy that can be extracted to Rln2 (= 5.76 $\mathrm{J\,K^{-1}\,mol_{Dy}^{-1}}$) whereas for $Gd_3Ga_5O_{12}$, negligible crystal electric field effects mean that the full magnetic entropy (= 17.29 $\mathrm{J\,K^{-1}\,mol_{Gd}^{-1}}$) can be extracted in higher magnetic fields [178, 184]. However, $Dy_3Al_5O_{12}$ undergoes a sharp antiferromagnetic transition at T = 2.49 K [196], limiting its use in cooling below 2 K. Dysprosium gallium garnet (DGG), isostructural with GGG and DAG, undergoes magnetic ordering at T = 0.373 K [197] and like DAG, the ground state is an effective $S = 1/2$ doublet with $\Delta S_{mag,max}$ = Rln2. Crystal electric field investigations of DGG have indicated quasi-planar nature of Dy^{3+} spins [198]. Therefore DGG offers the same advantage of higher magnetocaloric efficiency in fields below 2 T as DAG due to the substantial single-ion anisotropy of the Dy^{3+} spins with the additional benefit of cooling down to much lower temperatures [199]. Numazawa et. al showed that DGG is a better MCM than GGG in fields below 2 T [200]. A more recent investigation by Saines et. al [201] on the magnetocaloric properties of $Ln(HCOO)_3$ has also shown that the MCE in $Tb(HCO_2)_3$ is significantly higher than $Gd(HCO_2)_3$ at higher temperatures and lower fields as the Tb^{3+} have Ising-like spins in contrast to the Heisenberg nature of the Gd^{3+} spins. Another key focus of this thesis will be exploring the impact of changing the single-ion anisotropy of the magnetic lanthanide ion on the magnetocaloric properties of complex lanthanide oxides.

Although this thesis focuses entirely on ceramic oxide materials, the discussion on low temperature magnetic refrigeration would remain incomplete without the mention of lanthanide intermetallics. All the dilute paramagnetic salts as well as ceramic oxide magnetic refrigerants discussed so far are thermally insulating which poses a great challenge for the ADR design. Usually the magnetocaloric material has to be enclosed in a mesh of thermally conducting silver wire or metallic canister to enhance the thermal conductivity and allow for good thermal contact and proper thermalisation [170, 202, 203]. In contrast, intermetallics have good thermal conductivities and can be directly used in ADRs without the need for silver [204]. Therefore if one could develop lanthanide intermetallics with magnetocaloric efficiencies comparable to ceramics, it would offer significant advantages in terms of ADR design, efficiency and cost. Two recent advances in this field for cooling to temperatures below 2 K are discussed here.

Jang et. al reported a large magnetocaloric effect in the intermetallic compound $YbPt_2Sn$ for cooling from 2 K down to 0.25 K [204]. Although the MCE in volumetric units (127 $mJ\,cc^{-1}\,K^{-1}$) was lower than GGG (363 $mJ\,cc^{-1}\,K^{-1}$), it was significantly higher than the dilute paramagnetic salts CPA (42 $mJ\,cc^{-1}\,K^{-1}$) and FAA (52 $mJ\,cc^{-1}\,K^{-1}$). The cooling limit, 0.25 K, was higher than the temperatures of a few mK reached using dilute paramagnetic salts but lower than GGG (0.8 K) and DGG (0.4 K). This was attributed to the unique weak magnetic coupling between Yb atoms which inhibited ordering at higher temperatures. Therefore $YbPt_2Sn$ offered a balanced tradeoff between simultaneously attaining low temperatures and achieving high magnetocaloric efficiency. Further, being a good metal, it was thermally conducting and could be cast into different shapes, allowing for direct implementation in an ADR as an alternative to a ^{3}He cryostat.

Another intermetallic, $YbCo_2Zn_{20}$, was shown to be an efficient magnetic refrigerant for cooling from 2.5 K to $\approx$ 0.2 K [205]. More remarkably, the study demonstrated optimisation of the cooling power by altering the chemical pressure in the material $Yb_{1-x}Sc_xCo_2Zn_{20}$ through partial Sc substitution. The magnetocaloric effect was further enhanced in the Sc substituted materials allowing cooling well below 0.1 K. In particular, a minimum temperature of 0.04 K could be achieved for $x = 0.19$. The study highlighted the importance of intermetallics as viable alternatives to refrigeration without cryogens at ultra-low temperatures, $T < 1$ K and altering the chemical pressure to optimise the cooling limit. The impact of chemical pressure on the magnetocaloric effect of a specific class of lanthanide oxide ceramics will be explored in this thesis.

1.7 Overview of thesis

In this thesis, two main research themes have been followed. The first is a systematic study of a known geometrically frustrated system: the lanthanide garnets with the general formula $Ln_3A_2X_3O_{12}$, a family of three-dimensionally frustrated materials where the magnetic Ln^{3+} ions are located at the vertices of corner-sharing triangles which form two interpenetrating networks of bifurcated ten membered rings. Previous investigations have mainly focussed on one member of this family: the canonical spin liquid candidate gadolinium gallium garnet (GGG) [149, 150], which is also an efficient magnetocaloric in fields above 5 T [183]. In this thesis, the magnetic properties of other lanthanide garnets with substantial single-ion anistropy have been studied to explore the possibility of observing unique magnetic ground states as well as developing efficient magnetocalorics in fields below 2 T. Further, other Gd based garnets have been studied as they could show different magnetic behaviour and improved magnetocaloric efficiencies as compared to GGG. A variety of approaches have been adopted to study the magnetic properties through chemical control of the structure, including changing the magnetic lanthanide ion, variation of the non-magnetic cations in the lattice (defined as changing the chemical pressure) and introduction of additional spins through partial substitution on the non-magnetic cation sites. The crystal structure, bulk magnetic properties and the magnetocaloric efficiency of the materials so prepared have been investigated.

The second theme has been exploring new complex lanthanide oxide systems both for their novel magnetic properties as well as for magnetic refrigeration purposes. The magnetism and magnetocaloric performance of two families of lanthanide borates have been studied for the first time: the lanthanide orthoborates, $LnBO_3$, and the lanthanide metaborates, $Ln(BO_2)_3$. In $LnBO_3$, the magnetic Ln^{3+} form a slightly distorted edge-sharing triangular lattice, a prototype for two-dimensional frustration. Recent reports point to unique physics associated with such two-dimensional frustrated geometries of lanthanide spins, such as a possible quantum spin liquid state and emergent charge order [122, 159]. Therefore the lanthanide orthoborates are promising candidates for exhibiting novel magnetic phases. The other family studied, lanthanide metaborates, contain one-dimensional chains of magnetic lanthanide ions, leading to the possibility of observing exotic properties associated with quasi-one-dimensional magnetism such as spin liquid states, quantum phase transitions and multiple magnetisation plateaux associated with quantum tunnelling of the magnetisation [206, 207]. Additionally, the possibility of using the lanthanide borates as efficient magnetocalorics for refrigeration in the liquid helium temperature regime has been explored.

The thesis is organised as follows: The current chapter, Chapter 1, contains a general introduction while Chapter 2 describes the experimental methods used in this thesis. Chapters

3 - 6 contain results of the research undertaken. The results of tuning the fundamental magnetic properties and magnetocaloric performance in the lanthanide garnets through changes in the single-ion anisotropy and chemical pressure are discussed in Chapter 3 while the impact of partially introducing other magnetic ions on the non-magnetic cation sites are elaborated in Chapter 4. Chapters 5 and 6 contain results on the magnetic and magnetocaloric properties of the lanthanide orthoborates and lanthanide metaborates respectively. Finally, a summary of the key results and future outlook is presented in Chapter 7.

Chapter 2

Experimental methods

This chapter describes the experimental techniques used for the research presented in this thesis. Details specific to the materials will be discussed in subsequent chapters.

2.1 Solid state synthesis

Materials were synthesised by ceramic (solid state) methods [208] where two or more (usually non-volatile) solid reactants are heated together at high temperatures to form the final product. Stoichiometric amounts of the reactants are weighed out, ground in a mortar and pestle to get a homogeneous mixture and finally heated in a furnace for a prolonged period of time in alumina crucibles to complete the reaction. Typically $\approx$ 1 g of the desired material was prepared. However, for neutron scattering experiments, larger batches of $\approx$ 3 - 5 g of products were synthesised.

Solid state reactions occur at the interface of the reactant solids. After the surface layer has reacted, the reactants diffuse from the bulk to the interface. Therefore it is extremely important to grind the starting materials properly and mix them well to increase the surface area in contact and reduce the distance that the particles need to diffuse. Direct contact between the crystallite faces can be increased by pressing the mixed powders into pellets using a hydraulic press.

The reaction time is usually measured in hours but a particular reaction may take several days. During this time, the mixture may be reground to bring new surfaces in contact and reheated several times. Intermediate grindings as well as increasing the temperature can reduce the diffusion pathways and aid the solid state reaction. This is continued until a phase-pure product is formed as determined from powder X-ray diffraction.

The optimal conditions for a solid state reaction such as time taken, number of intermediate grindings, temperature steps and % of excess starting material needed (if any) depend on the material. They are adapted from references for synthesis of similar materials and modified accordingly.

A slightly different mechanism was implemented for the synthesis of the lanthanide orthoborates and lanthanide metaborates discussed in this thesis. The starting materials namely boric acid and lanthanide oxide powders were weighed out, mixed, and a pre-reaction was carried out by heating to 350°C and holding for 2 hours. Boric acid melts during the heating and forms B_2O_3 on dehydration. This acts like a 'self-flux' with the lanthanide oxide dissolving in the B_2O_3 melt, forming a $Ln_2O_3{\cdot}xB_2O_3$ glass. This glassy intermediate product is ground and mixed again prior to the final heat treatment at temperatures between $\approx 900-1050$°C. During the final heating, the reaction proceeds via usual solid state diffusion of the powders.

2.2 Structural characterisation

2.2.1 Crystal systems

Crystals can be classified using symmetry operations. A crystal is a solid containing a repeating array of atoms, ions, or molecules in three-dimensions with translational symmetry. Symmetry operations are those that leave an object invariant with respect to a clearly defined transformation. Symmetry operations include the identity, translation, proper rotation, inversion, reflection from a plane and improper rotation (which is a combination of proper rotation and inversion). In order to introduce a classification of crystal structures, the concept of lattice and unit cell is required. A lattice is an infinite array of points in three dimensions, generated using translational invariance. It is a purely mathematical construct but serves as the fundamental way of quantitatively describing crystal structures containing actual atoms or molecules or ions. The primitive translation vector **T** is defined as [4, 209]:

$$\mathbf{T} = n_1\mathbf{a} + n_2\mathbf{b} + n_3\mathbf{c} \tag{2.1}$$

Here n_i is an integer and **a**, **b**, **c** are vectors from a common origin such that **a**, **b** are non-collinear and **c** does not lie in the same plane as **a**, **b**. The lattice points are given by the end points of **T**. The crystal can be represented using a unit cell which is the smallest repeating entity used to generate the entire crystal structure in three-dimensions. The unit cell is the parallelopiped formed by the vectors **a**, **b**, **c** that encloses a volume $\mathbf{a} \cdot \mathbf{b} \times \mathbf{c}$. If a unit cell contains only one lattice point, it is a primitive unit cell. However, sometimes it is more convenient to describe a unit cell with more than one lattice point. This is due to ease of visualising stacking of cubes or cuboids as opposed to arbitrary geometries as well as to respect the underlying symmetry of a crystal structure. When a unit cell contains more than one lattice point, it is said to be a non-primitive unit cell. In the unit cell, the position of a point is expressed in terms of coordinates as fractions of the lengths of the unit cell. Thus a point (x, y, z) has the position vector ($x\mathbf{a}$, $y\mathbf{b}$, $z\mathbf{c}$) from the origin. Such fractional coordinates are also called atomic positions because they are used to denote the positions of the atoms in the crystal structure.

The concept of a reciprocal lattice in momentum space or reciprocal space can be defined; this is crucial in developing the formalism of scattering theory, crystal structures and magnetic structures. The term ‘reciprocal’ comes from the fact that the dimensions of the vectors in reciprocal space are inverse of length, that is ‘reciprocal’ of the dimensions of vectors in real space. The reciprocal lattice is the Fourier transform of a lattice in real space; the reciprocal lattice unit vectors $\mathbf{a}^*$, $\mathbf{b}^*$, $\mathbf{c}^*$ are related to the real space unit vectors $\mathbf{a}$, $\mathbf{b}$, $\mathbf{c}$ as [4]:

$$\mathbf{a}^* = 2\pi\frac{\mathbf{b}\times\mathbf{c}}{V_0} \qquad \mathbf{b}^* = 2\pi\frac{\mathbf{c}\times\mathbf{a}}{V_0} \qquad \mathbf{c}^* = 2\pi\frac{\mathbf{a}\times\mathbf{b}}{V_0} \tag{2.2}$$

where $V_0 = \mathbf{a}\cdot\mathbf{b}\times\mathbf{c}$ is the volume of the parallelepiped enclosed by the unit cell vectors in real space. Hence the relation $\mathbf{x}_i\cdot\mathbf{x}_j^* = 2\pi\delta_{ij}$ is satisfied where $x = a, b, c$ and δ_{ij} is the Kronecker delta symbol. One can define the reciprocal lattice vector $\mathbf{G}$ as:

$$\mathbf{G} = m_1\mathbf{a}^* + m_2\mathbf{b}^* + m_3\mathbf{c}^* \tag{2.3}$$

where m_i is an integer. Therefore the translation vector $\mathbf{T}$ and the reciprocal lattice vector $\mathbf{G}$ satisfy the relation $\exp(i\mathbf{G}\cdot\mathbf{T}) = 1$.

Lattice directions or planes can be uniquely represented by three integers h, k and l, known as Miller indices [4]. The notation (hkl) denotes the family of planes orthogonal to the reciprocal lattice vector $\mathbf{g}_{hkl} = h\mathbf{a}^* + k\mathbf{b}^* + l\mathbf{c}^*$ where $\mathbf{a}^*$, $\mathbf{b}^*$, $\mathbf{c}^*$ are the reciprocal lattice unit vectors. The related notation $[hkl]$ denotes the directions $\mathbf{t}_{hkl} = h\mathbf{a} + k\mathbf{b} + l\mathbf{c}$ where $\mathbf{a}$, $\mathbf{b}$, $\mathbf{c}$ are the unit cell lattice vectors in real space. $[hkl]$ and (hkl) are orthogonal to each other for a cubic lattice but this is not true for lattices with lower symmetry. Additionally, the notation $\{hkl\}$ denotes the family of planes equivalent to (hkl) by the lattice symmetry and $\langle hkl\rangle$ denotes the family of directions equivalent to $[hkl]$ by symmetry of the lattice. The integers Miller indices h, k, l usually have a greatest common divisor of 1 and negative integers are denoted by a bar.

When the basic symmetry operations are applied to a lattice, these impose certain constraints on the lattice parameters (denoted by a, b, c) and the interaxial angles (denoted by α, β, γ). Applying proper and improper rotations to the translation vectors generates seven crystal systems: triclinic, monoclinic, orthorhombic, tetragonal, cubic, hexagonal and

Table 2.1 The seven crystal systems and 14 Bravais lattices in three dimensions; note that here $\neq$ has to be taken to mean 'not necessarily equal to' since accidental equalities can always occur for crystal structures in actual materials [4, 209].

Crystal System	Unit cell dimensions and angles	Bravais lattices
Triclinic	$a \neq b \neq c$, $\alpha \neq \beta \neq \gamma \neq 90^\circ$	P
Monoclinic	$a \neq b \neq c$, $\alpha = \gamma = 90^\circ$, $\beta \neq 90^\circ$	P, C
Orthorhombic	$a \neq b \neq c$, $\alpha = \beta = \gamma = 90^\circ$	P, I, F, C
Tetragonal	$a = b \neq c$, $\alpha = \beta = \gamma = 90^\circ$	P, I
Cubic	$a = b = c$, $\alpha = \beta = \gamma = 90^\circ$	P, I, F
Hexagonal	$a = b \neq c$, $\alpha = \beta = 90^\circ$, $\gamma = 120^\circ$	P
Rhombohedral	$a = b = c$, $\alpha = \beta = \gamma \neq 90^\circ$	P

rhombohedral. In order to generate all the possible Bravais (distinct) lattices, in addition to the primitive unit cells (denoted by P), centering must be considered: these are body-centering (denoted by I), face-centering (denoted by F) and base-centering (denoted by C). If both the primitive unit cells and centering for the seven crystal systems are considered, it gives rise to 14 Bravais lattices in three dimensions; these are compiled in Table 2.1.

2.2.2 Crystallographic point groups and space groups

The formalism of crystallographic point groups and space groups is one of the most important concepts for classifying and understanding crystal structures. A group is defined as a set of mathematical operations carried out on elements subject to the following conditions:

(a) Closure: The product (here product refers to any general operation) of any two elements, X and Y belonging to the group, $XY = Z$, is also a member of the group.

(b) Existence of Identity: An element E exists in the group such that for any element X belonging to the group, the relation $EX = XE = X$ is obeyed.

(c) Existence of Inverse: For each and every element X in the group, there exists an element X^{-1} belonging to the group such that the relation $XX^{-1} = X^{-1}X = E$ is obeyed where E denotes the identity.

(d) Associativity: The product (again product refers to any general operation) is associative, that is, for any elements, X, Y and Z belonging to the group, $(XY)Z = X(YZ)$.

The number of elements in a group is known as its order. The set of symmetry operations described in the previous section satisfy all these conditions and form a group. There are 32 crystallographic point groups which can be generated using symmetry operations ('point' means that all the symmetry operations are carried out about one common fixed point, defined as the origin) [209]:

(a) 11 crystallographic point groups corresponding to proper rotations.

(b) Additional 11 centrosymmetric point groups obtained by adding inversion to each of the 11 pure rotation point groups.

(c) 10 distinct non-centrosymmetric subgroups.

Point groups describe the symmetry with respect to a specific point in the crystal and the Bravais lattices describe the symmetry of the unit cells. However, in order to completely describe the entire crystal structure in three dimensions, one needs to define a space group. A crystallographic space group is a complete set of symmetry operations that takes an entity periodic in three-dimensions into itself. In order to generate space groups, two new spatial symmetry operations must be defined in addition to point groups and Bravais lattices. These are screw rotations (proper rotation along with a non-primitive translation parallel to the rotation axis) and glide operations (reflection and translation). Crystallographic space groups can be classified as follows [209]:

(a) Symmorphic space group: Can be completely specified by the symmetry operations related to point groups and does not involve translation.

(b) Non-symmorphic space group: Requires at least one non-primitive translation operation.

In total, there are 230 space groups in three dimensions. 73 distinct symmorphic space groups can be obtained by combining the 32 point groups with the 14 Bravais lattices. If in addition non-symmorphic operations (screw rotations and glide reflections) are considered, the remaining 157 non-symmorphic space groups are generated.

2.2.3 Scattering experiments on crystals

Scattering experiments have emerged as one of the powerful probes to investigate the structure and magnetism in crystalline solids. In a scattering experiment, a beam of incident radiation (or equivalently particles, considering the wave-particle duality) impinge upon the sample and the proportion of incident radiation (or particles) that are scattered with a specified energy and momentum transfer are measured. Figure 2.1 shows the schematic of a particle being scattered by the sample. If the incident particle has a wavevector $\mathbf{k}_i$ and angular frequency

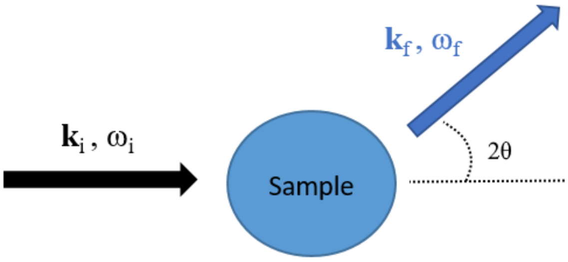

Figure 2.1 Schematic showing a basic scattering process. Image adopted from [210].

ω_i and the scattered radiation/particle has a wavevector $\mathbf{k}_f$ and angular frequency ω_f, the momentum transfer, $\mathbf{Q}$, is given by $\mathbf{k}_i - \mathbf{k}_f$ and the energy transfer to the sample, E, is given by $\hbar\omega = \hbar(\omega_i - \omega_f)$. The quantity measured in a scattering experiment is a function $\mathbf{S}(\mathbf{Q}, \omega)$ with four components, three for $\mathbf{Q}$ and one for ω. In general, a sample will undergo both elastic and inelastic scattering processes:

(a) Elastic scattering: No energy loss, $E = 0$. This implies that the magnitude of the wave vector remains constant on scattering and the magnitude of the momentum transfer $\mathbf{Q}$ is defined by the relation:

$$Q = \frac{4\pi \sin\theta}{\lambda} \tag{2.4}$$

where 2θ is the angle between the incident and scattered wave vectors.

(b) Inelastic scattering: Involve a finite loss in energy, $E \neq 0$.

In this thesis, only diffraction experiments, which are elastic scattering processes have been carried out and so, inelastic scattering will not be discussed in further detail. It is worth noting that diffraction measurements do not only measure purely elastic scattering (for which $E = 0$), but instead integrate over energy transfer (up to a maximum energy dictated by the energy of the incoming particle/wave). This assumes importance in the context of diffuse scattering, because it means that diffraction measurements can be used to study liquids or paramagnets, where the scattering has a finite energy width.

The nature of interactions of the incident radiation/particles with the sample also need to examined. The mechanism depends on the charge, spin, energy, etc of the incoming particles. Typical scattering experiments include electrons, X-rays or neutrons as incident probes [210]. Electrons are repelled by electrostatic forces of the orbital electrons of the atoms and therefore cannot penetrate beyond the surface of the material. Hence electron scattering is mainly a surface probe. Orbital electrons interact with X-ray photons via electromagnetic interactions: this effect is weaker than electrostatic repulsion and so, X-rays can be used to investigate the structure of bulk materials. Neutrons are not affected by the charge of orbital electrons

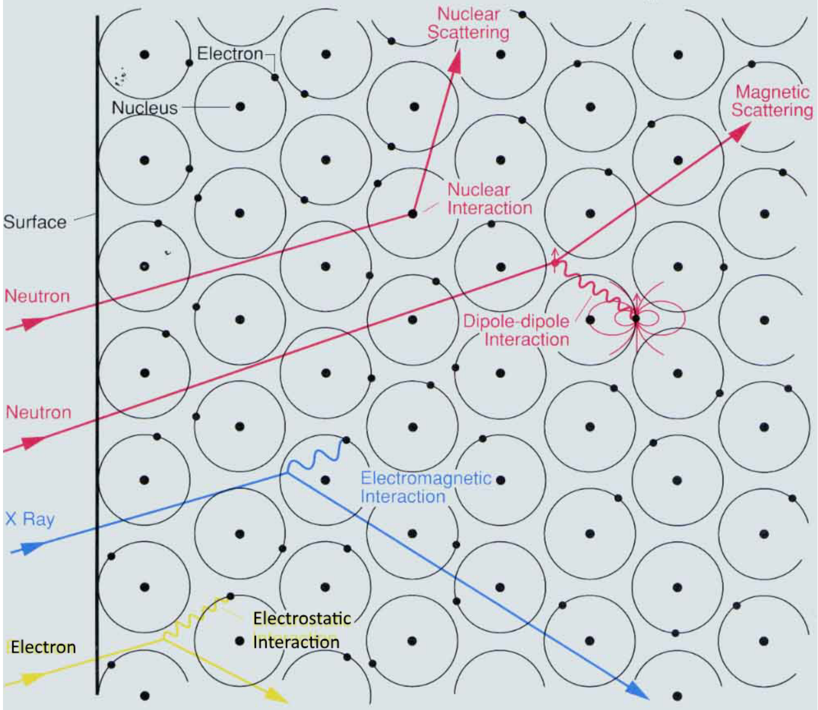

Figure 2.2 Schematic showing the basic interactions of incident particles with matter. Image taken from [211].

and are able to penetrate deeply, thus serving as an effective probe for the bulk properties. However, as they only interact with the atomic nuclei via the short-ranged strong nuclear force, the scattering signal is weaker as compared to X-rays. Neutrons also interact with the unpaired orbital electrons of paramagnetic atoms via the dipole-dipole spin interaction; this effect is negligible for electrons and X-rays as compared to electromagnetic or electrostatic interactions. Neutrons have thus emerged as one of the most effective probes for studying magnetic materials via scattering experiments. A schematic of these basic interactions of incoming particles with matter are shown in Figure 2.2. In this thesis, X-ray and neutron diffraction experiments have been carried out. The principles of diffraction with reference to X-rays and neutrons as well as details of structural and magnetic refinement procedures are described in the following sections.

2.2.4 Diffraction

Crystalline solids have a periodic array of atoms or ions or molecules with interatomic spacings of the order of magnitude of ≈ 1 Å. Due to the periodic arrangement of the structure, crystalline solids can act as three-dimensional diffraction grating to incident beam of radiation (X-rays or neutrons). Diffraction occurs when conditions for constructive interference are

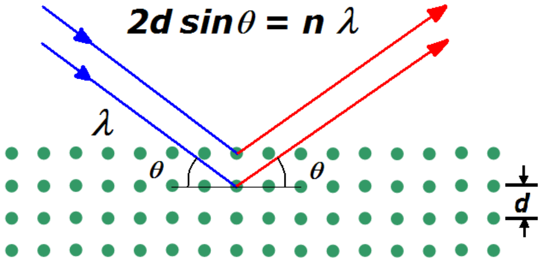

Figure 2.3 Schematic showing Bragg's law.

satisfied. When a crystal sample is placed in front of a monochromatic radiation beam, diffraction occurs for crystallite planes satisfying the Bragg condition, equation (2.5) [4].

$$2d\sin\theta = n\lambda \tag{2.5}$$

where θ is the angle at which the planes are oriented, d is the distance between the planes, λ is the wavelength of the incident radiation and n is an integer. The angle between the diffracted and incident beam is 2θ. This is shown in Figure 2.3.

One can also define Bragg's law in reciprocal space more concisely as $\mathbf{Q} = \mathbf{G}$ where $\mathbf{Q}$ and $\mathbf{G}$ are the scattering vector and reciprocal lattice vector respectively, defined in previous sections of this chapter. This reduces to equation (2.5) when the magnitudes of $\mathbf{Q}$ and $\mathbf{G}$ are substituted.

The structure factor F_{hkl} mathematically describes the amplitude and phase of a wave diffracted from crystal lattice planes with Miller indices (hkl) and is given by [4, 212]:

$$F_{hkl} = \sum_{j=1}^{n} f_j(\theta)\exp[2\pi i(hx_j + ky_j + lz_j)] \tag{2.6}$$

where (x_j, y_j, z_j) are the coordinates for the jth atom respectively and the summation is carried out over all the n atoms in the unit cell. The amplitude $f_j(\theta)$ is the atomic scattering factor or form factor for the jth atom that takes account of the number of electrons in the atom and the distribution of the electrons around the point (x_j, y_j, z_j). In general, $f_j(\theta)$ varies as a function of θ. The atomic scattering factor is different for X-rays and neutrons as shall be discussed in a later section.

The structure factor defined in equation (2.6) assumes that all the atoms present in the unit cell are stationary and that they are all located at their crystallographic (average) positions. However, when the temperature increases, the vibrations of the atoms from their mean positions increases. A thermal factor is introduced to include contributions from both thermal and static disorder. In the first approximation, the atomic displacements are assumed to be harmonic and the atomic scattering factor $f(\theta)$ for each atom is altered to incorporate the effect of broadening of the surrounding electron cloud according to the following equation:

$$f_{thermal} = f(\theta)\exp(\frac{-B_{iso}\sin\theta}{\lambda^2}) \tag{2.7}$$

where λ is the wavelength of the incident radiation and B_{iso} is known as the Debye-Waller factor or B factor, defined by the equation:

$$B_{iso} = 8\pi^2 < U_{iso}^2 > \tag{2.8}$$

where $< U_{iso}^2 >$ is the root mean-squared deviation of the jth atom from its mean position (x_j, y_j, z_j). B_{iso} has units of Å^2 and typically has values in the range 0.2 - 0.8 Å^2; this value increases with temperature. Equation (2.7) assumes isotropic B_{iso} values, that is, the thermal motion of the atom is same in all directions. It is also possible to model anisotropic Debye-Waller factors and generate thermal ellipsoids modelling the thermal motion of each atom. This analysis is much more challenging and typically requires single crystal samples to obtain unambiguous values though it is also possible to obtain anisotropic Debye-Waller factors for powders from high quality powder neutron diffraction data. All the results discussed in this thesis are for polycrystalline samples with no evident anisotropy and so the structural analysis has been carried out using isotropic B_{iso} values only.

One final point to consider while modelling the structure factor is that crystallographic sites in the structure may be partially occupied or there may be atomic disorder on a particular site. This can be included in the structure factor by defining N_j, a multiplier for the occupancy of the atomic site. The modified structure factor, incorporating the Debye-Waller factor and atomic disorder then becomes:

$$F_{hkl} = \sum_{j=1}^{n} f_j(\theta)N_j\exp[2\pi i(hx_j + ky_j + lz_j)]\exp(\frac{-B_{iso}\sin\theta}{\lambda^2}) \tag{2.9}$$

where all the symbols have their previously defined meanings.

As mentioned before, any atom in a unit cell is related to other atoms through symmetry operations. It is possible to express simplified relations for the structure factors for such groups of symmetry related atoms by considering the relations between their coordinates. For example, whenever the crystal structure has a centre of symmetry, the resultant structure factor is always entirely real and so the phase angles are always either 0 or π. This is because for every atom at x, y, z, there is another at $-x, -y, -z$ and hence the imaginary component of the structure factor cancels out. The lattice centering, screw axis and glide plane symmetry operations generate reflection conditions, giving rise to certain missing reflections in the diffraction pattern known as systematic absences. Conversely for an experimental diffraction pattern, if the unit cell geometry is known, quantitative information about the lattice type and symmetry elements (that is, the space group) can be obtained by studying these systematic absences. This can lead towards an ab initio 'unique' crystal structure solution for single crystals. For polycrystalline samples, collapsing of the three-dimensional data onto one dimension results in loss of information and so, one it is most common to 'solve' the structure by fitting to a pre-existing structural model. *Ab initio* structural solution from PXRD data is much more complex and will not be discussed here.

2.2.5 Powder X-ray diffraction (PXRD)

Powder X-ray diffraction is one of the most commonly used techniques for structural characterisation in solid state chemistry [212]. It is used as a tool for checking phase purity during initial stages of sample preparation as well as for refining the crystal structure of a solid when the desired final product is finally obtained.

X-rays are produced when an electrically heated tungsten filament emits electrons that are accelerated by a high potential difference (20-50 kV) and allowed to strike a metal target or anode which is water cooled. The anode emits a continuous spectrum of white X-ray radiation but there are sharp intense characteristic X-ray peaks, Kα and Kβ, superimposed on this continuous spectrum. The frequencies of the Kα and Kβ lines are unique to the anode metal under consideration (usually Cu or Mo). The accelerated electrons knock out electrons from the innermost K shell and the vacancies are filled by electrons from outer shells; the decrease in energy appears as the characteristic radiation. So Kα line appears when electrons descend from L shell to K shell and Kβ lines are seen when electrons descend from M shell to K shell. Usually for PXRD experiments monochromatic radiation is desired so the Kβ line is filtered out using a thin metal foil of the adjacent (Z-1) element in the periodic table; thus Ni for Cu and Nb for Mo. A monochromatic X-ray beam can also be obtained by reflecting the beam from the plane of a single crystal like graphite. The Kα lines are very closely spaced doublets because of the slightly different energies depending on spin-orbit interaction energy between the electron spin and the orbital momentum of the $2p$ orbital. A schematic of the electronic energy levels and the characteristic transitions for Cu is shown in Figure 2.4.

Usually a Cu Kα source ($\lambda_{K\alpha_1}$ = 1.54056 Å, $\lambda_{K\alpha_2}$ = 1.54439 Å) is used because the atomic spacings d_{hkl} are comparable with the wavelength. PXRD patterns are collected using automatic diffractometers by varying θ and hence 2θ over a predefined range using a scintillator or CCD detector. The diffracted beams are represented as intensity versus 2θ plots. A polycrystalline sample contains a large number of randomly oriented crystallites. The diffracted beams make an angle of 2θ to the incident beam. Thus in a measurement, the

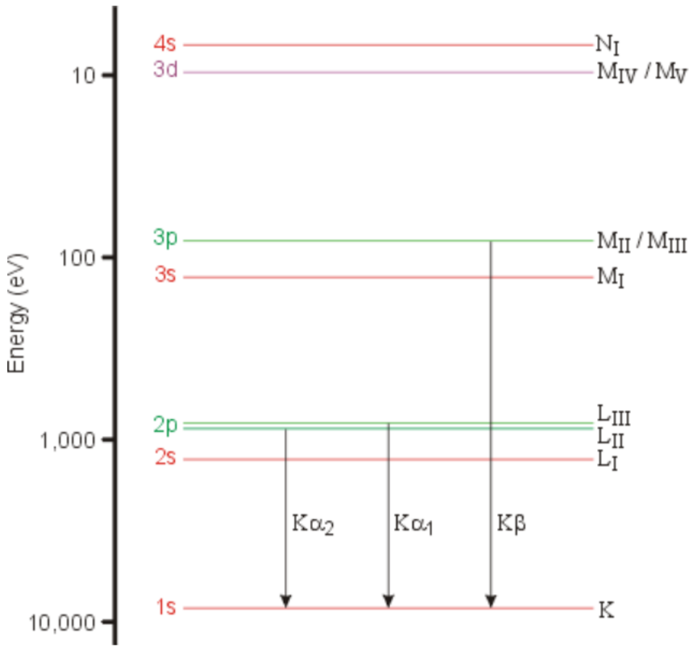

Figure 2.4 Electronic energy levels and characteristic lines for a Cu atom. Image taken from [213].

crystallites satisfying the Bragg condition are randomly oriented so the reflections lie on the surface of a cone of semi-vertical angle 2θ, Figure 2.5.

The experimentally measured intensity of the diffracted beam, I_{hkl}, can be expressed as:

$$I_{hkl} = j \cdot P \cdot L \cdot A \cdot \left|F_{hkl}^{2}\right| \tag{2.10}$$

where F_{hkl} is the structure factor as defined previously and j, P, L and A are ’correction’ factors relating to the actual collection of an experimental diffraction pattern. The intensity also depends on the temperature but this effect is ingrained in the structure factor itself, equation (2.9). j is the multiplicity of a reflection hkl and accounts for the fact that depending on the crystal symmetry, different lattice planes may have the same d_{hkl} and so, for a polycrystalline sample with randomly oriented crystallites, the intensity at a particular 2θ will be the sum of the diffracted beams from all these planes. P is the polarisation factor accounting for the change in direction of polarisation of X-ray photons on diffraction. Three main cases can be considered:

(a) X-rays are polarised in the plane of diffraction, $P = \cos^2 2\theta$: Undesirable as it leads to a huge loss in intensity of the diffracted beam

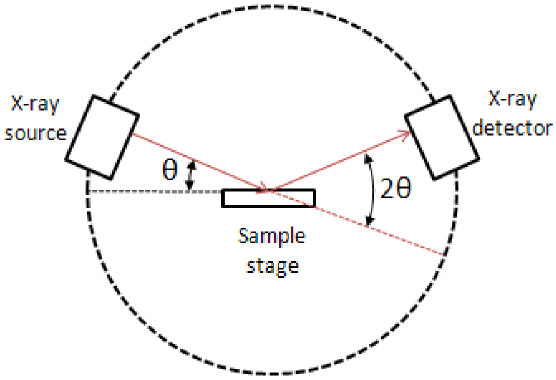

Figure 2.5 PXRD arrangement.

(b) X-rays are polarised perpendicular to the plane of diffraction, $P = 1$: Ideal case as there is no reduction of intensity. This is the typical setting for synchrotron sources at large-scale facilities where extremely high diffracted intensities are required

(c) X-rays are unpolarised (that is, equal probability of polarisation in all directions), $P = (1 + \cos^2 2\theta)/2$: This is the usual setting for a laboratory diffractometer.

The Lorentz factor, L, corrects for the fact that diffraction in the crystallites does not occur from a single point, but has a finite spread such that the Bragg condition, equation (2.5), is satisfied for a certain spread of angles around the mean 2θ value. The expression for the Lorentz factor for a polycrystalline sample is given by:

$$L = \frac{C}{\sin\theta \sin 2\theta} = \frac{C}{2\sin^2\theta \cos\theta} \tag{2.11}$$

where C is a constant. The final 'correction' factor, A, accounts for the fact that as X-rays pass through a material, they are absorbed according to the general equation $I = I_0 \exp(-\mu t)$ where I is the reduced intensity, I_0 is the initial intensity, t is the thickness and μ is the absorption coefficient which increases with atomic number and X-ray wavelength. For a powder sample under Bragg-Brentano geometry, the effect of absorption is negligible as it almost remains constant with 2θ.

For this project, PXRD patterns were collected using a PANalytical EMPYREAN X-ray diffractometer (Cu Kα radiation, Bragg-Brentano geometry, 40mA and 40kV beam) at the Department of Chemistry, University of Cambridge or a Bruker D8 X-ray diffractometer with similar configuration at the Maxwell Centre, Department of Physics, University of Cambridge. The Bragg-Brentano geometry is a flat-plate reflection geometry where the divergent and diffracted beams are focussed at a fixed radius from the sample position. This can be achieved by fixing the source and rotating the sample and detector by θ and 2θ or by keeping the sample fixed in a horizontal position and rotating the source and the detector by $-\theta$ and θ respectively. For certain samples, high resolution XRD scans were measured on a Bruker D8 Advance diffractometer (Cu Kα radiation, 1.540598 Å, Ge monochromator and Sol-XE energy dispersive detector) at the Department of Earth Sciences, University of Cambridge. In all cases, minute quantities of powder, < 2-3 mg were uniformly smeared over a glass slide using Dow corning grease which was then mounted onto plastic or alumina sample holders. Sample spinning was carried out to reduce the effects of preferential orientation which may arise on the surface due to flattening of the sample. Short scans of 10 minutes were collected ($5^\circ \leq 2\theta \leq 60^\circ$) to determine the progress of the solid state reaction and finally confirm the formation of a phase-pure product. With successive intermediate grindings and heating, the PXRD patterns became sharper indicating the improved crystallinity of the sample and the impurity phases gradually disappeared. For phase-pure materials, a long scan for 2 hours ($10^\circ \leq 2\theta \leq 90^\circ$) was collected to give high quality data for further analysis. The Bruker D8 X-ray Diffractometer at the Department of Physics was also equipped with an Oxford Cryosystems PheniX stage allowing PXRD measurements down to 12 K, enabling investigation of any low-temperature structural transitions for the samples being measured.

2.2.6 Powder neutron diffraction (PND)

Powder neutron diffraction (PND) can be used to obtain structural information [214]. Just as Cu Kα radiation with wavelength 1.54 Å is generally used for PXRD, the velocity of the neutrons should be such that the resultant wavelength is of comparable order of magnitude to the interatomic spacings. The wavelength of neutrons is given by:

$$\lambda = \frac{\mathrm{h}}{m_n v_n} \tag{2.12}$$

where h is Planck's constant and m_n and v_n are the mass and velocities of the neutrons. When neutrons have made a large number of collisions with atoms in a reactor at temperature T. they will have a root-mean square velocity v given by:

$$\frac{1}{2} m_n v^2 = \frac{3}{2} k_B T \tag{2.13}$$

where k_B is Boltzmann's constant. Combining the two results we get

$$\lambda^2 = \frac{\mathrm{h}^2}{3 m_n k_B T} \tag{2.14}$$

and the wavelengths corresponding to the root-mean square velocities of neutrons in equilibrium at temperatures of 0 °C and 100 °C are 1.55 Å and 1.33 Å. The neutrons are slowed down by collisions with a moderator like heavy water and come into thermal equilibrium with the temperature T of the reactor. They will follow the Maxwellian distribution for velocities at that temperature. The neutron radiation spectrum is thus 'white' and contains no characteristic lines as found in the spectrum of an X-ray tube. A monochromatic beam of neutrons can be obtained by using a collimator and impinging on a large monochromating crystal. At any particular angle, neutrons are reflected if they lie within a small wavelength range centred about λ obeying equation (2.5). By suitable choice of the angle θ, a beam of neutrons of any wavelength can be separated out by the crystal and could be used for diffraction experiments on a sample. This is how a monochromatic beam of neutrons is produced from a nuclear reactor source such as at the Institut Laue-Langevin (ILL), Grenoble, France. Neutron spallation sources also exist such as at ISIS, Oxfordshire, United Kingdom. Here the neutrons are produced by bombarding metal targets with high energy protons. The X-ray and constant wavelength neutron diffraction experiments are set up at a single wavelength λ and the Bragg angle θ is varied to collect the entire diffraction pattern. In contrast, at a spallation source, the entire beam with all the wavelengths can be used at a particular angle. The diffraction pattern is recorded as a function of time of flight the time (delay from the start of a neutron burst at the source), t, of the neutrons. The time of flight is related to the wavelength of incident radiation as:

$$t = \frac{m_n L \lambda}{\mathrm{h}} \tag{2.15}$$

The frequency of the source is usually fixed for a particular spallation source facility and the diffractometer is located at a fixed flight path L: these determine the range of d_{hkl} accessible to the detectors located at fixed scattering angles, according to the following relation:

$$d_{hkl} = \frac{\mathrm{h}t}{2m_n L sin\theta} \tag{2.16}$$

where θ is the scattering angle for a particular detector.

In this thesis, most of the PND measurements for samples have been carried out on the D2B powder diffractometer at ILL, Grenoble, France for structural characterisation. The D2B diffractometer [215, 216] is a two-axis powder diffractometer with very high resolution ($\Delta d/d \approx 10^{-4}$) and relatively high flux, where in principle, the resolution is only limited by the size of the powder particles. It is mainly used for structural analysis of powders. However, it can also be used for determination of magnetic structures. D2B is characterised by a very high take-off angle (the angle between the monochromator and the neutron beam direction) of 135° to obtain high resolution. A Ge [115] monochromator is used. However, the wavelength can be easily changed by a simple rotation of the Ge crystal in the [*hhl*] plane. Larger wavelengths can be accessed using graphite and cold-Be filters for magnetic studies. The sample to be measured is usually in the form of a cylindrical vanadium can containing the powder. A range of sample environments (cryostats, dilution fridges, furnaces, magnets, pressure cells) can be accommodated on D2B and it can be used for structural and magnetic studies of polycrystalline samples as a function of temperature, field and pressure. Data is collected by a bank of 128 ^{3}He detectors spaced at $\Delta 2\theta = 1.25°$, which move so that the average over several detectors is taken in each scan. A scan spanning the entire angular range would take typically 30 minutes and then can be repeated to improve the statistics. D2B has an automated sample changer, including a slot for an external sample environment such as a cryostat such that multiple samples can be loaded and set to measure consecutively.

Some measurements in this thesis were also carried out on the D1B and D20 powder diffractometers at ILL and on the WISH powder diffractometer at ISIS, Oxfordshire, UK. D1B [217] and D20 [218] are constant wavelength powder diffractometers with very high flux (flux on D20 is higher than D1B) at large wavelengths (typically 2.5 Å) and dedicated low temperature orange cryostats (T_{min} = 1.5 K) which make them ideal for low temperature magnetic scattering studies. They are equipped with a large bank of position-sensitive detectors which enable rapid data collection. Due to the extremely high flux, it is possible to measure very small quantities of samples on these instruments and to collect high-quality statistics in a very short period of time. For both D1B and D20, a complete scan can be obtained within 1-5 minutes and complete temperature dependence or reaction kinetics for a sample can be obtained within 3-5 hours. D1B and D20 can also accommodate a range of external sample environments for studies as a function of external parameters such as ultra-low temperatures (< 1.5 K), magnetic field or pressure, though a sample changer is not available. It is possible to change the wavelength on D1B or D20 using a Ge monochromator but the resolution is not as good as D2B. Therefore, ideally, structural characterisation of the sample has to be carried out using a high resolution diffractometer like D2B and then, the magnetic scattering can be measured on D1B and D20 which have high flux at higher wavelengths.

The WISH (wide angle in a single histogram) diffractometer [219] is a high flux, very high resolution time-of-flight powder diffractometer located in Target Station 2 at ISIS. As the data is collected across different banks, both structural and magnetic characterisation can be carried out. However, the main applicability of WISH is cold powder neutron diffraction for the investigation of complex magnetic structures. The combination of high flux at low

Q with high resolution in Q offered by WISH (Q = momentum transfer in elastic scattering = $4\pi \sin\theta/\lambda$) makes it the ideal instrument for combined magnetic Bragg and diffuse scattering measurements to study long range ordering and short-range magnetic correlations respectively. The coverage in d spacing is from 0.7 - 17 Å. enabling analysis of structures with very large unit cells. The large bank of position sensitive detectors (pixellated ^{3}He detectors) covering the scattering angles in the range 10 - 170° enables rapid data collection with a quick scan taking $\approx$ 5 minutes and a complete temperature dependence measurement taking a few hours. Very small volume of samples, samples with small moments as well as absorbing samples can be measured in a reasonable amount of time ($<$ 1 day). Apart from a dedicated cryostat (T_{min} = 1.5 K) and a sample changer, WISH can accommodate a variety of sample environments simultaneously (such as dilution fridge, magnet, pressure cell) to study magnetism under extreme conditions (ultra-low temperatures, high fields and high pressures).

For most neutron scattering measurements in this thesis, the powders were loaded into cylindrical cans made of thin vanadium metal (to minimise background scattering) with a diameter of 6 mm or 8 mm depending on the quantity of powder available. The cans were screwed onto the sample changer or to the end of the cryostat depending on the measurement being carried out. Vanadium has a very low coherent neutron scattering length (b = -0.38 fm) and therefore the contribution to the PND Bragg pattern is almost negligible. In case of ultra-low temperature measurements ($T < 1.5$ K) on WISH to study the nature of magnetic ordering for $Tb(BO_2)_3$, a copper can had to be used to ensure cooling and thermalisation. The powder-filled copper can was made airtight with an indium seal and filled with helium exchange gas to facilitate cooling. Bragg peaks corresponding to Cu were observed in the PND data and a difference plot was taken to analyse the magnetic scattering from the sample only.

2.2.7 Comparison of PXRD and PND techniques

The production of neutrons is both expensive and carries higher risks and so PND can only be carried out at large-scale facilities. It also requires use of much larger volume of sample as compared to PXRD because of the relatively weaker flux of neutrons produced as compared to X-rays. Therefore, PND is not a substitute for PXRD and all structural characterisation of polycrystalline solids must initially be carried out using PXRD. However, PND can be used as a non-routine technique to obtain complementary structural information to PXRD.

There is a difference in the scattering intensity of X-rays and neutrons because X-rays are scattered by the electrons around the nucleus via the long-ranged electromagnetic interaction whereas the neutrons are scattered by the nucleus itself via the short-range strong force (except for magnetic scattering which shall be taken up separately in a later section). The atomic scattering factor for X-rays, f_X:

(a) falls off as $\sin\theta/\lambda$ and so as θ increases, the structure factor, equation (2.9), and hence the intensity, equation (2.10), also falls off.

(b) has the same sign for all elements.

(c) increases linearly with the number of electrons in the atom (atomic number Z) so heavy atoms scatter X-rays more than lighter atoms. Scattering lengths for different isotopes of the same element are identical for X-rays.

For neutrons the scattering lengths:

(a) are distinct for different isotopes.

(b) can have different values for nuclei which have a non-zero value of spin. The usual formalism splits the scattering length into coherent (average) and incoherent (variance) parts.

(c) do not have a simple functional dependence on atomic number: most atoms scatter neutrons similarly to within a factor of two or three.

(d) can be positive or negative.

The neutron scattering amplitude is independent of θ due to the negligible dimensions of the nucleus compared to the wavelength (typically of the order of 1 Å). Hence the form factor for neutrons plotted as a function of $\sin\theta/\lambda$ is a flat line parallel to the x axis. The coherent scattering length used in the structure factor calculation, equation (2.9), for neutrons, denoted by b_r, is the value of the scattering length b averaged over all isotopes (assuming natural abundance) as well as over parallel and antiparallel spin states for isotopes with finite nuclear spin for that element [220].

There is also no angular dependent polarisation factor P for neutrons in equation (2.10) unlike X-rays; however polarized neutrons (incident beam in a specific spin state with $S = \frac{1}{2}$ or $S = -\frac{1}{2}$) may be generated in magnetic scattering experiments to unambiguously determine the direction of magnetisation of the samples. However, this technique is beyond the scope of this thesis. Another important point of difference between PXRD and PND is that apart from a few exceptions (Gd, Cd, B and some other elements), the neutron absorption coefficients are about two or three orders of magnitude smaller than X-rays, meaning that in most cases, the effect of absorption may be neglected for neutrons. For carrying out PND experiments on samples containing elements with high absorption coefficients, strategies include:

(a) Isotopic enrichment: : This is used but it can be prohibitively expensive, especially as a large number of absorbing elements are rare-earths. Isotopic enrichment, specifically deuteration, is also used for all samples containing hydrogen because it has a very high incoherent scattering cross-section for neutrons such that the background completely dominates the PND pattern.

    In this thesis, isotopic enrichment has been used for preparing lanthanide orthoborates, $Ln\mathrm{BO}_3$, and lanthanide metaborates, $Ln(\mathrm{BO}_2)_3$, for neutron diffraction experiments in order to reduce the absorption from naturally occurring ^{10}B.

(b) Measuring very small amounts of samples and using very long counting times or using high-flux diffractometers (like WISH, D20, D1B).

(c) Using 'hot' neutrons with wavelengths $\lambda \approx 0.5$ Å as neutron absorption is lowered at small wavelengths.

The main applications of PXRD include:

(a) It can be used to uniquely identify the presence of a crystalline phase in the product. Thus it can be used to track the progress of solid-state reactions, examine the phase stability of the product(s), check the purity of samples and identify the impurity phases, if present.

(b) It can be used to determine crystallite size. As the crystallite size decreases, the width of the diffraction peak would increase. The crystallite size can be calculated from the peak width using the Debye Scherrer formula:

$$T = \frac{C\lambda}{B\cos\theta} = \frac{C\lambda}{(B_M^2 - B_S^2)^{\frac{1}{2}}\cos\theta} \tag{2.17}$$

    where T is the thickness of the crystallite, λ is the wavelength of the X-rays, θ is the Bragg angle and B is the full-width at half-maximum (FWHM) of the peak in radians, corrected for instrumental broadening. B_M and B_S are the FWHMs of the sample and of a standard respectively. A highly crystalline sample is chosen to give B_S, the measure of broadening due to the instrumental effects. For solid-state reactions, the product becomes more and more crystalline on heating and this is manifested as the PXRD pattern becoming sharper.

Some important uses of PND are:

(a) Neutron diffraction can be used to determine the positions and occupancies of lighter atoms in the crystal structure even in the presence of other heavier atoms because the neutron scattering factors would be similar.

For example, in this thesis, neutron diffraction has been used to determine the positions of B and O in lanthanide metaborates, $Ln(BO_2)_3$.

(b) Atoms that lie near each other in the periodic table have very similar X-ray scattering factors and one may not be able to distinguish among them using PXRD. PND can yield useful structural information in this case. One of the most canonical examples is Fe and Co (b_{Fe} = 9.45 fm, b_{Co} = 2.49 fm) [221].

In this thesis, PND has been used to distinguish between Cr and Ga or Mn and Ga in the lanthanide garnets (b_{Cr} = 3.635 fm, b_{Ga} = 7.288 fm, b_{Mn} = - 3.73 fm) [221].

(c) Neutrons can be used to distinguish among isotopes of a single atom because the neutron scattering lengths are different.

(d) Neutrons have spin and hence magnetic moment and can interact with the magnetic moment of magnetic materials. They are sensitive to local spin-spin correlations and serve as a powerful tool for magnetic structure determination.

For example, in this thesis, low temperature PND measurements have been carried out to determine the magnetic structure of Mn^{3+} substituted holmium gallium garnet.

2.2.8 Rietveld refinement

Rietveld analysis [222] is a least squares method of determining (or more precisely refining) crystal structures from powder diffraction data. It requires a prexisting trial structure, either for an isostructural material or a hypothetical model. The method involves calculating a powder diffraction profile for the trial structure and comparing it to the experimental data. A PXRD or PND pattern has two characteristic features:

(a) Positions of the lines $2\theta_{hkl}$ or equivalently spacings of the lines d_{hkl} (Bragg's law) which represents the lattice parameters and space group symmetry of the unit cell

(b) Intensities of the lines which represent the atoms, their positions, occupancies and thermal vibration parameters within the unit cell

The Rietveld method involves analysing both the position and the intensity of the line profile. The trial structure is modified by altering the refinable parameters, including lattice constants, atomic positions, thermal parameters, site occupancies until a best-fit match is obtained with the experimental diffraction pattern. The fit can be measured numerically in terms of R values [223]. The weighted-profile R value, R_{wp}, is given by:

$$R_{wp} = \sqrt{\frac{\sum_i w_i[y_i(obs) - y_i(calc)]^2}{\sum_i w_i[y_i(obs)]^2}} \tag{2.18}$$

where $y_i(obs)$ is the experimentally observed intensity at step i, $y_i(calc)$ is the calculated intensity at step i and w_i is the weight. The quantity in the numerator is minimised during Rietveld refinement by the least squares method. R_{wp} should ideally approach R_{exp}, the statistically expected value, which is given by:

$$R_{exp} = \sqrt{\frac{N - P}{\sum_{i=1}^{N} w_i[y_i(obs)]^2}} \tag{2.19}$$

where N is the number of observed values and P is the number of parameters. The refinement can be characterised by the value of χ^2 and a difference plot of the modelled and experimental patterns where χ^2 is given by:

$$\chi^2 = \frac{R_w^2}{R_{exp}^2} \tag{2.20}$$

χ^2 is also minimised during refinement.

In order to carry out a Rietveld refinement, the background contribution to the diffraction pattern is estimated using linear interpolation between data points or pre-defined mathematical functions. In this thesis, linear interpolation was used to model the background in all cases. Each peak is assigned an analytical shape function to model the peak shape. The peak shapes observed depend on both the instrument parameters (geometry, radiation source, etc) and the sample (size or strain effects). For PXRD and constant wavelength PND data, a pseudo-Voigt function, which is the convolution of a Gaussian and a Lorentzian function, was used to model the peak shape. The full-width at half maximum (FWHM) for the Gaussian component was modelled by the Caglioti function:

$$FWHM = U \tan^2\theta + V \tan\theta + W \tag{2.21}$$

and that for the Lorentzian component was modelled by:

$$FWHM = X \tan\theta + \frac{Y}{\cos\theta} \tag{2.22}$$

The initial values of U, V, W, X and Y were obtained from an instrument resolution function (IRF) file, generated by collecting the diffraction pattern for a well-characterised highly crystalline sample on the instrument (for example LaB_6 or Si or Al_2O_3). The assumption made is that for a highly crystalline sample, any peak broadening would arise from the instrument configuration only. This was usually sufficient to model the peak shape well except for some important exceptions:

(a) Due to the high crystallinity and high cubic symmetry of the garnets, the effect of asymmetry arising from axial divergence of the diffracted beam at low angles [224] was particularly prominent in the constant wavelength PXRD and PND patterns and it was necessary to use additional asymmetry parameters to model the peak shape accurately.

(b) The functions describing the FWHM could not be used to model (hkl) dependent line-broadening arising from size or strain effects. In such cases, the FWHM parameters were set to the IRF values and additional spherical harmonic functions [225] were used to model the peak shape. In case of both size and shape broadening, these were phenomenological models constrained to the symmetry of the unit cell.

The peaks in time-of flight PND patterns contained additional asymmetric broadening arising from the pulsed nature of the neutron source. Hence a convolution of an Ikeda-Carpenter function and a pseudo-Voigt function is used to model the peak shape. The Ikeda-Carpenter function is itself the convolution of two functions: the first represents the slowing of the neutrons by a moderator and the second is a combination of a delta function and a decaying exponential. In general, it was much more difficult to model the peak shape satisfactorily for time-of flight PND data as compared to PXRD or constant wavelength PND data.

Finally, a model structure is taken to calculate a PXRD or PND pattern, compared with the experimental data and refined until χ^2 is minimised. Values of χ^2 close to 1 (which indicates perfect fitting) and a flat line difference pattern indicates that the model structure is valid. This method works best if the initial model structure is close to the actual crystal structure. However, in several cases, it is found that the modelled intensities in the diffraction pattern deviate significantly from the actual data or only a partial structural model is available. In such cases, it is possible to carry out a ‘structure-free’ LeBail refinement [226], also known as the diffraction pattern profile matching technique. Here the intensities of the reflections are modified to fit the experimentally observed intensities in order to obtain initial values of the profile parameters (unit cell parameters, peak shape, etc). The parameters thus obtained from the LeBail refinement can serve as initial values to be refined when a complete structural Rietveld refinement is carried out.

For this thesis, the initial crystal structures were taken from the Inorganic Crystal Structure Database (ICSD). Specific references for the materials are given in subsequent chapters.

Rietveld analysis was carried out using the FullProf Suite of programmes [227] and the refined patterns were plotted using the WinPLOTR program [228]. The Rietveld analysis also gives the weight percentages of the different phases present at intermediate steps. This made it possible to determine strategies for facilitating the desired solid state reaction by changing the reaction conditions (such as increasing temperature or time or percentage of excess starting material to be added). When a phase-pure product was synthesised, Rietveld analysis was carried out more carefully on the long PXRD scan and detailed quantitative structural information could be obtained. For select samples, PND scans were collected to obtain complementary information about the crystal structure. In such cases combined structural PXRD and PND Rietveld refinements were carried out to utilise the full potential of obtaining complementary structural information from these diffraction techniques, leading to a precise determination of the crystal structure. Specific examples are mentioned in the relevant results chapters.

2.2.9 Magnetic neutron scattering

The neutron has spin $S = \frac{1}{2}$ and a moment = -1.9 μ_N (1 μ_N (nuclear magneton) $\approx \frac{1}{2000}$ 1 μ_B). An interesting fact is that the non-zero moment of the neutron was one of the first indications that it is not an elementary particle, but has substructure composed of quarks [229, 230]. The scattering of neutrons by atoms is a nuclear process. However, for paramagnetic atoms, there is additional scattering due to the dipole-dipole interaction between the neutron magnetic moment and the magnetic moment of the atom. Since the scattering occurs due to interaction between the neutrons and the unpaired electrons in the outer shell of the atom, the magnetic scattering is [210]:

(a) specific to the magnetic ion under consideration.

(b) governed by a form factor: However the decay as a function of $(\sin\theta/\lambda)$ is much faster than X-rays because it only involves the electrons in the outermost shell of the atom.

(c) does not increase linearly with atomic number unlike X-rays.

Another important point is that a neutron only experiences the component of magnetisation M perpendicular to the direction of momentum transfer $\mathbf{Q}$. This arises from the fundamental nature of the magnetic force: the effect of a magnetic field is only experienced in the direction perpendicular to the magnetic field.

An ideal paramagnet has a disordered arrangement of magnetic moments and so, the magnetic scattering will be completely diffuse in nature and will only contribute to the background in the PND pattern. However, for a magnetically ordered material (such as a ferromagnetic or antiferromagnetic material below the Curie or Néel temperature respectively), the magnetic moments are oriented in a specific direction . This gives rise to coherent magnetic scattering for the neutrons and hence the PND pattern consists of magnetic Bragg peaks in addition to the nuclear Bragg peaks. Thus if PND measurements are carried out below the temperature at which the sample is magnetically ordered, the diffraction pattern provides information on both orientation and magnitude of the atomic magnetic moments,that is, the magnetic structure of the crystal, in addition to the position of the atoms in the crystal lattice.

The equivalent of the scattering length for a magnetic ion is given by [231]:

$$F^2 = b^2 + 2bp\mathbf{q}\cdot\boldsymbol{\lambda} + p^2q^2 \tag{2.23}$$

Here b denotes the nuclear scattering amplitude, p is the magnetic scattering amplitude and $\boldsymbol{\lambda}$ is a unit vector denoting the direction of polarisation of the scattered neutron. $\mathbf{q}$ is defined according to the relation:

$$\mathbf{q} = \boldsymbol{\varepsilon}(\boldsymbol{\varepsilon}\cdot\boldsymbol{\kappa}) - \boldsymbol{\kappa} \tag{2.24}$$

where $\boldsymbol{\varepsilon}$ is a unit vector along the scattering direction and $\boldsymbol{\kappa}$ is a unit vector parallel to the direction of magnetic moment of the magnetic ion under consideration. The magnetic scattering amplitude p is given by the expression:

$$p = \frac{e^2\gamma}{m_ec^2}Sf \tag{2.25}$$

where e, m_e are the electron charge and mass, c is the velocity of light, γ is the neutron magnetic moment in nuclear Bohr magneton, S is the spin quantum number of the magnetic atom and f is the magnetic form factor specific to the electrons generating the magnetic moment. p can be rewritten as:

$$p = \frac{e^2\gamma}{2m_ec^2}2Sf = \frac{e^2\gamma}{2m_ec^2}g_SSf \tag{2.26}$$

where g_SS is the magnetisation along the perpendicular direction of momentum transfer for atoms where the orbital angular momentum is completely quenched. For atoms where both orbital and spin angular momenta contribute to the total angular momentum J, (as for lanthanide ions which are being studied in this thesis), the equivalent expression is:

$$p = \frac{e^2\gamma}{2m_ec^2}g_JJf \tag{2.27}$$

In case of unpolarised neutrons, the average value of $(\mathbf{q} \cdot \boldsymbol{\lambda})$ in equation (2.23) is zero and hence, the nuclear and magnetic Bragg scattering intensities are additive. In order to analyse the magnetic structure, the nuclear Bragg scattering has to be determined accurately. This is achieved by collecting PND data at a temperature well above the magnetic ordering temperature where the material is fully paramagnetic and carrying out a structural Rietveld refinement of the nuclear Bragg peaks. Then the sample is cooled below the magnetic ordering transition (usually to the minimum temperature of the cryogenic environment available) and the structural refinement is repeated to account for variations in lattice parameters, atomic positions and thermal vibration parameters with temperature. Once a satisfactory fit is obtained, the parameters for the structural refinement are kept fixed and the magnetic scattering is analysed to determine the magnetic structure.

2.2.10 Magnetic structure determination

As the magnetic moments are vectors (more precisely, axial vectors), it is possible to form long-range periodic magnetic structures that do not have the same periodicity as the unit cell for the crystal structure corresponding to the nuclear Bragg scattering. However, as the magnetic structures are also periodic, the propagation of magnetic structures in a crystalline solid can be defined using Bloch waves, which are plane waves with a propagation vector or wave vector **k** relating the magnetic moments of equivalent atoms located in different unit cells:

$$\mathbf{m}_j = \mathbf{m}_i \exp(i\mathbf{k} \cdot \mathbf{T}) \tag{2.28}$$

where $\mathbf{m}_i = (m_{ai}, m_{bi}, m_{ci})$ is the magnetic moment of the i^{th} atom with components m_{ai}, m_{bi}, m_{ci} along the crystallographic axes and $\mathbf{m}_j = (m_{aj}, m_{bj}, m_{cj})$ is the magnetic moment of an equivalent j^{th} atom with components m_{aj}, m_{bj}, m_{cj} along the crystallographic axes. $\mathbf{m}_j$ and $\mathbf{m}_i$ are related by the lattice translation vector **T**, defined in equation (2.1), as $\mathbf{m}_j = \mathbf{m}_i + \mathbf{T}$. Here **k** is restricted to the first Brillouin zone (set of points in reciprocal space that can be reached from the origin without crossing any Bragg plane) of the nuclear unit cell [232].

Just as the condition for nuclear Bragg scattering was $\mathbf{Q} = \mathbf{G}$, the condition for magnetic Bragg scattering becomes: $\mathbf{Q} = \mathbf{G} + \mathbf{k}$ where **Q** is the scattering vector, **G** is the reciprocal lattice vector and **k** is the magnetic propagation vector. While most magnetic structures can be described by a single propagation vector, multi-**k** structures are also possible. When the vector **k** can be defined in terms of rational part of a principal reciprocal lattice vector, the associate magnetic structure is said to be commensurate. Physically this means that the magnetic unit cell can be defined as a ‘simple multiple’ of the nuclear unit cell. This is true for most of the common forms of bulk magnetism such as ferromagnets and antiferromagnets.

When the vector **k** cannot be expressed in terms of rational parts of principal reciprocal lattice vectors, it results in an incommensurate magnetic structure. The first step for determination of the magnetic structure is indexing the **k** propagation vector from the magnetic reflections.

For commensurate magnetic structures with **k** = (0, 0, 0), the magnetic unit cell is the same size as the nuclear unit cell and the magnetic Bragg peaks occur at points in the reciprocal lattice satisying the relation $\mathbf{Q} = \mathbf{G}$. If a primitive unit cell with a single magnetic atom is considered (magnetic Bravais lattice), the propagation vector **k** = (0, 0, 0) would correspond to a simple ferromagnet, with all the magnetic moments aligned parallel to one another and the magnetic intensity appears on the nuclear reflections. Another special case is **k** = **G**/2; this represents specific high symmetry points in the Brillouin zone for all 14 Bravais lattices and results in an antiferromagnetic structure. The magnetic scattering occurs at points in the reciprocal space where nuclear Bragg scattering is completely absent [233]. For a unit cell with multiple magnetic atoms, **k** = (0, 0, 0) no longer definitively implies a ferromagnetic structure and can result in ferromagnetic, antiferromagnetic or ferrimagnetic alignment of the magnetic moments, depending on the space group. More generally, if the crystallographic unit cell contains more than one magnetic atom site, complex non-collinear magnetic structures can be stabilised for **k** = (0, 0, 0) depending on the magnetic interactions and the single-ion anisotropy of the magnetic ion. It is only the intensities of the different magnetic peaks that enables one to differentiate between the different configurations of magnetic moments. Irrational values of **k** give rise to incommensurate magnetic structures such as a spin density wave or sine-wave modulated structure (where the magnetic structure is represented by a sine-wave modulation of the moment value propagating along the **k** direction) or a helical structure (magnetic moments rotate in a plane when propagating along the **k** direction).

Having determined the propagation vector, the next step is to find the magnitude and directions of the magnetic moments by fitting the intensities of the magnetic reflections to a model. A magnetic structure can be represented by defining an axial vector function $\mathbf{S}(\mathbf{r})$ for each magnetic atom in the crystal structure. $\mathbf{S}(\mathbf{r})$ may remain invariant or transform into another axial vector function $\mathbf{S}^{'}(\mathbf{r})$ under symmetry operations of a group. Two approaches are possible for describing magnetic structures:

(a) Magnetic symmetry approach: Defining the set of operations that leave $\mathbf{S}(\mathbf{r})$ invariant.

(b) Representation analysis approach: Defining $\mathbf{S}^{'}(\mathbf{r})$ from a given $\mathbf{S}(\mathbf{r})$ under all symmetry operations.

The representation analysis approach, which has been used in this thesis, is more general and can be used to solve commensurate and incommensurate structures. It involves decomposition of the magnetic configurations into basis functions that transform according to various irreducible representations (IRs) of the wave vector group $\mathbf{G_k}$. The subset of symmetry operations g of the crystallographic space group $\mathbf{G}_0$ that leave the **k** vector invariant are known as the wave vector group $\mathbf{G_k}$ or the 'little group'.

There are two independent effects of the symmetry operations:

(a) The permutation of labels of equivalent atoms under action of all symmetry operations can be represented using a permutation representation, $\boldsymbol{\Gamma}_{perm}$.

(b) The transformations of the components of the axial moment vectors under the symmetry operations are defined by the axial vector representation, $\boldsymbol{\Gamma}_{axial}$.

The entire magnetic representation, $\boldsymbol{\Gamma}_{mag}$ describes the results of the symmetry operations on both the atomic positions and the axial vectors representing the magnetic moments. Being independent effects, the overall magnetic representation is given by the direct product:

$$\boldsymbol{\Gamma}_{mag} = \boldsymbol{\Gamma}_{perm} \times \boldsymbol{\Gamma}_{axial} \tag{2.29}$$

$\boldsymbol{\Gamma}_{mag}$ is reducible and can be written in terms of the irreducible representations (IRs) of the group $\mathbf{G_k}$. IRs are the smallest unique blocks out of which other representations for a group can be generated. Therefore $\boldsymbol{\Gamma}_{mag}$ can be written as:

$$\boldsymbol{\Gamma}_{mag} = \sum_{\nu} n_{\nu} \Gamma_{\nu} \tag{2.30}$$

where n_ν is the number of times the IR Γ_ν appears in $\boldsymbol{\Gamma}_{mag}$. The decomposition of $\boldsymbol{\Gamma}_{mag}$ into the IRs of $\mathbf{G_k}$ also gives the number of basis vectors ψ_ν contributing to $\boldsymbol{\Gamma}_{mag}$ from each IR. The basis vectors ψ_ν for each IR Γ_ν have the same symmetry as the IR and are obtained by using a projection operator technique (taking axial unit vectors as test functions and projecting it from the part that transforms according to each of the IRs). The magnetic moments can be represented as a linear combination of these basis vectors.

In summary, the determination of the magnetic structure of a crystalline solid by PND involves two main steps [234]:

(a) Determination of the magnetic propagation vector (wave vector) from the observed magnetic reflections. This has been carried out using the k-search program included in the FullProf suite of programs [227].

(b) Determination of magnitude and directions of all the atomic magnetic moments by comparison of the observed intensities of the magnetic Bragg peaks with the theoretically predicted intensities. This is carried out using a magnetic Rietveld refinement and just like a structural Rietveld refinement, requires a ‘trial magnetic structure’ against which a least squares fitting is carried out. In this thesis, the ‘trial magnetic structures’ have been generated using the SARAh software [235] which generates the IRs and basis vectors using representation analysis. The FullProf suite of programs [227] has been used to carry out Rietveld refinement of low temperature PND data by adding the magnetic structure as an additional ‘phase’ along with the structural phase.

2.3 Magnetic measurements

The theory of magnetism and the various quantities measured such as magnetic susceptibility and magnetisation have already been described in the introduction. Here, the techniques for the measurement of these physical quantities are discussed.

2.3.1 Sample preparation for measurement

The samples of complex lanthanide oxides being measured have very large magnetic moments and so, care had to be taken to ensure that the moment signal did not exceed the capability of the measurement system. 10-20 mg of powders were weighed out and wrapped in cling film. These were encased in between two plastic powder capsules or in an agar capsule. This setup was placed in a brass rod or plastic drinking straw and used for measurement. The contribution from the cling film, capsule and brass rod or drinking straw was measured separately and found to be diamagnetic and four orders of magnitude lower than the typical sample moments at all temperatures (2 - 300 K) and magnetic fields (0 - 14 T) being measured.

2.3.2 Measurements using a Magnetic Properties Measurement System (MPMS)

Magnetic measurements were carried out using a Quantum Design MPMS. The MPMS system utilises different superconducting components (these have the advantage of being able to withstand large amounts of current without any dissipation as heat) [236]:

(a) Superconducting magnet: Generates large magnetic fields. For the MPMS used to carry out measurements in this thesis, the field range was -7 T $< \mu_0 H <$ 7 T.

(b) Superconducting detection coil: This provides inductive coupling to the sample.

(c) SQUID (Superconducting QUantum Interference Device): This is the most important component and is linked to the detection coil.

(d) Superconducting magnetic shield: Surrounds the SQUID.

The dc SQUID consists of two Josephson junctions arranged on a superconducting ring. A constant biasing current applied to the SQUID causes Cooper pairs (of electrons) to tunnel through the junctions. If this current is greater than the critical current for the Josephson junction, a voltage is produced across the SQUID. Changes in the magnetic flux (as a result of altering the magnetic field, inserting a magnetic sample) causes the voltage to oscillate between a minimum and maximum value. So the wave functions for the two Josephson junctions interfere to produce the voltage swings which can be detected by conventional electronics. Thus the SQUID serves as a highly sensitive linear current-to-voltage converter [237].

During MPMS measurements, the sample moves through the detection coils which are placed at the centre of the magnet, outside the sample chamber. As per Faraday's law, this induces an electric current in the detection coils. The detection coils, connecting wires and SQUID input coil are arranged to form a closed superconducting loop and so, the change in magnetic flux associated with the detection coil produces a proportional change in the persistent current. The functionality of the SQUID as an ultra-sensitive linear current-to-voltage converter means that the resultant variations in the SQUID output voltage are proportional to the changes in current in the detection coils, and hence proportional to the moment of the sample. The system is pre-calibrated in units of emu using a magnetic material with known mass and magnetic susceptibility (in this case Er:YAG). Hence, the SQUID detector provides an extremely precise measurement of a sample's magnetic moment (sensitivity of the MPMS used for this thesis is 10^{-8} emu).

For this thesis, the MPMS has been used to measure the magnetisation (M) of the sample as a function of applied magnetic field ($\mu_0 H$) and temperature (T). Initially for all samples, the Zero Field Cooled (ZFC) scan of magnetisation as a function of temperature (2-300 K) for an applied field of 100 Oe was measured. In a low applied field of 100 Oe, the magnetisation varies linearly and so the linear approximation for susceptibility is valid. Thus the molar susceptibility as a function of temperature, $\chi(T)$, was plotted for all samples. While the $\chi(T)$ curve would indicate any magnetic ordering transition in the temperature range of the measurement, subtle changes in the gradient, indicative of a change in the nature of short-range magnetic correlations, can be studied using the $\frac{d\chi}{dT}$ vs T curve. The reciprocal susceptibility was also plotted and the Curie-Weiss law was fit to the linear region of the $\chi^{-1}(T)$ curve (typically in the temperature range 100 - 300 K).

2.3.3 Measurements using a AC Measurement System (ACMS) on the Physical Properties Measurement System (PPMS)

Isothermal magnetisation measurements for selected samples were carried out using the ACMS option on the PPMS in the field range 0-9 T or 0-14 T at selected temperatures between 2 K and 100 K. The DC magnetisation measurement mode was used.

The basic operating principle for the DC magnetization measurement is similar to a vibrating sample magnetometer (VSM). Due to the vibration of the sample concentrically within a coil set, there is a change in the associated magnetic flux which induces a voltage in the pickup coils. The pickup coil set consists of two counterwound coils connected in series and located just above and below the sample. The time-dependent induced voltage is given by [238]:

$$V_{coil} = \frac{d\Phi}{dt} = \frac{d\Phi}{dz}\frac{dz}{dt} \tag{2.31}$$

where Φ is the magnetic flux through the pickup coils, z is the vertical position of the sample with respect to the coil and t is the time. For a sinusoidally oscillating sample position, the voltage is given by the equation:

$$V_{coil} = 2\pi f C m A \sin(2\pi f t) \tag{2.32}$$

where C is the coupling constant, m is the DC magnetic moment of the sample and A and f are the amplitude and frequency of oscillation respectively.

The magnetisation was converted to units of Bohr magneton per formula unit and $M(H)$ curves were plotted at different temperatures to study the variation in isothermal magnetisation as a function of field. The presence of any single-ion anisotropy can be inferred from the $M(H)$ curves, as the magnetisation would saturate or tend to saturate at a value less than the theoretical saturation magnetisation.

2.3.4 Quantification of the magnetocaloric effect from the isothermal magnetisation data

The MCE was quantified by calculating the change in magnetic entropy, ΔS_m. In order to calculate ΔS_m from the $M(H)$ curves, the following steps were followed:

(a) Interpolation of $M(H)$ data in uniform field steps of $\mu_0 H$ = 0.2 T.

(b) Calculation of $\frac{dM}{dT}$ for interpolated values of $\mu_0 H$.

(c) Calculation of the integral in equation (1.64) for different values of T.

(d) Calculation of ΔS_m in units of $\mathrm{J\,K^{-1}\,mol_{\mathit{Ln}}^{-1}}$, $\mathrm{J\,K^{-1}\,kg^{-1}}$, $\mathrm{mJ\,K^{-1}\,cc^{-1}}$.

The value of ΔS_m in units of $\mathrm{JK^{-1}mol_{\mathit{Ln}}^{-1}}$ can be compared with that in Table 1.2. ΔS_m values calculated per unit mass or per unit volume are more relevant for practical applications where a fixed mass or fixed volume of the magnetic refrigerant is used and so these values were also calculated.

2.4 Heat capacity measurements

2.4.1 Heat capacity

The heat capacity of material is the quantity of heat required to raise the temperature of the substance by a specific amount. Mathematically it can be defined as:

$$C_p = \left(\frac{dQ}{dT}\right)_P \tag{2.33}$$

From the second law of thermodynamics:

$$dQ = TdS \tag{2.34}$$

Hence the entropy is related to the heat capacity as:

$$S = \int_0^{T_{max}} \left(\frac{C(T)}{T}\right) dT \tag{2.35}$$

where T_{max} is the maximum temperature up to which the heat capacity has been measured as a function of temperature. The total heat capacity is the sum of several terms. For the materials discussed in this thesis the main contributions are:

$$C_{tot} = C_{lat} + C_{mag} + C_{el} + C_{nuc} \tag{2.36}$$

where C_{lat} is the lattice heat capacity, C_{mag} is the magnetic contribution, C_{el} is the electronic Schottky term and C_{nuc} is the hyperfine contribution. The lattice contribution arises due to vibration of lattice modes called phonons, as the temperature increases and is modelled using the Debye equation for molar specific heat [239]:

$$C_{lat} = \frac{9n\mathrm{R}T^3}{\theta_D^3} \int_0^{\theta/T} \frac{x^4 \mathrm{e}^x}{(\mathrm{e}^x - 1)^2} dx \tag{2.37}$$

where n is the number of atoms per molecule of the solid, R is the universal gas constant and θ_D is the Debye temperature which typically lies in the range 250 - 500 K for complex lanthanide oxides. The exact value is estimated by fitting the high temperature heat capacity data to equation (2.37).

When a material contains closely spaced electronic or nuclear energy states, a broad anomalous peak in the specific heat appears at a temperature where the thermal excitations match the energy spacing between these states. This is called a Schottky anomaly. This is not a phase transition but rather, a cusp appears because there is an abrupt change in entropy associated with the population of electronic or nuclear states, as the case may be [240]. The expression for the electronic Schottky anomaly for a two level system is given by:

$$C_{el} = R(\frac{E}{k_B T})^2 \frac{e^{\frac{E}{k_B T}}}{(e^{\frac{E}{k_B T}} + 1)^2} \tag{2.38}$$

where E is the energy separation between the two levels. This expression can be used to model the electronic specific heat by using E as a fitting parameter, however in some cases, a more involved analysis considering N energy levels may be required. In this case, information about the energy levels has to be obtained by a complementary technique; this is beyond the scope of discussion of this thesis. Typically, it is quite difficult to separate the effects of lattice and Schottky contributions from the total heat capacity. One can attempt to subtract the Schottky contribution correctly from the total specific heat by comparing the theoretical and experimental values of the entropy.

The nuclear Schottky contribution for rare-earths becomes important at very low temperatures $T \leq 1 - 2$ K. An atomic nucleus with magnetic moment μ_N may have a series of energy levels in an internal field H_{eff} arising from orbital and conduction electrons. The interaction of the quadrupolar moment of the nucleus, if non-zero (as for Ho), with neighbouring fields of atoms would also lead to hyperfine splitting. Among the samples being investigated in this thesis, an appreciable hyperfine contribution was only observed in Tb, Ho and Mn containing samples; the nuclear Schottky anomaly for other rare-earths occurs at temperatures below the experimental measurement limit of the He3 heat capacity option (0.4 K) and so did not contribute significantly to the heat capacity. The nuclear Schottky anomaly for Ho samples (which has a peak at $\approx$ 0.3 K) has a particularly dominant contribution, masking the effect of any magnetic ordering transition, if present, at $T \leq 1$ K. Complete modelling of the nuclear Schottky anomaly is not possible from the heat capacity data as it would require estimation of the nuclear energy levels using an external probe. However, for all the samples measured, the ‘high-temperature tail’ of the hyperfine contribution to the heat capacity can be approximated as:

$$C_{nuc} = \frac{A}{T^2} \tag{2.39}$$

where A is a constant that can be fitted to the data.

2.4.2 Sample preparation for measurement

All the samples discussed in this thesis are insulators and have very poor thermal conductivity [241, 242]. Therefore in order to obtain a proper heat capacity measurement, the sample has to be mixed with a good thermal conductor. Silver was chosen for this purpose. Equal amounts of the sample and silver powder were mixed and pressed into a pellet. A small portion of the pellet was sliced off and used for the heat capacity measurement. The heat capacity values for silver in the temperature range of measurement (usually 0.4 - 30 K) are well documented in the literature [243]; this was scaled by mass and subtracted to obtain the contribution from the sample heat capacity only.

In some instances, it was observed that mixing equal amounts of silver and the sample still did not provide sufficient thermal conductivity. In such cases, the measurement was repeated with a higher weight of silver powder mixed with the sample.

2.4.3 Measurements using a PPMS

Heat capacity measurements were carried out using a Quantum Design PPMS [244] using the two-tau model relaxation technique. The standard heat capacity option enables measurements in the temperature range 1.8 - 400 K in the magnetic field range 0 - 9 T. The He3 option enables heat capacity measurements down to a minimum temperature of 0.4 K in the same field range. The sample to be measured is placed on a calorimeter puck, which is calibrated over the entire temperature and field range in which measurements are to be carried out. A small quantity of Apiezon N grease or H grease is used for providing thermal contact between the sample and the wires depending on the temperature range of the measurement. Prior to measuring the sample, the contribution from the stage, puck and grease are measured separately as the addenda. This is then subtracted from the total heat capacity to give the contribution from the sample only.

2.4.4 Thermal models

The raw numbers obtained during measurement are converted into heat capacity values using the following mathematical models [245]:

(a) Simple model: This model assumes that the sample platform and the sample are in good thermal contact with each other and are at the same temperature, T, during measurement. T as a function of time, t, is given by:

$$C_{tot}\frac{dT}{dt} = -K_w(T - T_b) + P(t) \tag{2.40}$$

where C_{tot} is the total heat capacity, K_w is the thermal conductance of the supporting wires , T_b is the temperature of the puck frame and $P(t)$ is the power applied by the heater. The software uses the simple model to measure the addenda.

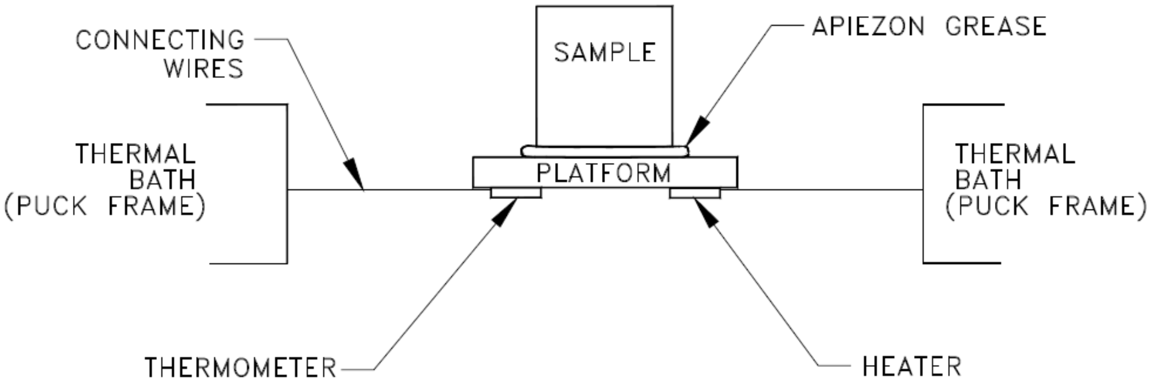

Figure 2.6 Thermal contacts to the sample and the sample platform in the Quantum Design PPMS Heat Capacity option. Image taken from [245].

(b) Two-tau model: This model assumes that the sample platform and the sample are not in good thermal contact with each other. This is the case for all the sample measurements described in this thesis because the samples are thermal insulators. The two-tau model simulates both the effect of heat flowing between the sample platform and sample and the effect of heat flowing between the sample platform and puck frame as shown in Figure 2.6. This is expressed by the following equations:

$$C_{plat}\frac{dT_p}{dt} = P(t) - K_w(T_p(t) - T_b) + K_g(T_s(t) - T_p(t)) \tag{2.41}$$

$$C_{sample}\frac{dT_s}{dt} = -K_g(T_s(t) - T_p(t)) \tag{2.42}$$

where C_{plat} is the heat capacity of the sample platform, C_{sample} is the heat capacity of the sample, and K_g is the thermal conductance between the two from the grease. The sample platform and sample temperatures are given by $T_p(t)$ and $T_s(t)$.

Data fitting is carried out using a non-linear least square algorithm. The goodness of fit is given by a χ^2 value and the degree of thermal contact can be ascertained from the sample coupling. For reliable measurements, a sample coupling of $>90\%$ is desirable. However a sample coupling of 100% indicates an error as it implies that the sample is poorly attached or the heat capacity of the sample is not large compared to the platform.

In this thesis, heat capacity measurements were primarily carried out to probe the existence of any magnetic ordering transitions in the temperature range $0.4 \leq T \leq 2$ K as the minimum temperature for the susceptibility and magnetisation measurements was 2 K. A sharp λ type anomaly in the $C_{mag}(T)$ or C_{mag}/T vs T curve is indicative of a second order magnetic phase transition, corresponding to three-dimensional magnetic ordering. For an antiferromagnet, any such anomaly in the specific heat would be accompanied by a similar peak in $\frac{d(\chi T)}{dT}$, where χ is the magnetic susceptibility [246]. More subtle magnetic features are apparent in the C_{mag}/T vs T plots, such as broader peaks, implying short-range magnetic ordering or van Vleck paramagnetism corresponding to a non-magnetic ground state. Instances of such magnetic features will be presented in subsequent chapters while discussing the results for different families of complex lanthanide oxides.

Chapter 3

Magnetic properties of lanthanide garnets, $Ln_3A_2X_3O_{12}$: Part I

This chapter discusses the effect of varying the single-ion anisotropy (by changing the magnetic ion) and chemical pressure (by varying the non-magnetic cations) on the magnetic and magnetocaloric properties of a well-known family of geometrically frustrated lanthanide oxides: the lanthanide garnets, $Ln_3A_2X_3O_{12}$. Results are presented for garnets with Ln = Gd, Tb, Dy, Ho. Inclusion of magnetic cations on the non-magnetic cation sites will be discussed in the next chapter.

3.1 Background

The magnetic properties of geometrically frustrated lanthanide oxides can vary dramatically with the magnetic Ln^{3+} due to changes in the magnitude of spin interactions, the crystal electric field scheme and the associated single-ion anisotropy [45]. As discussed in the introduction, this has been observed for families of materials like $Ln_2B_2O_7$ [45], $Ln_3A_2Sb_3O_{14}$ [119] and $SrLn_2O_4$ [127]. Even for a particular frustrated geometry and magnetic Ln^{3+}, the magnetic properties can vary radically with small changes in the structure [2]. One way of systematically studying such variations is by exploring the effect of chemical pressure, that is, changing the size of the non-magnetic cation in the lattice. The effect of doing so is twofold [59, 247]: Firstly, it alters the lattice parameter and hence the distances between the magnetic Ln^{3+}, which changes the dipolar and exchange interactions. Secondly, it causes subtle changes to the Ln-O environment, which affects the crystal electric field (CEF) and hence the single-ion anisotropy of the magnetic Ln^{3+} and the superexchange interactions. Such studies have been carried out for the highly frustrated lanthanide pyrochlores, $Ln_2B_2O_7$ (B = non-magnetic cation), where the dominant interactions are the nearest-neighbour exchange, the dipolar interaction and CEF effects. The classical spin ice state in pyrochlores with Ln = Dy, Ho is remarkably robust to chemical pressure for different B cations [59]. On the other hand, varying the chemical pressure radically changes the fragile magnetic ground state in quantum spin ice candidates with Ln = Tb, Yb. [45, 248, 249]. The chemical pressure also changes the nature of magnetic ordering in Heisenberg pyrochlores with Ln = Gd [49, 247, 250]. This indicates that the impact of chemical pressure is highly dependent on the magnetic Ln^{3+} and the exact nature of the magnetic ground state.

The lanthanide garnets, having the general formula $Ln_3A_2X_3O_{12}$, are a well-known three-dimensionally frustrated system. They crystallise in a cubic structure and contain three distinct cation sites based on the coordination with oxygen: dodecahedral occupied by Ln, octahedral occupied by A and tetrahedral occupied by X [251, 252], Figure 3.1a. The magnetic Ln^{3+} ions are located at the vertices of corner-sharing triangles which form two interpenetrating networks of bifurcated ten membered rings, giving rise to a high degree of three-dimensional geometrical frustration [108], Figure 3.1b. Since there are two non-magnetic cation sites, there is a lot of potential for exploring the magnetic phase diagram in the lanthanide garnets by varying the non-magnetic cations and hence the chemical pressure on either or both A and X sites. Changing the chemical pressure allows tuning of the magnetic interactions as well as subtle changes to the CEF and single-ion anisotropy, offering an opportunity to study the physics of frustration in these materials. Any changes in the magnetic properties will also impact the magnetocaloric effect (MCE). This is significant because as discussed in the introduction, gadolinium gallium garnet (GGG), $Gd_3Ga_5O_{12}$, and dysprosium gallium garnet (DGG), $Dy_3Ga_5O_{12}$, are standard magnetocaloric materials (MCMs) for solid state magnetic refrigeration in the liquid helium temperature regime [183, 187, 199, 200]. Therefore, it may be possible to optimise the MCE further by varying the cations on the A and X sites. While this has been reported for Al^{3+} substituted GGG [185], the impact on the MCE for the other Ln^{3+} as well as for other combinations of A and X have not been explored.

Prior to discussing the results, the current state of knowledge regarding the magnetic properties of the lanthanide garnets with non-magnetic cations on the A and X sites are reviewed for the magnetic lanthanide ions studied in this chapter, Ln = Gd, Tb, Dy, Ho.

3.1.1 $Gd_3A_2X_3O_{12}$

Most of the experimental work on lanthanide garnets has focused on $Gd_3Ga_5O_{12}$ (GGG), where both the octahedral and tetrahedral sites are occupied by Ga^{3+}. A detailed review has

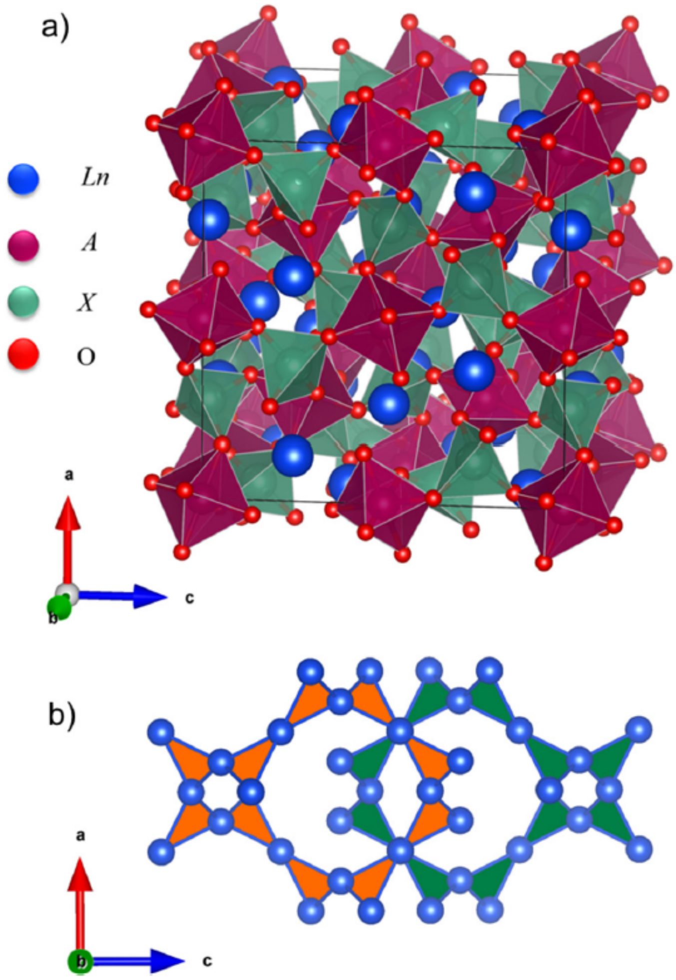

Figure 3.1 a) Crystal structure of lanthanide garnets $Ln_3A_2X_3O_{12}$: Ln occupy the dodecahedral sites, A occupy the octahedral sites while the tetrahedral sites are occupied by X. b) Connectivity of magnetic Ln^{3+} ions: The Ln^{3+} lie at the vertices of corner-sharing equilateral triangles forming two interpenetrating ten-membered rings. This results in a highly frustrated three-dimensional network.

already been presented in the introduction but the salient points will be summarised here for clarity. GGG is a canonical spin liquid candidate with no long-range ordering down to 0.025 K and a glassy transition at $T_g \approx 0.14$ K below the spin liquid state [141, 143, 145, 149, 153]. Recent experiments have pointed to the existence of a hidden multipolar order on the ten-membered loops in the spin liquid state [150], as well as existence of dispersionless spin waves on the ten-membered loops in applied magnetic fields [154].

Quilliam et. al [253] carried out a study comparing the magnetic properties of $Gd_3Ga_5O_{12}$, $Gd_3Al_5O_{12}$ (with both octahedral and tetrahedral sites occupied by Al^{3+}) and $Gd_3Te_2Li_3O_{12}$ (with octahedral sites occupied by Te^{6+} and tetrahedral sites occupied by

Li^+). Heat capacity measurements showed the onset of short-range magnetic correlations at ≈ 0.8 K for $Gd_3Ga_5O_{12}$ and ≈ 1 K for $Gd_3Te_2Li_3O_{12}$ and $Gd_3Al_5O_{12}$. A sharp transition was observed at 0.243 K for $Gd_3Te_2Li_3O_{12}$ in contrast to the absence of order for $Gd_3Ga_5O_{12}$. $Gd_3Al_5O_{12}$ was reported to behave like a 'material bridge' between $Gd_3Ga_5O_{12}$ and $Gd_3Te_2Li_3O_{12}$ with a smaller and broader transition at an intermediate temperature, 0.175 K. Calculations from the Curie-Weiss fit parameters showed that the dipolar interaction (D) was almost identical for all three materials and the nearest-neighbour exchange interaction (J_1) gradually increased from $Gd_3Ga_5O_{12}$ to $Gd_3Te_2Li_3O_{12}$ to $Gd_3Al_5O_{12}$. The onset of short-range magnetic correlations at higher temperatures in $Gd_3Te_2Li_3O_{12}$ and $Gd_3Al_5O_{12}$ as compared to $Gd_3Ga_5O_{12}$ was attributed to the stronger J_1 interactions. The fact that $Gd_3Ga_5O_{12}$ showed no conventional ordering while $Gd_3Te_2Li_3O_{12}$ and $Gd_3Al_5O_{12}$ showed long-range ordering features was attributed to one of two possibilities: a) finely-tuned D and J_1 interactions in $Gd_3Ga_5O_{12}$ which led to a disordered state while $Gd_3Te_2Li_3O_{12}$ and $Gd_3Al_5O_{12}$ appeared to resemble conventional dipolar antiferromagnets, with the increasing ratio of D/J_1 from $Gd_3Al_5O_{12}$ to $Gd_3Te_2Li_3O_{12}$ relieving the frustration. b) extreme sensitivity of $Gd_3Ga_5O_{12}$ to off-stoichiometry (random excess of Gd^{3+} on the octahedral Ga^{3+} sites) as compared to $Gd_3Te_2Li_3O_{12}$ and $Gd_3Al_5O_{12}$. The sharp magnetic ordering transition in $Gd_3Te_2Li_3O_{12}$ was shown to be robust to random site dilution, providing stronger support for hypothesis b).

More recently, Florea et. al reported a spin-freezing transition at ≈ 0.3 K in $Gd_3Al_5O_{12}$ and absence of any long-range ordering down to 0.06 K, indicating the presence of a spin-liquid phase similar to $Gd_3Ga_5O_{12}$ [254]. The higher spin-freezing temperature in $Gd_3Al_5O_{12}$ (≈ 0.3 K) as compared to $Gd_3Ga_5O_{12}$ (≈ 0.15 K [143]) was attributed to the stronger J_1 interactions in $Gd_3Al_5O_{12}$. Magnetisation measurements at ultra-low temperatures in magnetic field showed a magnetic phase diagram similar to $Gd_3Ga_5O_{12}$. It was proposed that the magnetic phase diagram of $Gd_3Ga_5O_{12}$, including the zero field spin liquid behaviour, was robust to variations in the D and J_1 interactions, in contrast to the pyrochlores $Gd_2B_2O_7$ (B = Ti, Sn) which have different magnetic structures [45]. These results are in contrast to the long-range ordering proposed by Quilliam et. al and the exact nature as well as the robustness of the magnetic ground state in Gd garnets remains an open question.

3.1.2 $Ln_3A_2X_3O_{12}$, Ln = Tb, Dy, Ho

The lanthanide gallium garnets with Ln = Tb, Dy, Ho have been studied less extensively. $Tb_3Ga_5O_{12}$ and $Ho_3Ga_5O_{12}$ undergo antiferromagnetic ordering below $T_N = 0.25$ K and 0.19 K respectively [255, 256]. They have local Ising anisotropy and order in a six sublattice antiferromagnetic type A (AFA) structure, where moments of equal magnitude are aligned along [100], [$\bar{1}$00], [010], [0$\bar{1}$0], [001], [00$\bar{1}$] [257–259]. Heat capacity measurements on $Dy_3Ga_5O_{12}$ reported broad short-range ordering at 0.6 - 0.7 K and a sharp transition at T_N = 0.373 K [260]. Crystal field studies suggested a quasi-planar anisotropy for $Dy_3Ga_5O_{12}$ [198] while neutron diffraction measurements at 0.07 K reported antiferromagnetic ordering below T_N although the exact magnetic structure was not elucidated [197]. A later neutron scattering experiment on $Ho_3Ga_5O_{12}$ reported the onset of short-range order below 0.6 K and coexistence of long and short-range order below 0.3 K down to 0.05 K [261]. This behaviour is similar to that reported in the bulk measurements for $Dy_3Ga_5O_{12}$ [260], however in both cases, the exact nature of the short-range order is yet to be determined. $Dy_3Al_5O_{12}$ has strong Ising anisotropy and undergoes antiferromagnetic ordering at T_N = 2.49 K in the same AFA structure as reported for $Tb_3Ga_5O_{12}$ and $Ho_3Ga_5O_{12}$ [196, 259, 262]. $Tb_3Al_5O_{12}$ and $Ho_3Al_5O_{12}$ also order in the AFA structure at T_N = 1.35 K and 0.95 K respectively [263, 264]. The lanthanide aluminium garnets $Ln_3Al_5O_{12}$ (Ln = Tb, Dy, Ho) undergo transitions at much higher temperatures as compared to the corresponding $Ln_3Ga_5O_{12}$, and thus, much like their Gd counterparts, are less frustrated. The increased transition temperatures in $Ln_3Al_5O_{12}$ (Ln = Tb, Dy, Ho) have been attributed to increased dipolar interactions and stronger Ising anisotropy [265]. A previous study on the lanthanide tellurate lithium garnets, $Ln_3Te_2Li_3O_{12}$, with aliovalent (differently charged) A (Te^{6+}) and X (Li^+), reported a transition at 2 K for Ln = Dy; no transition was reported for Ln = Tb and Ho at $T \geq 2$ K [266].

In this chapter, a comprehensive study on the synthesis, structural characterisation and bulk magnetic properties of polycrystalline samples of $Ln_3Ga_5O_{12}$, $Ln_3Sc_2Ga_3O_{12}$, $Ln_3Sc_2Al_3O_{12}$, $Ln_3In_2Ga_3O_{12}$ and $Ln_3Te_2Li_3O_{12}$ for Ln = Gd, Tb, Dy, Ho is presented for the first time. Magnetic susceptibility and isothermal magnetisation measurements have been carried out to study the magnetic behaviour for $T \geq 2$ K, while zero field heat capacity measurements have been carried out to investigate the existence of magnetic ordering transitions for $T \geq 0.4$ K. The change in magnetic entropy has been evaluated to characterise the MCE. The magnetic properties and the degree of magnetic frustration are discussed in relation to the previously reported literature for $Ln_3Ga_5O_{12}$ and $Ln_3Al_5O_{12}$, which has been summarised above.

3.2 Sample preparation

Powder samples of $Ln_3A_2X_3O_{12}$ (Ln = Gd, Tb, Dy, Ho; A = Ga, Sc, In, Te; X = Ga, Al, Li) were prepared using a solid-state synthesis. Samples of $Ln_3Ga_5O_{12}$ were prepared by mixing stoichiometric amounts of Ln_2O_3 (Ln = Gd, Dy, Ho) or Tb_4O_7 and Ga_2O_3. To ensure the correct stoichiometry, Gd_2O_3 and Ga_2O_3 were pre-dried at 800 °C and 500 °C respectively prior to weighing out. The powders were pressed into pellets and heated between 1200 - 1300 °C for 24 - 72 hours with intermediate re-grindings, until a pure phase was obtained. The sample of $Gd_3Ga_5O_{12}$ was prepared by Alice Sackville Hamilton [185]. Samples of $Ln_3Sc_2Ga_3O_{12}$ and $Ln_3In_2Ga_3O_{12}$ were prepared by mixing stoichiometric amounts of Ln_2O_3 (*Ln* = Gd, Dy, Ho) or Tb_4O_7, Ga_2O_3 and Sc_2O_3 or In_2O_3. Pellets were heated at increasingly higher temperatures between 1200 – 1350 °C for 48-72 hours with intermittent re-grindings. An alternative synthesis route was followed for $Ln_3Sc_2Al_3O_{12}$ to prevent the formation of a $LnAlO_3$ perovskite impurity phase. The starting materials $Ln(NO_3)_3$ (*Ln* = Gd, Tb, Dy, Ho) and $Al(NO_3)_3$ were dried overnight at 80 °C and 60 °C respectively to remove any excess water of crystallisation. Stoichiometric amounts of $Ln(NO_3)_3$ (*Ln* = Gd, Tb, Dy, Ho), $Al(NO_3)_3$ and Sc_2O_3 were mixed well. Following a pre-reaction at 1000 °C, pellets were heated at increasingly higher temperatures between 1200 – 1400 °C for 48-72 hours with intermittent re-grindings. Samples of $Ln_3Te_2Li_3O_{12}$ were prepared by mixing stoichiometric amounts of Ln_2O_3 (*Ln* = Gd, Dy, Ho) or Tb_4O_7, TeO_2 and Li_2CO_3 and pressing into pellets. Li_2CO_3 was dried at 180 °C prior to weighing out to prevent hydration. Pellets were heated at 850 °C for 20 hours with one intermediate regrinding after 10 hours. Attempts to substitute Sc^{3+} and In^{3+} on the *X* site resulted in the formation of $LnScO_3$ and $LnInO_3$ impurities. It is postulated that Sc^{3+} and In^{3+} are not stable in the tetrahedral coordination. Attempts to synthesise $Ln_3ScGa_4O_{12}$ yielded a mixed phase of $Ln_3Sc_2Ga_3O_{12}$ and $Ln_3Ga_5O_{12}$. Synthesis of $Ln_3InGa_4O_{12}$ was not attempted. Attempts to synthesise $Ln_3In_2Al_3O_{12}$ by solid state as well as sol-gel methods resulted in the formation of $LnAlO_3$, $LnInO_3$ and In_2O_3 impurities and it was concluded that this synthesis was not possible due to the large difference in the size of In^{3+} and Al^{3+} ions [267].

3.3 Structural characterisation

In order to track the progress of the reaction, initial structural characterisation was carried out using PXRD. Short scans were collected over the angular range $5^\circ \leq 2\theta \leq 60^\circ$ using a Panalytical Empyrean X-ray diffractometer (Cu Kα radiation, λ = 1.540 Å). Once a phase pure product was obtained, longer PXRD scans for 2 hours over a wider angular range $5^\circ \leq 2\theta \leq 90^\circ$ were collected on the same instrument for quantitative structural analysis. For garnets with *Ln* = Ho, room temperature (RT) PND experiments were carried out on the D2B diffractometer, ILL, Grenoble (λ = 1.595 Å) at 300 K except $Ho_3Ga_5O_{12}$, for which only PXRD scans were performed. Rietveld refinement was carried out using the Fullprof

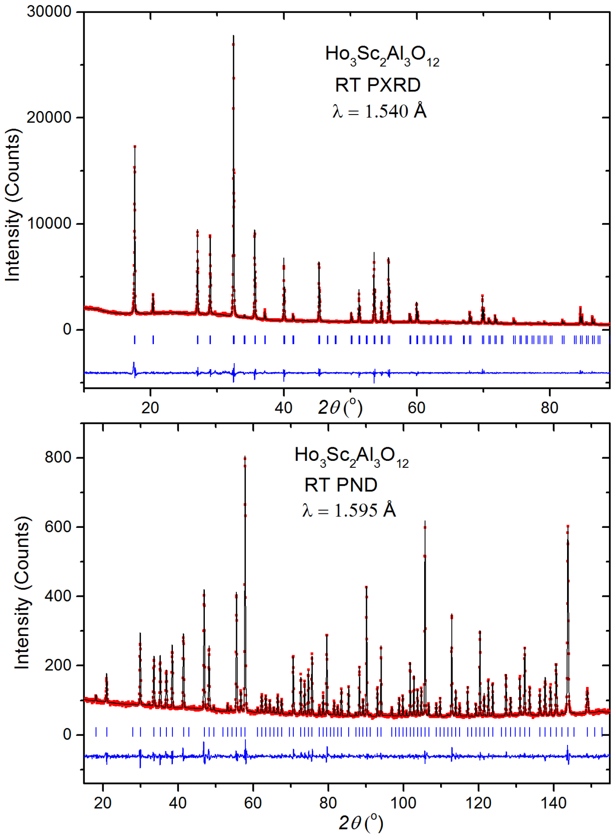

Figure 3.2 RT PXRD (upper panel) + PND (lower panel) pattern for $Ho_3Sc_2Al_3O_{12}$: Red dots - Experimental data, Black line - Modelled data, Blue line - Difference pattern, Blue ticks - Bragg positions).

suite of programs. Backgrounds were fitted using linear interpolation and the peak shape was modelled using a pseudo-Voigt function.

RT structural refinements for garnets with Ln = Gd, Tb, Dy were carried out using PXRD only. Combined RT PXRD + PND structural refinements were carried out for garnets with Ln = Ho, except $Ho_3Ga_5O_{12}$. Figure 3.2 shows a representative combined PXRD + PND refinement for $Ho_3Sc_2Al_3O_{12}$. The combined RT PXRD + PND refinements for $Ho_3Sc_2Ga_3O_{12}$, $Ho_3In_2Ga_3O_{12}$, $Ho_3Te_2Li_3O_{12}$ and PXRD refinement for $Ho_3Ga_5O_{12}$ can be found in Appendix A. All the garnets crystallise in the same cubic structure with space group $Ia\bar{3}d$. The magnetic Ln^{3+} (Ln = Gd, Tb, Dy, Ho) occupy the dodecahedral 24c (0, 0.25, 0.125) site. Ga^{3+}, Sc^{3+}, In^{3+} or Te^{6+} occupy the octahedral 16a (0, 0, 0) site while the tetrahedral 24d (0, 0.25, 0.375) site is occupied by Ga^{3+}, Al^{3+} or Li^{+} in the respective garnets. O^{2-} occupies the 96h (x, y, z) site. Structural parameters for all the lanthanide garnets are summarised in Table 3.1. Rietveld analysis shows that the lattice volume varies linearly with the ionic radius of the Ln^{3+} ion for a given combination of A and X ions, Figure 3.3a. A similar relationship was expected between the lattice volume and the weighted ionic radii of the A and X ions for each Ln^{3+}, $r_{av} = \frac{2r_A+3r_X}{5}$. However, as is seen in Figure 3.3b, this is not the case for all combinations of A and X. While the $Ln_3A_2Ga_3O_{12}$ families (A = Ga, Sc, In) follow a linear trend for all Ln, the $Ln_3Sc_2Al_3O_{12}$ and $Ln_3Te_2Li_3O_{12}$ families deviate from a straight line implying that there are other effects to be considered such as the difference in sizes or charges of the A and X sites.

Table 3.1 Structural parameters for $Ln_3Ga_5O_{12}$, $Ln_3Sc_2Ga_3O_{12}$, $Ln_3Sc_2Al_3O_{12}$, $Ln_3In_2Ga_3O_{12}$ and $Ln_3Te_2Li_3O_{12}$; Ln = Gd, Tb, Dy, Ho. PXRD refinements were carried out for all garnets with Ln = Gd, Tb, Dy and $Ho_3Ga_5O_{12}$ while combined PXRD + PND refinements were carried out for all other garnets with Ln = Ho. All refinements were carried out in the space group $Ia\bar{3}d$, with Ln on the 24c sites (0, 0.25, 0.125), Ga_{oct}/Sc/In/Te on the 16a sites (0, 0, 0), Ga_{tetr}/Al/Li on the 24d sites (0, 0.25, 0.375) and O on the 96h (x, y, z) sites.

Ln		Gd	Tb	Dy	Ho
$\boldsymbol{Ln_3Ga_5O_{12}}$					
a (Å)		12.38348(2)	12.34191(4)	12.31057(5)	12.28157(5)
Ln	B_{iso} (Å^2)	0.5	0.5	0.5	0.5
Ga_{oct}	B_{iso} (Å^2)	0.5	0.5	0.5	0.5
Ga_{tetr}	B_{iso} (Å^2)	0.5	0.5	0.5	0.5
O	x	-0.0327(2)	-0.0307(3)	-0.0299(3)	-0.02976(2)
	y	0.0542(2)	0.0541(3)	0.0539(3)	0.05150(3)
	z	0.1490(2)	0.1499(4)	0.1495(4)	0.1494(3)
	B_{iso} (Å^2)	0.5	0.5	0.5	0.5
R_{wp}		10.2	9.98	10.1	9.74
χ^2		2.86	2.92	2.59	4.32
$\boldsymbol{Ln_3Sc_2Ga_3O_{12}}$					
a (Å)		12.57321(7)	12.53907(6)	12.50241(6)	12.47517(3)
Ln	B_{iso} (Å^2)	0.5	0.5	0.5	0.08(2)
Sc	B_{iso} (Å^2)	0.5	0.5	0.5	0.19(2)
Ga	B_{iso} (Å^2)	0.5	0.5	0.5	0.30(2)
O	x	-0.0299(5)	-0.0310(3)	-0.3035(3)	-0.0283(8)
	y	0.0571(5)	0.0574(3)	0.0567(3)	0.0582(9)
	z	0.1521(5)	0.1552(3)	0.1581(3)	0.1545(8)
	B_{iso} (Å^2)	0.5	0.5	0.5	0.422(15)
R_{wp}		15.6	10.7	10.9	10.6
χ^2		1.57	1.87	1.68	2.96

$Ln_3Sc_2Al_3O_{12}$					
a (Å)		12.43448(6)	12.39878(5)	12.35927(6)	12.32972(3)
Ln	B_{iso} (Å^2)	0.5	0.5	0.5	0.13(2)
Sc	B_{iso} (Å^2)	0.5	0.5	0.5	0.17(2)
Al	B_{iso} (Å^2)	0.5	0.5	0.5	0.32(4)
O	x	-0.0328(3)	-0.3120(3)	-0.0328(3)	-0.03155(10)
	y	0.5335(4)	0.5483(4)	0.5402(3)	0.56744(11)
	z	0.1561(4)	0.6559(4)	0.1562(4)	0.1566(9)
	B_{iso} (Å^2)	0.5	0.5	0.5	0.43 (2)
R_{wp}		13.2	14.7	12.8	12.4
χ^2		2.27	3.18	2.06	2.88
$Ln_3In_2Ga_3O_{12}$					
a (Å)		12.66112(6)	12.62654(5)	12.59268(6)	12.55859(9)
Ln	B_{iso} (Å^2)	0.5	0.5	0.5	0.11(2)
In	B_{iso} (Å^2)	0.5	0.5	0.5	0.03(3)
Ga	B_{iso} (Å^2)	0.5	0.5	0.5	0.37(2)
O	x	-0.0318(3)	-0.0319(3)	-0.0330(6)	-0.0283(7)
	y	0.0583(3)	0.0598(3)	0.0608(4)	0.0599(8)
	z	0.1573(4)	0.1565(4)	0.1571(5)	0.1567(8)
	B_{iso} (Å^2)	0.5	0.5	0.5	0.476(15)
R_{wp}		10.1	10.0	11.7	11.5
χ^2		1.80	2.38	2.75	2.15
$Ln_3Te_2Li_3O_{12}$					
a (Å)		12.39402(2)	12.34898(2)	12.31050(2)	12.27401(7)
Ln	B_{iso} (Å^2)	0.5	0.5	0.5	0.545(19)
Te	B_{iso} (Å^2)	0.5	0.5	0.5	0.222(24)
Li	B_{iso} (Å^2)	0.5	0.5	0.5	0.52(7)
O	x	-0.0274 (3)	-0.0255(4)	-0.0274(3)	-0.0264(7)
	y	0.0501 (4)	0.0504(4)	0.0512(4)	0.0527(8)
	z	0.1450(4)	0.1432(4)	0.1457(3)	0.1453(8)
	B_{iso} (Å^2)	0.5	0.5	0.5	0.330(15)
R_{wp}		12.5	13.1	14.3	12.0
χ^2		1.89	2.96	2.21	2.75

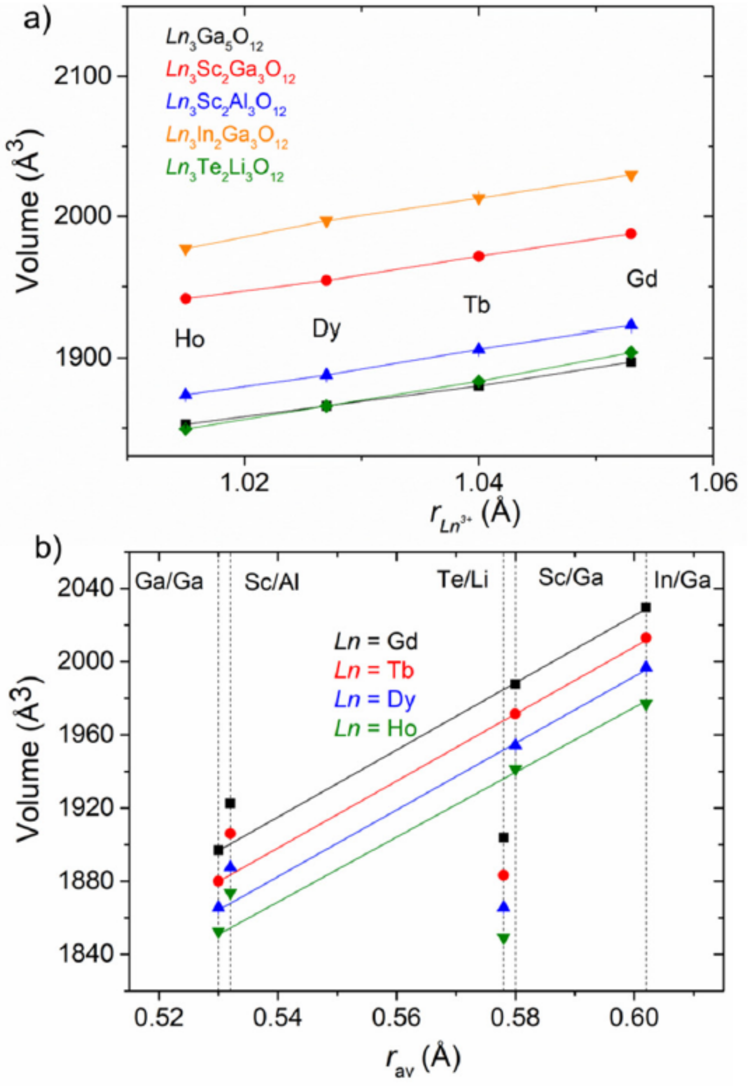

Figure 3.3 Variation of lattice volume with: a) ionic radii of *Ln* b) weighted ionic radii of *A* and *X*. Lines are a guide to the eye. Error bars are smaller than size of symbols.

Selected bond lengths are given in Table 3.2. As expected for the cubic symmetry, the changes in *Ln*-*Ln* bond lengths follow the same trend as the changes in the lattice parameters. For a particular *Ln*, there are subtle changes in the *Ln*-O bond lengths which may impact the local CEF and hence the single-ion anisotropy of the magnetic Ln^{3+}.

Table 3.2 Selected bond lengths for $Ln_3Ga_5O_{12}$, $Ln_3Sc_2Ga_3O_{12}$, $Ln_3Sc_2Al_3O_{12}$, $Ln_3In_2Ga_3O_{12}$ and $Ln_3Te_2Li_3O_{12}$; *Ln* = Gd, Tb, Dy, Ho.

Ln	Gd	Tb	Dy	Ho
$Ln_3Ga_5O_{12}$				
Ln-*Ln* (Å)	3.79169(5) × 4	3.77892(3) × 4	3.76933(3) × 4	3.76045(3) × 4
Ln-O (Å)	2.413(2) × 4	2.380(5) × 4	2.368(5) × 4	2.354(4) × 4
	2.476(2) × 4	2.467(4) × 4	2.461(4) × 4	2.483(3) × 4
<*Ln*-O>(Å)	2.444	2.424	2.414	2.418
Ga_{oct}–O (Å)	2.005(2) × 6	2.003(4) × 6	1.991(4) × 6	1.975(3) × 6
Ga_{tetr}-O (Å)	1.820(3) × 4	1.824(4) × 4	1.828(4) × 4	1.815(4) × 4
$Ln_3Sc_2Ga_3O_{12}$				
Ln-*Ln* (Å)	3.84974(3) × 4	3.83929(3) × 4	3.82807(3) × 4	3.81964(3) × 4
Ln-O (Å)	2.414(7) × 4	2.422(4) × 4	2.405(4) × 4	2.372(4) × 4
	2.477(7) × 4	2.469(4) × 4	2.468(4) × 4	2.495(3) × 4
<*Ln*-O>(Å)	2.446	2.446	2.436	2.434
Sc –O (Å)	2.077(7) × 6	2.069(4) × 6	2.063(4) × 6	2.074(4) × 6
Ga-O (Å)	1.861(7) × 4	1.852(4) × 4	1.846(4) × 4	1.815(4) × 4
$Ln_3Sc_2Al_3O_{12}$				
Ln-*Ln* (Å)	3.80727(3) × 4	3.79634(3) × 4	3.78424(3) × 4	3.77464(3) × 4
Ln-O (Å)	2.378(5) × 4	2.361(5) × 4	2.365(5) × 4	2.313(5) × 4
	2.508(4) × 4	2.481(4) × 4	2.486(4) × 4	2.460(4) × 4
<*Ln*-O>(Å)	2.443	2.421	2.426	2.386
Sc –O (Å	2.092(5) × 6	2.085(5) × 6	2.082(4) × 6	2.075(4) × 6
Al-O (Å)	1.766(5) × 4	1.782(5) × 4	1.757(5) × 4	1.792(5) × 4
$Ln_3In_2Ga_3O_{12}$				
Ln-*Ln* (Å)	3.87666(3) × 4	3.86608(3) × 4	3.85571(3) × 4	3.84282 (3) × 4
Ln-O (Å)	2.423(5) × 4	2.427(5) × 4	2.432(6) × 4	2.394 (5) × 4
	2.494(4) × 4	2.467(4) × 4	2.452(6) × 4	2.477 (4) × 4
<*Ln*-O>(Å)	2.458	2.447	2.442	2.436
In –O (Å)	2.162(4) × 6	2.153(5) × 6	2.162(6) × 6	2.154 (4) × 6
Ga-O (Å)	1.820(5) × 4	1.829(5) × 4	1.816(6) × 4	1.796(5) × 4
$Ln_3Te_2Li_3O_{12}$				
Ln-*Ln* (Å)	3.79488(3) × 4	3.78109(3) × 4	3.76930(3) × 4	3.75812(3) × 4
Ln-O (Å)	2.376(5) × 4	2.363(5) × 4	2.360(5) × 4	2.374(4) × 4
	2.513(5) × 4	2.495(5) × 4	2.484(4) × 4	2.484(3) × 4
<*Ln*-O>(Å)	2.444	2.429	2.422	2.429
Te –O (Å)	1.931(5) × 6	1.901(5) × 6	1.931(5) × 6	1.892(4) × 6
Li-O (Å)	1.882(5) × 4	1.906(5) × 4	1.867(5) × 4	1.877(4) × 4

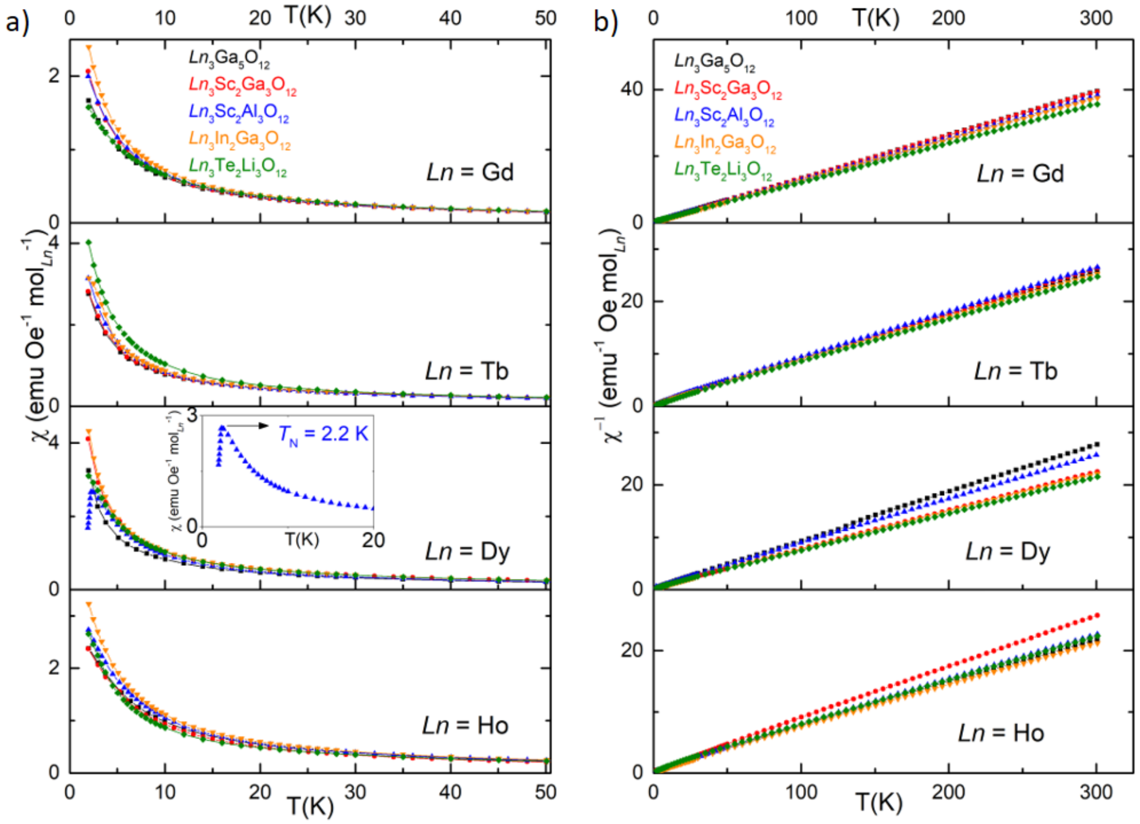

Figure 3.4 a) ZFC $\chi(T)$ and b) $\chi^{-1}(T)$ from 2- 300 K in a field of 100 Oe for $Ln_3Ga_5O_{12}$, $Ln_3Sc_2Ga_3O_{12}$, $Ln_3Sc_2Al_3O_{12}$, $Ln_3In_2Ga_3O_{12}$ and $Ln_3Te_2Li_3O_{12}$; *Ln* = Gd, Tb, Dy, Ho. Inset in third panel of a) shows a sharp ordering transition at T_N = 2.2 K for $Dy_3Sc_2Al_3O_{12}$.

3.4 Bulk magnetic measurements

3.4.1 Magnetic susceptibility

The ZFC magnetic susceptibility, $\chi(T)$, measured in a field of 100 Oe in the temperature range 2 - 300 K is shown in Figure 3.4a. An ordering transition is observed for $Dy_3Sc_2Al_3O_{12}$ at T = 2.2(1) K. None of the other garnets show any magnetic ordering at $T \geq 2$ K.

The inverse susceptibility, Figure 3.4b, can be fit to the Curie-Weiss law, equation (1.59). The magnetic moment, μ_{eff}, is determined from the Curie constant according to equation (1.26). For garnets with *Ln* = Gd, the fit to the Curie-Weiss law is carried out in the temperature range 100 - 300 K to calculate θ_{CW} and μ_{eff}. However, for the lanthanide ions with strong single-ion anisotropy, *Ln* = Tb, Dy, Ho, the presence of low-lying crystal electric field states [198, 258, 268] impact the values of θ_{CW}. Therefore the fit was carried out at low temperatures, between 2 - 10 K. Parameters determined from the fits are summarised in Table 3.3. The negative values of the Curie-Weiss temperature, θ_{CW}, indicate net antiferromagnetic

Table 3.3 Curie-Weiss fit parameters for $Ln_3Ga_5O_{12}$, $Ln_3Sc_2Ga_3O_{12}$, $Ln_3Sc_2Al_3O_{12}$, $Ln_3In_2Ga_3O_{12}$ and $Ln_3Te_2Li_3O_{12}$; *Ln* = Gd, Tb, Dy, Ho. The theoretical value quoted is the free-ion moment, $g_J\sqrt{J(J+1)}$, g_J is given by equation (1.20).

Ln		Gd	Tb	Dy	Ho
	Theoretical μ_{eff} (μ_B)	7.94	9.72	10.65	10.61
$Ln_3Ga_5O_{12}$	Experimental μ_{eff} (μ_B)	7.814(3)	8.34(10)	8.34(14)	10.3(3)
	θ_{CW} (K)	-1.4(2)	-1.16(4)	-1.00(6)	-3.29(10)
$Ln_3Sc_2Ga_3O_{12}$	Experimental μ_{eff} (μ_B)	7.837(9)	8.50(10)	9.37(10)	9.87(15)
	θ_{CW} (K)	-2.2(3)	-1.2(3)	-0.8(3)	-2.9(5)
$Ln_3Sc_2Al_3O_{12}$	Experimental μ_{eff} (μ_B)	7.952(7)	8.5(3)	9.1(3)	10.5(2)
	θ_{CW} (K)	-1.3(3)	-0.84(10)	-1.2(2)	-2.91(6)
$Ln_3In_2Ga_3O_{12}$	Experimental μ_{eff} (μ_B)	8.019(8)	8.5(3)	9.48(15)	10.44(13)
	θ_{CW} (K)	-0.6(3)	-0.57(11)	-0.66(5)	-2.09(4)
$Ln_3Te_2Li_3O_{12}$	Experimental μ_{eff} (μ_B)	8.233(4)	9.43(13)	9.7(2)	8.98(13)
	θ_{CW} (K)	-2.7(2)	-0.63(4)	-1.52(7)	-1.60(5)

interactions. For *Ln* = Gd, the experimentally determined magnetic moments derived from the Curie-Weiss fit are consistent with the theoretical free-ion values given by $\mu_{th} = g_J\sqrt{J(J+1)}$. However, for *Ln* = Tb, Dy, Ho they are slightly underestimated compared to the free ion values. This can be attributed to partial quenching of the angular momentum due to the crystal field; similar results have been previously reported for $Ln_3Ga_5O_{12}$, *Ln* = Tb, Dy, Ho [198, 255, 258, 265].

Table 3.4 Dipolar interaction energy, *D*, and nearest-neighbour exchange interaction energy, J_1, for $Ln_3Ga_5O_{12}$, $Ln_3Sc_2Ga_3O_{12}$, $Ln_3Sc_2Al_3O_{12}$, $Ln_3In_2Ga_3O_{12}$ and $Ln_3Te_2Li_3O_{12}$; *Ln* = Gd, Tb, Dy, Ho.

Ln		Gd	Tb	Dy	Ho
$Ln_3Ga_5O_{12}$	*D* (K)	0.69	0.80	0.81	1.23
	J_1 (K)	0.51	0.43	0.38	1.23
$Ln_3Sc_2Ga_3O_{12}$	*D* (K)	0.67	0.80	0.98	1.09
	J_1 (K)	0.83	0.46	0.30	1.10
$Ln_3Sc_2Al_3O_{12}$	*D* (K)	0.71	0.83	0.96	1.29
	J_1 (K)	0.48	0.32	0.44	1.09
$Ln_3In_2Ga_3O_{12}$	*D* (K)	0.69	0.78	0.98	1.20
	J_1 (K)	0.23	0.21	0.25	0.78
$Ln_3Te_2Li_3O_{12}$	*D* (K)	0.77	1.02	1.11	0.95
	J_1 (K)	1.02	0.24	0.57	0.6

The dipolar interaction energy, D , can be estimated from equation (1.42) and the nearest-neighbour exchange interaction energy, J_1, can be approximated from equation (1.60). Here n = the number of nearest neighbour Ln^{3+} surrounding one Ln^{3+} ion = 4. For Gd, $S = \frac{7}{2}$ and for Ln = Tb, Dy, Ho an effective $S = \frac{1}{2}$ state has been assumed. Effective spin $\frac{1}{2}$ states have been observed in $Ln_3Ga_5O_{12}$ and $Ln_3Al_5O_{12}$ for Ln = Tb, Dy, Ho [198, 258, 263, 264, 268]. However the origin of the effective $S = \frac{1}{2}$ state differs. For Ln = Dy, it is due to the ground state being an isolated Kramer's doublet at low temperatures whereas for Ln = Tb, Ho, it is an admixture of two low-lying singlet states [259, 264]. The values of D and J_1 are given in Table 3.4.

3.4.2 Isothermal magnetisation

Isothermal magnetisation measurements were carried out at select temperatures in the field range 0 – 9 T using the ACMS option on a Quantum Design PPMS. The $M(H)$ at 2 K for all the garnets is shown in Figure 3.5 and the maximum values of magnetisation per formula unit Ln (f.u.Ln), M_{max}, at 2 K, 9T are given in Table 3.5. The isothermal magnetisation is non-linear at low T for all samples. The magnetisation of the Gd garnets saturates in a field of 9 T, with the saturation value close to 7 μ_B/f.u.$_{Gd}$ as expected for Heisenberg type spins ($g_J J = 2 \times \frac{7}{2} = 7\mu_B$/f.u.$_{Gd}$). Care has to be taken when considering the isothermal magnetisation of polycrystalline samples for magnetic ions with substantial single-ion anisotropy (Ln = Tb, Dy, Ho) due to the powder averaging. However, these measurements have been used to remark on the nature of the spins in other frustrated lanthanide oxide systems [269]. In the limiting field of 9 T, none of the $M(H)$ curves for the garnets with Ln = Tb, Dy, Ho reach complete saturation. All of the observed M_{max} are significantly lower than the saturation magnetisation of a Heisenberg system, $M_{sat} = g_J J$, possibly due to partical quenching of the angular momentum by the CEF, but are consistent with the magnetisation values reported for $Ln_3Ga_5O_{12}$ [198, 258, 268]. It is therefore postulated that the garnets with Ln = Tb, Dy, Ho retain strong single-ion anisotropy. However, further analysis of the CEF scheme is required to determine the exact nature of the spins. In addition, there are some subtle differences:

(a) the magnetisation for $Tb_3Te_2Li_3O_{12}$ is significantly higher than the other Tb garnets, possibly indicating a deviation in the single-ion anisotropy.

(b) among the Dy garnets, $Dy_3Sc_2Al_3O_{12}$ exhibits a greater tendency to saturate whereas a gradual increase in magnetisation with field is observed for the others. Again, this could possibly indicate a difference in single-ion anisotropy or be due to the higher Néel temperature, T_N = 2.2(1) K, as compared to the other Dy garnets.

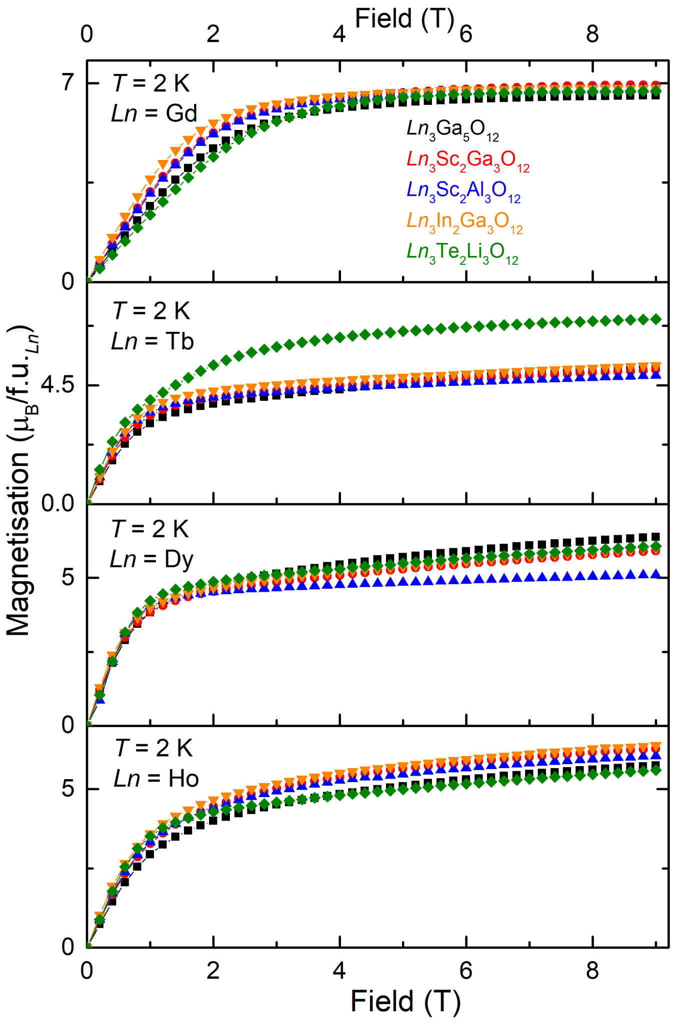

Figure 3.5 $M(H)$ curves at 2 K from 0 – 9 T for $Ln_3Ga_5O_{12}$, $Ln_3Sc_2Ga_3O_{12}$, $Ln_3Sc_2Al_3O_{12}$, $Ln_3In_2Ga_3O_{12}$ and $Ln_3Te_2Li_3O_{12}$; Ln = Gd, Tb, Dy, Ho.

Table 3.5 Maximum magnetisation per f.u.Ln for $Ln_3Ga_5O_{12}$, $Ln_3Sc_2Ga_3O_{12}$, $Ln_3Sc_2Al_3O_{12}$, $Ln_3In_2Ga_3O_{12}$ and $Ln_3Te_2Li_3O_{12}$; Ln = Gd, Tb, Dy, Ho.

Ln	Gd	Tb	Dy	Ho
Theoretical M_{sat} (μ_B/f.u.Ln)	7	9	10	10
M at $T = 2$ K, $\mu_0 H = 9$ T (μ_B/f.u.Ln)				
$Ln_3Ga_5O_{12}$	6.56(2)	5.21(2)	6.39(2)	5.74(2)
$Ln_3Sc_2Ga_3O_{12}$	6.92(3)	5.08(2)	5.91(2)	6.27(2)
$Ln_3Sc_2Al_3O_{12}$	6.77(3)	4.87(2)	5.09(2)	6.04(2)
$Ln_3In_2Ga_3O_{12}$	6.82(3)	5.25(2)	6.01(2)	6.38(2)
$Ln_3Te_2Li_3O_{12}$	6.73(3)	6.99(3)	6.07(2)	5.60(2)

3.4.3 Heat capacity

Heat capacity measurements were performed in zero field from 0.4 to 10 K using the He3 option on a Quantum Design PPMS. Equal amounts of the sample and silver powder (99.99% Alfa Aesar) were mixed and pressed into a pellet which was then used for measurement. The contribution from silver was subtracted using values from the literature [243] in order to obtain the sample heat capacity. The magnetic heat capacity, C_{mag}, was obtained by subtracting the lattice contribution using a Debye model (equation 2.37), with Debye temperatures ranging between 285 to 420 K.

The zero field heat capacities for $Gd_3Sc_2Ga_3O_{12}$, $Gd_3Sc_2Al_3O_{12}$ and $Gd_3In_2Ga_3O_{12}$ show no discernible ordering features down to 0.4 K (Figure 3.6). The zero field heat capacities for $Gd_3Ga_5O_{12}$ and $Gd_3Te_2Li_3O_{12}$ have been reported previously [253] and were not measured. Figure 3.7 shows the zero-field magnetic heat capacity from 0.4 – 10 K for the garnets with Ln = Tb, Dy, Ho. The zero field heat capacities for $Ln_3Ga_5O_{12}$, Ln = Tb, Dy, Ho, were not measured as they are known to order below 0.4 K, the limiting temperature of the heat capacity measurements. Ordering temperatures, T_0, and estimates of the frustration index, f, given by equation (1.63), are given in Table 3.6.

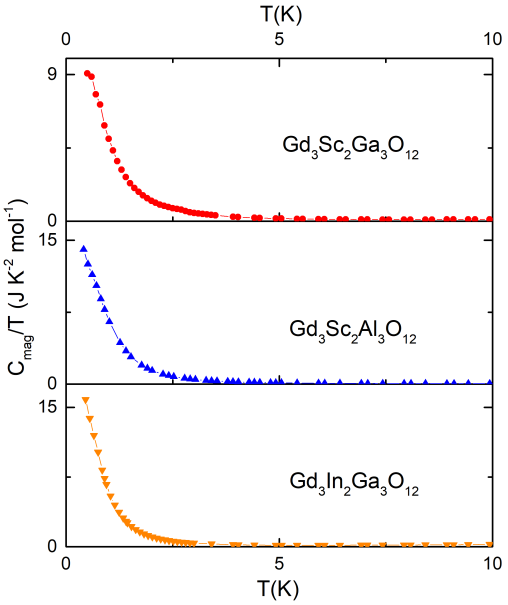

Figure 3.6 Zero field heat capacity from 0.4 – 10 K for $Gd_3Sc_2Ga_3O_{12}$, $Gd_3Sc_2Al_3O_{12}$ and $Gd_3In_2Ga_3O_{12}$.

Sharp λ type anomalies indicative of three-dimensional antiferromagnetic ordering are observed for $Tb_3Sc_2Ga_3O_{12}$, $Tb_3Sc_2Al_3O_{12}$ and $Tb_3In_2Ga_3O_{12}$. $Tb_3Te_2Li_3O_{12}$ shows a cusp at 1.04(3) K, which is more reminiscent of short-range ordering or glassy behaviour. The

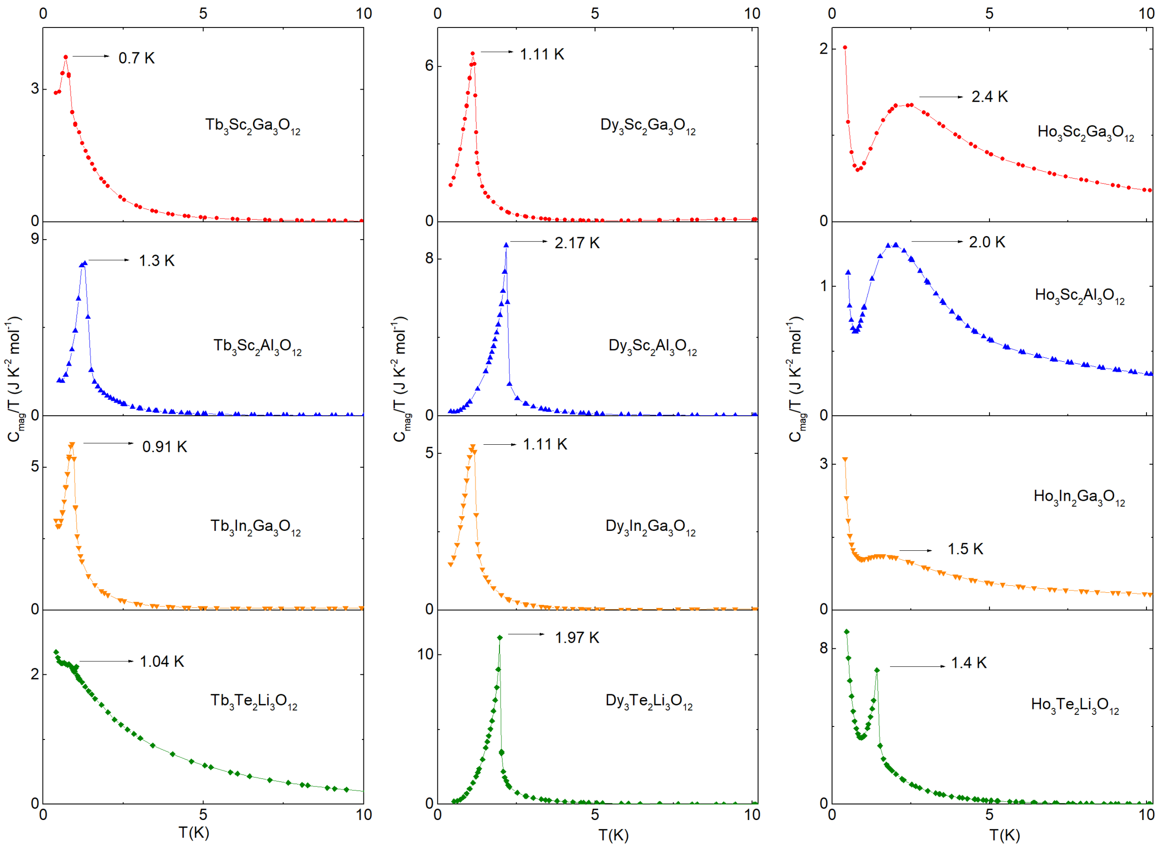

Figure 3.7 Zero field heat capacity from 0.4 – 10 K for $Ln_3Sc_2Ga_3O_{12}$, $Ln_3Sc_2Al_3O_{12}$, $Ln_3In_2Ga_3O_{12}$ and $Ln_3Te_2Li_3O_{12}$; Ln = Tb, Dy, Ho.

Table 3.6 Comparison of ordering temperature, T_0, and frustration index, f, as determined from zero field heat capacity data, for $Ln_3Sc_2Ga_3O_{12}$, $Ln_3Sc_2Al_3O_{12}$, $Ln_3In_2Ga_3O_{12}$ and $Ln_3Te_2Li_3O_{12}$ with values in the literature reported for $Ln_3Ga_5O_{12}$; Ln = Tb, Dy, Ho [197, 255]. In case of three-dimensional antiferromagnetic ordering, T_0 is the Néel temperature, T_N.

Ln	Tb		Dy		Ho	
	T_0 (K)	f	T_0 (K)	f	T_0 (K)	f
$Ln_3Ga_5O_{12}$	0.25	4.6	0.373	2.7	0.19	17.3
$Ln_3Sc_2Ga_3O_{12}$	0.7(1)	1.7	1.11(5)	0.7	2.4(2)	1.4
$Ln_3Sc_2Al_3O_{12}$	1.3(1)	0.6	2.17(5)	0.5	2.0(2)	1.4
$Ln_3In_2Ga_3O_{12}$	0.91(5)	0.6	1.11(5)	0.6	1.5(1)	1.4
$Ln_3Te_2Li_3O_{12}$	1.04(3)	0.6	1.97(5)	0.8	1.4(1)	1.1

upturn seen below 0.6-0.8 K for all the Tb garnets is due to the onset of the nuclear Schottky anomaly for Tb^{3+} [255]. All the Dy garnets show sharp λ type anomalies, indicative of three-dimensional antiferromagnetic ordering. The transition for $Dy_3Te_2Li_3O_{12}$ is at 1.97(5) K, consistent with previous reports of a transition around 2 K. $Ho_3Sc_2Ga_3O_{12}$, $Ho_3Sc_2Al_3O_{12}$ and $Ho_3In_2Ga_3O_{12}$ show broad features in the heat capacity at $T \approx 2.4(2)$, 2.0(2) and 1.5(1) K respectively, indicative of short range magnetic correlations. It is not possible to determine if there is any transition below 1 K due to the sharp increase in the heat capacity from the nuclear Schottky contribution for Ho^{3+} [255, 270], which would mask any transition, if present. $Ho_3Te_2Li_3O_{12}$ shows a sharp λ type transition at 1.4(1) K, which points to long-range antiferromagnetic order.

3.5 Discussion

Polycrystalline samples of lanthanide garnets $Ln_3Ga_5O_{12}$, $Ln_3Sc_2Ga_3O_{12}$, $Ln_3Sc_2Al_3O_{12}$, $Ln_3In_2Ga_3O_{12}$ and $Ln_3Te_2Li_3O_{12}$ have been prepared for Ln = Gd, Tb, Dy, Ho and their structure has been evaluated using PXRD and PND. The synthesis of $Ln_3Ga_5O_{12}$, $Ln_3Te_2Li_3O_{12}$, Ln = Gd, Tb, Dy, Ho, and $Gd_3Sc_2Ga_3O_{12}$, $Gd_3Sc_2Al_3O_{12}$, $Gd_3In_2Ga_3O_{12}$ has been reported previously but this is the first time that samples of $Ln_3Sc_2Ga_3O_{12}$, $Ln_3Sc_2Al_3O_{12}$ and $Ln_3In_2Ga_3O_{12}$ have been prepared for Ln = Tb, Dy, Ho. Structural refinements show that all the lanthanide garnets crystallise in a cubic structure with space group $Ia\bar{3}d$ with Ln (Ln = Gd, Tb, Dy, Ho) occupying the dodecahedral site, A (A = Ga, Sc, In, Te) occupying the octahedral site) and X (X = Ga, Al, Li) occupying the tetrahedral site.

The bulk magnetic properties, including magnetic susceptibility, isothermal magnetisation and zero field heat capacity have been measured for all samples. While the properties of $Ln_3Ga_5O_{12}$ and $Ln_3Te_2Li_3O_{12}$, Ln = Gd, Tb, Dy, Ho, have been studied previously, this is the first study on the magnetic properties of $Ln_3Sc_2Ga_3O_{12}$, $Ln_3Sc_2Al_3O_{12}$ and $Ln_3In_2Ga_3O_{12}$, Ln = Gd, Tb, Dy, Ho. Heat capacity measurements on $Ln_3Te_2Li_3O_{12}$, Ln = Tb, Dy, Ho, to study the magnetic properties below 2 K are also reported for the first time.

Approximations for the dipolar and exchange interactions have been calculated for all samples, Table 3.4. When considering the magnetic interactions, it is important to consider the impact of changes in the crystal structure. In the case of the lanthanide garnets, it is seen that the variation in D for a particular Ln for different combinations of A and X is small while J_1 varies more significantly (Table 3.4). However, these values of D and J_1 are only an order of magnitude approximation for the respective interactions, the true values are expected to vary considerably. The dipolar interaction is a long-ranged interaction, decaying as $\frac{1}{r^3}$, and so further neighbour contributions could be significant [140, 264, 271, 272]. The value of J_1 is highly dependent on the temperature range of the fit; further neighbour exchange interactions are also likely to play a role [140, 154, 272]. Despite these limitations, some qualitative conclusions may be drawn. The results for each *Ln* are discussed separately below.

3.5.1 $Gd_3A_2X_3O_{12}$

$Gd_3Te_2Li_3O_{12}$ and $Gd_3Al_5O_{12}$ have been previously reported to order at 0.243 K and 0.175 K respectively while $Gd_3Ga_5O_{12}$ shows no conventional magnetic ordering [253]. However, a very recent study has reported absence of conventional magnetic ordering in $Gd_3Al_5O_{12}$ as well [254]. The remaining Gd garnets are expected to show magnetic ordering, if any, at $T < 0.4$ K, below the temperature limit of the measurements. The physics of the garnets with *Ln* = Gd should be well approximated by a microscopic Hamiltonian with D and J_1 interaction terms; crystal field effects are expected to be less important for the isotropic Gd^{3+} spins ($L = 0, J = S = \frac{7}{2}$) [253]. D and J_1 are comparable for the Gd garnets (Table 3.4) and the magnetic ground state would be determined mainly by the interplay of these interactions. However for $Gd_3Ga_5O_{12}$, it has been reported that higher order exchange interactions may play an important role [272]. Also, there may be a small single-ion anisotropy. In fact for $Gd_3Ga_5O_{12}$, it has been recently reported that the presence of both nearest neighbour antiferromagnetic correlations and a subtle XY anisotropy leads to hidden multipolar order [150]. Thus, further neighbour contributions and subtle changes to the single-ion anisotropy caused by variation in A and X (especially in the case where A and X are aliovalent) could also impact the magnetic properties. Ultra-low temperature experimental investigations at $T < 0.4$ K as well as a more accurate modelling of the interactions is required to understand the magnetic behaviour of the Gd garnets. It remains to be seen whether the spin liquid state is unique to $Gd_3Ga_5O_{12}$ or if it is a robust feature of Gd garnets.

3.5.2 $Ln_3A_2X_3O_{12}$, *Ln* = Tb, Dy, Ho

As seen in Table 3.4, the dipolar and exchange interaction energies for the garnets with *Ln* = Tb, Dy, Ho are found to be comparable. However, unlike the Gd containing garnets, *Ln* = Tb, Dy, Ho have non-zero value of orbital angular momentum L and CEF effects play an important role in addition to the dipolar and exchange interactions in determining the magnetic properties [259]. Precise determination of the CEF requires a detailed study of the crystal field levels from inelastic neutron scattering experiments, and so only qualitative statements regarding the CEF levels and the single-ion anisotropy will be discussed here.

$Tb_3Sc_2Ga_3O_{12}$, $Tb_3Sc_2Al_3O_{12}$, $Tb_3In_2Ga_3O_{12}$ all show signatures of long-range antiferromagnetic ordering in the zero-field heat capacity with transition temperatures in between that of $Tb_3Ga_5O_{12}$ (0.25 K) and $Tb_3Al_5O_{12}$ (1.35 K) [258, 263]. It is proposed that the ordering is still driven by interactions between the two lowest singlet states. However, the frustration is relieved as compared to $Tb_3Ga_5O_{12}$. This could be due to variations in D and J_1 or changes in the CEF resulting in subtle changes to the single-ion anisotropy. The nature of ordering for $Tb_3Te_2Li_3O_{12}$ is very different. The transition resembles a feature observed at 0.8 K in the heat capacity for $Gd_3Ga_5O_{12}$ which was reported to indicate the onset of short range magnetic correlations [253]. Neutron scattering experiments below the transition temperature are required to elucidate the nature of the transition. Changes in D and J_1 alone are not sufficient to explain the difference in the behaviour of $Tb_3Te_2Li_3O_{12}$. Tb^{3+} is a non-Kramer's ion consisting of singlet levels and the energy separation between the two lowest singlet states competes with the magnetic interactions to determine the magnetic ground state. It is postulated that the aliovalent A and X environments in $Tb_3Te_2Li_3O_{12}$ (all the other Tb garnets under consideration have trivalent A and X) dramatically changes the single-ion anisotropy, as is also indicated from the $M(H)$ data at $T = 2$ K, causing it to behave differently to the other Tb garnets.

$Dy_3Sc_2Ga_3O_{12}$, $Dy_3Sc_2Al_3O_{12}$, $Dy_3In_2Ga_3O_{12}$ and $Dy_3Te_2Li_3O_{12}$ also show signatures of long-range antiferromagnetic ordering, with transition temperatures in between that of $Dy_3Ga_5O_{12}$ (0.373 K) and $Dy_3Al_5O_{12}$ (2.49 K) [196, 197]. Dy^{3+} is a Kramer's ion and so the ground state doublet is protected by symmetry for all the Dy garnets. The variation in transition temperatures and the reduction of frustration compared to $Dy_3Ga_5O_{12}$ can once again be explained by subtle changes in the magnetic interactions and the single-ion anisotropy. $Dy_3Sc_2Al_3O_{12}$, with the maximum transition temperature, shows the greatest tendency for saturation in the $M(H)$ curves: this is also consistent with the strongly Ising behaviour reported for $Dy_3Al_5O_{12}$ [262].

The Ho garnets show magnetic ordering that is very different from the Tb and Dy garnets. Since the magnitude of the D and J_1 interactions are very similar for the garnets with Ln = Tb, Dy, Ho for a particular combination of A and X, it is postulated that the changes in CEF causes the difference in magnetic properties. The behaviour of $Ho_3Sc_2Ga_3O_{12}$, $Ho_3Sc_2Al_3O_{12}$ and $Ho_3In_2Ga_3O_{12}$ shows similarities with $Ho_3Ga_5O_{12}$, where short range order is reported to set in below 0.6 K and long and short-range order coexist below 0.3 K [261]. Therefore, it seems, the changes in CEF for Ln = Ho shift the onset of short-range order to higher temperatures in the absence of long-range order at $T \geq 1$ K. However, although the heat capacity for $Ho_3Sc_2Ga_3O_{12}$ shows an ordering feature at 2.4 K, Figure 3.7, no signatures of ordering are observed in the magnetic susceptibility down to 2 K, Figure 3.4a. This could be due to a mismatch in the calibration of the thermometer for the SQUID MPMS and the PPMS He3 heat capacity option or the feature at 2.4 K could be due to an electronic Schottky anomaly and not short-range magnetic ordering. Measurements of the field dependence of the heat capacity as well as neutron diffraction experiments below 2.4 K would help resolve the disparity in susceptibility and heat capacity measurements for $Ho_3Sc_2Ga_3O_{12}$. Much like in the case of the Tb garnets, $Ho_3Te_2Li_3O_{12}$ behaves differently to the other Ho garnets. It exhibits a sharp λ type anomaly, indicative of three-dimensional antiferromagnetic ordering. It is proposed that like $Tb_3Te_2Li_3O_{12}$, the CEF is changed dramatically for $Ho_3Te_2Li_3O_{12}$ due to the different charged environments of Te^{6+} and Li^{+}.

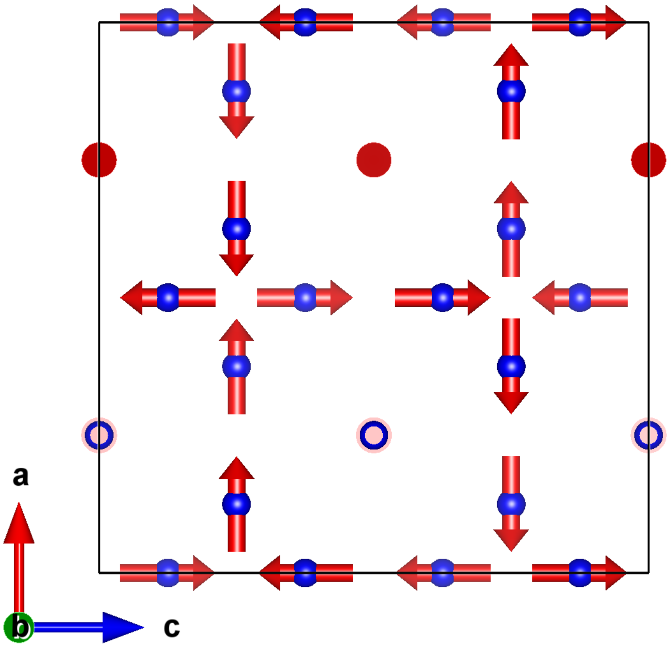

Figure 3.8 The six sublattice antiferromagnetic structure predicted by Capel [259] for lanthanide gallium and aluminium garnets with strong Ising anisotropy: Ln^{3+} spins of equal magnitude are aligned along the three crystallographic axes [100], $[\bar{1}00]$, [010], $[0\bar{1}0]$, [001], $[00\bar{1}]$.

Now, some speculation on the possible magnetic ground states for the garnets with *Ln* = Tb, Dy, Ho is presented. Capel has predicted three possible kinds of magnetic ordering depending on the single-ion anisotropy (Ising, XY or Heisenberg) of the magnetic Ln^{3+} ion [259]: a) Type A antiferromagnetic ordering (AFA) where moments of equal magnitude are aligned parallel to the crystallographic axes [100], $[\bar{1}00]$, [010], $[0\bar{1}0]$, [001], $[00\bar{1}]$ resulting in a six sublattice antiferromagnetic structure, Figure 3.8. b) Type B antiferromagnetic ordering (AFB) where the moments are aligned along the directions perpendicular to one of the crystallographic axes, that is, perpendicular to the directions of the spins in Figure 3.8. The magnetisation of sublattices (110) and $(1\bar{1}0)$ may not be equal and antiparallel, however the net sublattice magnetisation is zero. c) Type C ferrimagnetic ordering (FC) where there is a net magnetisation parallel to one of the three crystallographic axes, that is, the resultant spins point along one of the three possible directions in Figure 3.8. For the Type A magnetic structure, there is only one possible orientation for all the magnetic moments. However, there are multiple ways in which the moments can align to form the Type B or Type C magnetic structure.

For $4f$ ions with a strong Ising anisotropy, type A antiferromagnetic ordering is predicted while type B antiferromagnetic ordering (AFB) or type C ferrimagnetic (FC) ordering is predicted for $4f$ ions with XY or Heisenberg anisotropy [259]. This theory is directly applicable for $4f$ ions with an odd number of electrons, like Dy^{3+}, where the ground state is a $S = \frac{1}{2}$ Kramer's doublet, well-separated from excited states at sufficiently low temperatures. For non-Kramer's ions, like Tb^{3+} and Ho^{3+}, the degeneracy is entirely lifted due to the orthorhombic point symmetry of the Ln^{3+} site and thus the ground state is a singlet. Here, the energy separation between the ground state and first excited state singlet, Δ, is also a factor. If Δ is much greater than the magnetic interactions, the ground state would be a non-magnetic singlet showing temperature-independent paramagnetism. However if the energy separation, Δ, is small compared to the magnetic interactions, any of the three types of magnetic ordering predicted by Capel would be possible depending on the single-ion anisotropy of the Ln^{3+} ion [259, 265]. The sharp λ type anomalies observed in the heat capacities for the Dy garnets and majority of the Tb garnets are consistent with AFA type ordering that has also been reported for $Ln_3Ga_5O_{12}$, $Ln_3Al_5O_{12}$ (Ln = Tb, Ho) and $Dy_3Al_5O_{12}$ below T_N [257, 262, 263]. However the short range ordering observed for most of the Ho garnets and the differences in magnetic behaviour in the aliovalent $Ln_3Te_2Li_3O_{12}$ (Ln = Tb, Ho) remain to be accounted for. Capel's analysis was carried out considering dipolar and exchange interactions up to a limit, further analysis of the interactions may lead to different predictions. Also, this theory does not take into account aliovalent environments (as present in $Ln_3Te_2Li_3O_{12}$) which could lead to different magnetic ground states. Neutron scattering experiments would be the ideal tool to elucidate the exact nature of the magnetic ground state below the ordering transition in these garnets.

3.6 Magnetocaloric effect

The MCE for the lanthanide garnets is characterised by the change in magnetic entropy, ΔS_m per mole Ln, which is calculated from the $M(H)$ curves using equation (1.64). As discussed in the introduction, previous studies have shown that at lower fields, $\mu_0 H \leq 2$ T, $Dy_3Ga_5O_{12}$ (DGG) is a better MCM whereas at higher fields, $\mu_0 H > 2$ T, the change in magnetic entropy for $Gd_3Ga_5O_{12}$ (GGG) is maximised [200]. This is shown explicitly in Figure 3.9. Therefore, here the MCE for the garnets with substantial single-ion anisotropy

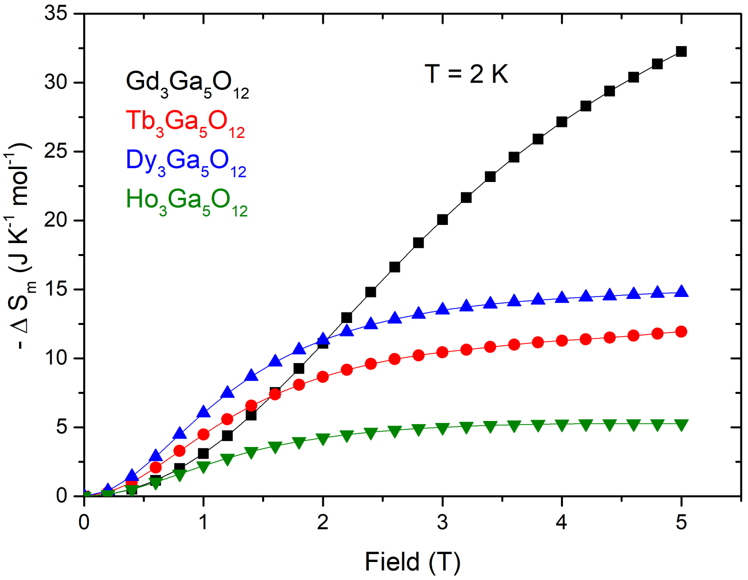

Figure 3.9 ΔS_m per mole *Ln* as a function of external magnetic field from 0 - 5 T at T = 2 K for $Ln_3Ga_5O_{12}$, *Ln* = Gd, Tb, Dy, Ho; the MCE for $Dy_3Ga_5O_{12}$ is maximised up to 2 T whereas at fields above this, the MCE of $Gd_3Ga_5O_{12}$ is much higher than $Ln_3Ga_5O_{12}$; *Ln* = Tb, Dy, Ho.

(*Ln* = Tb, Dy, Ho) are compared in a field of 2 T and the MCE for the Gd based garnets are compared in the experimentally limiting field of 9 T. The variation in ΔS_m per mole *Ln* as a function of temperature for all the garnets is shown in Figure 3.10; the inset shows the variation of ΔS_m per mole *Ln* as a function of magnetic field. Quantitative comparisons of the MCE with the parent gallium garnets using the values of ΔS_m per mole *Ln* are given in Table 3.7.

For *Ln* = Gd, at 2 K, 9 T, a 4 - 10% increase in ΔS_m is seen compared to GGG (14.12 $\mathrm{J\,K^{-1}\,mol_{Gd}^{-1}}$) on changing the *A* and *X* site ions except for $Gd_3Te_2Li_3O_{12}$, for which a decrease is seen. DGG has the maximum ΔS_m (3.77 $\mathrm{J\,K^{-1}\,mol_{Dy}^{-1}}$) compared to all the other Dy garnets and so, varying the *A* and *X* site ions does not improve the MCE at 2 K. Among the Tb garnets, an increase in the MCE is observed for all compared to $Tb_3Ga_5O_{12}$ (2.88 $\mathrm{J\,K^{-1}\,mol_{Tb}^{-1}}$), with a maximum of 22.2 % increase in ΔS_m for $Tb_3In_2Ga_3O_{12}$ (3.52 $\mathrm{J\,K^{-1}\,mol_{Tb}^{-1}}$). However, the ΔS_m values are less than that for DGG. The most dramatic increase in ΔS_m values are observed for *Ln* = Ho, where the MCE in $Ho_3Te_2Li_3O_{12}$ (3.03 $\mathrm{J\,K^{-1}\,mol_{Ho}^{-1}}$) is more than doubled compared to $Ho_3Ga_5O_{12}$ (1.41 $\mathrm{J\,K^{-1}\,mol_{Ho}^{-1}}$). Again, the absolute values of ΔS_m for the Ho garnets are less than DGG. Overall the conclusion is that DGG remains the best MCM in the low field ($\leq$ 2 T) regime while in a field of 9 T, the performance of GGG can be improved by changing the *A* and *X* site cations ($\approx$ 10%). If the calculations are carried out in gravimetric units that are more relevant for practical

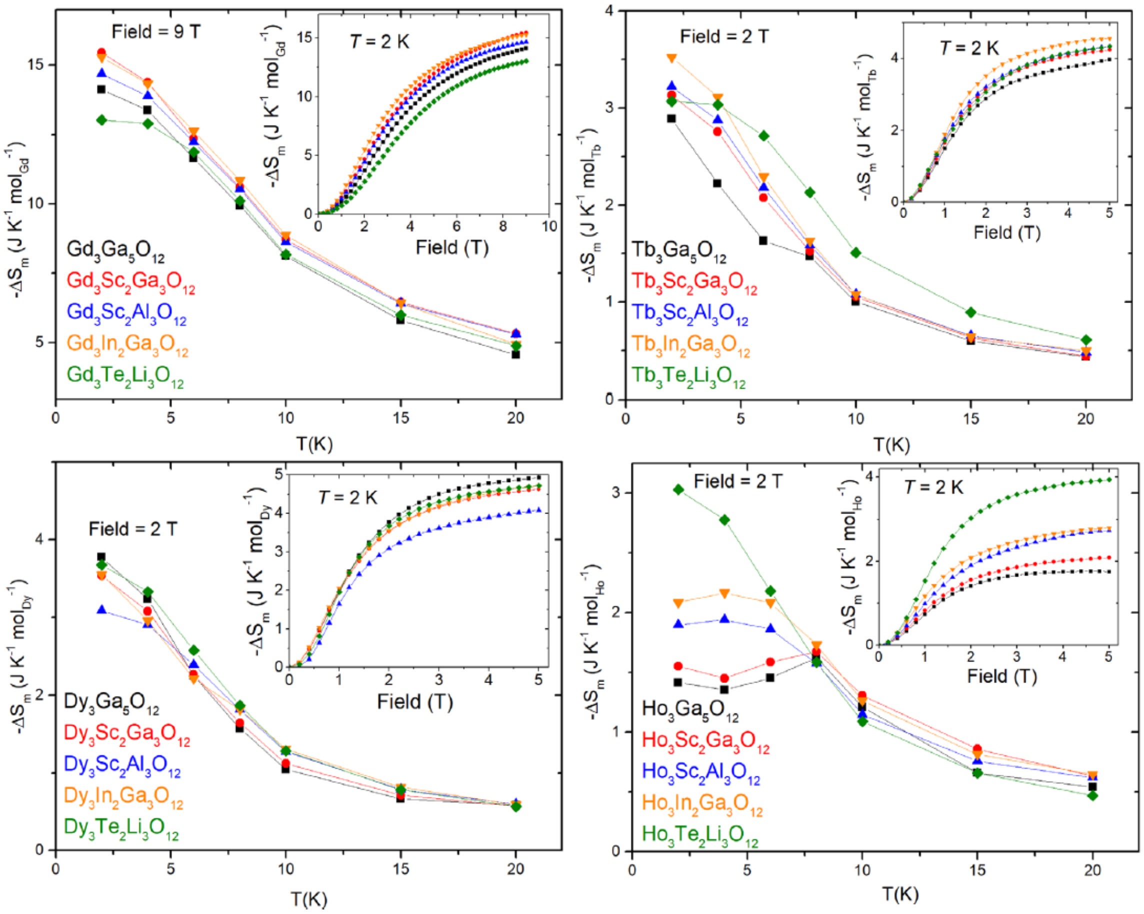

Figure 3.10 ΔS_m per mole *Ln* vs temperature; inset: ΔS_m per mole *Ln* as a function of external magnetic field at $T = 2$ K for lanthanide garnets $Ln_3Ga_5O_{12}$, $Ln_3Sc_2Ga_3O_{12}$, $Ln_3Sc_2Al_3O_{12}$, $Ln_3In_2Ga_3O_{12}$ and $Ln_3Te_2Li_3O_{12}$; *Ln* = Gd, Tb, Dy, Ho.

applications, a 15% and 26% increase in ΔS_m at 2 K, 9 T is observed for $Gd_3Sc_2Ga_3O_{12}$ and $Gd_3Sc_2Al_3O_{12}$ respectively as compared to $Gd_3Ga_5O_{12}$.

3.7 Conclusion

Polycrystalline samples of $Ln_3Ga_5O_{12}$, $Ln_3Sc_2Ga_3O_{12}$, $Ln_3Sc_2Al_3O_{12}$, $Ln_3In_2Ga_3O_{12}$ and $Ln_3Te_2Li_3O_{12}$ for *Ln* = Gd, Tb, Dy, Ho have been prepared and the structure and bulk magnetic properties have been studied. The magnetic susceptibility shows no long-range ordering down to 2 K for any of the samples except $Dy_3Sc_2Al_3O_{12}$ which undergoes antiferromagnetic ordering at 2.2(1) K. Isothermal magnetisation measurements are consistent with the Heisenberg nature of the Gd^{3+} spins and the substantial single-ion anisotropy reported for Tb^{3+}, Dy^{3+}, Ho^{3+} in $Ln_3Ga_5O_{12}$ and $Ln_3Al_5O_{12}$. Gd garnets do not

Table 3.7 Comparison of ΔS_m per mole Ln at $T = 2$ K for $Ln_3Ga_5O_{12}$, $Ln_3Sc_2Ga_3O_{12}$, $Ln_3Sc_2Al_3O_{12}$, $Ln_3In_2Ga_3O_{12}$ and $Ln_3Te_2Li_3O_{12}$; Ln = Gd, Tb, Dy, Ho. % changes are calculated with respect to the ΔS_m values for the parent gallium garnets $Ln_3Ga_5O_{12}$.

Ln		Gd	Tb	Dy	Ho
Field		9 T	2 T	2 T	2 T
$Ln_3Ga_5O_{12}$	ΔS_m (J K^{-1} mol$_{Ln}^{-1}$)	14.12	2.88	3.77	1.41
$Ln_3Sc_2Ga_3O_{12}$	ΔS_m (J K^{-1} mol$_{Ln}^{-1}$)	15.45	3.13	3.53	1.55
	% change	9.4	8.7	-6.4	9.9
$Ln_3Sc_2Al_3O_{12}$	ΔS_m (J K^{-1} mol$_{Ln}^{-1}$)	14.68	3.21	3.09	1.9
	% change	4.0	11.4	-18	35.5
$Ln_3In_2Ga_3O_{12}$	ΔS_m (J K^{-1} mol$_{Ln}^{-1}$)	15.29	3.52	3.55	2.08
	% change	8.3	22.2	-5.8	47.5
$Ln_3Te_2Li_3O_{12}$	ΔS_m (J K^{-1} mol$_{Ln}^{-1}$)	13.02	3.07	3.68	3.03
	% change	-7.8	6.6	-2.4	114.9

show any magnetic ordering features down to 0.4 K, the temperature limit of the heat capacity measurements. However, garnets with Ln = Tb, Dy, Ho (except $Ln_3Ga_5O_{12}$) show magnetic ordering features at $0.4 < T < 2.5$ K, the nature of which varies for the different Ln and combinations of A and X. The ordering transitions for the magnetic ground states for the lanthanide garnets with Ln = Tb, Dy, Ho have been summarised in Table 3.6. For $Ho_3Sc_2Ga_3O_{12}$, there is a disparity between the magnetic susceptibility and heat capacity measurements: while no ordering is seen in the former down to 2 K, the latter shows a broad feature at 2.4 K . It remains to be seen whether this is due to a mismatch in temperature calibration of the two measurement systems or if the feature is not magnetic in nature. The majority of the changes in the ordering temperature for garnets with Ln = Tb, Dy, Ho can be explained by tuning of the CEF and magnetic interactions, however for non-Kramer's ions Tb^{3+} and Ho^{3+}, in the case of A and X being aliovalent, other effects associated with the difference in charge must be considered. Evaluation of the MCE shows that the magnetocaloric performance of the Gd based garnets can be improved by varying the A and X cations, with a 10% increase observed for $Gd_3Sc_2Ga_3O_{12}$ compared to GGG in a field of 9 T. For the garnets with Ln = Tb, Dy, Ho, DGG remains the best MCM in lower fields, $\mu_0 H \leq 2$ T. Neutron scattering experiments to determine the magnetic ground states and CEF scheme as well as a more accurate modelling of the relevant magnetic interactions and single-ion anisotropy is required to enable a detailed comparison of the magnetic behaviour of the different garnets. It is hoped that this work will motivate further investigations into the magnetic properties of the frustrated lanthanide garnets.

Chapter 4

Magnetic properties of lanthanide garnets, $Ln_3A_2X_3O_{12}$: Part II

The previous chapter has discussed how the magnetic properties of lanthanide garnets are impacted by altering the non-magnetic cations on the *A* and *X* sites. It has been shown that subtle variations in the magnetic interactions and CEF effects can cause dramatic changes in the magnetic ground state. This chapter discusses the effect of introducing additional spins (specifically Cr^{3+} and Mn^{3+}) in the lanthanide garnet lattice on the magnetic and magnetocaloric properties of these materials. As in the previous chapter, results are discussed for magnetic Ln^{3+} with different single-ion anisotropies, *Ln* = Gd, Tb, Dy, Ho.

4.1 Background

The magnetic properties of geometrically frustrated magnetic materials can be dramatically altered by chemical substitution due to the fragility of the magnetic ground state [2]. In particular, the frustration can be partially or completely relieved through site dilution or site disorder of spins. This has been reported for several frustrated materials such as the spin liquid kagome system $SrCr_8Ga_4O_{19}$ (SCGO), the ACr_2O_4 spinels (*A* = Zn, Mg) and the classical spin ice pyrochlores $Ln_2Ti_2O_7$ (*Ln* = Dy Ho). Cu^{2+} substitution in SCGO shifts the spin-glass transition, T_f, to higher temperatures [273]. Introduction of Cu^{2+} on the Zn^{2+} site in the $ZnCr_2O_4$ spinel causes a structural transition accompanied by increase in ‘cluster glass’ behaviour [274] while Cu^{2+} substitution on the Mg^{2+} site also increases the ordering temperature in the spinel $MgCr_2O_4$ [275]. Ln_2CrSbO_7 (*Ln* = Dy, Ho), isostructural with the geometrically frustrated classical spin ice pyrochlores, $Ln_2Ti_2O_7$ and Ln_2GaSbO_7, show ferromagnetic ordering transitions at 16 K and 10 K as opposed to the complete absence of long range order in the latter two sets of compounds [46].

Previous studies on magnetic ion substitution in the geometrically frustrated lanthanide garnets have focussed on $Ln_3Fe_5O_{12}$ where the Ln^{3+} occupy the dodecahedral sites and the Fe^{3+} occupy both octahedral and tetrahedral sites. The magnetic Fe^{3+} order in a ferrimagnetic structure at temperatures of 130 - 160 K while for most Ln^{3+}, the rare earth spins order at temperatures of a few K in a double umbrella structure with spins canted away from the [111] direction on either side [276–279]. Studies have shown that Fe^{3+} substitution increases the magnetocaloric performance, however the temperature at which maximum change in magnetic entropy is obtained is also increased making it less effective for cooling in the liquid helium temperature regime [280–282].

A recent neutron diffraction study on the garnet $CaY_2Co_2Ge_3O_{12}$, which contains magnetic Co^{2+} on the *A* sites, has revealed a unique magnetic ground state as well as a field-induced magnetic transition around 6 T [283]. Room temperature PND showed that the Co^{2+} ions exclusively occupy the octahedral sites and have local $\langle 111 \rangle$ Ising anisotropy. The garnet orders at $T_N = 6$ K in a magnetic structure with antiferromagnetically coupled spin chains along the body diagonals. This indicates that if additional 3*d* spins are introduced in the lanthanide gallium garnets by means of chemical substitution, they may show novel magnetic ordering as well as field-induced transitions.

In this chapter, substitution of a number of 3*d* magnetic ions in the lanthanide gallium garnets $Ln_3Ga_5O_{12}$ was attempted for the first time for *Ln* = Gd, Tb, Dy, Ho: these are V^{3+}, Cr^{3+}, Mn^{3+} and Co^{3+}. These transition metal ions were chosen because they have reported stable 3+ oxidation states which is required in order to maintain the balance of electrical charge in the garnet. Substitution of V^{3+} and Co^{3+} for Ga^{3+} was unsuccessful while Cr^{3+} and Mn^{3+} could be partially incorporated into the $Ln_3Ga_5O_{12}$ structure. The impact on the structure, bulk magnetic properties and MCE is discussed. Results on the magnetic structure of $Ho_3MnGa_4O_{12}$ from neutron diffraction are also presented. The background literature, sample preparation, structural characterisation, bulk magnetic properties and MCE in $Ln_3Ga_5O_{12}$, *Ln* = Gd, Tb, Dy, Ho have already been discussed in the previous chapter and here, the results will be used for comparison.

4.2 Sample preparation

All sample preparation was carried out using solid state synthesis. Samples of $Ln_3Ga_5O_{12}$ (*Ln* = Gd, Tb, Dy, Ho) were prepared as described in the previous chapter. The common starting materials for preparation of the samples discussed in this chapter were Ln_2O_3, *Ln*

= Gd, Dy, Ho (99.999% purity, Alfa Aesar) or Tb_4O_7 (99.999% purity, Alfa Aesar) and Ga_2O_3 (99.99% purity, Alfa Aesar). Gd_2O_3 and Ga_2O_3 were pre-dried at 800 °C and 500 °C respectively prior to weighing out to ensure accurate chemical composition. The starting material for Cr^{3+}, Mn^{3+} V^{3+} and Co^{3+} substitution in $Ln_3Ga_5O_{12}$ were Cr_2O_3 (99.99% purity, Alfa Aesar), MnO_2 (99.999%, Alfa Aesar), VO_2 (99.99% purity, Alfa Aesar) and Co_3O_4 (99.99% purity, Alfa Aesar) respectively. Stoichiometric amounts of the starting materials were weighed out, mixed well and pressed into pellets in all cases.

Powder samples of $Ln_3CrGa_4O_{12}$ (*Ln* = Gd, Tb, Dy, Ho) were prepared by heating the pellets between 1200 – 1400 °C for 48-72 hours with intermittent regrindings. A reaction was deemed completed when PXRD indicated the formation of a phase-pure product. Powder samples of $Ln_3MnGa_4O_{12}$ (*Ln* = Gd, Tb, Ho, Dy) and $Y_3MnGa_4O_{12}$ were prepared by heating the pellets at 1200 °C repeatedly for 48-72 hours with intermittent regrindings. For preparing $Y_3MnGa_4O_{12}$, Y_2O_3 (99.999% purity, Alfa Aesar) was used as a starting material instead of the rare earth oxide. Attempts to synthesise $Ln_3Cr_xGa_{5-x}O_{12}$ and $Ln_3Mn_xGa_{5-x}O_{12}$ (*Ln* = Gd, Tb, Dy, Ho) with $x > 1$, resulted in the formation of $LnCrO_3$ and $LnMnO_3$ (*Ln* = Gd, Tb, Dy, Cr) perovskite phases respectively. The perovskite phase did not reduce on increasing the temperature for the heat treatments. Thus it was concluded that only partial substitution of Ga on the octahedral site with Cr or Mn is possible using this synthetic route. Synthesis of $Ln_3Mn_xAl_{5-x}O_{12}$ (*Ln* = Gd, Tb, Dy, Ho), x = 1,2, was attempted by Freya Johnson during her summer project. Only $LnMnO_3$ and $LnAlO_3$ perovskite phases were observed and so, the synthesis was discontinued.

For attempts to prepare $Ln_3VGa_4O_{12}$ and $Ln_3V_2Ga_3O_{12}$, *Ln* = Gd, Tb, Dy, Ho, the pellets were heated at 1200 °C under flowing argon to create a reducing atmosphere in order to stabilise the V^{3+} oxidation state. PXRD after heat treatment showed only perovskite impurities, $LnVO_3$ and $LnGaO_3$, and no garnet peaks were observed. Further heat treatments showed no change in the PXRD pattern. It was concluded that although the V^{3+} state was successfully stabilised, it could not be incorporated into the $Ln_3Ga_5O_{12}$ structure and the synthesis attempts were stopped. Synthesis of $Ln_3CoGa_4O_{12}$ and $Ln_3Co_2Ga_3O_{12}$ was attempted by carrying out heat treatments at 1200 °C. This yielded a PXRD pattern with Ln_3GaO_6 and CoO impurity phases along with the main $Ln_3Ga_5O_{12}$ phase. Next, the heat treatments were carried out under flowing oxygen to see if the Co^{2+} could be oxidised to Co^{3+} but this was not successful. Finally a slow cooling at 1° C per minute in air successfully eliminated the CoO phase, however the PXRD pattern contained the $LnCoO_3$ phase along with a garnet phase. Further heat treatments did not reduce the weight percentage of the $LnCoO_3$ impurity phase. Also, there was no change in the lattice parameter of the garnet phase obtained as compared to $Ln_3Ga_5O_{12}$, meaning that there was no indication of Co^{3+} being substituted for Ga^{3+} in the garnet structure. Thus this synthesis was discontinued.

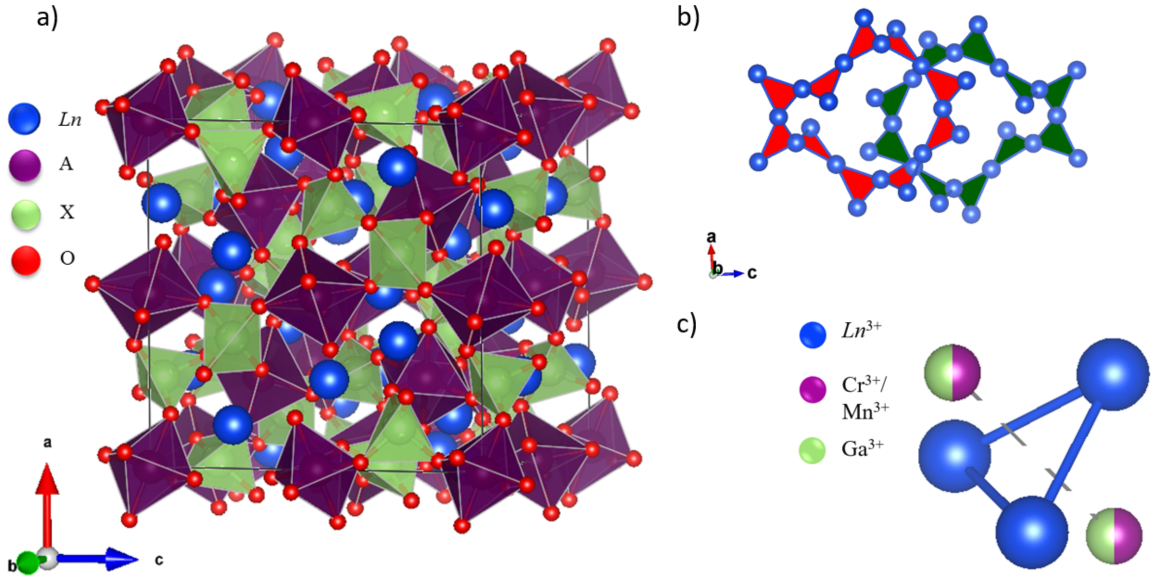

Figure 4.1 a) General crystal structure of lanthanide garnets $Ln_3A_2X_3O_{12}$ with the three cations occupying distinct crystallographic sites– here Ln = Gd/Tb/Dy/Ho, A = Cr/Mn/Ga, X = Ga. b) The Ln^{3+} lie at the vertices of corner-sharing equilateral triangles forming two interpenetrating ten-membered rings. c) Relative position of Cr^{3+} or Mn^{3+} relative to Ln^{3+} - each Ln_3 triangle with Ln^{3+} at the vertices has a Cr^{3+} or Mn^{3+} ion above and below the centroid of the triangle. Each octahedral site is occupied by Cr^{3+} or Mn^{3+} 50% of the time for $Ln_3CrGa_4O_{12}$ and $Ln_3MnGa_4O_{12}$ respectively.

4.3 Structural characterisation

PXRD was used to confirm the formation of phase pure products, $Ln_3CrGa_4O_{12}$ and $Ln_3MnGa_4O_{12}$, Ln = Gd, Tb, Dy, Ho. Initially short scans were collected over $10^\circ \leq 2\theta \leq 60^\circ$ ($\Delta 2\theta = 0.015^\circ$) using a Panalytical Empyrean X-ray diffractometer (Cu Kα radiation, λ = 1.540 Å) to track the progress of the reaction. Longer scans over a wider angular range $10^\circ \leq 2\theta \leq 90^\circ$ ($\Delta 2\theta = 0.008^\circ$) were collected for quantitative structural analysis. Room temperature (RT) PND experiments for structural characterisation were carried out on the D2B diffractometer, ILL, Grenoble (λ= 1.595 Å) at 300 K for $Ln_3CrGa_4O_{12}$ (Ln = Tb, Ho) and $Ho_3MnGa_4O_{12}$.

Combined RT PXRD + PND structural refinements were carried out for $Ln_3CrGa_4O_{12}$ (Ln = Tb, Ho) and $Ho_3MnGa_4O_{12}$. For all other samples, the crystal structure was determined from RT PXRD alone. The crystallographic parameters obtained from the structural Rietveld refinements for $Ln_3CrGa_4O_{12}$ (Ln = Gd, Tb, Dy, Ho) and $Ln_3MnGa_4O_{12}$ are given in Table 4.1. The cubic $Ia\bar{3}d$ structure of $Ln_3Ga_5O_{12}$ (Ln = Gd, Tb, Dy, Ho) is preserved on Cr^{3+} substitution. The crystal structure and the connectivity of magnetic Ln^{3+} ions are shown in Figure 4.1a and Figure 4.1b respectively. The combined RT PXRD + PND Rietveld refinements for $Ho_3CrGa_4O_{12}$ and $Ho_3MnGa_4O_{12}$ are shown in Figure 4.2.

Very little change in lattice parameter is observed on Cr^{3+} substitution ($\approx$ 0.05% for all Ln). This is expected given the similar size of Cr^{3+} and Ga^{3+} ions. On substitution with Mn^{3+}, the lattice parameter is observed to increase slightly as expected ($\approx$ 0.2% for all Ln). The difference in the neutron scattering factors for Cr (b_{Cr} = 3.635 fm), Mn (b_{Mn} = -3.73 fm) and Ga (b_{Ga}= 7.288 fm) [221] allowed for the position and amount of Cr/Mn to be determined in $Ln_3CrGa_4O_{12}$, Ln = Tb, Ho, and $Ho_3MnGa_4O_{12}$. Cr^{3+} and Mn^{3+} are found to exclusively occupy the octahedral site, as would be expected from CEF considerations. The refined composition for Ln = Tb, Ho was determined to be the same as the nominal composition within error. The fractional occupancy of the octahedral site was refined for $Ho_3MnGa_4O_{12}$ and the actual composition was found to be $Ho_3Mn_{1.12(2)}Ga_{3.88(2)}O_{12}$. It was assumed that Cr^{3+} exclusively occupies the octahedral site in $Ln_3CrGa_4O_{12}$, Ln = Gd and Dy and the composition was fixed at the nominal composition as PXRD is not sensitive enough to refine the Cr/Ga occupancy. Similarly, the position and amount of Mn in $Ln_3MnGa_4O_{12}$, Ln = Gd, Tb, Dy, for which only PXRD data were available, were fixed to the nominal values. The large neutron scattering length of oxygen, b_O = 5.80 fm, also enabled the possibility of oxygen vacancies in the $Ho_3MnGa_4O_{12}$ lattice to be explored. The oxygen vacancies were only explored for $Ho_3MnGa_4O_{12}$ and not $Ln_3CrGa_4O_{12}$ (Ln = Tb, Ho) because the Mn^{2+} oxidation state in a garnet was possible whereas the Cr^{2+} oxidation state is unlikely. However, no oxygen vacancies were observed in $Ho_3MnGa_4O_{12}$. Therefore the nominal composition will be used in all further discussions for simplicity. For $Ln_3CrGa_4O_{12}$ or $Ln_3MnGa_4O_{12}$, the relative position of a Cr^{3+} or Mn^{3+} ion with respect to a Ln_3 triangle is shown in Figure 4.1c: each Ln_3 triangle has a Cr^{3+} or Mn^{3+} ion above and below the centroid of the triangle 50% of the time.

On Cr^{3+} substitution, the changes in the Ln-O, Ln-Ln, Cr/Ga_{oct}-O and Ga_{tetr}-O bond lengths are negligibly small and almost constant within error, Table 4.2. Therefore no significant change in Ln^{3+} single-ion anisotropy is expected in $Ln_3CrGa_4O_{12}$, Ln = Gd, Tb, Dy, Ho as compared to $Ln_3Ga_5O_{12}$. There is no evidence for Jahn-Teller distortion, as expected for d^3 Cr^{3+} ions. The resultant change in the dipolar interaction ($D \propto 1/r^3_{Ln-Ln}$) between adjacent Ln^{3+} ions on Cr^{3+} substitution is also small, less than 0.1% for all samples. For $Ln_3MnGa_4O_{12}$, the increase in the lattice parameter as Mn^{3+} is substituted into the

Table 4.1 Crystallographic parameters for $Ln_3CrGa_4O_{12}$ and $Ln_3MnGa_4O_{12}$, Ln = Gd, Tb, Dy, Ho. The structural Rietveld refinements were carried out in the $Ia\bar{3}d$ space group, with Ln (Ln = Gd, Tb, Dy, Ho) on the dodecahedral 24c (0, 0.25, 0.125) site, Cr/Mn/Ga$_{\mathrm{oct}}$ on the octahedral 16a (0, 0, 0) site, Ga$_{\mathrm{tetr}}$ on the tetrahedral 24d (0, 0.25, 0.375) site and O on the 96h (x, y, z) site. Combined PXRD + PND refinements have been carried out for $Ln_3CrGa_4O_{12}$, Ln = Tb, Ho, and $Ho_3MnGa_4O_{12}$ while the structural parameters for all other samples have been determined using PXRD only.

$Ln_3CrGa_4O_{12}$	Ln	Gd	Tb	Dy	Ho
	a (Å)	12.3776(4)	12.34563(6)	12.3014(2)	12.28390(7)
Ln	B_{iso} (Å^2)	0.5	0.18(2)	0.5	0.04(2)
Cr/Ga$_{\mathrm{oct}}$	Frac Cr	0.5	0.51(1)	0.5	0.50(1)
	B_{iso} (Å^2)	0.5	0.21(4)	0.5	0.16(4)
Ga$_{\mathrm{tetr}}$	B_{iso} (Å^2)	0.5	0.28(2)	0.5	0.27(2)
O	x	-0.0314(4)	-0.02845(6)	-0.0287(3)	-0.02784(6)
	y	0.0536(3)	0.05477(8)	0.0534(3)	0.05559(7)
	z	0.1482(4)	0.14987(7)	0.1501(4)	0.15006(7)
	B_{iso} (Å^2)	0.5	0.349(13)	0.5	0.347(12)
	R_{wp}	13.6	10.60	14.7	9.72
	χ^2	2.05	2.84	2.33	3.02
$Ln_3MnGa_4O_{12}$	Ln	Gd	Tb	Dy	Ho
	a (Å)	12.3948(6)	12.35938(4)	12.32703(4)	12.3049(3)
Ln	B_{iso} (Å^2)	0.5	0.5	0.5	0.14(2)
Mn/Ga$_{\mathrm{oct}}$	Frac Mn	0.5	0.5	0.5	0.56(2)
	B_{iso} (Å^2)	0.5	0.5	0.5	0.20(9)
Ga$_{\mathrm{tetr}}$	B_{iso} (Å^2)	0.5	0.5	0.5	0.42(2)
O	x	-0.0298(4)	-0.0300(4)	-0.0288(4)	-0.02796(7)
	y	0.0540(4)	0.0532(5)	0.0545(4)	0.05579(8)
	z	0.1498(5)	0.1501(5)	0.1497(5)	0.15044(8)
	B_{iso} (Å^2)	0.5	0.5	0.5	0.515(14)
	R_{wp}	12.5	17.8	11.2	10.7
	χ^2	1.67	3.38	3.37	2.55

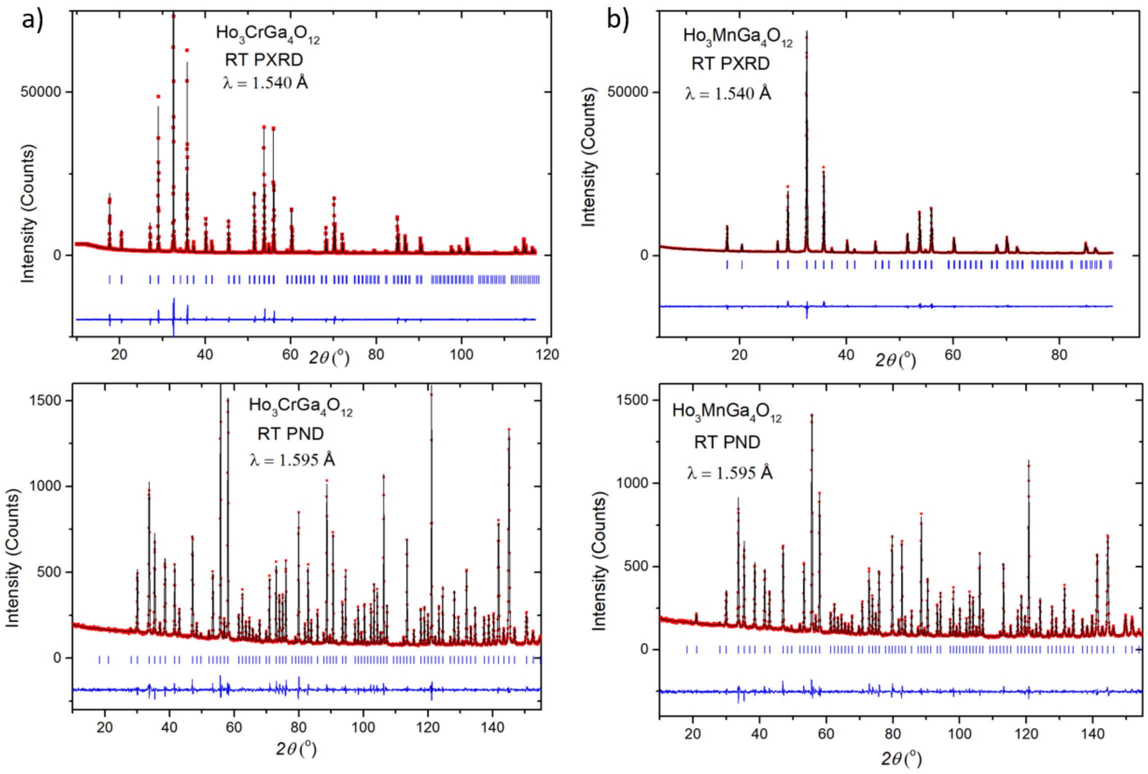

Figure 4.2 RT PXRD and PND pattern for a) $Ho_3CrGa_4O_{12}$ b) $Ho_3MnGa_4O_{12}$: Red dots - Experimental data, Black line - Modelled data, Blue line - Difference pattern, Blue ticks - Bragg positions.

structure results in an increase in the *Ln*-*Ln* bond lengths (Table 4.2). Despite the change in the lattice parameter, there are no significant changes in the *Ln*-O interactions on Mn^{3+} substitution or in the Mn/Ga_{oct}-O and Ga_{tetr}-O bond lengths. No evidence for Jahn-Teller distortion due to the Mn^{3+} (d^4) ions is detected, however the possibility of local disordered Jahn-Teller distortions such as that observed in $NaMnO_2$ [284] cannot be ruled out. The changes in the crystal structure would be expected to lead to a small decrease ($<1\%$) in the dipolar interactions ($D \propto 1/r^3_{Ln-Ln}$) between adjacent Ln^{3+} ions, but no significant change in the Ln^{3+} single-ion anisotropy is expected. The structural parameters of $Y_3MnGa_4O_{12}$ with non-magnetic Y^{3+} and $Ho_3MnGa_4O_{12}$ with magnetic Ho^{3+} are found to be analogous, as shown in Table 4.3. Hence $Y_3MnGa_4O_{12}$ is an appropriate non-magnetic analogue for $Ho_3MnGa_4O_{12}$ and the interactions between the Mn^{3+} spins in the absence of magnetic Ln^{3+} in the garnet structure can be studied using $Y_3MnGa_4O_{12}$.

Table 4.2 Selected bond lengths from RT PXRD refinements for $Ln_3Ga_5O_{12}$, $Ln_3CrGa_4O_{12}$ and $Ln_3MnGa_4O_{12}$, Ln = Gd, Tb, Dy, Ho. Bond lengths for $Ln_3Ga_5O_{12}$, Ln = Gd, Tb, Dy, Ho, were taken from the previous chapter.

Ln	Gd		Tb		Dy		Ho	
	$Ln_3Ga_5O_{12}$	$Ln_3CrGa_4O_{12}$	$Ln_3Ga_5O_{12}$	$Ln_3CrGa_4O_{12}$	$Ln_3Ga_5O_{12}$	$Ln_3CrGa_4O_{12}$	$Ln_3Ga_5O_{12}$	$Ln_3CrGa_4O_{12}$
Ln-*Ln* (Å)	3.79169(5) × 4	3.78985(4) × 4	3.77892(4) × 4	3.77994(6) × 4	3.76933(5) × 4	3.76891(3) × 4	3.76045(5) × 4	3.76117(7) × 4
Ln-O (Å)	2.413(2) × 4	2.403(5) × 4	2.380(5) × 4	2.373(4) × 4	2.368(5) × 4	2.350(5) × 4	2.354(4) × 4	2.364(3) × 4
	2.476(2) × 4	2.479(4) × 4	2.467(5) × 4	2.462(4) × 4	2.461(5) × 4	2.465(4) × 4	2.483(3) × 4	2.462(3) × 4
<*Ln*-O>(Å)	2.444	2.441	2.424	2.418	2.415	2.408	2.419	2.413
Ga_{oct} -O or Cr/Ga_{oct}-O (Å)	2.005(2) × 6	1.989(4) × 6	2.003(4) × 6	1.992(3) × 6	1.991(4) × 6	1.993(4) × 6	1.975(3) × 6	1.981(3) × 6
Ga_{tetr}-O (Å)	1.820(3) × 4	1.836(4) × 4	1.824(5) × 4	1.842(4) × 4	1.828(5) × 4	1.830(4) × 4	1.815(4) × 4	× 4
	$Ln_3Ga_5O_{12}$	$Ln_3MnGa_4O_{12}$	$Ln_3Ga_5O_{12}$	$Ln_3MnGa_4O_{12}$	$Ln_3Ga_5O_{12}$	$Ln_3MnGa_4O_{12}$	$Ln_3Ga_5O_{12}$	$Ln_3MnGa_4O_{12}$
Ln-*Ln* (Å)	3.79169(5) × 4	3.79512(2) × 4	3.77892(4) × 4	3.78427(2) × 4	3.76933(5) × 4	3.77437(2) × 4	3.76045(5) × 4	3.76692(3) × 4
Ln-O (Å)	2.413(2) × 4	2.382(6) × 4	2.380(5) × 4	2.372(7) × 4	2.368(5) × 4	2.361(6) × 4	2.354(4) × 4	2.346(4) × 4
	2.476(2) × 4	2.476(5) × 4	2.467(5) × 4	2.480(5) × 4	2.461(5) × 4	2.455(5) × 4	2.483(3) × 4	2.474(3) × 4
< *Ln*-O> (Å)	2.444	2.429	2.424	2.426	2.415	2.408	2.419	2.410
Ga_{oct} -O or Mn/Ga_{oct}-O (Å)	2.005(2) × 6	2.008(6) × 6	2.003(4) × 6	2.003(6) × 6	1.991(4) × 6	1.996(6) × 6	1.975(3) × 6	1.987(3) × 6
Ga_{tetr}-O (Å)	1.820(3) × 4	1.839(6) × 4	1.824(5) × 4	1.826(6) × 4	1.828(5) × 4	1.840(6) × 4	1.815(4) × 4	1.827(3) × 4

Table 4.3 Comparison of structural parameters for $Ho_3MnGa_4O_{12}$ and $Y_3MnGa_4O_{12}$.

		$Ho_3MnGa_4O_{12}$	$Y_3MnGa_4O_{12}$
	a (Å)	12.3049(3)	12.29337(4)
Ln	B_{iso} (Å^2)	0.14(2)	0.5
Mn/Ga_{oct}	Frac Mn	0.56(2)	0.5
	B_{iso} (Å^2)	0.20(9)	0.5
Ga_{tetr}	B_{iso} (Å^2)	0.42(2)	0.5
O	x	-0.02796(7)	-0.0272(3)
	y	0.05579(8)	0.0550(3)
	z	0.15044(8)	0.1510(3)
	B_{iso} (Å^2)	0.515(14)	0.5
	R_{wp}	10.7	10.5
	χ^2	2.55	5.56
Ln-*Ln* (Å)		3.76692(3) × 4	3.76406(4) × 4
Ln-O (Å)		2.346(4) × 4	2.332(4) × 4
		2.474(3) × 4	2.441(4) × 4
< *Ln*-O> (Å)		2.410	2.386
Mn/Ga_{oct}-O (Å)		1.987(3) × 4	2.004(4) × 4
Ga_{tetr}-O (Å)		1.827(4) × 4	1.840(4) × 4

4.4 Bulk magnetic measurements

4.4.1 Magnetic susceptibility

The ZFC magnetic susceptibility, $\chi(T)$, of $Ln_3CrGa_4O_{12}$ and $Ln_3MnGa_4O_{12}$, *Ln* = Gd, Tb, Dy, Ho, measured in a field of 100 Oe from 2- 300 K using a Quantum Design MPMS with a SQUID magnetometer is shown in Figure 4.3. No long-range magnetic ordering is observed down to 2 K for $Ln_3CrGa_4O_{12}$, *Ln* = Gd, Tb, Dy, Ho and $Gd_3MnGa_4O_{12}$. Magnetic ordering transitions are observed at $T_N = 4.6$ K, 5.6 K and 5.8 K for $Tb_3MnGa_4O_{12}$, $Dy_3MnGa_4O_{12}$ and $Ho_3MnGa_4O_{12}$ respectively. Above $T > 100$ K, the inverse susceptibility χ^{-1} is linear for all samples. Fits to the Curie-Weiss law were carried out in in the temperature range 100 - 300 K in order to calculate the experimental magnetic moment, μ_{eff}, and the Curie-Weiss temperature, θ_{CW}. Parameters for fits to the Curie-Weiss law for $Ln_3CrGa_4O_{12}$ and $Ln_3MnGa_4O_{12}$, *Ln* = Gd, Tb, Dy, Ho are summarised in Table 4.4. The values of θ_{CW} and μ_{eff} for $Ln_3Ga_5O_{12}$, *Ln* = Gd, Tb, Dy, Ho from carrying out the Curie-Weiss fit in the same temperature range (100 - 300 K) are given for comparison. The negative values of θ_{CW} for all compositions indicate net antiferromagnetic correlations. However, these values do not account for low-lying crystal-field effects which are known to significantly impact the

Curie-Weiss parameters in $Ln_3Ga_5O_{12}$, Ln = Tb, Dy, Ho [198, 255, 258]. The experimental values of magnetic moments obtained from fitting to the Curie-Weiss law are consistent with the theoretical values, $\mu_{eff}^2 = 3\mu_{Ln}^2 + \mu_A^2$ for $Ln_3AGa_4O_{12}$, A = Cr, Mn.

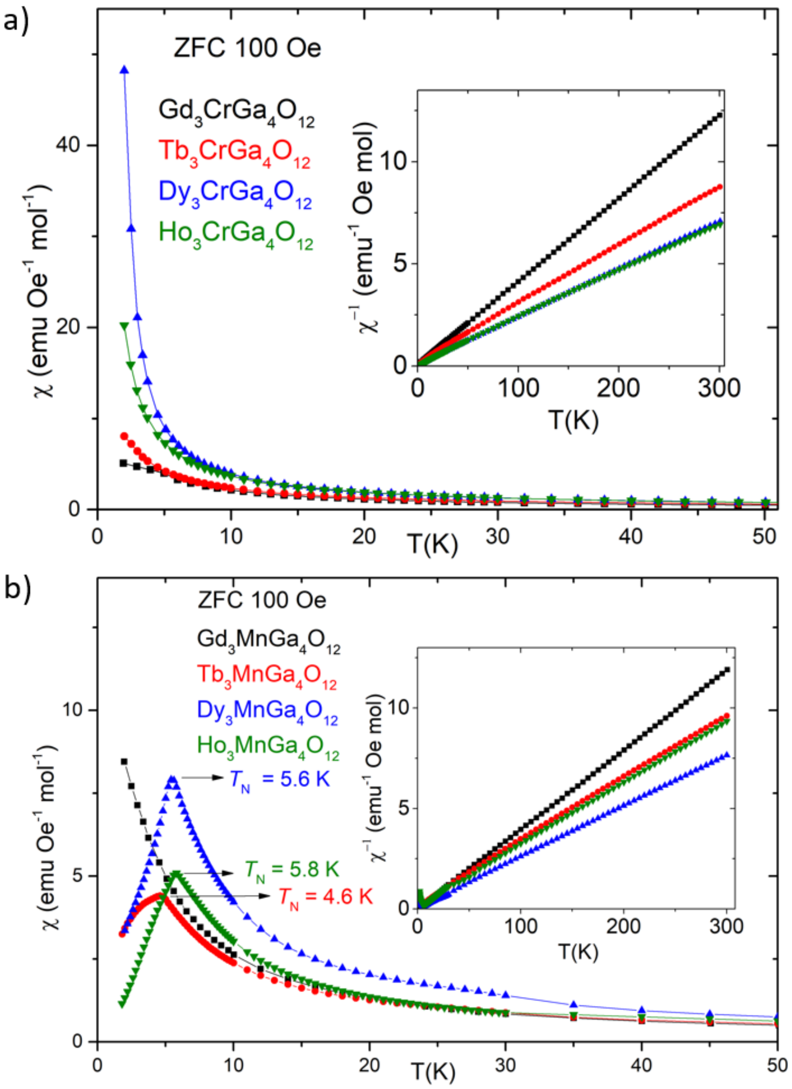

Figure 4.3 ZFC molar susceptibility $\chi(T)$ for a) $Ln_3CrGa_4O_{12}$ b) $Ln_3MnGa_4O_{12}$,Ln = Gd, Tb, Dy, Ho, measured from 2 - 300 K in a field of 100 Oe. Inset: inverse molar susceptibility $\chi^{-1}(T)$.

For $Y_3MnGa_4O_{12}$, where Mn^{3+} is the only magnetic ion, the ZFC-FC $\chi(T)$ shows a deviation at $T_0 = 18$ K (Figure 4.4). This is indicative of spin glass-like behaviour. Given the site disorder, formation of a spin-glass state is not unexpected and has been observed in other systems with dilute spins along the [111] direction [285]. The Curie-Weiss fit between 100 -

Table 4.4 Bulk magnetisation parameters for $Ln_3Ga_5O_{12}$, $Ln_3CrGa_4O_{12}$ and $Ln_3MnGa_4O_{12}$, *Ln* = Gd, Tb, Dy, Ho. T_0 for *Ln* = Tb, Dy, Ho is determined from previous literature reports for $Ln_3Ga_5O_{12}$ [197, 255], from zero field heat capacity data for $Ln_3CrGa_4O_{12}$ and from magnetic susceptibility data for $Ln_3MnGa_4O_{12}$. The magnetic susceptibility data for $Ln_3Ga_5O_{12}$ has been taken from the previous chapter. In case of three-dimensional antiferromagnetic ordering, T_0 is the Néel temperature, T_N.

Compound	T_0 (K)	θ_{CW} (K)	f	Th. μ_{eff} (μ_B)	Exptl. μ_{eff} (μ_B)	Th. M_{sat} (μ_B/f.u.)	$M_{2K,9T}$ (μ_B/f.u.)
$Gd_3Ga_5O_{12}$	<0.025	-1.36(15)	> 54.4	13.75	13.536(6)	21	19.7
$Gd_3CrGa_4O_{12}$	<0.4	-1.0(4)	> 2.5	14.29	14.03(3)	24	23.4
$Gd_3MnGa_4O_{12}$	< 0.4	-1.6(1.3)	> 4.0	14.6	1424(8)	25	23
$Tb_3Ga_5O_{12}$	0.25	-9.2(5)	36.8	16.84	17.0(2)	27	15.6
$Tb_3CrGa_4O_{12}$	1.72(5)	-10(2)	5.6	17.27	16.77(8)	30	18.7
$Tb_3MnGa_4O_{12}$	4.6(2)	-14(5)	3.0	17.53	16.0(2)	31	18.8
$Dy_3Ga_5O_{12}$	0.373	-6.8(4)	18.2	18.45	16.32(2)	30	19.2
$Dy_3CrGa_4O_{12}$	1.75(5)	-4.1(1.5)	2.3	18.85	18.50(7)	33	22.7
$Dy_3MnGa_4O_{12}$	5.6(2)	-4.1(9)	0.7	19.08	16.14(5)	34	20.1
$Ho_3Ga_5O_{12}$	0.19	-12(2)	63.2	18.38	18.43(10)	30	17.2
$Ho_3CrGa_4O_{12}$	1.55(5)	-9(3)	5.8	18.78	18.80(19)	33	21.2
$Ho_3MnGa_4O_{12}$	5.8(2)	-6(3)	1.0	19.02	16.1(2)	34	21.1

300 K gives $\mu_{eff} = 4.83\mu_B$ consistent with the theoretical value of $4.89\mu_B$ for Mn^{3+} spins and $\theta_{CW} = -9(4)$K, indicating net antiferromagnetic interactions between Mn^{3+} spins.

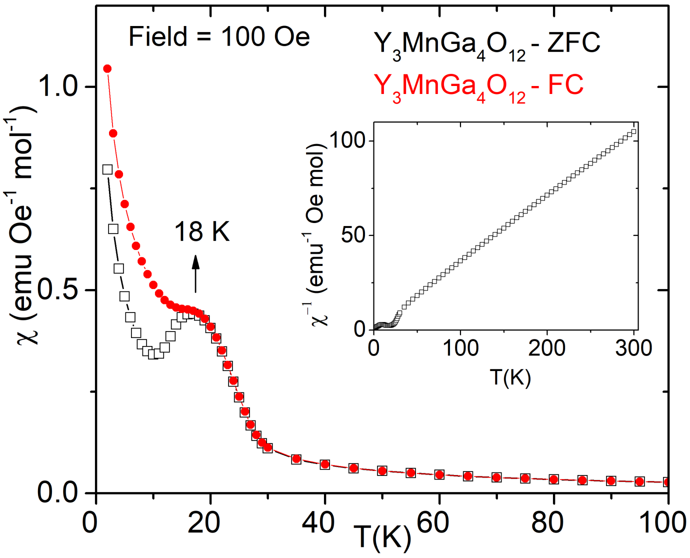

Figure 4.4 ZFC-FC molar susceptibility $\chi(T)$ for $Y_3MnGa_4O_{12}$ measured from 2 - 300 K in a field of 100 Oe; inset: inverse ZFC molar susceptibility $\chi^{-1}(T)$.

4.4.2 Isothermal magnetisation

The isothermal magnetisation $M(H)$ was measured from 0 - 9 T at select temperatures using the ACMS option on a Quantum Design PPMS. The $M(H)$ curves at 2 K for $Ln_3CrGa_4O_{12}$ and $Ln_3MnGa_4O_{12}$ compared to $Ln_3Ga_5O_{12}$, *Ln* = Gd, Tb, Dy, Ho, are shown in Figure 4.5. The maximum values of magnetisation/f.u., M_{max}, are compiled in Table 4.4. The isothermal magnetisation is increased on both Cr^{3+} and Mn^{3+} substitution in $Ln_3Ga_5O_{12}$. The magnetisation for $Gd_3CrGa_4O_{12}$ and $Gd_3MnGa_4O_{12}$ saturates at 2 K, 9 T. For $Gd_3CrGa_4O_{12}$, the maximum magnetisation value is consistent with that expected for a Heisenberg system, $M_{sat} = 3g_JJ + g_SS = (3 \times 2 \times \frac{7}{2}) + (2 \times \frac{3}{2})$ = 24 μ_B/f.u. However, for $Gd_3MnGa_4O_{12}$, the saturation value is below the theoretical saturation value for a Heisenberg system, $M_{sat} = 3g_JJ + g_SS = (3 \times 2 \times \frac{7}{2}) + (2 \times 2) = 25\mu_B$/f.u. This may be due to the Mn^{3+} spins having some single-ion anisotropy or due to the actual Mn^{3+} content being less than the nominal composition.

The $M(H)$ for $Ln_3CrGa_4O_{12}$ and $Ln_3MnGa_4O_{12}$, *Ln* = Tb, Dy, Ho increases rapidly at fields $\mu_0H < 2$ T, and much more gradually in higher fields, $\mu_0H > 2$ T. None of the $M(H)$ curves attain saturation in the experimentally limiting field of 9 T. The observed M_{max} for $Ln_3CrGa_4O_{12}$ and $Ln_3MnGa_4O_{12}$, *Ln* = Tb, Dy, Ho, is much lower than the theoretical saturation value for a Heisenberg system. However, for Tb^{3+}, Dy^{3+} and Ho^{3+} spins that have substantial single-ion anisotropy in $Ln_3Ga_5O_{12}$ [198, 258, 268], the powder-averaged saturation magnetisation value is expected to be close to $3g_JJ/2$. The M_{max} values are in agreement with this and so it is proposed that the single-ion anisotropy of the Ln^{3+} spins (*Ln* = Tb, Dy, Ho) is retained on Cr^{3+} or Mn^{3+} substitution in $Ln_3Ga_5O_{12}$. The contribution of Cr^{3+} and Mn^{3+} spins to the net magnetisation is small compared to Ln^{3+} and so one cannot definitively comment on their nature. However, Cr^{3+} (d^3) spins are likely to have Heisenberg nature [286] and the M_{max} values are consistent with this. Similarly, the isothermal magnetisation for $Y_3MnGa_4O_{12}$ at 2 K, Figure 4.6, hints at the presence of single-ion anisotropy for the Mn^{3+} (d^4) spins.

As shown in Figure 4.7, field-induced transitions are observed for $Tb_3MnGa_4O_{12}$, $Dy_3MnGa_4O_{12}$ and $Ho_3MnGa_4O_{12}$ at $T = 2$ K, at 0.4 T, 0.3 T and 0.46 T respectively. No field-induced transitions are observed for $Ln_3Ga_5O_{12}$, $Ln_3CrGa_4O_{12}$ (*Ln* = Gd, Tb, Dy, Ho) and $Gd_3MnGa_4O_{12}$ at $T = 2$ K. Previously, field-induced transitions have been reported for $Gd_3Ga_5O_{12}$ [154], $Tb_3Ga_5O_{12}$ [256] and $Ho_3Ga_5O_{12}$ [261] at temperatures well below 2 K, the temperature limit of the magnetisation measurements. It is likely that field-induced transitions for $Ln_3CrGa_4O_{12}$ (*Ln* = Gd, Tb, Dy, Ho) and $Gd_3MnGa_4O_{12}$, if any, also occur below 2 K. Further measurements using a dilution refrigerator are required to explore this.

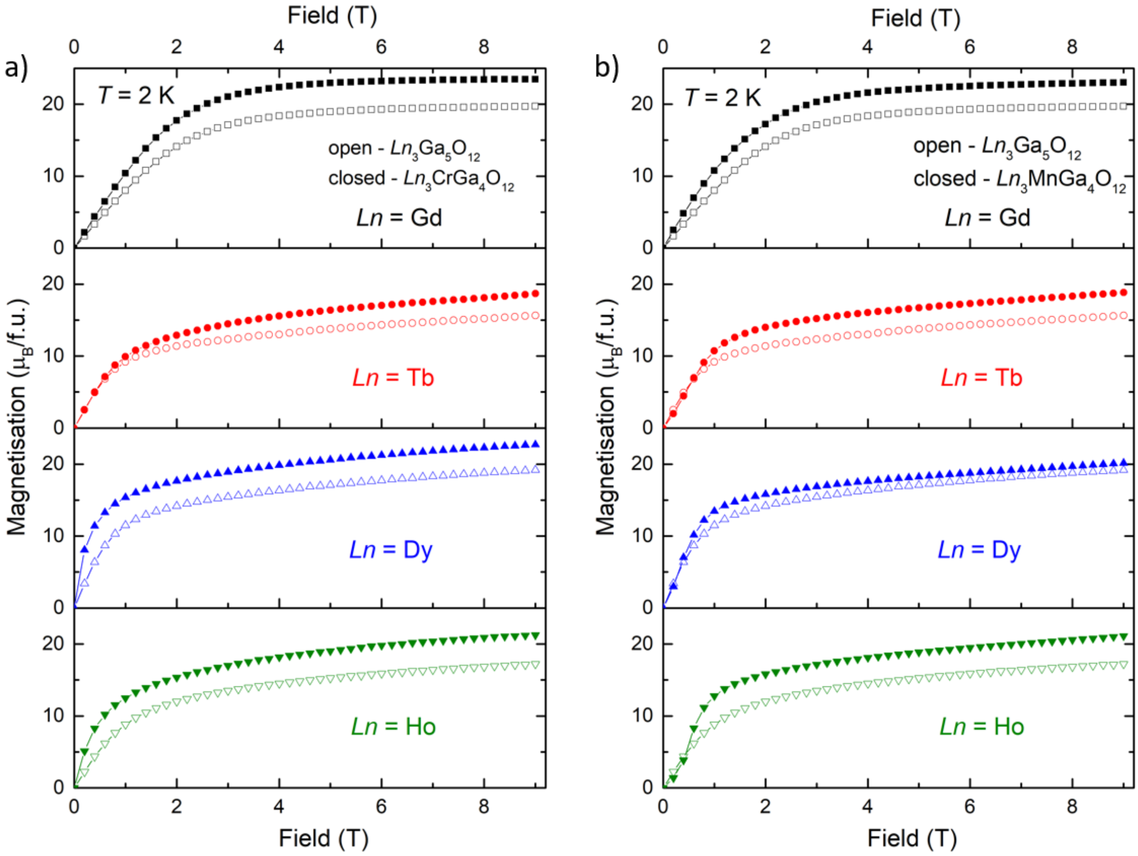

Figure 4.5 $M(H)$ curves from 0 – 9 T at $T = 2$ K for a) $Ln_3CrGa_4O_{12}$ b) $Ln_3MnGa_4O_{12}$ compared to $Ln_3Ga_5O_{12}$ (Ln = Gd, Tb, Dy, Ho). $M(H)$ data for $Ln_3Ga_5O_{12}$ has been taken from the previous chapter.

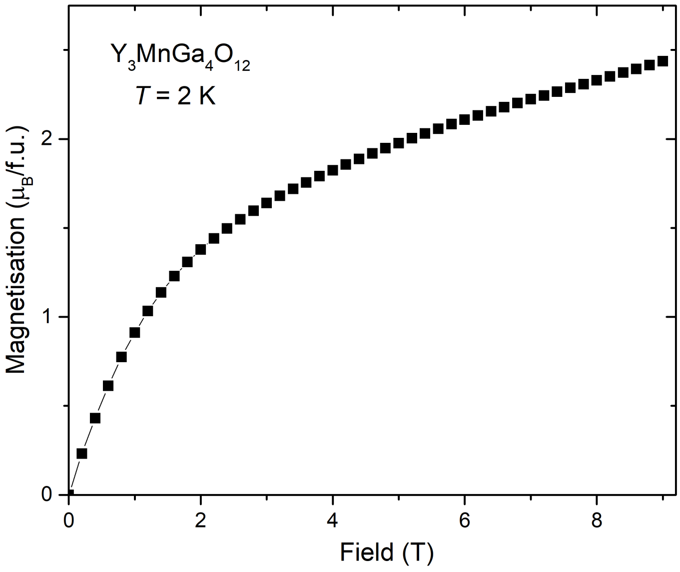

Figure 4.6 $M(H)$ curve from 0 – 9 T at $T = 2$ K for $Y_3MnGa_4O_{12}$.

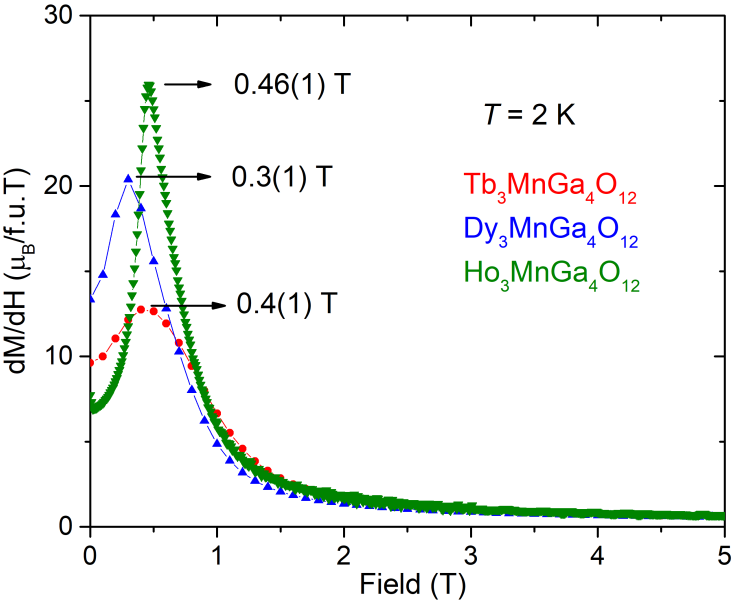

Figure 4.7 $\frac{dM}{dH}$ curves at $T = 2$ K for $Ln_3MnGa_4O_{12}$, Ln = Tb, Dy, Ho, showing the onset of field-induced transitions at 0.4 T, 0.3 T and 0.46 T for Ln = Tb, Dy and Ho respectively.

4.4.3 Heat capacity

The zero field magnetic heat capacity, C_{mag}, from 0.4 - 20 K for $Ln_3CrGa_4O_{12}$, Ln = Gd, Tb, Dy, Ho, and $Gd_3MnGa_4O_{12}$ was measured using the He3 option on a Quantum Design PPMS to investigate the existence of magnetic ordering for $0.4 \leq T \leq 2$ K. Equal amounts of sample and silver powder were mixed to increase the thermal conductivity and pressed into pellets which were then used for measurement. The contribution from silver was subtracted using values from the literature [243] to obtain the sample heat capacity. The lattice contribution was subtracted using a Debye model (equation 2.37) with θ_D in the range of 330 - 360 K. The nuclear Schottky anomaly for $Ho_3CrGa_4O_{12}$ was subtracted using a model for the hyperfine interactions for $HoCrO_3$ [287].

Figure 4.8 shows the plot of C_{mag}/T as a function of temperature in zero field for $Ln_3CrGa_4O_{12}$, Ln = Gd, Tb, Dy, Ho, where C_{mag} is the magnetic heat capacity. No magnetic ordering is seen down to 0.4 K for $Gd_3CrGa_4O_{12}$. $Tb_3CrGa_4O_{12}$, $Dy_3CrGa_4O_{12}$ and $Ho_3CrGa_4O_{12}$ show magnetic ordering features at 1.72 K, 1.75 K and 1.55 K respectively. The zero field magnetic heat capacity for $Gd_3MnGa_4O_{12}$, Figure 4.9, shows a feature at 0.45 K. However, as the temperature limit of the measurement is 0.4 K, sufficient data points are not available to comment on whether this is a real feature or an artifact of the measurement.

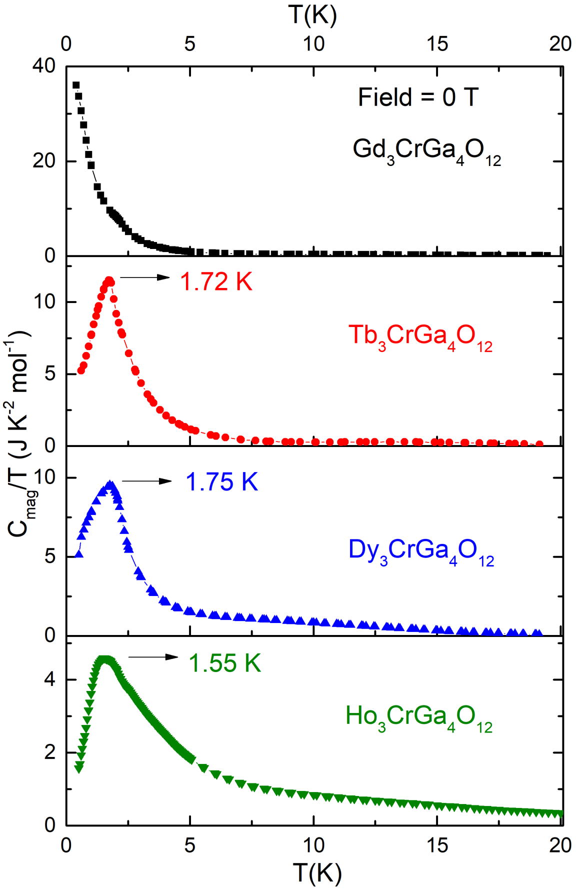

Figure 4.8 Zero field heat capacity from 0.4 - 20 K for $Ln_3CrGa_4O_{12}$, Ln = Gd, Tb, Dy, Ho.

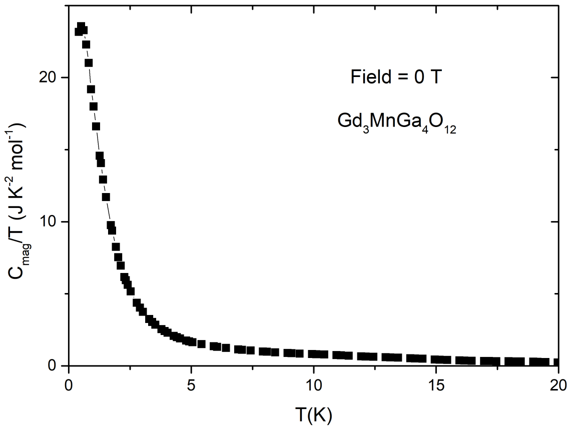

Figure 4.9 Zero field heat capacity from 0.4 - 20 K for $Gd_3MnGa_4O_{12}$.

4.5 Low temperature powder neutron diffraction

4.5.1 $Ln_3CrGa_4O_{12}$, *Ln* = Tb, Dy, Ho

PND measurements, $T \geq 2$ K, were carried out on $Tb_3CrGa_4O_{12}$ and $Ho_3CrGa_4O_{12}$ on the D20 diffractometer at ILL, Grenoble (λ = 1.542 Å). Magnetic Bragg peaks were absent and only subtle changes in the magnetic diffuse scattering were observed. This is expected as the minimum temperature for the experiments, $T_{min} = 2$ K, was above the ordering transition for both $Tb_3CrGa_4O_{12}$ (1.72 K) and $Ho_3CrGa_4O_{12}$ (1.55 K). No quantitative analysis of the magnetic diffuse scattering could be carried out as the background from the empty can in the cryostat had not been measured separately and the maximum temperature at which data was collected on D20, $T_{max} = 15$ K, was not sufficiently high enough to serve as a 'high temperature' background since the presence of magnetic correlations was still possible. For $Dy_3CrGa_4O_{12}$, PND measurements were carried out on the WISH diffractometer at ISIS, Oxfordshire by Dr Pascal Manuel. Scans were collected at 1.5 K and 100 K. An absorption correction could not be carried out as the dimensions of the sample can and sample mass had not been recorded prior to measurement. Weak magnetic Bragg peaks are observed at 1.5 K, below the transition temperature T_0 = 1.75(5) K, as shown in Figure 4.10. No magnetic diffuse scattering is observed at 1.5 K. The magnetic Bragg peaks can be indexed with the propagation vector **k** = (0, 0, 0) and are consistent with AFA type ordering reported for $Dy_3Al_5O_{12}$ [262]. However, due to the limited number of magnetic Bragg peaks (two) and the weak intensity (due to the high absorption from naturally occurring Dy), it was not possible to carry out further analysis and determine the magnetic structure definitively or ascertain whether the Cr^{3+} spins contribute to the magnetic ordering.

4.5.2 $Ho_3MnGa_4O_{12}$

In order to explore the magnetic ordering of $Ho_3MnGa_4O_{12}$, PND experiments, $T \geq 1.5$ K were carried out on the D1B (λ = 2.525 Å) and D20 (λ = 1.542 Å) diffractometers at ILL, Grenoble. Strong magnetic Bragg peaks were observed below the transition temperature, $T_N = 5.8$ K. No magnetic diffuse scattering was observed for $T \geq 1.5$ K suggesting that unlike in $Ho_3Ga_5O_{12}$ [261], long and short-range magnetic order do not coexist in $Ho_3MnGa_4O_{12}$. Indexing for $Ho_3MnGa_4O_{12}$ was carried out using the k-search program in the Fullprof suite and found to have a **k** = (0, 0, 0) magnetic propagation vector.. Different combinations of irreducible representations for Ho^{3+} and Mn^{3+} were tested using the SARAH program and used to generate a single magnetic phase for the magnetic Rietveld refinement in Fullprof.

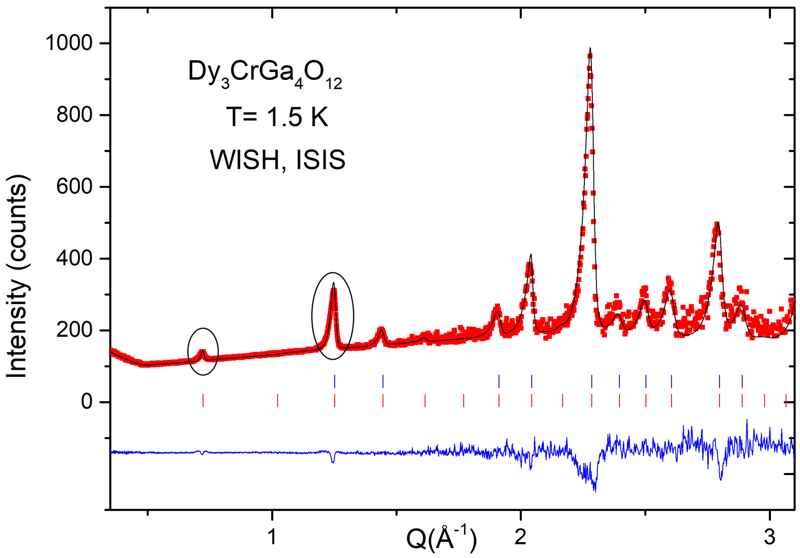

Figure 4.10 PND Rietveld refinement at 1.5 K for $Dy_3CrGa_4O_{12}$: Red dots - Experimental data, Black line - Modelled data, Blue line - Difference pattern, Blue ticks - nuclear Bragg positions, Red ticks - magnetic Bragg positions. The two magnetic Bragg peaks observed are circled in black.

Table 4.5 The basis vectors Ψ_1 for Ho (24c) and Mn(16a) in nonzero IR Γ_3^1.

Atoms in non-primitive basis for Ho		Components of Ψ_1	Atoms in non-primitive basis for Mn		Components of Ψ_1
Atom label	Coordinates		Atom label	Coordinates	
Ho1	$(0, \frac{1}{4}, \frac{1}{8})$	(0 0 1)	Mn1	(0, 0, 0)	(1 1 1)
Ho2	$(0, \frac{3}{4}, \frac{3}{8})$	(0 0 -1)	Mn2	$(\frac{1}{2}, 0, \frac{1}{2})$	(-1 -1 1)
Ho3	$(\frac{1}{8}, 0, \frac{1}{4})$	(1 0 0)	Mn3	$(0, \frac{1}{2}, \frac{1}{2})$	(-1 1 -1)
Ho4	$(\frac{3}{8}, 0, \frac{3}{4})$	(-1 0 0)	Mn4	$(\frac{1}{2}, \frac{1}{2}, 0)$	(1 -1 -1)
Ho5	$(\frac{1}{4}, \frac{1}{8}, 0)$	(0 1 0)	Mn5	$(\frac{3}{4}, \frac{1}{4}, \frac{1}{4})$	(-1 -1 1)
Ho6	$(\frac{3}{4}, \frac{3}{8}, 0)$	(0 -1 0)	Mn6	$(\frac{3}{4}, \frac{3}{4}, \frac{3}{4})$	(1 1 1)
Ho7	$(0, -\frac{1}{4}, -\frac{1}{8})$	(0 0 1)	Mn7	$(\frac{1}{4}, \frac{1}{4}, \frac{3}{4})$	(-1 1 -1)
Ho8	$(0, \frac{1}{4}, \frac{5}{8})$	(0 0 -1)	Mn8	$(\frac{1}{4}, \frac{3}{4}, \frac{1}{4})$	(1 -1 -1)
Ho9	$(-\frac{1}{8}, 0, -\frac{1}{4})$	(1 0 0)			
Ho10	$(\frac{5}{8}, 0, \frac{1}{4})$	(-1 0 0)			
Ho11	$(-\frac{1}{4}, -\frac{1}{8}, 0)$	(0 1 0)			
Ho12	$(\frac{1}{4}, \frac{5}{8}, 0)$	(0 -1 0)			

Symmetry analysis for the propagation vector **k** = (0, 0, 0) and space group $Ia\bar{3}d$ gave eight nonzero irreducible representations (IRs) for the magnetic Ho (24*c*) site: 2 one-dimensional (Γ^1_3, Γ^1_4) and 2 two-dimensional representations (Γ^2_5, Γ^2_6) all occurring once, 2 three-dimensional (Γ^3_7, Γ^3_8) occurring twice and 2 three-dimensional representations (Γ^3_9, Γ^3_{10}) that are repeated thrice. According to Kovalev's notation [288], the magnetic representation Γ_{magHo} is given by:

$$\Gamma_{\mathrm{magHo}} = 1\Gamma^1_3 + 1\Gamma^1_4 + 1\Gamma^2_5 + 1\Gamma^2_6 + 2\Gamma^3_7 + 2\Gamma^3_8 + 3\Gamma^3_9 + 3\Gamma^3_{10} \tag{4.1}$$

Of these, only Γ^2_5 and Γ^2_6 have both real and imaginary components while the others only have real components. Similar representational analysis for the magnetic Mn (16*a*) site gave five nonzero IRs: 2 one-dimensional (Γ^1_1, Γ^1_3) repeated once, 1 two-dimensional (Γ^2_6) repeated twice and 2 three-dimensional IRs (Γ^3_8, $\Gamma_1 0^3$) repeated thrice in the decomposition. Then in the same notation Γ_{magMn} is given by:

$$\Gamma_{\mathrm{magMn}} = 1\Gamma^1_1 + 1\Gamma^1_3 + 2\Gamma^2_6 + 3\Gamma^3_8 + 3\Gamma^3_{10} \tag{4.2}$$

Of these, only Γ^2_6 has both real and imaginary components and all the others have real components only. All combinations of irreducible representations for Ho^{3+} and Mn^{3+} ions were tested in turn including allowing for magnetic ordering in a single magnetic sublattice, only a model with both ions having the Γ^1_3 irreducible representation (Table 4.5) allowed for a good fit to the data, Figure 4.11a.

The magnitude of the ordered Ho^{3+} and Mn^{3+} moments increase on cooling (Figure 4.11a inset), though the values are smaller than the theoretical moments (10.61 μ_B for Ho^{3+} and 4.89 μ_B for Mn^{3+} respectively). This may be due to low-lying CEF effects or screening of the moments. Previous neutron diffraction studies of $Ho_3Ga_5O_{12}$ and $Ho_3Al_5O_{12}$ have also reported reduced moments [257, 263] in close agreement with the results for $Ho_3MnGa_4O_{12}$. Reduced magnetic moments for Mn^{3+} determined from neutron diffraction have also previously been observed [289].

The magnetic structure (Figure 4.11b) has the same long range ordered arrangement of the Ho^{3+} spins as that reported for $Ho_3Ga_5O_{12}$ and $Ho_3Al_5O_{12}$ [257, 263]. The 24 Ho^{3+} spins in each unit cell are arranged into six sublattices with the Ho^{3+} spins aligned along the crystallographic axes [100], [$\bar{1}$00], [010], [0$\bar{1}$0], [001] and [00$\bar{1}$] such that the net moment is zero. The Mn^{3+} spins in each unit cell are aligned along the body diagonals, as reported for the Ising garnet $CaY_2Co_2Ge_3O_{12}$ [283]. However, their relative orientation is completely different. The Mn^{3+} spins are oriented along [111], [$\bar{1}\bar{1}$1], [$\bar{1}$1$\bar{1}$] and [1$\bar{1}\bar{1}$] such that there is a resultant moment from the Mn^{3+} spins along [111].

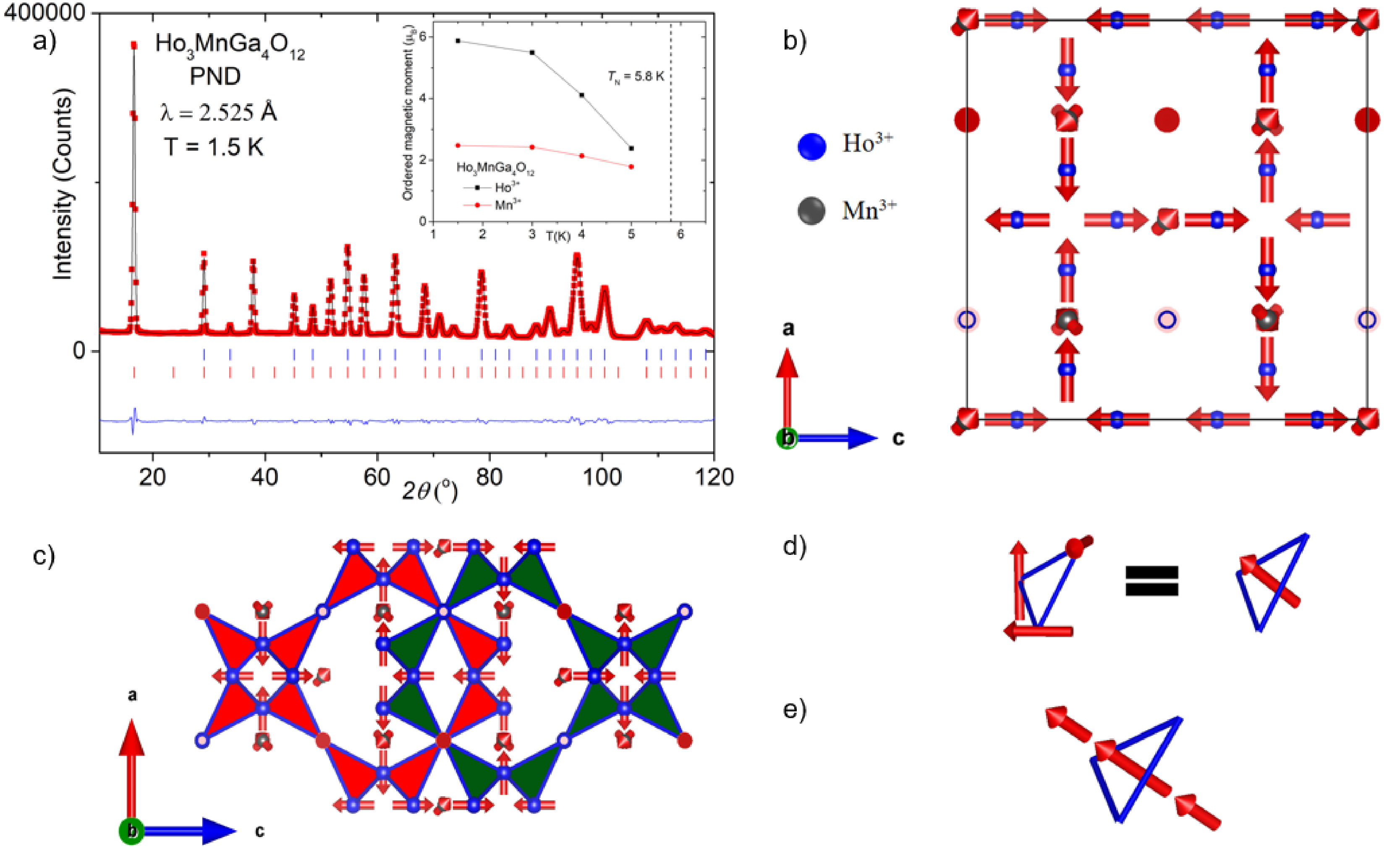

Figure 4.11 a) Rietveld refinement of the neutron diffraction pattern at 1.5 K for $Ho_3MnGa_4O_{12}$: Blue ticks – nuclear Bragg reflections, red ticks – magnetic Bragg reflections; inset shows the ordered magnetic moment as a function of temperature. b) Magnetic structure for $Ho_3MnGa_4O_{12}$. c) Arrangement of Ho^{3+} and Mn^{3+} spins for $Ho_3MnGa_4O_{12}$ in the two interpenetrating ten-membered rings in the garnet lattice. d) Each Ho_3 triangle has three orthogonal spins orientated along the three crystallographic axes with the net Ho^{3+} *quasi-spin* along [111]. e) The resultant Ho^{3+} *quasi-spin* couples ferromagnetically with the Mn^{3+} spins located above and below the triangle.

4.6 Discussion

Polycrystalline samples of $Ln_3CrGa_4O_{12}$ and $Ln_3MnGa_4O_{12}$, *Ln* = Gd, Tb, Dy, Ho have been prepared for the first time. Their structure has been evaluated using PXRD and PND and the bulk magnetic properties have been studied. $Ln_3CrGa_4O_{12}$ and $Ln_3MnGa_4O_{12}$ (*Ln* = Gd, Tb, Dy, Ho) crystallise in the same cubic garnet structure as $Ln_3Ga_5O_{12}$ with the magnetic Cr^{3+} and Mn^{3+} occupying the octahedral cation sites, consistent with CEF considerations. It was not possible to synthesise $Ln_3A_xGa_{5-x}O_{12}$, *Ln* = Gd, Tb, Dy, Ho, *A* = Cr, Mn, with $x > 1$; the cause for this limited solubility is unclear. It was also not possible to substitute Mn^{3+} into $Ln_3Al_5O_{12}$; this could be due to the mismatch in radii between Mn^{3+} and Al^{3+} or the fact that the perovskite phases $LnAlO_3$ and $LnMnO_3$ are more stable than the garnet phase. Whilst there is very little change in the crystallographic parameters on Cr^{3+} and Mn^{3+} substitution in $Ln_3Ga_5O_{12}$, there is a dramatic change in the magnetic properties.

Cr^{3+} or Mn^{3+} substitution significantly enhances the transition temperature for lanthanide gallium garnets with *Ln* = Tb, Dy, Ho, Table 4.4, although the transition temperature is enhanced by a much greater extent on Mn^{3+} substitution. The frustration index f of the $Ln_3Ga_5O_{12}$ magnetic lattice, defined by equation (1.63), is reduced on Cr^{3+} as well as Mn^{3+} substitution. As seen in Table 4.4, the frustration is relieved to a much greater extent for $Ln_3MnGa_4O_{12}$ than $Ln_3CrGa_4O_{12}$ for *Ln* = Tb, Dy, Ho.

The results for $Ln_3CrGa_4O_{12}$ and $Ln_3MnGa_4O_{12}$, *Ln* = Tb, Dy, Ho are now discussed separately. No further remarks can be made for *Ln* = Gd because $Gd_3CrGa_4O_{12}$ and $Gd_3MnGa_4O_{12}$ do not order magnetically down to 0.4 K. Further measurements below 0.4 K are required to investigate the existence of any ordering features in $Gd_3CrGa_4O_{12}$ and $Gd_3MnGa_4O_{12}$ and to compare with $Gd_3Ga_5O_{12}$, which shows no long range ordering down to 0.025 K [141].

4.6.1 $Ln_3CrGa_4O_{12}$, *Ln* = Tb, Dy, Ho

On Cr^{3+} substitution in $Ln_3Ga_5O_{12}$, T_0 is increased from 0.25 K to 1.72 K for *Ln* = Tb, from 0.373 K to 1.75 K for *Ln* = Dy and from 0.19 K to 1.55 K for *Ln* = Ho. In the most extreme case, for $Dy_3CrGa_4O_{12}$, the frustration index $f = 2.3$ is only slightly higher than would be expected for an antiferromagnet and is significantly reduced from $f \approx 18$ for $Dy_3Ga_5O_{12}$. The origin of the changes in the magnetic frustration is not clear from the bulk magnetic data alone. It has been reported that increased single-ion anisotropy and strength of dipolar interactions in $Ln_3Al_5O_{12}$ garnets increases T_0 [259, 264, 265]. However, the lack of any significant changes in the *Ln*-O environment and the *Ln*-*Ln* bond lengths would suggest that this is not the case here and other effects such as the impact of the *Ln* – Cr interactions need to be considered. The low temperature PND data collected is inconclusive and further neutron scattering studies well below the transition temperature are required to determine the nature of magnetic ordering in $Ln_3CrGa_4O_{12}$, Ln = Tb, Dy, Ho.

4.6.2 $Ln_3MnGa_4O_{12}$, Ln = Tb, Dy, Ho

A comparison of the transition temperatures of $Ln_3Ga_5O_{12}$ and $Ln_3MnGa_4O_{12}$ shows that T_0 is increased from 0.25 K to 4.6 K for Ln = Tb, from 0.373 K to 5.6 K for Ln = Dy and from 0.19 K to 5.8 K for Ln = Ho. The frustration is almost completely relieved for Ln = Dy and Ho with $f = 0.7$ for $Dy_3MnGa_4O_{12}$ and 1.0 for $Ho_3MnGa_4O_{12}$ as compared to $f \approx 18$ and ≈ 60 for $Dy_3Ga_5O_{12}$ and $Ho_3Ga_5O_{12}$ respectively. The origin of the magnetic frustration being relieved in $Ho_3MnGa_4O_{12}$ will now be discussed by considering the magnetic ground state.

Magnetic ground state for $Ho_3MnGa_4O_{12}$

When the magnetic ground state of $Ho_3MnGa_4O_{12}$ (as discussed in Section 4.5.2) is considered in terms of the two interpenetrating networks of ten-membered rings of Ho_3 triangles, Figure 4.11c, the relative orientations of the Ho^{3+} and Mn^{3+} spins assume special significance. For each ten-membered ring, the net magnetic moment is zero, however there is a net ferromagnetic interaction between the Ho^{3+} and Mn^{3+} moments. When these interactions are summed over a Ho_3 triangle then the resultant Ho^{3+} *quasi-spin* is orientated in or out of the centroid of the triangle, that is, along [111] (Figure 4.11d), and is located directly above or below the site partially occupied by Mn^{3+}. The Mn^{3+} spin aligns co-parallel with the Ho^{3+} *quasi-spin* (Figure 4.11e). Whilst the construct of the Ho^{3+} *quasi-spins* allows for the magnetic structure to be rationalised it should be noted that in the parent material, $Ho_3Ga_5O_{12}$, exchange coupling between any two of the Ho^{3+} spins on an individual triangle ($\propto \boldsymbol{S}_1 \cdot \boldsymbol{S}_2$) results in no net interaction as they are orthogonal. However, in the case of $Ho_3MnGa_4O_{12}$, each individual Ho^{3+}-Mn^{3+} interaction is non-zero enabling the formation of resultant Ho^{3+} *quasi-spins*.

The concurrent magnetic ordering of both Ho^{3+} and Mn^{3+} observed in $Ho_3MnGa_4O_{12}$ is unique when compared to other rare-earth – transition metal oxides with complex magnetic structures. Studies on magnetic substituents in lanthanide garnets have been restricted to $Ln_3Fe_5O_{12}$ where the two Fe^{3+} sublattices order in a ferrimagnetic structure at $\approx$ 130 – 140 K while the Ln^{3+} ions order in a double umbrella structure around few K with spins canted away from the [111] direction on both sides. [276–279]. In $HoMnO_3$, the Mn^{3+} spins order at $\approx$ 72 K while onset of ordering of the Ho^{3+} spins is seen at the spin-rotation transition for the Mn^{3+} spins $\approx$ 33 K followed by an increase in the ordered Ho^{3+} moments below 5 K [290–292]. However, in $Ho_3MnGa_4O_{12}$, no features are observed in the neutron diffraction data corresponding to individual ordering of the Mn^{3+} spins at $T > T_N$. In the pyrochlore $Ho_2Mn_2O_7$, complex short-range order is observed at $T_0 \approx 33$ K with coexistence of random spin-canted domains (leading to glassy behaviour) and smaller ferromagnetic domains [293, 294]. In contrast, no magnetic diffuse scattering is observed for $Ho_3MnGa_4O_{12}$ implying that the structure is fully long-range ordered. The ordering mechanism is also distinct from the 'ordered spin-ice' structure reported for Ho_2CrSbO_7, where the frustration is proposed to be relieved through local ferromagnetic correlations between the Cr^{3+} spins, as is evidenced by a positive Curie-Weiss constant for the isostructural Y_2CrSbO_7 [46, 295]. However, in $Ho_3MnGa_4O_{12}$, the Mn-Mn and Ho-Ho exchange interactions are antiferromagnetic suggesting that the ordering is driven by a different mechanism, the origin of which is discussed below.

The partial substitution of Ga^{3+} for Mn^{3+} in $Ho_3MnGa_4O_{12}$ significantly changes the magnetic interactions which need to be considered. In addition to Ho-Ho interactions present in $Ho_3Ga_5O_{12}$, Mn-Mn and Ho-Mn interactions also need to be considered. First, the dipolar and exchange interactions between the magnetic Ho^{3+} are considered. As the Ho-Ho bond lengths are not significantly changed on Mn^{3+} substitution, there is no significant change in the Ho-Ho dipolar interaction energy, calculated using equation (1.42), $D \approx 0.9$ K. A priori calculation of the Ho-Ho exchange interactions is complex, as the Curie-Weiss constant for $Ho_3MnGa_4O_{12}$ contains contributions from multiple interactions. An order of magnitude approximation for the nearest-neighbour exchange energy, J_1 in unsubstituted $Ho_3Ga_5O_{12}$ can be obtained using equation (1.60) where n = number of nearest-neighbour Ho^{3+} = 4. This gives J_1 = - 4.5 K and an order of magnitude estimation of J_1 for $Ho_3MnGa_4O_{12}$. The Mn-Mn exchange interactions can be approximated by considering isostructural $Y_3MnGa_4O_{12}$, where the only magnetic contribution is from the Mn^{3+} spins and which has analogous lattice parameter and bond lengths as $Ho_3MnGa_4O_{12}$. The Curie-constant, θ_{CW} = -9(4) K corresponds to $J_1 \approx$ - 6.8 K if each Mn^{3+} spin is assumed to have two nearest neighbours. Determination of the Ho-Mn exchange interactions is nontrivial and further inelastic neutron scattering experiments are required for quantitative analysis. However, the resultant spin structure, although constrained by the CEF, has a ferromagnetic component between adjacent Ho^{3+} and Mn^{3+} spins, suggesting the resulting moment is not minimised. Finally, the Ho-Mn dipolar interactions are considered. The local internal dipolar fields due to the Mn^{3+} spins above and below the Ho_3 triangles can be approximated as $\mu_0 H \approx \frac{\mu_0 \mu_{eff}}{2\pi r^3} = \frac{\mu_0 g_S \sqrt{S(S+1)}}{2\pi r^3}$ where $g_S = 2$, $S = 2$ for Mn^{3+} and r is the distance between the centroid of the Ho_3 triangle and the Mn^{3+} spin = 2.65 Å. This gives a value of $\approx$ 0.5 T which corresponds to an energy $\approx$

Table 4.6 Comparison of ΔS_m per mole *Ln* at T = 2 K for $Ln_3Ga_5O_{12}$ and $Ln_3CrGa_4O_{12}$; *Ln* = Gd, Tb, Dy, Ho. % changes are calculated with respect to the ΔS_m values for the parent gallium garnets $Ln_3Ga_5O_{12}$.

Field		9 T	2 T	2 T	2 T
Ln		Gd	Tb	Dy	Ho
$Ln_3Ga_5O_{12}$	ΔS_m (J K^{-1} mol^{-1})	40.79	8.66	11.32	4.24
$Ln_3CrGa_4O_{12}$	ΔS_m (J K^{-1} mol^{-1})	51.37	8.49	13.25	9.29
	% change	25.9	-1.9	17.0	119.1

3.2 K. In $Ho_3Ga_5O_{12}$, the formation of a long range ordered state is observed on application of a 2 T field along [111] [261]. Whilst the exact nature of field-induced long-range ordering in $Ho_3Ga_5O_{12}$ is unknown, this highlights the role of an applied field in the magnetic ordering in the lanthanide gallium garnets with strong single-ion anisotropy. Thus, the local internal dipolar field may play a role in the magnetic ordering in $Ho_3MnGa_4O_{12}$.

4.7 Magnetocaloric effect

The magnetocaloric effect (MCE) of $Ln_3CrGa_4O_{12}$ and $Ln_3MnGa_4O_{12}$, *Ln* = Gd, Tb, Dy, Ho, has been characterised by the change in magnetic entropy, ΔS_m per mole, calculated from the isothermal magnetisation curves according to equation (1.64). As has already been discussed in Chapter 3, the garnets with *Ln* = Tb, Dy, Ho having substantial single-ion anisotropy have optimum MCE in fields ≤ 2 T whereas the MCE of $Gd_3Ga_5O_{12}$ is maximised in fields > 2 T. It was also shown in Chapter 3 that among $Tb_3Ga_5O_{12}$, $Dy_3Ga_5O_{12}$ and $Ho_3Ga_5O_{12}$, $Dy_3Ga_5O_{12}$ has the highest MCE. The isothermal magnetisation data indicates that the single-ion anisotropy is retained in $Ln_3CrGa_4O_{12}$ and $Ln_3MnGa_4O_{12}$, *Ln* = Tb, Dy, Ho. Therefore, the MCE for the garnets with *Ln* = Tb, Dy, Ho are compared in a field of 2 T and the MCE for $Gd_3CrGa_4O_{12}$, $Gd_3MnGa_4O_{12}$ and $Gd_3Ga_5O_{12}$ are compared in the experimental limiting field of 9 T. Figure 4.12 shows the comparison of the MCE for $Ln_3CrGa_4O_{12}$, $Ln_3MnGa_4O_{12}$ and $Ln_3Ga_5O_{12}$, *Ln* = Gd, Tb, Dy, Ho in the relevant field regimes. The insets show the variation of ΔS_m per mole as a function of magnetic field at $T = 2$ K. The results for $Ln_3CrGa_4O_{12}$ and $Ln_3MnGa_4O_{12}$ are discussed separately.

For *Ln* = Gd, there is a $\approx$ 25% increase in the value of ΔS_m over 2 - 20 K for $Gd_3CrGa_4O_{12}$ as compared to $Gd_3Ga_5O_{12}$. Therefore the MCE is significantly enhanced on Cr^{3+} substitution in $Gd_3Ga_5O_{12}$. $Dy_3CrGa_4O_{12}$ has the largest change in magnetic entropy over the entire temperature and field range among $Tb_3CrGa_4O_{12}$, $Dy_3CrGa_4O_{12}$ and

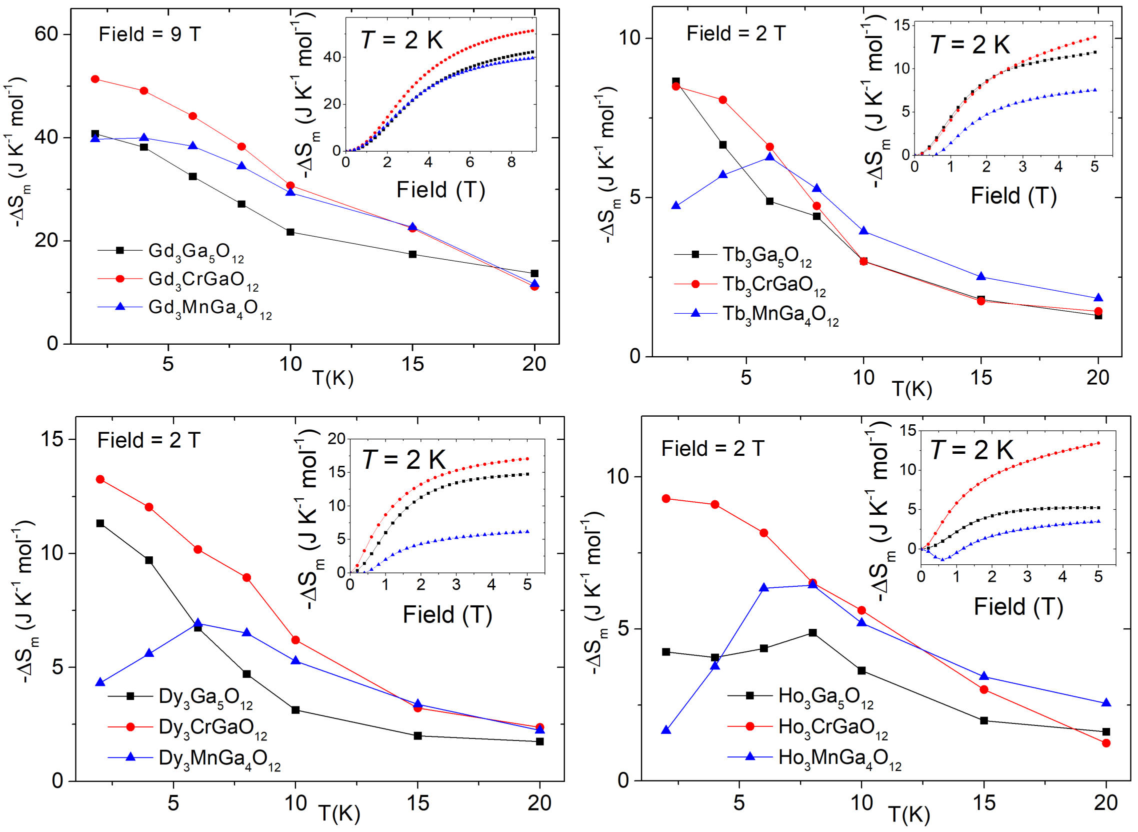

Figure 4.12 ΔS_m per mole as a function of temperature for $Ln_3CrGa_4O_{12}$ and $Ln_3MnGa_4O_{12}$ compared to $Ln_3Ga_5O_{12}$ in a field of 9 T for Ln = Gd and 2 T for Ln = Tb, Dy, Ho; insets show field dependence of ΔS_m per mole at T = 2 K. Data for $Ln_3Ga_5O_{12}$ has been taken from the previous chapter.

$Ho_3CrGa_4O_{12}$. The differences in the effect of Cr^{3+} substitution on the MCE for Ln = Tb, Dy, Ho is striking. For Ln = Tb, the difference in the MCE on Cr^{3+} substitution is minimal in low fields. However, an increase in ΔS_m is observed at fields above 2.5 T. There is a $\approx$ 20% increase in ΔS_m at 2 K, 2 T for $Dy_3CrGa_4O_{12}$. The most dramatic increase is seen for Ln = Ho where ΔS_m shows $\approx$ 120% increase for $Ho_3CrGa_4O_{12}$ compared to $Ho_3Ga_5O_{12}$ at 2 K, 2 T. Selected ΔS_m values are given in Table 4.6.

The origin of the impact of Cr^{3+} substitution on ΔS_m is likely due to changes in the magnetic ordering and nature of the magnetic ground state, indicated by the dramatic change in the magnetic frustration and enhancement of the ordering temperature for $Ln_3CrGa_4O_{12}$, Ln = Tb, Dy, Ho. For a magnetocaloric material, the maximum change in the magnetic entropy is obtained around the ordering temperature, T_0. The minimum temperature for the $\Delta S_m(T)$ calculations, 2 K, is very close to T_0 for $Ln_3CrGa_4O_{12}$ (Table 4.4) and so, an enhancement in T_0 is observed. The values of T_0 for $Ln_3CrGa_4O_{12}$ (Ln = Dy, Ho) in gravimetric units are comparable to the maximum values reported for other rare-earth transition metal systems like *Ln*CrO$_4$, *Ln*VO$_4$ (*Ln* = Dy, Ho) [296–298] and Er$_2$Mn$_2$O$_7$ [299]. However for these systems, ΔS_m is maximized at higher temperatures, $T > 20$ K, restricting their use for cooling in the liquid helium temperature regime. On the other hand, *Ln*$_3$CrGa$_4$O$_{12}$ (*Ln* = Dy, Ho) can be used as effective MCMs for $T \geq 2$ K in fields up to 2 T. Further *Ln*$_3$CrGa$_4$O$_{12}$ and *Ln*$_3$Ga$_5$O$_{12}$ (*Ln* = Dy, Ho) could be used to develop graded magnetocalorics so that the cooling limit is further reduced to $T \geq 0.4$ K ($\approx T_0$ for *Ln*$_3$Ga$_5$O$_{12}$, *Ln* = Dy, Ho).

The changes in the MCE for *Ln*$_3$MnGa$_4$O$_{12}$ are very different to *Ln*$_3$CrGa$_4$O$_{12}$ (*Ln* = Tb, Dy, Ho). There is almost no difference in the MCE for Gd$_3$MnGa$_4$O$_{12}$ as compared to Gd$_3$Ga$_5$O$_{12}$; whereas a $\approx$ 25% increase was observed for Gd$_3$CrGa$_4$O$_{12}$. An enhancement in the ΔS_m values for *Ln*$_3$MnGa$_4$O$_{12}$ (*Ln* = Tb, Dy, Ho) is observed for $T > 6$ K as compared to *Ln*$_3$Ga$_5$O$_{12}$, however the ΔS_m values decrease below this temperature restricting their use for cooling down to 2 K. The T_0 values for *Ln*$_3$MnGa$_4$O$_{12}$ (Table 4.4) are consistent with the temperature at which the peak in the $\Delta S_m(T)$ curves is obtained. The maximum magnetic entropy is extracted around this temperature leading to a decrease in ΔS_m on further cooling. Dy$_3$MnGa$_4$O$_{12}$ has the maximum value of ΔS_m at T = 6 K, 2 T (6.93 J K^{-1} mol^{-1}) among the Mn^{3+} substituted garnets with *Ln* = Tb, Dy, Ho. However, this value is only marginally higher than Dy$_3$Ga$_5$O$_{12}$ (6.74 J K^{-1} mol^{-1}) and significantly lower than Dy$_3$CrGa$_4$O$_{12}$ (10.18 J K^{-1} mol^{-1}). Therefore, Mn^{3+} substitution in *Ln*$_3$Ga$_5$O$_{12}$ (*Ln* = Tb, Dy, Ho) does not offer any significant advantages in solid state magnetic refrigeration whereas the MCE is significantly enhanced for *Ln*$_3$CrGa$_4$O$_{12}$ (*Ln* = Dy, Ho) at $T \geq 2$ K. It is unclear why the magnetic and magnetocaloric properties of *Ln*$_3$CrGa$_4$O$_{12}$ and *Ln*$_3$MnGa$_4$O$_{12}$ are so different and further experiments are required to explain this.

4.8 Conclusion

The impact of introducing additional Cr^{3+} and Mn^{3+} spins on the magnetic properties and magnetocaloric performance in lanthanide gallium garnets, *Ln* = Gd, Tb, Dy, Ho, has been studied for the first time. Polycrystalline samples of *Ln*$_3$CrGa$_4$O$_{12}$ and *Ln*$_3$MnGa$_4$O$_{12}$, *Ln* = Gd, Tb, Dy, Ho, have been prepared and the crystal structure has been determined from powder X-ray and neutron diffraction. No magnetic ordering is observed down to 0.4 K for Gd$_3$CrGa$_4$O$_{12}$ and Gd$_3$MnGa$_4$O$_{12}$. Magnetic susceptibility and heat capacity measurements reveal ordering transitions for *Ln*$_3$CrGa$_4$O$_{12}$ and *Ln*$_3$MnGa$_4$O$_{12}$, *Ln* = Tb, Dy, Ho, at temperatures much greater than that reported for the corresponding *Ln*$_3$Ga$_5$O$_{12}$. This indicates that the frustration in the *Ln*$_3$Ga$_5$O$_{12}$ lattice is relieved on magnetic ion substitution.

The ordering transitions for the magnetic ground states of $Ln_3CrGa_4O_{12}$ and $Ln_3MnGa_4O_{12}$, Ln = Gd, Tb, Dy, Ho, are summarised in Table 4.4. Calculation of the frustration index, Table 4.4, shows that the frustration is relieved by a greater extent in $Ln_3MnGa_4O_{12}$ as compared to $Ln_3CrGa_4O_{12}$ for Ln = Tb, Dy, Ho. Isothermal magnetisation measurements indicate that the isotropic nature of the Gd^{3+} spins and the single-ion anisotropy of Ln^{3+} (Ln = Tb, Dy, Ho) in $Ln_3Ga_5O_{12}$ is retained on Cr^{3+} or Mn^{3+} substitution, although subtle changes to the CEF cannot be ruled out.

Powder neutron diffraction measurements on $Ho_3MnGa_4O_{12}$ below T_N show that the Mn^{3+} moments, disordered on the octahedral site, couple ferromagnetically with the Ho^{3+} *quasi-spins* and lift the degeneracy associated with magnetic ordering in the garnet lattice. The elevation of the ordering temperature almost completely relieves the magnetic frustration – $f \approx 1$ for $Ho_3MnGa_4O_{12}$ compared to $f \approx 63$ for $Ho_3Ga_5O_{12}$. The similar results obtained for $Ln_3MnGa_4O_{12}$ (Ln = Tb, Dy) and $Ln_3CrGa_4O_{12}$ (Ln = Tb, Dy, Ho) from the bulk magnetic measurements hint at a universal mechanism for relieving the magnetic frustration in lanthanide garnets with strong single-ion anisotropy that is tuneable through control of the extent and type of magnetic ion substitution. Further neutron scattering experiments are required to determine the nature of the magnetic ground state in $Ln_3Ga_5O_{12}$, $Ln_3CrGa_4O_{12}$, Ln = Gd, Tb, Dy, Ho, and $Ln_3MnGa_4O_{12}$, Ln = Gd, Tb, Dy, in order to model the relevant magnetic interactions and examine whether there are any differences in the magnetic ground state for the different Ln and the the different magnetic substituents on the octahedral site.

Calculation of the change in magnetic entropy showed that Mn^{3+} substitution does not show any significant improvement of the MCE in $Ln_3Ga_5O_{12}$ for Ln = Gd, Tb, Dy, Ho. In contrast, Cr^{3+} substitution leads to a large enhancement in the magnetocaloric performance for Ln = Gd, Dy, Ho. For $T \geq 2$ K, $Gd_3CrGa_4O_{12}$ can be used as an improvement to $Gd_3Ga_5O_{12}$ in magnetic fields $\mu_0H \geq 5$ T while the magnetic refrigeration performance of $Ln_3CrGa_4O_{12}$, Ln = Dy, Ho, is significantly improved as compared to the corresponding $Ln_3Ga_5O_{12}$, in fields $\mu_0H \leq 2$ T.

This work provides a path to understanding the nature of frustration in lanthanide gallium garnets with additional spins on the non-magnetic cation sites and optimising their performance as functional magnetocaloric materials in the liquid helium temperature regime. It is hoped that this will motivate more detailed studies on the magnetic properties of these lanthanide garnets.

Chapter 5

Magnetic properties of lanthanide orthoborates, $LnBO_3$

This chapter discusses the magnetic and magnetocaloric properties of the lanthanide orthoborates, $LnBO_3$ for Ln = Eu, Gd, Tb, Dy, Ho, Er, Yb, where the magnetic Ln^{3+} form layers of edge-sharing triangles, a prototype of two -dimensional geometrical frustration.

5.1 Background

A two-dimensional geometrically frustrated triangular lattice (edge-sharing or kagome) can host exotic states of matter [108], such as the much sought after quantum spin liquid state [35, 69]. Work on such lattices containing magnetic Ln^{3+} has recently started gaining momentum, including investigation of the $Ln_3X_2Sb_3O_{14}$ (X = Mg, Zn) family containing two-dimensional kagome planes of magnetic Ln^{3+} and the quantum spin liquid candidate $YbMgGaO_4$ where the magnetic Yb^{3+} form edge-sharing triangles. The current state of research in these materials has been reviewed in Chapter 1. The bulk magnetic properties, $T \geq 2$ K, of the $KBaLn(BO_3)_2$ family with two-dimensional edge-sharing triangular lattices of Ln^{3+} have also been investigated recently [300]. There is a continuing search for more candidate rare-earth materials with two-dimensionally frustrated lattices that can exhibit novel magnetic properties. Such frustrated systems could also be competitive low temperature magnetocaloric materials in the liquid helium temperature regime.

Lanthanide orthoborates, $LnBO_3$, Ln = La – Lu, have been reported to crystallise in different structures depending on the size of the lanthanide ion. Levin et. al proposed that the orthoborates crystallise in the same three structures as $CaCO_3$: aragonite for the larger Ln^{3+} (La - Nd), vaterite for the smaller Ln^{3+} (Eu - Yb) and calcite for the smallest Ln^{3+} ion, Lu [301]. SmBO_3 was reported to crystallise in the vaterite phase between 1100 and 1300 °C and in a different triclinic structure at other temperatures [302, 303]. High-temperature polymorphs were reported for the aragonite type $Ln\mathrm{BO}_3$ which was corroborated by a later study [301, 302]. No polymorphism was reported for the vaterite-type borates, referred to as π-$Ln\mathrm{BO}_3$ in the literature. The optical properties of the orthoborates have been actively researched because they have several features that make them ideal candidates for applications as phosphors in vacuum discharge lamps and screens such as high ultraviolet transparency and high optical damage threshold [304–306]. However, the magnetic properties of these materials have not been explored in any detail, except for some early studies on magnetic susceptibility [307, 308].

Table 5.1 Summary of different crystal structures proposed for π-$Ln\mathrm{BO}_3$, Ln = Eu - Yb.

No.	Description of structure proposed for π-$Ln\mathrm{BO}_3$	Reference
1.	Structure reported to be pseudo-vaterite type based on similarity of PXRD pattern with CaCO_3; a phase transition into μ-$Ln\mathrm{BO}_3$ reported.	Levin et. al, Am. Mineral 46 (1961) 1030 [301]
2.	First structural model: distorted hexagonal structure with $\mathrm{BO}_3{}^{3-}$ triangles shown in Figure 5.1a.	Newnham et. al, J. Am. Ceram. Soc. 46 (1963) 253 [309]
3.	Hexagonal structure based on Newnham's model; both $\mathrm{BO}_3{}^{3-}$ triangles similar to vaterite or 3 membered rings of $\mathrm{B}_3\mathrm{O}_9{}^{9-}$ tetrahedra said to be possible.	Bradley et. al, Act. Cryst. 20 (1966) 283 [310]
4.	Single crystal data, hexagonal structure with partial occupation of B and O sites; $\mathrm{BO}_4{}^{5-}$ tetrahedra identified as main structural unit.	Chadeyron et. al, J. Solid State Chem. 128 (1997) 261 [311]
5.	Monoclinic structure with $\mathrm{B}_3\mathrm{O}_9{}^{9-}$ units, Figure 5.1b ; also reported a reversible phase transition to a high temperature monoclinic phase with $\mathrm{BO}_3{}^{3-}$ triangles, Figure 5.1c.	Lin. et. al, Chem. Mater. 16 (2004) 2418 [312]
6.	Single crystal data, monoclinic structure as reported by Lin et. al.	Pitscheider et. al, J. Solid State Chem. 184 (2011) 149 [313]

There has been much controversy about the crystal structure of the π-$Ln\mathrm{BO}_3$, Ln = Eu – Yb, summarised in Table 5.1. However, for all the reported crystal structures, the magnetic Ln^{3+} link to form layers of edge-sharing triangles. This is the exact prototype of the two-dimensional frustrated triangular lattice and hence these materials could exhibit geometrical frustration. Also, the lower molar mass of the π-$Ln\mathrm{BO}_3$ could result in higher changes in magnetic entropy in gravimetric units as compared to the lanthanide garnets discussed in the

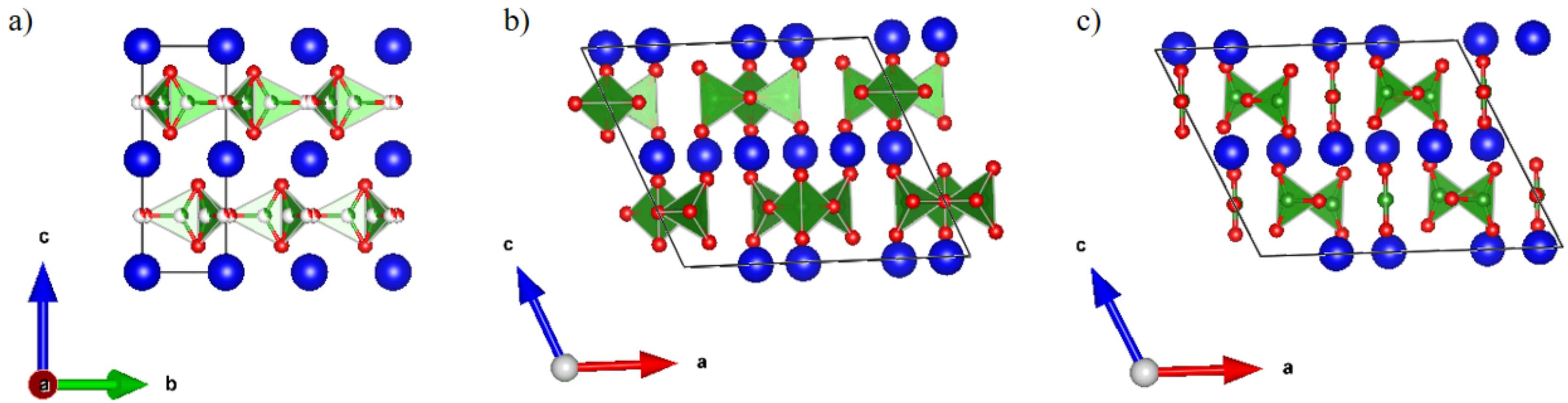

Space group: P63/mmc (hexagonal)
B-O arrangement: BO_3^{3-} triangles

Space group: C2/c (monoclinic)
B-O arrangement: 3 membered rings of $B_3O_9^{9-}$ tetrahedra

Space group: C2/c (monoclinic)
B-O arrangement: BO_3^{3-} triangles

Figure 5.1 Some of the main structural models proposed for the π-*Ln*BO$_3$ with *Ln* - blue, B - green, O - red: a) shows the distorted hexagonal structure with BO_3^{3-} triangles while b) and c) show the monoclinic structure with $B_3O_9^{9-}$ tetrahedra and BO_3^{3-} triangles respectively.

previous chapters. Thus they have the potential to serve as more efficient magnetocaloric materials in the liquid helium temperature regime. This chapter presents a systematic study of the crystal structure, bulk magnetic properties and magnetocaloric effect for the π-*Ln*BO$_3$, *Ln* = Eu, Gd, Tb, Dy, Ho, Er, Yb, for the first time.

5.2 Sample preparation

Samples of *Ln*BO$_3$ (*Ln* = Eu, Gd, Tb, Dy, Ho, Er and Yb) were prepared using a solid state synthesis method. The starting materials *Ln*$_2$O$_3$ (*Ln* = Eu, Gd) were pre-dried at 800 °C overnight prior to being weighed out in order to ensure the correct stoichiometry. Stoichiometric amounts of *Ln*$_2$O$_3$ (*Ln* = Eu, Gd, Dy, Ho, Er, Yb) or Tb_4O_7 and H_3BO_3 (5% excess added to compensate for the loss of B due to volatilisation during heating) were mixed well. A pre-reaction was carried out at 350 °C for 2 hours to allow for the decomposition of H_3BO_3. After regrinding, the samples were heated to 1000 °C for either 24 or 48 hours to obtain the final product.

*Ln*BO$_3$ samples, *Ln* = Tb, Ho, Er, Yb, for PND experiments were prepared by the same process except enriched boric acid (^{11}B) (99% purity, Sigma Aldrich) was used as starting material to reduce the absorption of neutrons from ^{10}B [221] during the experiment.

5.3 Structural characterisation

The progress of the reaction was tracked using PXRD. Initially, short scans were collected over the angular range $5° \leq 2\theta \leq 60°$ ($\Delta\, 2\theta = 0.015°$) using a Panalytical Empyrean X-ray diffractometer (Cu Kα radiation, λ = 1.541 Å). For more detailed structural analysis, high resolution scans were collected using a Bruker D8 Advance diffractometer (Cu Kα radiation, λ = 1.541 Å, Ge monochromator and Sol-XE energy dispersive detector). Measurements were carried out for one day per sample over an angular range $10° \leq 2\theta \leq 120°$ ($\Delta\, 2\theta = 0.01°$). The latter measurements were carried out by Dr Giulio Lampronti, Department of Earth Sciences, University of Cambridge. Rietveld refinements were carried out using the Fullprof suite of programs.

Phase pure polycrystalline samples of *Ln*BO$_3$, *Ln* = Eu, Gd, Tb, Dy, Ho, Er and Yb were synthesised. The PXRD pattern for $HoBO_3$ is shown in Figure 5.2. The PXRD refinements for the other *Ln*BO$_3$ can be found in Appendix A. As previously discussed, there has been much debate as to whether the crystal structure of these materials should be described by a hexagonal or monoclinic unit cell. When the Rietveld refinement was carried out, it was found that the intensities of the peaks were not correctly modelled by the hexagonal phase whereas the monoclinic phase could model the PXRD peak intensities correctly. The monoclinic structure can also be verified by a comparison of the peak shape for selected peaks as follows: Figure 5.2 inset for $HoBO_3$ shows two peaks at 20.1° and 34.1°. The former corresponds to a single reflection in both the hexagonal setting, $(002)_{hex}$, and monoclinic setting, $(002)_{mon}$, while the latter corresponds to a single reflection in hexagonal setting, $(102)_{hex}$, but two reflections in monoclinic setting, $(311)_{mon}$ and $(022)_{mon}$. The peak shape for the latter is consistent with a lower symmetry monoclinic structure. Thus according to the Rietveld refinement of the PXRD data, the structure for the π-$LnBO_3$ samples synthesised is definitely monoclinic, with space group $C2/c$.

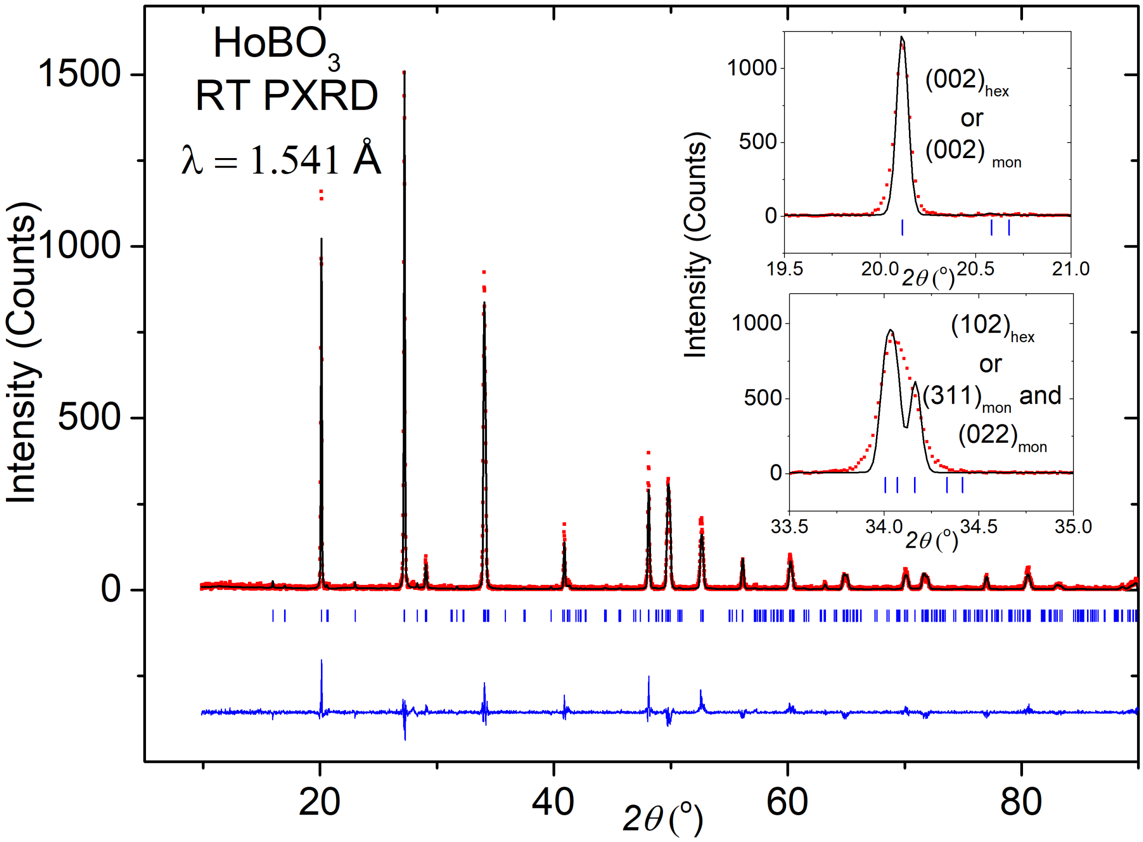

Figure 5.2 PXRD pattern for $HoBO_3$: Red dots - Experimental data, Black line - Modelled data, Blue line - Difference pattern, Blue ticks - Bragg positions; Inset: Peaks at 20.1° and 34.1° with different asymmetry. The peak at $\approx 20.1°$ corresponds to a single reflection in both hexagonal setting, $(002)_{hex}$, and monoclinic setting, $(002)_{mon}$. The peak at $\approx 34.1°$ corresponds to a single reflection in hexagonal setting, $(102)_{hex}$, but two reflections in monoclinic setting, $(311)_{mon}$ and $(022)_{mon}$. When the peak shape parameters are set to the instrumental resolution file values, the peak at $\approx 20.1°$ can be fitted to a single peak with the reflection $(002)_{mon}$ while the peak at $\approx 34.1°$ can only be fitted to two peaks with reflections $(311)_{mon}$ and $(022)_{mon}$, confirming the monoclinic phase.

Parameters from the structural Rieveld refinements are given in Table 5.2. In the PXRD Rietveld refinement, the *Ln* positions were refined but the B and O positions were kept fixed to the values reported in the literature [306, 312, 313] for the monoclinic structure. This is because PXRD is not sensitive to B and O in the presence of *Ln* with significantly higher atomic numbers. There are two *Ln* sites: *Ln*1 occupies the 4*c* site (0.25, 0.25, 0) while *Ln*2 occupies the general $8f$ (x, y, z) position. There are also two B sites: B1 at the general $8f$ (x, y, z) site and B2 at the 4*e* site (0, *y*, 0.25). There are 5 possible O positions: O1, O2, O3, O4 all occupy the general $8f$ (x, y, z) position while O5 occupies the 4*e* site (0, *y*, 0.25). The B and O positions were kept fixed to the following values: B1 = (0.12011, 0.03790, 0.24691), B2 = (0, 0.67520, 0.25), O1 = (0.12550, 0.09200, 0.10199), O2 = (0.22293, 0.09316, 0.38870), O3 = (0.04837, 0.56643, 0.39233), O4 = (0.39142, 0.30823, 0.25174) and O5 = (0, 0.135, 0.25). The values of thermal parameters were kept fixed at B_{iso} = 0.8 Å^2 for all atoms. The lattice parameters *a*, *b*, *c*, the in-plane area and the lattice volume for the monoclinic $\mathit{Ln}BO_3$ all follow a linear relationship with the ionic radii of the lanthanide ions. This is shown in Figure 5.3.

The crystal structure for the π-$\mathit{Ln}BO_3$ is shown in Figure 5.4. The structural model used for Rietveld refinement assumes that the triangular Ln^{3+} layers are separated by sheets of three membered-rings of corner sharing $BO_4{}^{5-}$ tetrahedra forming isolated $B_3O_9{}^{9-}$ units. The Ln^{3+} layers are found to be eclipsed meaning that they stack directly on top of one another [108].

The bond-lengths of the Ln^{3+} triangles are now considered. For a hexagonal structure, the magnetic Ln^{3+} would have formed flat layers of edge-sharing equilateral triangles, forming an ideal two-dimensional frustrated lattice. However, the structure has monoclinic symmetry and the triangles have unequal bond lengths, Table 5.2, resulting in a distorted triangular lattice. There are three different sets of triangles comprising six different bond lengths as is shown in Figure 5.5. The triangular layers also have a slight pucker resulting in two different interlayer *Ln*-*Ln* distances, *Ln*1-*Ln*2 and *Ln*2-*Ln*2. The distortion compared to the ideal triangular lattice can be quantified in terms of the deviation in bond angles compared to an ideal equilateral triangle. Figure 5.6 shows the deviation for a particular triangle for the different π-$\mathit{Ln}BO_3$. The deviation is identical for all three sets of triangles as shown in Figure 5.7. All the deviations are $< 1.5\%$. However, in other materials with frustrated triangular lattices, even very small distortions in the two-dimensional triangular lattice have been shown to radically impact the magnetic properties such as in $KFe(MoO_4)_2$ [314], $CuFeO_2$ [315], α-$CaCr_2O_4$ [316] and α-$SrCr_2O_4$ [317].

Table 5.2 Crystal structure parameters for monoclinic $Ln\mathrm{BO}_3$, Ln = Eu, Gd, Tb, Dy, Ho, Er, Yb, from PXRD refinements, space group $C2/c$.

Ln	Eu	Gd	Tb	Dy	Ho	Er	Yb
a (Å)	11.5288(13)	11.4968(6)	11.4299(4)	11.3755(3)	11.3357(4)	11.2911(3)	11.2006(2)
b (Å)	6.6678(7)	6.6402(3)	6.6037(2)	6.5757(3)	6.5502(2)	6.5236(2)	6.47250(14)
c (Å)	9.7121(7)	9.6796(4)	9.6408(2)	9.6092(3)	9.5776(2)	9.5475(2)	9.4901(2)
β (°)	113.081(5)	113.048(5)	112.945(2)	112.919(2)	112.930(2)	112.914(2)	112.8116(2)
Volume (Å^3)	686.83(12)	679.96(6)	670.11(3)	662.04(4)	654.95(3)	647.76(2)	634.18(2)
χ^2	2.11	1.12	1.04	1.39	1.55	1.54	1.41
$Ln2$							
x	0.08310(2)	0.0816(15)	0.0811(8)	0.0826(12)	0.0819(6)	0.0851(3)	0.0839(4)
y	0.2576(2)	0.25282(19)	0.25387(8)	0.25351(10)	0.25405(5)	0.25280(5)	0.25346(5)
z	0.4896(2)	0.49251(13)	0.49894(11)	0.49614(14)	0.49743(8)	0.50038(6)	0.49993(6)
Ln –Ln (in-plane)(Å)							
1	3.851(5)	3.84(2)	3.789(11)	3.798(15)	3.772(8)	3.782(5)	3.740(5)
2	3.83(5)	3.82(3)	3.853(15)	3.78(3)	3.792(11)	3.727(6)	3.720(8)
3	3.86(14)	3.846(14)	3.845(7)	3.812(10)	3.808(5)	3.772(4)	3.752(4)
4	3.82(4)	3.81(2)	3.746(10)	3.762(14)	3.728(7)	3.753(5)	3.704(6)
5	3.83(4)	3.814(14)	3.801(7)	3.772(10)	3.761(5)	3.741(4)	3.713(4)
6	3.89(5)	3.88(2)	3.836(10)	3.842(14)	3.821(7)	3.816(5)	3.782(6)
$< Ln - Ln >$ (in-plane)(Å)	3.85	3.84	3.81	3.79	3.78	3.76	3.73
Ln –Ln (inter-plane) (Å)							
1	4.28(3)	4.32(3)	4.420(16)	4.36(3)	4.365(12)	4.394(6)	4.372(9)
2	4.56(2)	4.52(2)	4.449(12)	4.460(15)	4.434(9)	4.405(9)	4.375(6)
$< Ln - Ln >$ (inter-plane) (Å)	4.42	4.42	4.43	4.41	4.40	4.41	4.37

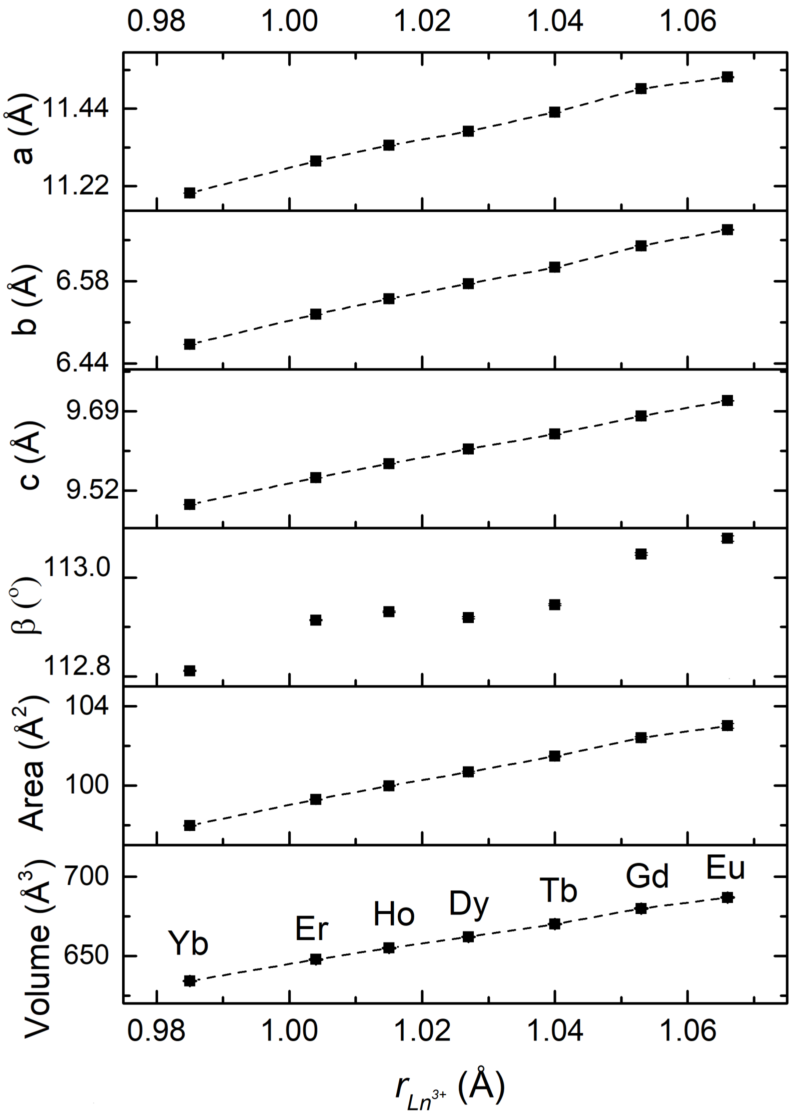

Figure 5.3 Lattice parameters as a function of ionic radii for monoclinic *Ln*BO$_3$; *Ln* = Eu, Gd, Tb, Dy, Ho, Er, Yb. The different plots show lattice parameters a, b, c, β, planar area = $ac\sin\beta$ and cell volume = $abc\sin\beta$. Lines are a guide to the eye. Error bars are smaller than size of symbols.

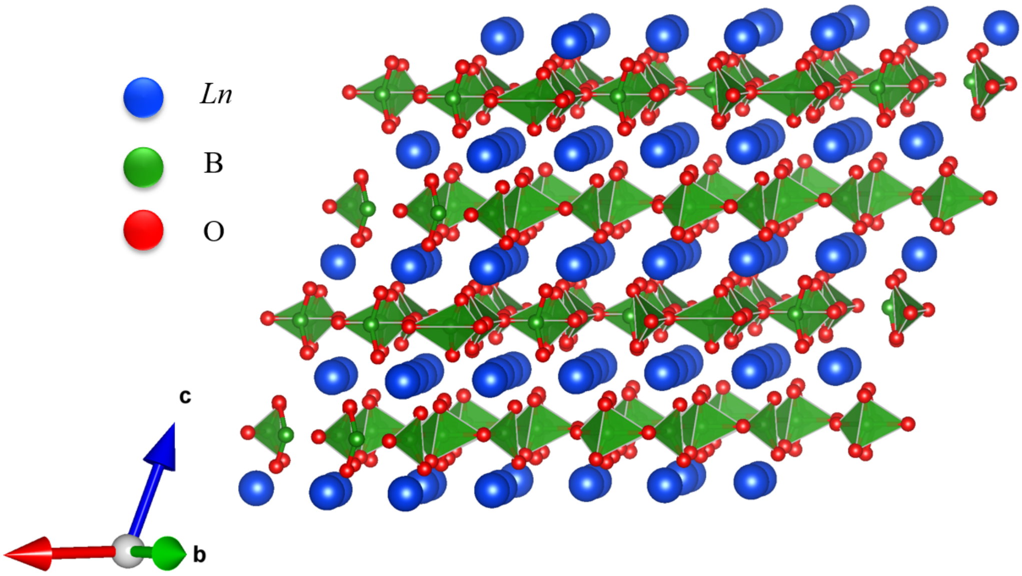

Figure 5.4 Crystal structure for monoclinic LnBO$_3$ with triangular sheets of Ln^{3+} separated by layers of $B_3O_9{}^{9-}$ units.

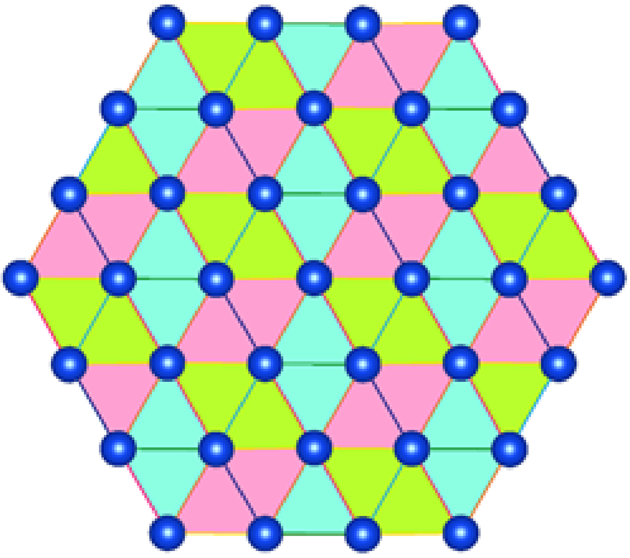

Figure 5.5 Connectivity of magnetic Ln^{3+} in monoclinic LnBO$_3$ showing three different kinds of edge-sharing triangles. The different colours represent different bond lengths.

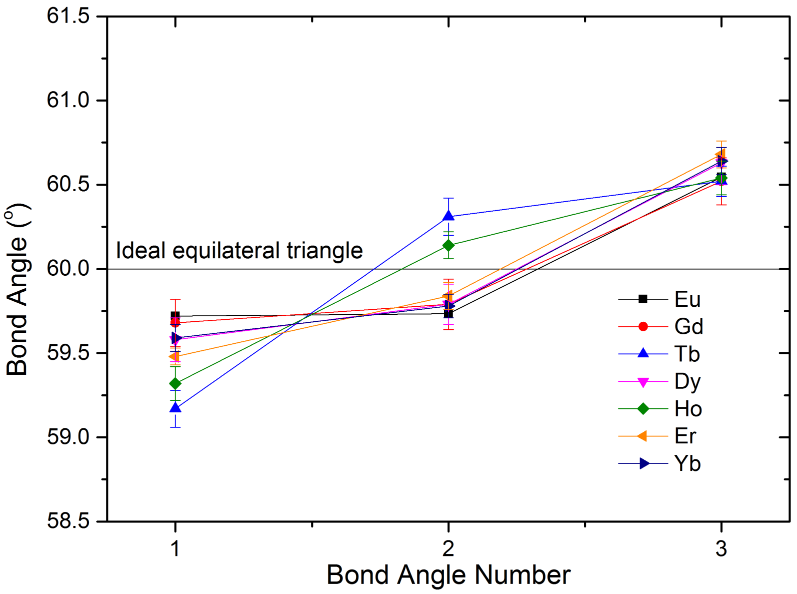

Figure 5.6 Bond angles for a triangle in monoclinic *Ln*BO$_3$; *Ln* = Eu, Gd, Tb, Dy, Ho, Er, Yb. For all the samples, the bond angles show deviations from an ideal equilateral triangle; the maximum % distortion is less than 1.5%.

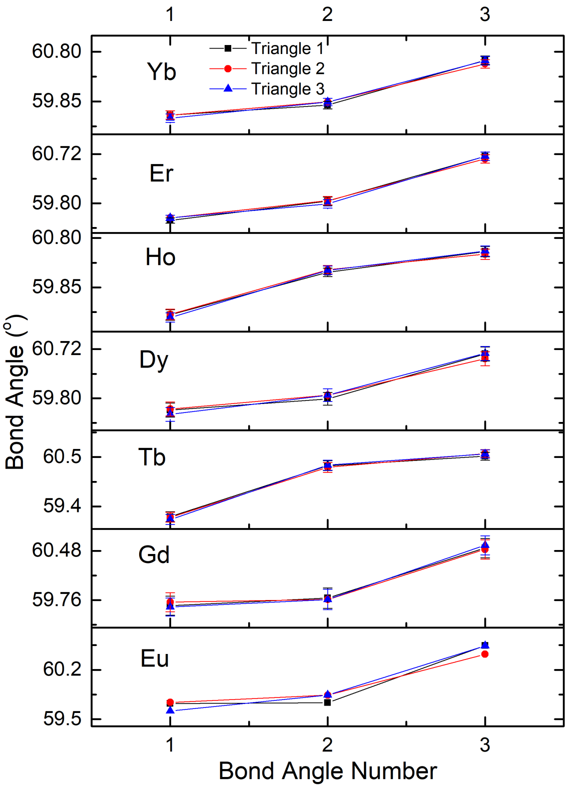

Figure 5.7 Bond angles for the three triangles for monoclinic *Ln*BO$_3$; *Ln* = Eu, Gd, Tb, Dy, Ho, Er, Yb. The deviations for the three sets of triangles are identical.

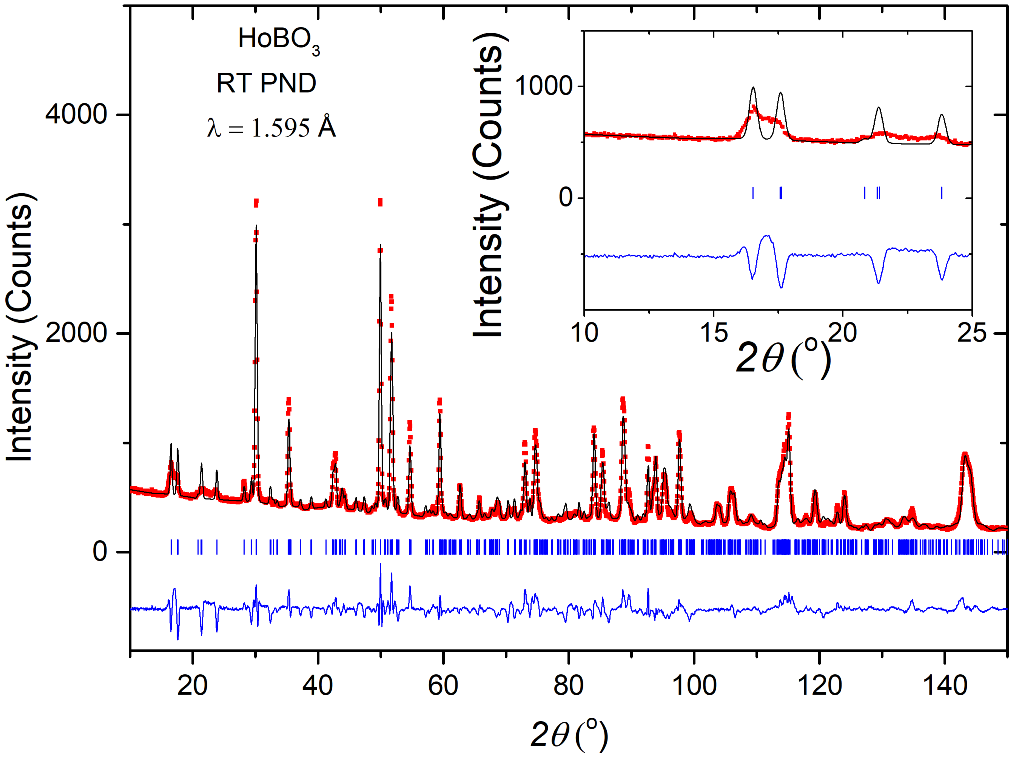

Figure 5.8 PND pattern for $HoBO_3$: Red dots - Experimental data, Black line - Modelled data, Blue line - Difference pattern, Blue ticks - Bragg positions; inset shows a zoomed-in plot highlighting the significant peak broadening observed in the PND data.

Although the monoclinic unit cell could be confirmed, the B and O positions could not be determined accurately from PXRD alone in presence of the Ln^{3+} with high atomic numbers. Room temperature PND experiments were carried out on the D2B instrument (λ = 1.595 Å) at ILL, Grenoble for LnBO$_3$, Ln = Tb, Ho, Er, Yb, with the aim of determining the crystal structure more accurately.

An attempt at a PND Rietveld refinement for $HoBO_3$ is shown in Figure 5.8. The refinement is consistent with the monoclinic unit cell. However, significant peak broadening is observed which cannot be captured by the standard size or strain models available in the Fullprof suite of programs. As this is a layered structure, the peak broadening may be caused by disorder or stacking faults in the layers. Significant peak broadening in PND (Figure 5.8) combined with the absence of the same in PXRD (Figure 5.2) implies that such disorder is present only in the borate framework for the π-LnBO$_3$ and there is no significant disorder in the registry of the magnetic Ln^{3+}. In the previous PND study by Lin.et. al [312], no such peak broadening was reported. This could be due to the difference in resolution of the neutron diffractometers used to collect the PND data or variations in sample preparation methods.

The disorder in the borate framework is possibly due to the breaking of some of the 3-membered rings of $B_3O_9{}^{9-}$ tetrahedra either completely into isolated $BO_3{}^{3-}$ triangles, as reported for the high temperature structure by Lin. et. al [312], or partially into a trigonal $BO_3{}^{3-}$ group and a unit comprising two $BO_4{}^{5-}$ tetrahedra, as reported for the high pressure phase, χ-*Ln*BO$_3$ [318]. Modelling either of these disordered structures has proved to be very complex because the disorder is restricted to the borate layers and the arrangement of the magnetic *Ln*$^{3+}$ layers has to be kept unchanged to be consistent with the PXRD. An attempt was made to refine the PND data using a structural model where the monoclinic unit cell was kept unchanged and both the $B_3O_9{}^{9-}$ and $BO_3{}^{3-}$ groups were incorporated by varying the occupancies. This did not give any improvement in the Rietveld refinement, indicating that the rings of $B_3O_9{}^{9-}$ tetrahedra may not be disintegrating completely into trigonal $BO_3{}^{3-}$ groups and the situation is most likely the one described for χ-*Ln*BO$_3$. However, developing a structural model poses a challenge because the χ-*Ln*BO$_3$ structure is triclinic and so the B positions are different. Triclinic subgroups of the monoclinic structure were examined to see if this was more appropriate to describe the structure but no improvement in the Rietveld fit was observed. An ongoing collaboration with Dr. Jared Allred, Department of Chemistry and Biochemistry, University of Alabama, to resolve the structural distortion using the existing PXRD and PND data has yet to realise a satisfactory structural model. Further work including measurements on single crystals is required to resolve the structural model for the π-*Ln*BO$_3$.

5.4 Bulk magnetic measurements

5.4.1 Magnetic susceptibility

The zero-field cooled (ZFC) susceptibility for all the monoclinic *Ln*BO$_3$ was measured in a field of 100 Oe in the temperature range 2 - 300 K using a Quantum Design MPMS. This is shown in Figure 5.9a. $\chi(T)$ is approximated by the linear relation, equation (1.22), because in a low field of 100 Oe, the $M(H)$ curve is linear at all temperatures. HoBO$_3$ shows a feature at T = 6 K; no ordering is observed down to 2 K for the other *Ln*BO$_3$. EuBO$_3$ shows van-Vleck paramagnetism due to thermal population of low-lying excited states, consistent with earlier reports [319]. The reciprocal susceptibility, Figure 5.9b, is linear at temperatures $>$ 100 K except for EuBO$_3$ which shows van Vleck paramagnetism. Fits to the Curie-Weiss law, equation (1.59), were carried out in different temperature regimes from 100 - 300 K. The average values were taken to calculate the experimental magnetic moment, μ_{eff} and the Curie-Weiss temperature, θ_{CW}. YbBO$_3$ shows significant temperature-independent paramagnetism χ_0 and so the Curie-Weiss fit was carried out in the low temperature range, 2 – 30 K, as has

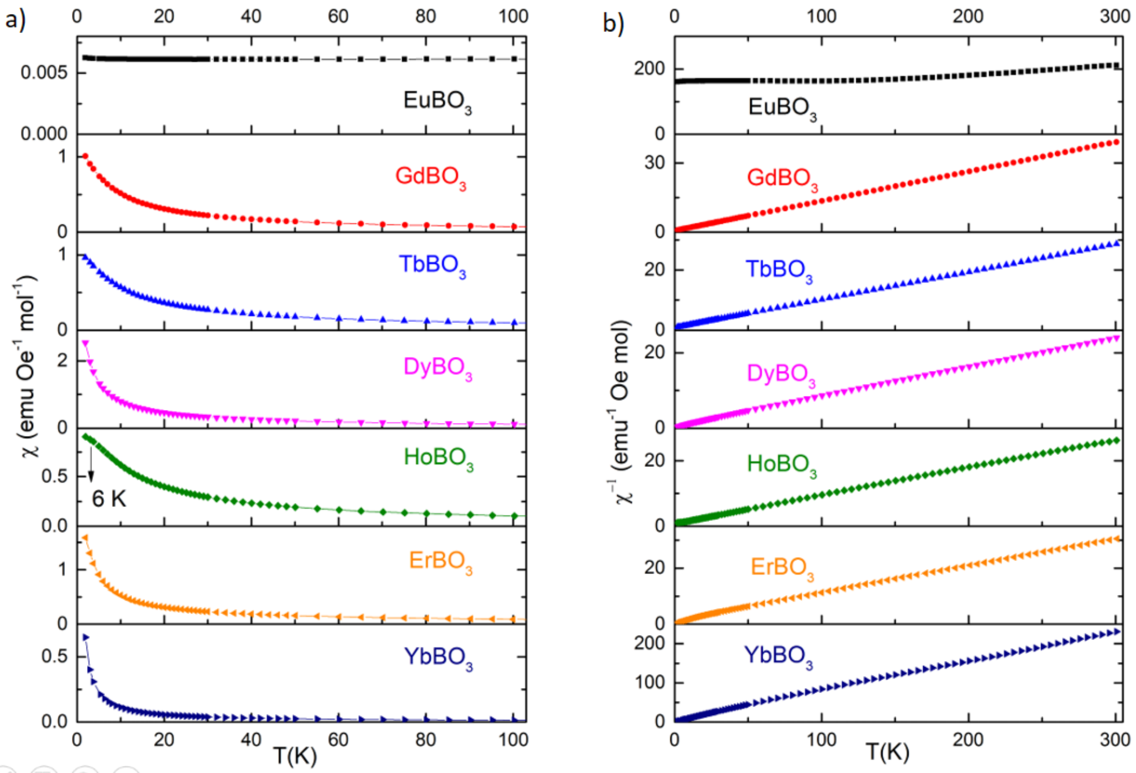

Figure 5.9 a) ZFC $\chi(T)$ from 2 - 300 K and b) Reciprocal of the molar susceptibility, $\chi^{-1}(T)$ for monoclinic *Ln*BO$_3$; *Ln* = Eu, Gd, Tb, Dy, Ho, Er, Yb.

been reported for other frustrated Yb^{3+} oxide systems [159, 269, 300, 320]. The Curie-Weiss parameters are summarised in Table 5.3. The values of μ_{eff} are found to be consistent with the theoretical values. The negative values of θ_{CW} indicate net antiferromagnetic interactions in the monoclinic *Ln*BO$_3$.

5.4.2 Isothermal magnetisation

Isothermal magnetisation measurements at selected temperatures in the field range, μ_0H = 0 – 9 T were carried out for all samples using the ACMS option on a Quantum Design PPMS. The $M(H)$ curves for the monoclinic *Ln*BO$_3$ are shown in Figure 5.10. EuBO$_3$ shows a completely linear $M(H)$ curve at all temperatures from 2 - 100 K, consistent with previous reports for Eu^{3+} systems [117, 118, 300]. GdBO$_3$ saturates in a field of 9 T at 2 K and the maximum value = 6.6 μ_B/f.u is consistent with the theoretical saturation magnetisation for Gd^{3+} Heisenberg spins given by $g_J J = 2 \cdot \frac{7}{2}$ = 7 μ_B/f.u. *Ln*BO$_3$, *Ln* = Tb, Dy, Ho, Er, do not show any signs of saturation in a field of 9 T. However the values of maximum magnetisation at 2K, 9T, M_{max}, given in Table 5.3, are consistent with previous reports for

Table 5.3 Parameters from bulk magnetic measurements for monoclinic LnBO$_3$; Ln = Gd, Tb, Dy, Ho, Er, Yb. In case of three-dimensional antiferromagnetic ordering, T_0 is the Néel temperature, T_N.

Compound	Theor. μ_{eff} (μ_B)	Expt. μ_{eff} (μ_B)	θ_{CW} (K)	T_0 (K)	f	Theor. M_{sat} (μ_B/f.u.)	M_{max} 2 K, 9T (μ_B/f.u.)
GdBO$_3$	7.94	7.904(4)	-5.4(2)	0.61, 1.72	3.1	7.0	6.6
TbBO$_3$	9.72	9.35(2)	-11.0(7)	2.02	5.5	9.0	4.6
DyBO$_3$	10.65	10.19(2)	-11.8(6)	0.56, 1.01	11.7	10.0	5.2
HoBO$_3$	10.61	9.73(5)	-14(2)	-	-	10.0	4.8
ErBO$_3$	9.58	9.12(3)	-18(1)	0.88	20.4	9.0	4.1
YbBO$_3$	4.54	3.058(8)	-0.28(9)	< 0.4	> 0.7	4.0	1.7

other geometrically frustrated oxides containing these magnetic ions that show substantial single-ion anisotropy [269].

5.4.3 Heat capacity

Zero field heat capacity (HC) measurements for LnBO$_3$, Ln = Gd, Tb, Dy, Ho, Er, Yb, were carried out using the He3 heat capacity option on a Quantum Design PPMS in the temperature range 0.4 – 20 K to investigate the existence of any magnetic ordering transitions for $T > 0.4$ K, which could not be determined from the standard MPMS measurements. In order to improve the thermal conductivity at low temperatures, the powders were mixed with approximately equal amounts of silver powder (99.99%, Alfa Aesar). The contribution of the silver powder to the heat capacity was then deducted using values published in the literature [243] to obtain the contribution to the heat capacity from the sample only. The lattice contribution was subtracted using a Debye model (equation 2.37) with Debye temperatures in the range 260 - 360 K to get the magnetic contribution C_{mag}. Figure 5.11 shows the plot of C_{mag}/T vs T in zero field from 0.4 – 20 K for LnBO$_3$, Ln = Gd, Tb, Dy, Ho, Er, Yb.

GdBO$_3$ shows two sharp ordering transitions at 0.61 K and 1.72 K; so does DyBO$_3$ at 0.56 and 1.01 K. ErBO$_3$ shows a single λ type transition at 0.88 K. No ordering for YbBO$_3$ is seen down to 0.4 K, however the sharp increase in the magnetic heat capacity at 0.4 K indicates onset of a magnetic ordering transition. Measurements at $T < 0.4$ K are required to determine the nature of the transition. A single broad feature is seen for TbBO$_3$ at 2.02 K while for HoBO$_3$, a very broad feature is seen at 6 K, consistent with the susceptibility

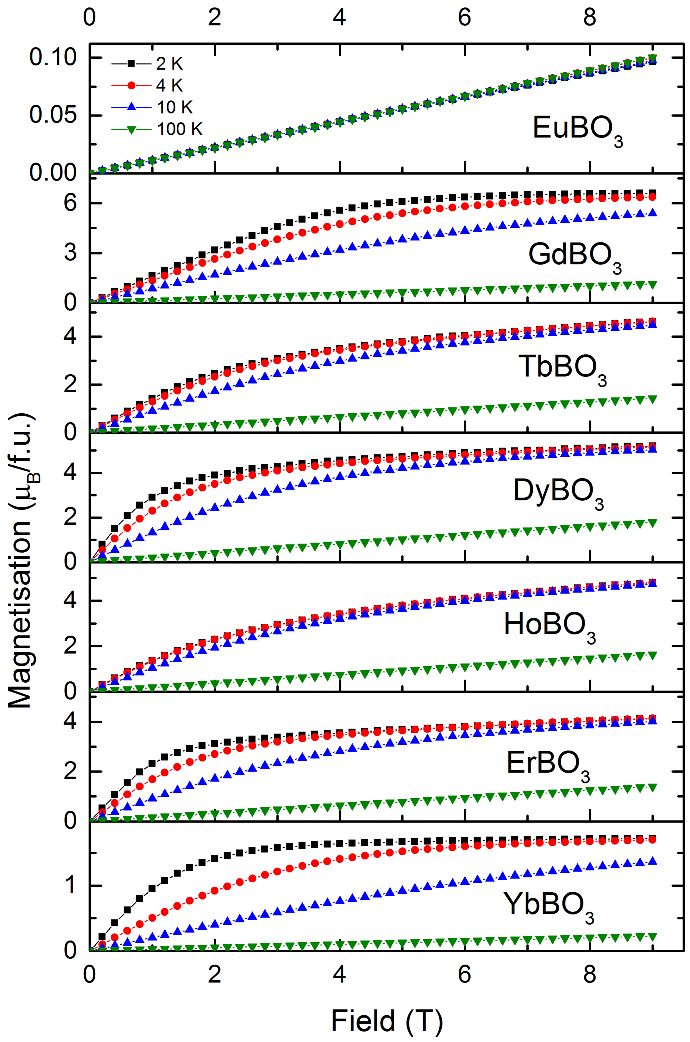

Figure 5.10 Isothermal magnetisation for monoclinic *Ln*BO$_3$; *Ln* = Eu, Gd, Tb, Dy, Ho, Er and Yb, at selected temperatures in the magnetic field range 0 - 9 T.

measurements. As has been reported for other Ho^{3+} compounds [270, 321, 322], the upturn in the heat capacity for HoBO$_3$ can be attributed to the nuclear Schottky anomaly for Ho^{3+} which dominates the heat capacity at temperatures below 1 K .

5.5 Low temperature powder neutron diffraction

5.5.1 HoBO$_3$

Low temperature powder neutron diffraction measurements, $T \geq 1.5$ K, were carried out for HoBO$_3$ on the D1B diffractometer, ILL, Grenoble to see if the feature observed at 6 K in the

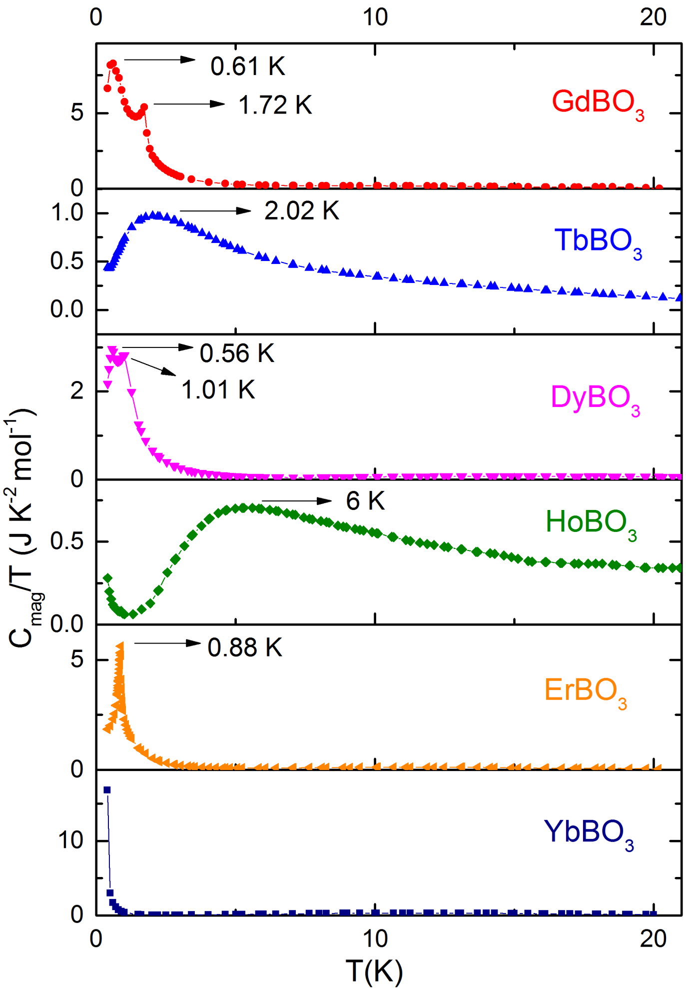

Figure 5.11 Magnetic heat capacity C_{mag}/T vs T in zero field from 0.4 – 20 K for *Ln*BO$_3$; *Ln* = Gd, Tb, Dy, Ho, Er, Yb.

magnetic susceptibility and heat capacity was due to any kind of magnetic ordering. As shown in Figure 5.12, there is no evidence for any long range or short range magnetic order down to 1.5 K. A similar result was obtained for the frustrated double perovskite Ba$_2$HoSbO$_6$, where the Ho^{3+} ions lie on a fcc lattice: No magnetic Bragg or diffuse scattering was observed down to 0.06 K in neutron scattering data. Inelastic neutron scattering revealed a non-magnetic doublet ground state with the magnetic moment having an expectation value of zero. The magnetic susceptibility had a significant van Vleck contribution due to thermal population of excited states [323]. Therefore it is proposed that HoBO$_3$ also has a non-magnetic ground state and the broad feature in the magnetic susceptibility and heat capacity is due to van Vleck paramagnetism. However, inelastic neutron spectroscopy and crystal electric field calculations are required to explicitly confirm this hypothesis.

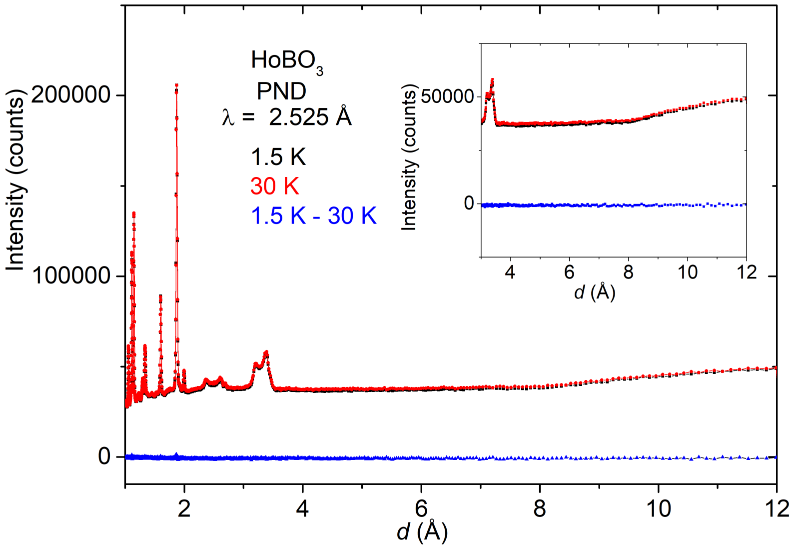

Figure 5.12 PND pattern for $HoBO_3$ on D1B, ILL at 1.5 K and 30 K and the difference plot; inset shows a zoomed-in plot of the same data in the high *d* spacing range; there is a complete absence of magnetic Bragg or diffuse scattering.

5.5.2 $TbBO_3$

For $TbBO_3$, low temperature powder neutron diffraction measurements, $T \geq 1.5$ K, were carried out on the WISH diffractometer, ISIS, Oxfordshire by Dr Pascal Manuel. A broad feature is observed at high *d* spacing indicative of short-range magnetic ordering, Figure 5.13, consistent with the broad feature in the zero field heat capacity at 2.02 K, Figure 5.11. The dimensions of the sample can and mass of the sample had not been recorded and so, a proper absorption correction could not be carried out. Hence it was not possible to perform further quantitative analysis of the short range ordering.

5.6 Discussion

Polycrystalline samples of π-$LnBO_3$, *Ln* = Eu, Gd, Tb, Dy, Ho, Er, Yb, have been prepared and their structure has been evaluated using PXRD and PND. They crystallise in a monoclinic structure with the Ln^{3+} forming layers of edge-sharing triangles separated by the borate layers. The PND data (sensitive to *Ln*, B, O) shows substantial peak broadening while the PXRD measurements (sensitive to *Ln*) show none, indicating a disordered structure. The PND structural refinements are not consistent with any of the previously reported structures from PXRD [309], single crystal XRD [311, 313] or PND [312] described in Table 5.1. While PXRD is not sensitive to B and O, the difference with the previously reported PND data could

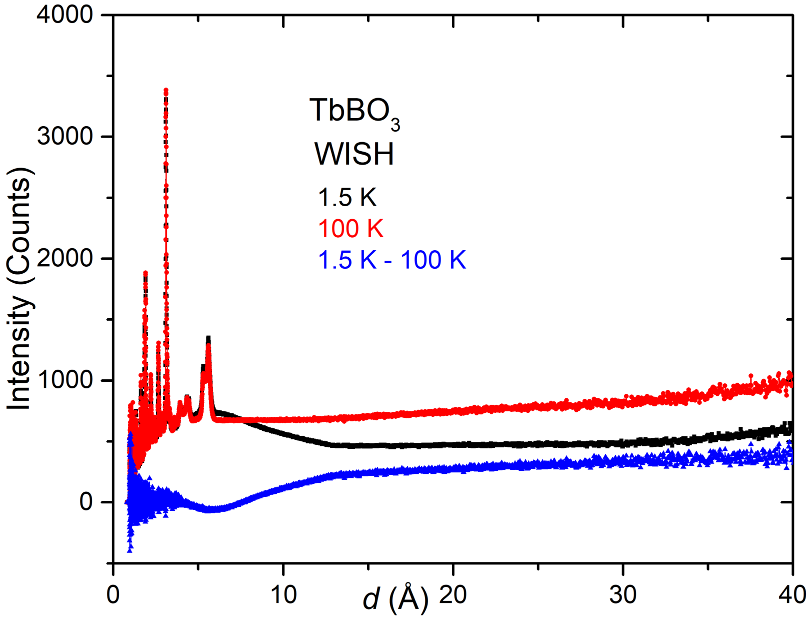

Figure 5.13 PND pattern for TbBO_3 on WISH, ISIS at 1.5 K and 100 K and the difference plot; strong magnetic diffuse scattering is seen at higher d spacing.

be due to difference in the resolution of the instruments used to collect the data or differences in sample preparation methods. The Ln^{3+} triangular lattice is also slightly distorted which indicates that the *Ln*-*Ln* intra-layer interactions may be disordered. Given the small distortion, this is likely to be a weak effect but it still may have a significant impact on the magnetic properties.

The bulk magnetic properties of the π-$Ln\mathrm{BO}_3$ are reported for the first time. The nature of magnetic ordering and the degree of frustration are different for the various $Ln\mathrm{BO}_3$. As has been reported for other frustrated lanthanide oxide systems like the tripod kagome lattices [119] and pyrochlores [45], it is proposed that the variations in magnetic ordering are due to differences in the magnetic interactions and crystal electric field effects. Further, lattice distortions could also be an important factor contributing to the differences in magnetic properties.

The frustration index f has been calculated according to the criterion proposed by Ramirez, equation (1.63), for $Ln\mathrm{BO}_3$, Ln = Gd, Tb, Dy, Er. f is not calculated for HoBO_3 as it has a non-magnetic ground state while a lower limit, $f > 0.7$, is determined for YbBO_3. As seen from Table 5.3, $Ln\mathrm{BO}_3$, Ln = Tb, Dy, Er can be considered to be geometrically frustrated.

The $M(H)$ curves indicate Heisenberg spins for GdBO_3 and substantial single-ion anisotropy for $Ln\mathrm{BO}_3$, Ln = Tb, Dy, Ho, Er, Yb. Of these, YbBO_3 saturates at 2K, 9T: the maximum value, 1.7 μ_B/f.u is close to $M_{sat}/2$. This value is consistent with that observed for other triangular lattice systems like $YbMgGaO_4$ [157] and $KBaYb(BO_3)_2)$ [300] and may indicate Ising nature of Yb^{3+} spins. The $M(H)$ curves for *Ln*BO_3, *Ln* = Tb, Dy, Ho, Er do not saturate in the limiting field of 9 T. However, the M_{max} values at 2 K, 9 T are close to $M_{sat}/2$, the value expected for powder averaged Ising spins [269].

The observation of two magnetic ordering features, as in $GdBO_3$ and $DyBO_3$, has been observed in other frustrated Heisenberg systems like $SrGd_2O_4$ [128], $Gd_2Ti_2O_7$ [49] as well as for Ising systems including $Ca_3Co_2O_6$ [324], $CoNb_2O_6$ [325] and $SrHo_2O_4$ [139]. In these systems, the transition at lower temperature is usually due to reorientation of spins, but further experiments are required to determine the origin of the magnetic ordering in $GdBO_3$ and $DyBO_3$. The sharp λ type anomaly in $ErBO_3$ points to three-dimensional antiferromagnetic ordering, as has been reported for $SrEr_2O_4$ [134] while the short-range ordering in $TbBO_3$ is reminiscent of short-range magnetic correlations reported for members of the $SrLn_2O_4$ family [127, 131, 139].

Further neutron diffraction experiments and theoretical modelling of the relevant interactions are needed to understand the fundamental magnetic behaviour of the monoclinic *Ln*BO_3. Inelastic neutron scattering experiments are required to determine the CEF and ascertain the nature of the single-ion anisotropy for *Ln*BO_3, *Ln* = Tb, Dy, Ho, Er, Yb.

5.7 Magnetocaloric effect

The magnetocaloric performance of the monoclinic *Ln*BO_3 (except *Ln* = Eu) is analysed in the liquid helium temperature regime, $T \geq 2$ K. $EuBO_3$ exhibits negligible change in magnetic entropy (the isothermal magnetisation curves at different temperatures coincide) and hence is excluded from this discussion. The change in magnetic entropy ΔS_m per mole was calculated from the $M(H)$ curves using Maxwell's thermodynamic relation, equation (1.64). As discussed in the previous chapters, Heisenberg systems perform better as magnetocaloric materials in high fields, $\mu_0 H \geq 5$ T, while materials with substantial single-ion anisotropy are better suited for use in lower fields, $\mu_0 H \leq 2$ T. Similar behaviour is observed here (Figure 5.14) and so, the MCE of $GdBO_3$ is considered in the experimentally limiting field of 9 T and the MCE of *Ln*BO_3, *Ln* = Tb, Dy, Ho, Er, Yb are considered in a field of 2 T. In addition to ΔS_m per mole, ΔS_m per unit mass and per unit volume has also been calculated as this is more relevant for practical applications. The ΔS_m values at 2 K are given in Table 5.4 and compared to the standard MCMs, GGG and DGG, discussed in previous chapters for fields of 9 T and 2 T respectively. At 2 K, 9 T the ΔS_m value of $GdBO_3$ in gravimetric units ($57.8\,\mathrm{J\,K^{-1}\,kg^{-1}}$) shows an increase of 38.1% as compared to $Gd_3Ga_5O_{12}$ ($41.8\,\mathrm{J\,K^{-1}\,kg^{-1}}$)

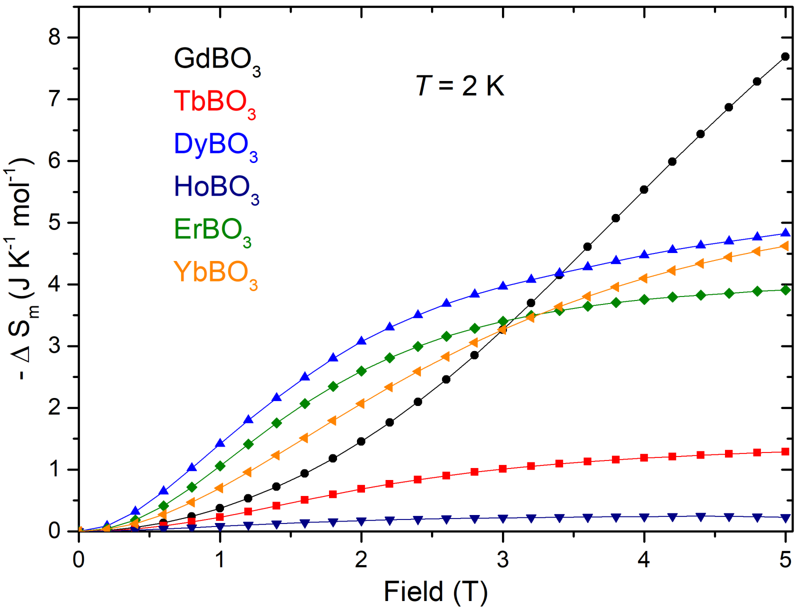

Figure 5.14 ΔS_m (J K^{-1} mol$_{Ln}^{-1}$) for the monoclinic *Ln*BO$_3$, *Ln* = Gd, Tb, Dy, Ho, Er, Yb in the field range $\mu_0 H = 0 - 5$ T at $T = 2$ K. It is seen that in fields $\mu_0 H \leq 2$ T, attainable by a permanent magnet, DyBO$_3$ has the highest magnetocaloric performance whereas in fields $\mu_0 H > 3.5$ T, GdBO$_3$ surpasses all the other *Ln*BO$_3$ as a magnetocaloric material.

while at 2 K, 2 T, the ΔS_m value for DyBO$_3$ (13.9 J K^{-1} kg^{-1}) is 26.4% greater than that of Dy$_3$Ga$_5$O$_{12}$ (11.0 J K^{-1} kg^{-1}). In Figure 5.15, the MCE of DyBO$_3$ and Dy$_3$Ga$_5$O$_{12}$ are shown in low fields ≤ 2 T, while the MCE of GdBO$_3$ and Gd$_3$Ga$_5$O$_{12}$ are compared in high fields ≥ 5 T.

Table 5.4 MCE in monoclinic *Ln*BO$_3$, *Ln* = Gd, Tb, Dy, Ho, Er, Yb at $T = 2$ K.

Compound	Field (T)	ΔS_m (J K^{-1} mol$_{Ln}^{-1}$)	ΔS_m (J K^{-1} kg^{-1})	ΔS_m (mJ K^{-1} cc^{-1})
GdBO$_3$	9	12.5	57.8	366.3
Gd$_3$Ga$_5$O$_{12}$ (GGG)	9	14.1	41.8	296.4
TbBO$_3$	2	0.7	3.2	20.8
DyBO$_3$	2	3.1	13.9	92.5
HoBO$_3$	2	0.2	0.9	6.1
ErBO$_3$	2	2.6	11.5	80.0
YbBO$_3$	2	2.1	9.1	66.0
Dy$_3$Ga$_5$O$_{12}$ (DGG)	2	3.8	11.0	80.6

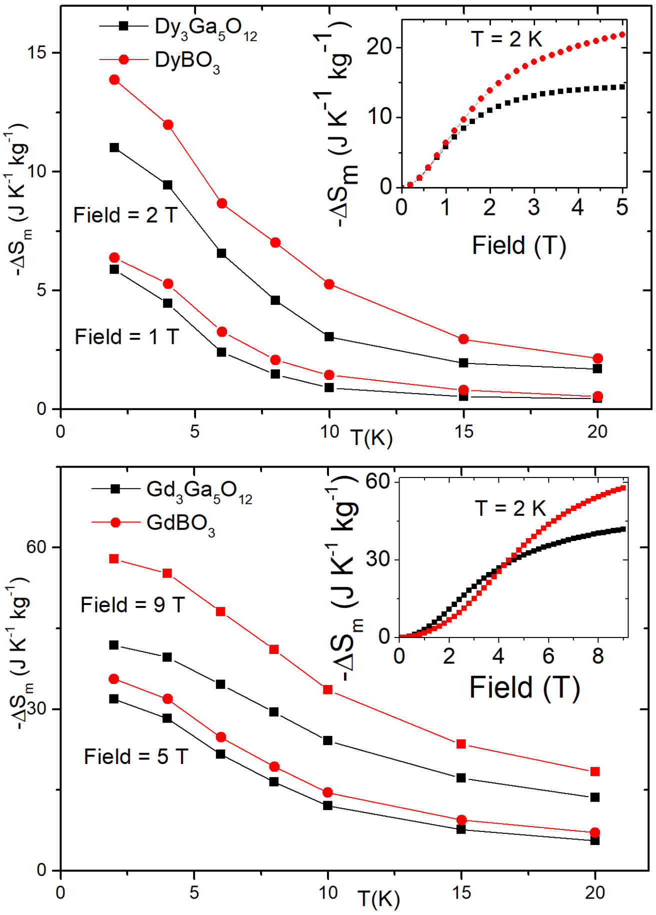

Figure 5.15 Change in magnetic entropy ΔS_m per unit mass for a) $DyBO_3$ compared to DGG in magnetic fields of 1 T and 2 T. b) $GdBO_3$ compared to GGG in magnetic fields of 5 T and 9 T.

The magnetocaloric performance of LnBO$_3$ is now compared to other low temperature magnetocaloric materials. In recent years, several other Gd^{3+} MCMs have been reported which have high MCE in high magnetic fields [185, 189–191, 193, 194]. However, for practical applications, different Ln^{3+} containing compounds can be viable low temperature MCMs in lower fields, up to 2 T [201, 297, 298] (also see Chapters 3 and 4). The MCE in $GdBO_3$ and $DyBO_3$ in gravimetric units, Table 5.4, are comparable to or greater than these materials. The origin of the competitive MCE per unit mass can be explained by considering the low mass per mole Ln ion in LnBO$_3$ ($\approx$ 218 g/mol$_{Ln}$) compared to other MCMs $Ln_3Ga_5O_{12}$ ($\approx$ 340 g/mol$_{Ln}$), LnPO$_4$ ($\approx$ 255 g/mol$_{Ln}$), LnCrO$_4$ ($\approx$ 273 g/mol$_{Ln}$), LnVO$_4$ ($\approx$ 276 g/mol$_{Ln}$) and Ln(HCOO)$_3$ ($\approx$ 295 g/mol$_{Ln}$). Also, LnBO$_3$ possess the advantage of a low temperature scalable synthesis; this is significant for practical usage. Most importantly, the existence of magnetic ordering transitions for both $GdBO_3$ and $DyBO_3$

below 2 K implies that they would suitable for cooling to temperatures below 2 K as further magnetic entropy can be extracted. Moreover mixed lanthanide orthoborates, $Ln_xLn'_{(1-x)}\mathrm{BO}_3$ could be developed in order to tune the MCE in different temperature and field regimes, as has been reported for other lanthanide oxide systems [201]. GdBO_3 and DyBO_3 are therefore competitive magnetocaloric materials in the liquid helium temperature regime.

5.8 Conclusion

Powder samples of a series of lanthanide orthoborates $Ln\mathrm{BO}_3$, Ln = Eu, Gd, Tb, Dy, Ho, Er and Yb, have been synthesised. PXRD and PND measurements have been carried out to resolve the crystal structure which has been the subject of much debate. PXRD shows that they crystallise in a monoclinic structure where the magnetic Ln^{3+} form a two-dimensional triangular lattice with slight deviations from ideal equilateral triangles ($< 1.5\%$) while PND shows the presence of significant disorder in the borate layers which has not been reported previously. While the arrangement of the Ln^{3+} layers could be determined, the exact arrangement of the borate layers remains an open question.

The bulk magnetic properties of $Ln\mathrm{BO}_3$, Ln = Eu, Gd, Tb, Dy, Ho, Er and Yb, are reported for the first time. Zero field heat capacity measurements reveal different magnetic transitions at $T \leq 2$ K for $Ln\mathrm{BO}_3$, Ln = Gd, Tb, Dy, Er, while the onset of magnetic ordering can be seen for YbBO_3 at 0.4 K. HoBO_3 is postulated to have a non-magnetic ground state. Isothermal magnetisation measurements have revealed different single-ion anisotropies for the various Ln^{3+}. Evaluation of the MCE shows that DyBO_3 and GdBO_3, are viable magnetocaloric materials in the liquid helium temperature regime in fields ≤ 2 T achievable using a permanent magnet and higher magnetic fields > 5 T respectively.

The monoclinic lanthanide orthoborates, Ln = Eu, Gd, Tb, Dy, Ho, Er, Yb, serve as a prototype of a slightly distorted frustrated rare-earth triangular lattice and exhibit many interesting magnetic properties. A more detailed investigation of the magnetic ground states in these materials will provide insight into the physics of two-dimensionally frustrated triangular lattices containing magnetic Ln^{3+}.

Chapter 6

Magnetic properties of lanthanide metaborates, $Ln(BO_2)_3$

The previous chapter had discussed the lanthanide borates, $LnBO_3$, with a slightly distorted edge-sharing triangular lattice of magnetic Ln^{3+} in two dimensions. This chapter discusses the magnetic and magnetocaloric properties of the lanthanide metaborates, $Ln(BO_2)_3$, Ln = Pr, Nd, Gd, Tb where the magnetic Ln^{3+} form one-dimensional chains, leading to the possibility of observing exotic magnetic properties associated with low-dimensional magnetism and frustrated interactions.

6.1 Background

Ideal one-dimensional magnetic materials do not show any long-range ordering [326] but in most real materials, there is some inter-chain coupling which leads to magnetic ordering in three dimensions. Such quasi one-dimensional magnetic materials can also exhibit frustration due to competition between nearest-neighbour and next nearest-neighbour interactions or the stacking arrangement of the magnetic chains in the lattice, giving rise to exotic magnetic behaviour such as field-induced transitions, multiple magnetisation plateaux and incommensurate magnetic structures [39]. A well-known example of such exotic behaviour is a spin-Peierls transition in $CuGeO_3$ where the linear Heisenberg Cu^{2+} spin chains transform to a system of dimerised (alternating) chains due to spin-phonon coupling [327]. Another example is a unique quantum critical point in the quasi one-dimensional Ising ferromagnet $CoNb_2O_6$ [207] with the underlying symmetry described by the E8 Lie group, the highest order symmetry group known in mathematics. Other examples include incommensurate spin correlations in quantum spin liquid $LiCuSbO_4$ [328], soliton excitations in CoV_2O_6 [329] and an order-order transition from a spin density wave (SDW) structure to commensurate antiferromagnetic (CAFM) structure in $Ca_3Co_2O_6$ [324].

Quasi one-dimensional systems containing magnetic lanthanide ions have not been explored in detail. However, recent studies on the magnetic properties of the lanthanide formates, *Ln*(HCOO)$_3$, have revealed one-dimensional chains of magnetic Ln^{3+} stacked to form a triangular lattice [201, 330]. Neutron scattering experiments carried out on Tb(HCOO)$_3$ reported the onset of magnetic ordering at 1.6 K, ascribed to one-dimensional ferromagnetic order along the chains, analogous to the triangular Ising antiferromagnet [330]. The lanthanide formates were also reported to be viable magnetocalorics in the temperature range 4 - 10 K, as an alternative to cooling using liquid helium [189, 201].

From the example of lanthanide formates, it would be reasonable to anticipate that other materials containing one dimensional chains of magnetic lanthanide ions could exhibit exotic magnetic properties and also show enhanced magnetocaloric performance in the liquid helium temperature regime. Lanthanide metaborates, *Ln*(BO_2)$_3$ are a family of materials that have been studied for their applications in phosphors [331–333]. They have been reported to crystallise in two structures depending on the size of the Ln^{3+} ion: an ambient pressure monoclinic phase for *Ln* = La – Tb and a high pressure orthorhombic phase for *Ln* = Tb – Er [303, 334–336]. When the arrangement of the magnetic Ln^{3+} in the reported monoclinic crystal structure for the *Ln*(BO_2)$_3$ is considered, it is found that the magnetic Ln^{3+} form chains in the structure (Figure 6.1). Thus the lanthanide metaborates, *Ln*(BO_2)$_3$, could be a rare example of a Ln^{3+} quasi-one-dimensional magnetic system but their magnetic properties have not been investigated previously. This chapter presents a study of the structure, magnetic and magnetocaloric properties of *Ln*(BO_2)$_3$, *Ln* = Pr, Nd, Gd, Tb.

6.2 Sample preparation

Samples of *Ln*(BO_2)$_3$ (*Ln* = Pr, Nd, Gd, Tb) were synthesised using a ceramic method by weighing out and mixing stoichiometric amounts of Ln_2O_3 (*Ln* = Nd, Gd) (99.999% Alfa Aesar), Pr_6O_{11} (99.999% Alfa Aesar), or Tb_4O_7 (99.999% Alfa Aesar) and H_3BO_3 (99.99% Alfa Aesar) A 50% excess of H_3BO_3 was added to compensate for the loss of B due to volatilisation during heating. Ln_2O_3 (*Ln* = Nd, Gd) and Pr_6O_{11} were pre-dried at 800 °C prior to being weighed out. The initial heating was carried out at 350 °C for 2 hours to enable decomposition of H_3BO_3. After regrinding, the samples were heated between 800 °C and 900 °C in air for 48 to 192 hours with intermediate regrindings. The reaction was considered to be complete when the impurity peaks in the PXRD did not change on heating.

The samples of *Ln*(BO_2)$_3$ (*Ln* = Pr, Nd, Tb) for PND experiments were prepared by the same synthesis method. In place of H_3BO_3, enriched boric acid (^{11}B) (99% purity, Sigma Aldrich) was used as starting material in order to reduce the absorption from ^{10}B [221] in the neutron beam.

Preparation of *Ln*(BO_2)$_3$ (*Ln* = Dy, Ho, Er) by the same method was unsuccessful. For *Ln* = Dy, a mixture of *Ln*(BO_2)$_3$ and *Ln*BO_3 was obtained and for *Ln* = Ho and Er, only the *Ln*BO_3 phase was obtained. The synthesis attempts were discontinued because it was concluded that the monoclinic phase cannot be obtained for *Ln*(BO_2)$_3$ (*Ln* = Dy, Ho, Er) by this method. A successful synthesis of the orthorhombic phase of *Ln*(BO_2)$_3$, *Ln* = Dy - Er, has been reported in the literature using high pressure methods [336]. This indicates that the monoclinic phase is not stable under ambient pressure conditions for *Ln*(BO_2)$_3$, *Ln* = Dy - Er.

6.3 Structural characterisation

PXRD was used to confirm formation of the desired products. Initially, in order to track the progress of the reaction, short scans were collected over $10^\circ \leq 2\theta \leq 60^\circ$ ($\Delta\, 2\theta = 0.015^\circ$) using a Bruker D8 X-ray diffractometer (Cu Kα radiation, λ = 1.540 Å). Once a sufficiently pure sample was obtained, longer scans for 2 hours over a wide angular range $10^\circ \leq 2\theta \leq 90^\circ$ ($\Delta\, 2\theta = 0.01^\circ$) were collected on the same diffractometer for more detailed structural analysis. Room temperature (RT) PND measurements were carried out on the D2B diffractometer, ILL, Grenoble (λ = 1.595 Å) for *Ln*(BO_2)$_3$ (*Ln* = Pr, Nd, Tb) for more precise structural determination.

Using previous structural reports as a starting point [335, 337, 338], a combined Rietveld refinement of the RT PND and PXRD data for *Ln*(BO_2)$_3$, *Ln* = Pr, Nd, Tb was used to refine the crystal structure. Gd has a very high absorption cross-section [221], due to which it was not possible to carry out RT PND and so, the structure was refined using only the PXRD data for Gd(BO_2)$_3$. The appropriate scattering length for enriched boron [221] was used for the PND Rietveld refinement. The primary motivation for collecting the high resolution D2B PND data was the sensitivity of PND to the B and O positions. Thus, very accurate information about the crystal structure was obtained from the combined Rietveld refinements. The thermal parameters, B_{iso}, and B and O positions were kept fixed to the values reported in the literature for Gd(BO_2)$_3$ as the refinement was only carried out using PXRD. Figure 6.2 shows the combined PXRD + PND refinement for Pr(BO_2)$_3$ and the crystal structure parameters for all the monoclinic *Ln*(BO_2)$_3$ are given in Table 6.1. The combined RT PXRD

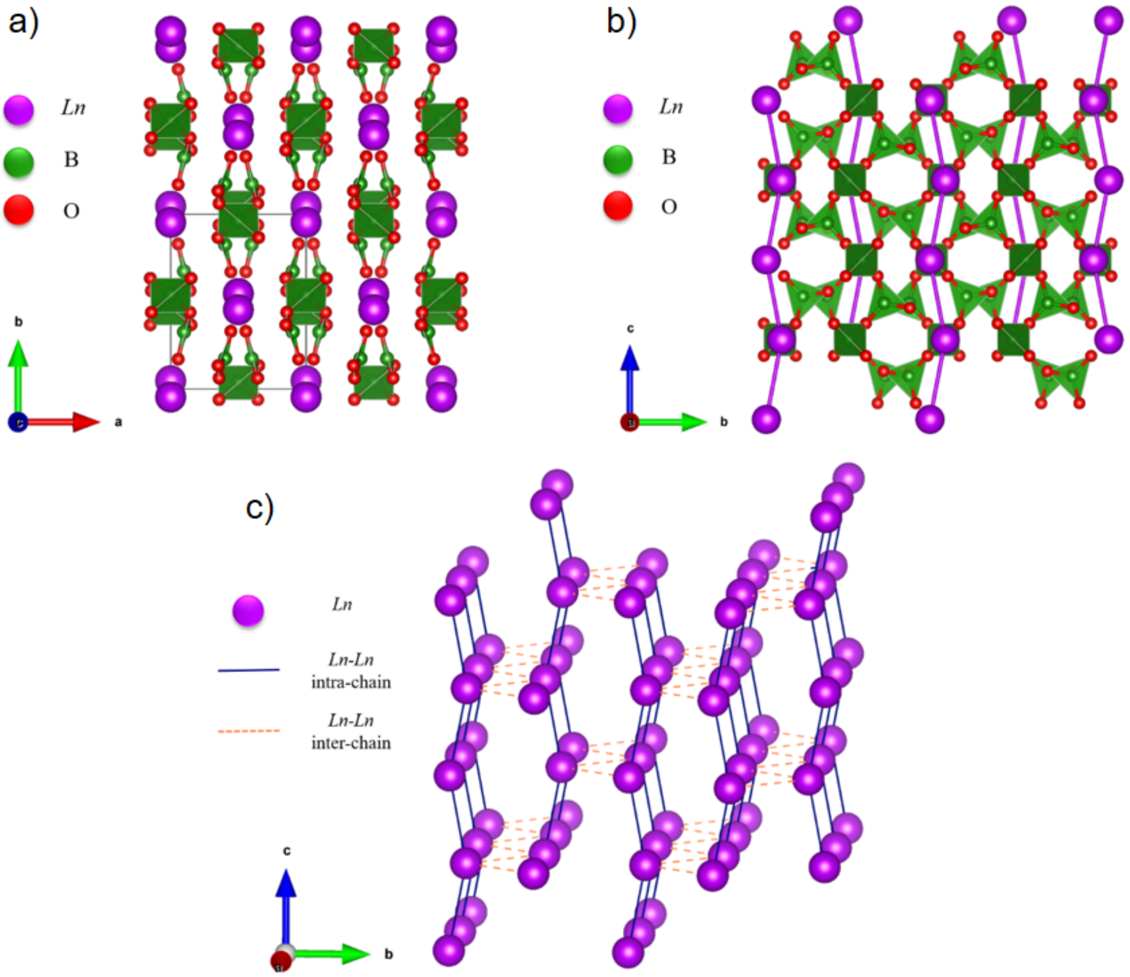

Figure 6.1 General crystal structure for monoclinic $Ln(BO_2)_3$: a) Ribbons of borate groups consisting of BO_4^{5-} tetrahedra and BO_3^{3-} triangles propagate along *c* axis. b) Magnetic Ln^{3+} form one-dimensional chains between these ribbons. c) Considering inter-chain dipolar interactions along with intra-chain interactions, the magnetic Ln^{3+} form a distorted three dimensional honeycomb lattice.

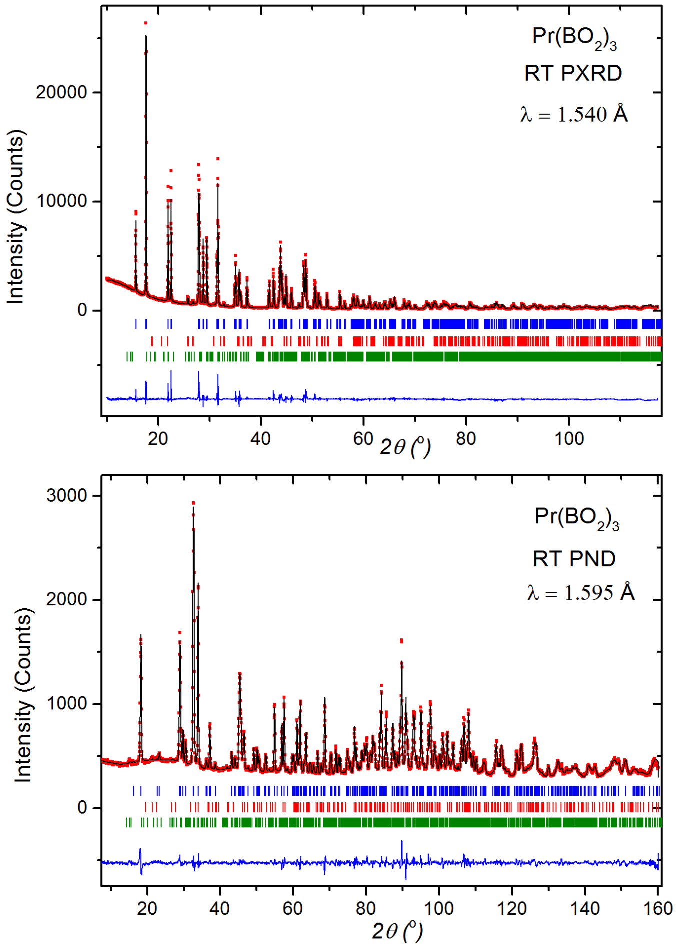

Figure 6.2 Room temperature PXRD and PND pattern for $Pr(BO_2)_3$: Red dots - Experimental data, Black line - Modelled data, Blue line - Difference pattern, Blue ticks - Bragg positions; for $Pr(BO_2)_3$, Red ticks - Bragg positions for $PrBO_3$, Green ticks - Bragg positions for H_3BO_3.

+ PND refinements for $Nd(BO_2)_3$ and $Tb(BO_2)_3$ and RT PXRD refinement for $Gd(BO_2)_3$ can be found in Appendix A.

The *Ln*$(BO_2)_3$, *Ln* = Pr, Nd, Gd, Tb, crystallise in a monoclinic unit cell with the space group $C2/c$. The structure consists of ribbons of borate units with alternating corner sharing $BO_3{}^{3-}$ triangles and $BO_4{}^{5-}$ tetrahedra that propagate along the *c* axis, shown in Figure 6.1a. The magnetic Ln^{3+} ions form one-dimensional chains between the ribbons, shown in Figure 6.1b. If the interactions between chains are considered, the arrangement of the Ln^{3+} ions is more complicated: they form a distorted three-dimensional honeycomb lattice, this is shown in Figure 6.1c.

Table 6.1 Crystal structure parameters for monoclinic $Ln(BO_2)_3$, Ln = Pr, Nd, Gd, Tb, space group $C2/c$. Structural parameters have been determined from combined PXRD + PND refinements for Ln = Pr, Nd, Tb and PXRD for Ln = Gd.

Ln		Pr	Nd	Gd	Tb
a (Å)		6.41249 (3)	6.37043 (6)	6.25159 (5)	6.21781 (5)
b (Å)		8.09827 (6)	8.07975 (9)	8.02602 (9)	8.02564 (6)
c (Å)		7.90730 (5)	7.88632 (9)	7.82649 (8)	7.80659 (4)
β (°)		93.7129 (5)	93.6935 (7)	93.6292 (8)	93.3723 (4)
Volume (Å^3)		409.765 (5)	405.078 (7)	391.909 (7)	388.889 (6)
χ^2		5.71	5.00	4.05	3.51
R_{wp}		3.58	3.32	5.72	2.66
Ln: 4e (0, y, ¼)	y	0.0501 (2)	0.0499 (2)	0.0464 (2)	0.04500 (13)
B_{iso} (Å^2)		0.61 (5)	1.55 (3)	0.5	0.76 (5)
B1: 4e(0, y, ¼)	y	0.4714 (4)	0.4699 (5)	0.4590	0.4728 (4)
B_{iso} (Å^2)		0.41 (4)	0.53 (8)	0.5	1.37 (8)
B2: 8f (x,y,z)	x	0.1074 (2)	0.1066 (5)	0.09800	0.1095 (2)
	y	0.31665 (18)	0.3164 (3)	0.32600	0.3137 (2)
	z	0.5249 (2)	0.5256 (4)	0.52100	0.5248 (2)
B_{iso} (Å^2)		0.183 (23)	0.23 (5)	0.5	0.135 (21)
O1: 8f (x,y,z)	x	0.1414 (2)	0.1430 (5)	0.15045	0.1493 (3)
	y	0.3629 (2)	0.3605 (4)	0.36671	0.3621 (2)
	z	0.3578 (2)	0.3571 (4)	0.35116	0.3553 (2)
B_{iso} (Å^2)		0.52 (3)	0.58 (5)	0.5	0.97 (3)
O2: 8f (x,y,z)	x	0.1395 (3)	0.1407 (5)	0.14316	0.1455 (2)
	y	0.4366 (2)	0.4362 (4)	0.43845	0.4351 (3)
	z	0.6480 (3)	0.6480 (4)	0.64816	0.6508 (3)
B_{iso} (Å^2)		0.70 (3)	0.47 (5)	0.5	0.75 (5)
O3: 8f (x,y,z)	x	0.0479 (3)	0.0491 (5)	0.05526	0.0522 (4)
	y	0.1617 (3)	0.1601 (5)	0.17006	0.1582 (4)
	z	0.5472 (3)	0.5476 (5)	0.55122	0.5434 (4)
B_{iso} (Å^2)		0.18 (2)	0.93 (7)	0.5	1.30 (7)
$LnBO_3$ wt %		1.3 (4)	1.8 (4)	0.4 (5)	1.8 (3)
H_3BO_3 wt %		0.56 (14)	1.8 (2)	-	0.90 (14)
$Ln-Ln$ (intra-chain) (Å)		4.0347 (4)	4.0241 (5)	3.9838 (5)	3.9696 (4)
$Ln-Ln$ (inter-chain) (Å)		4.5565 (14)	4.537 (2)	4.521 (2)	4.5269 (15)
Ln –O1 (Å)		2.602(3) × 2	2.580(4) × 2	2.472(9) × 2	2.489(4) × 2
		2.801(3) × 2	2.781(4) × 2	2.832(9) × 2	2.815(4) × 2
Ln–O2 (Å)		2.568(3) × 2	2.548(4) × 2	2.477 (9) × 2	2.457(6) × 2
Ln –O3 (Å)		2.383(4) × 2	2.364(5) × 2	2.373(10) × 2	2.330(4) × 2
		2.520(4) × 2	2.510(4) × 2	2.561(10) × 2	2.467(4) × 2
$<Ln$-O$>$ (Å)		2.575	2.557	2.543	2.512

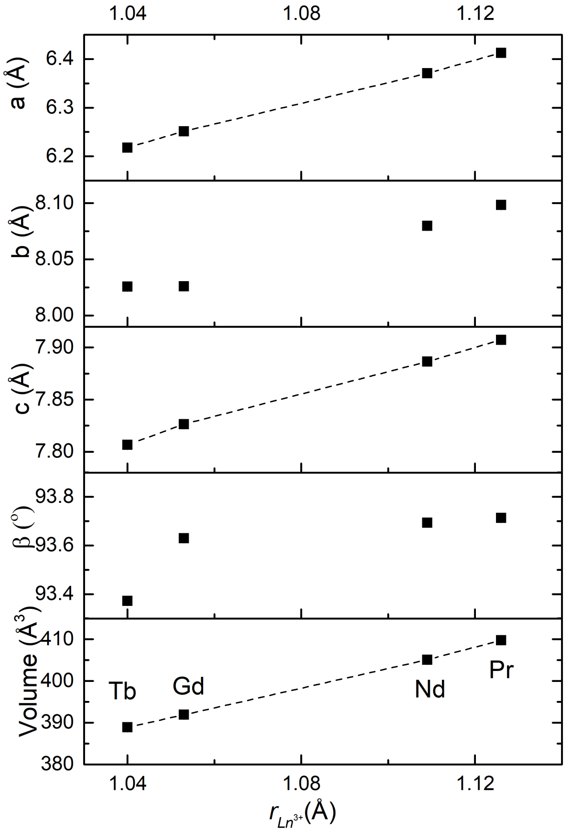

Figure 6.3 Lattice parameters for $Ln(BO_2)_3$, Ln = Pr, Nd, Gd, Tb, as a function of Ln^{3+} ionic radii. Lines are given as a guide to the eye. Error bars are smaller than size of symbols.

The structural parameters for $Ln(BO_2)_3$, Ln = Pr, Nd, Gd, Tb, are consistent with previous reports. The lattice parameters a and c vary linearly with the Ln^{3+} ionic radii while small deviations in the linear trend are observed for b and β, Figure 6.3. However the deviations in b and β compensate for each other and overall, the lattice volume given by $V = abc\sin\beta$ shows a linear variation with the Ln^{3+} ionic radii.

In order to investigate the existence of any structural transition for $Pr(BO_2)_3$, measurements were carried out at 3.5 K and 12 K using a cryocooler on D2B, ILL, Grenoble. Low temperature PXRD measurements were carried out for $Pr(BO_2)_3$ at 12 K using an Oxford Cryosystems PheniX stage. This was so that a combined (PXRD+PND) structural Rietveld refinement at 12 K could be carried out. The PND patterns showed no changes in peak positions or intensities between 3.5 K and 12 K. Hence only the structural refinements at room temperature and 12 K were compared. A decrease in the lattice parameters and slight shifts in the atomic positions (Table 6.2) were observed but the monoclinic crystal structure was found to be retained on cooling. The changes in the Pr-Pr and Pr-O bond lengths were negligible within error and so these are not tabulated separately. It can be concluded that there is no structural transition below room temperature in $Pr(BO_2)_3$, consistent with previous literature, where no structural transition has been reported for $Ln(BO_2)_3$, Ln = Pr, Nd, Gd at low temperatures [303].

According to previous reports, $Tb(BO_2)_3$ undergoes a structural transition around 150 K to a different monoclinic phase [303, 339]. In order to investigate this possibility, low temperature PND data for $Tb(BO_2)_3$ was collected on the WISH diffractometer, ISIS, Oxfordshire using a standard cryostat at 2, 3, 5, 10, 50, 100 and 150 K and low temperature PXRD scans at 12, 50, 100, 150, 200 and 300 K were collected using the Oxford Cryosystems PheniX stage on a Bruker D8 diffractometer. On cooling below 150 K, clear changes in intensities and additional peaks are observed which can be indexed with the reported low temperature structure for $Tb(BO_2)_3$. The additional peaks are more clearly distinguishable in the PXRD pattern. However, contrary to previous structural reports where a complete structural transition is reported [303, 339], the PXRD data collected shows coexistence of the room temperature and low temperature phase at temperatures below 150 K in a ratio of approximately 3.75:1 by weight. No structural model could account for all the structural peaks and both phases needed to be considered. The ratio of the two structural phases remains unchanged as the sample is cooled. No additional structural changes were noted between 2 K and 150 K and only slight changes in lattice parameters and positions on cooling were observed. The structural parameters for the combined PXRD + PND refinements at 100 K and 300 K for the room temperature (RT) monoclinic phase are compared in Table 6.3 while the parameters for the low temperature (LT) monoclinic crystal structure are given in Table 6.4.

Figure 6.4 shows the RT and LT structural modifications of $Tb(BO_2)_3$. The LT structure can be visualised as resulting from a spontaneous shear of the RT phase in the *ac* plane [339]. Comparisons between the phases are seen more clearly by viewing the RT structure along *c* and LT structure along *a* directions respectively (the LT structure is in a different monoclinic setting and so the convention for the crystallographic axes is different). The B-O coordination and connectivity of the borate groups in the two structures is similar, Figures 6.4a and 6.4b, but the coordination of the Tb ions is different, Figures 6.4c and 6.4d. In the RT phase there is an (8+2) coordination with oxygen with eight Tb-O distances less than 2.5 Å and two longer Tb-O bonds while in the LT phase, the coordination is 8 with all bond lengths shorter than 2.5 Å. The Tb^{3+} chains are also oriented differently in the two structures, Figures 6.4e and 6.4f, although the one-dimensional nature of the Ln^{3+} chains is retained in the LT phase. The ratio of intra-chain and inter-chain distances is smaller in the LT phase than the RT phase (Table 6.4) and this will have impact the dipolar interactions since $D \propto 1/r_{Ln-Ln}^3$.

Table 6.2 Comparison of structural information for $Pr(BO_2)_3$ from combined PXRD + PND refinements at 12 K and 300 K (RT).

		12 K	300 K
a (Å)		6.40092 (6)	6.41249 (3)
b (Å)		8.08400 (4)	8.09827 (6)
c (Å)		7.90419 (7)	7.90730 (5)
β (°)		93.9367 (7)	93.7129 (5)
Volume (Å^3)		408.038 (6)	409.765 (5)
χ^2		5.90	5.71
R_{wp}		3.61	3.58
Ln: 4e (0, y, ¼)	y	0.0509 (5)	0.0501 (2)
B_{iso} (Å^2)		0.38 (6)	0.61 (5)
B1: 4e (0, y, ¼)	y	0.4712 (3)	0.4714 (4)
B_{iso} (Å^2)		0.21 (5)	0.41 (4)
B2: 8f (x,y,z)	x	0.1072 (3)	0.1074 (2)
	y	0.3163 (2)	0.3166 (2)
	z	0.5248 (2)	0.5249 (2)
B_{iso} (Å^2)		0.16 (3)	0.18 (2)
O1: 8f (x,y,z)	x	0.1423 (3)	0.1414 (2)
	y	0.3628 (3)	0.3629 (2)
	z	0.3560 (3)	0.3578 (2)
B_{iso} (Å^2)		0.27 (4)	0.52 (3)
O2: 8f (x,y,z)	x	0.1397 (3)	0.1395 (3)
	y	0.4364 (3)	0.4368 (2)
	z	0.6481 (3)	0.6480 (3)
B_{iso} (Å^2)		0.36 (4)	0.70 (3)
O3: 8f (x,y,z)	x	0.0467 (3)	0.0479 (3)
	y	0.1609 (3)	0.1617 (3)
	z	0.5477 (3)	0.5472 (3)
B_{iso} (Å^2)		0.41 (4)	0.18 (2)
$Ln-Ln$ (intra-chain) (Å)		4.0369 (12)	4.0347 (4)
$Ln-Ln$ (inter-chain) (Å)		4.539 (5)	4.5565 (14)
Ln - O1 (Å)		2.587 (3) × 2	2.602 (3) × 2
		2.790 (5) × 2	2.801 (3) × 2
Ln - O2 (Å)		2.563 (3) × 2	2.568 (3) × 2
Ln - O3 (Å)		2.376 (4) × 2	2.383 (4) × 2
		2.514 (3) × 2	2.520 (4) × 2
$<Ln$-O$>$ (Å)		2.566	2.575

Table 6.3 Comparison of structural parameters for $Tb(BO_2)_3$ from combined PXRD + PND refinements at 100 K and 300 K (RT) for the room temperature phase, space group $C2/c$.

RT phase - space group $C2/c$		100 K	300 K
a (Å)		6.2078 (4)	6.21781 (5)
b (Å)		8.0322 (4)	8.02564 (6)
c (Å)		7.8026 (4)	7.80659 (4)
β (°)		93.278 (6)	93.3723 (4)
Volume (Å^3)		388.42 (4)	388.889 (6)
χ^2		6.31	3.51
R_{wp}		26.5	2.66
Ln: 4*e* (0, *y*, ¼)	*y*	0.0447 (7)	0.04500 (13)
B_{iso} (Å^2)		0.5	0.76 (5)
B1: 4*e* (0, *y*, ¼)	*y*	0.4799 (13)	0.4728 (4)
B_{iso} (Å^2)		0.5	1.37 (8)
B2: 8*f* (x,y,z)	*x*	0.1089 (9)	0.1095 (2)
	y	0.3052 (9)	0.3137 (2)
	z	0.5233 (9)	0.5247 (2)
B_{iso} (Å^2)		0.5	0.14 (21)
O1: 8*f* (x,y,z)	*x*	0.1519 (9)	0.1493 (3)
	y	0.3606 (10)	0.3621 (2)
	z	0.3583 (11)	0.3553 (2)
B_{iso} (Å^2)		0.5	0.97 (3)
O2: 8*f* (x,y,z)	*x*	0.1640 (11)	0.1455 (2)
	y	0.4300 (9)	0.4351 (3)
	z	0.6470 (9)	0.6508 (3)
B_{iso} (Å^2)		0.5	0.75 (5)
O3: 8*f* (x,y,z)	*x*	0.0399 (9)	0.0522 (4)
	y	0.1491 (7)	0.1582 (4)
	z	0.5468 (9)	0.5434 (4)
B_{iso} (Å^2)		0.5	1.30 (7)
Weight % of total $Ln(BO_2)_3$ phase		75 (2)	100
$Ln-Ln$ (intra-chain) (Å)		3.9674 (15)	3.9696 (4)
$Ln-Ln$ (inter-chain) (Å)		4.527 (6)	4.5269 (15)
Ln - O1 (Å)		2.482 (7) × 2	2.489 (4) × 2
		2.821 (10) × 2	2.815 (4) × 2
Ln - O2 (Å)		2.379 (8) × 2	2.457 (6) × 2
Ln - O3 (Å)		2.247 (8) × 2	2.330 (4) × 2
		2.460 (8) × 2	2.467 (4) × 2
< *Ln*-O> (Å)		2.478	2.512

Table 6.4 Structural parameters for low temperature phase of $Tb(BO_2)_3$ from a combined PXRD + PND refinement at 100 K.

LT phase - space group $P2_1/c$		100 K
a (Å)		7.7917 (10)
b (Å)		8.1862 (10)
c (Å)		6.1557 (5)
β (°)		90.669 (9)
Volume (Å^3)		392.61 (8)
χ^2		6.31
R_{wp}		26.5
Ln: 4*e* (x, y, z)	x	0.752 (6)
	y	0.991 (3)
	z	0.050 (2)
B_{iso} (Å^2)		0.5
B1: 4*e* (x, y, z)	x	0.014 (6)
	y	0.710 (6)
	z	0.100 (8)
B_{iso} (Å^2)		0.5
B2: 4*e* (x,y,z)	x	0.518 (6)
	y	0.841 (5)
	z	0.423 (8)
B_{iso} (Å^2)		0.5
B3: 4*e* (x,y,z)	x	0.268 (9)
	y	-0.989 (5)
	z	0.516 (9)
B_{iso} (Å^2)		0.5
O1: 4*e* (x,y,z)	x	0.055 (7)
	y	0.885 (5)
	z	0.088 (7)
B_{iso} (Å^2)		0.5
O2: 4*e* (x,y,z)	x	0.880 (8)
	y	0.666 (6)
	z	0.182 (8)
B_{iso} (Å^2)		0.5
O3: 4*e* (x,y,z)	x	0.153 (8)

	y	0.584 (6)
	z	0.138 (7)
B_{iso} (Å^2)		0.5
O4: 4e (x,y,z)	x	0.641 (9)
	y	0.899 (6)
	z	0.351 (9)
B_{iso} (Å^2)		0.5
O5: 4e (x,y,z)	x	0.505 (6)
	y	0.671 (5)
	z	0.463 (7)
B_{iso} (Å^2)		0.5
O6: 4e (x,y,z)	x	0.270 (7)
	y	0.884 (5)
	z	0.343 (9)
B_{iso} (Å^2)		0.5
Weight % of total $Ln(BO_2)_3$ phase		22.0 (1.0)
$Ln-Ln$ (intra-chain) (Å)		3.90 (7)
$Ln-Ln$ (inter-chain) (Å)		5.00 (3)
<Ln-O>(Å)		2.392

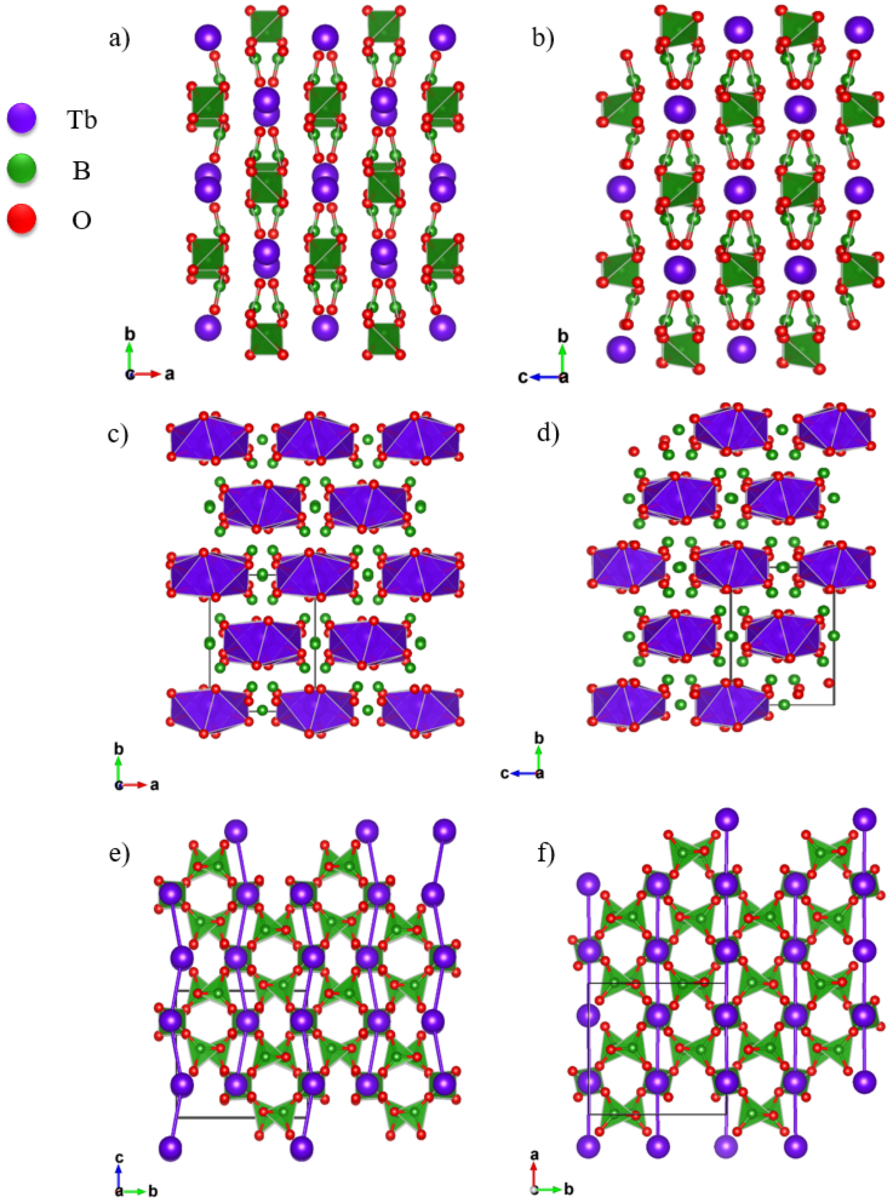

Figure 6.4 Comparison of RT and LT structural modifications for $Tb(BO_2)_3$: The connectivity of the borate groups in the a) RT b) LT phase and Tb-O coordination polyhedra in the c) RT d) LT phase. The connectivity of the magnetic Ln^{3+} chains in the e) RT f) LT phase.

6.4 Bulk magnetic measurements

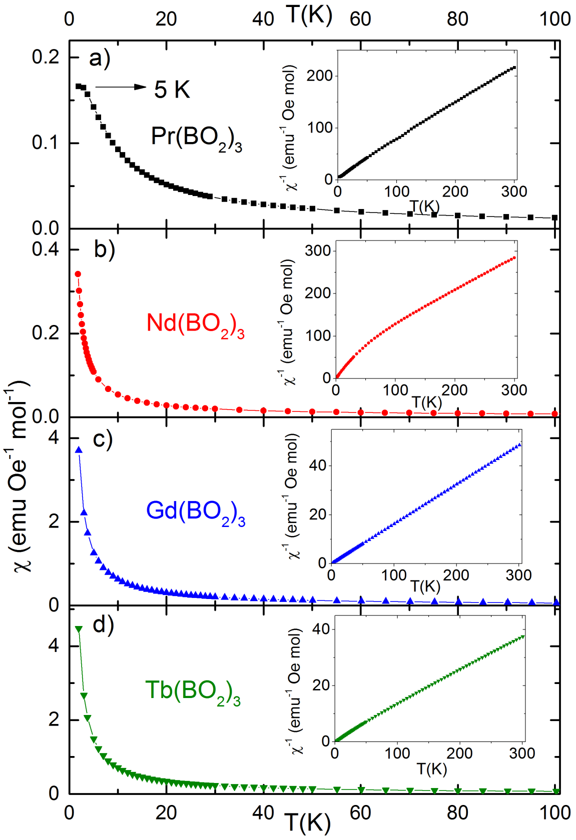

Figure 6.5 Zero field cooled (ZFC) magnetic susceptibility $\chi(T)$ measured in 100 Oe for *Ln*(BO_2)$_3$; *Ln* = Pr, Nd, Gd, Tb. Inset shows the inverse susceptibility, $\chi^{-1}(T)$.

6.4.1 Magnetic susceptibility

Magnetic susceptibility measurements for all *Ln*(BO_2)$_3$, *Ln* = Pr, Nd, Gd, Tb, were carried out on a Quantum Design MPMS with a SQUID magnetometer. The ZFC susceptibility, $\chi(T)$, was measured in a field of 100 Oe in the temperature range 2-300 K. The applied field of 100 Oe is sufficiently low such that the isothermal magnetisation $M(H)$ curve is linear at all temperatures, Therefore, the linear approximation for $\chi(T)$, equation (1.22), can be used. Figure 6.5 shows the ZFC magnetic susceptibility for the *Ln*(BO_2)$_3$. A broad feature is seen at $T = 5$ K for Pr(BO_2)$_3$; none of the other samples show any magnetic ordering features down to 2 K. The reciprocal susceptibility χ^{-1} is linear above 100 K and was fit to the Curie-Weiss law, equation (1.59), the parameters for which are given in Table 6.5. The negative values of the Curie-Weiss temperatures for all samples indicate the presence of

Table 6.5 Bulk magnetic properties of monoclinic *Ln*(BO_2)$_3$; *Ln* = Pr, Nd, Gd, Tb. In case of three-dimensional antiferromagnetic ordering, T_0 is the Néel temperature, T_N.

Ln	T_N (K)	θ_{CW} (K)	Theoretical		Experimental	
			μ_{eff} (μ_B)	M_{sat} (μ_B/f.u.)	μ_{eff} (μ_B)	$M_{max2K,9T}$ (μ_B/f.u.)
Pr	-	-14 (3)	3.58	3.2	3.38 (3)	1.3
Nd	<0.4	TIP	3.62	3.3	3.15 (7)	1.0
Gd	1.1	-0.4 (2)	7.94	7.0	7.032 (5)	6.0
Tb	1.05, 1.95	-12 (3)	9.72	9.0	8.11 (7)	2.9

antiferromagnetic interactions. Significant temperature-independent paramagnetism (TIP) is seen for Nd(BO_2)$_3$ due to which the high T fit to the Curie-Weiss law gives an unphysical value for θ_{CW}. This is not reported. Instead, as has been reported for other Nd^{3+} systems [119, 120, 247, 340, 341], a fit in the low T regime from 2 – 30 K was carried out. This gives μ_{eff} = 2.14 μ_B and θ_{CW} = -0.20 K. In general, the magnetic moments calculated from the Curie-Weiss fits agree well with the theoretical values.

6.4.2 Isothermal magnetisation

$M(H)$ measurements in the field range, μ_0H = 0 – 9 T were carried out at selected temperatures between 2 - 100 K using the ACMS II option on a Quantum Design PPMS. Figure 6.6 shows the $M(H)$ curves for *Ln*(BO_2)$_3$, *Ln* = Pr, Nd, Gd, Tb. Pr(BO_2)$_3$ shows no signs of saturation in a field of 9 T. Gd(BO_2)$_3$ saturates at 6 μ_B/f.u at 2 K in a field of 9 T, this is close to the theoretical M_{sat} for Gd^{3+} Heisenberg spins, $g_J J$ = 7 μ_B/f.u. A magnetisation plateau at $\approx 3\mu_B$/f.u. is seen for Tb(BO_2)$_3$ at 2 K. This corresponds to $M_{sat}/3$. A $M_{sat}/3$ plateau at 2 K is also seen for Nd(BO_2)$_3$. The magnetisation plateaux persists in a field of 14 T at 2 K for both Tb(BO_2)$_3$ and Nd(BO_2)$_3$ (Figure 6.7).

6.4.3 Heat capacity

Heat capacity measurements for *Ln*(BO_2)$_3$, *Ln* = Pr, Nd, Gd, Tb, were carried out using a Quantum Design PPMS in the temperature range 0.4 – 20 K in zero field using the He3 option. As all the samples are poor thermal conductors, they were mixed with approximately equal mass of silver powder (99.99%, Alfa Aesar) and pressed into pellets to enhance the thermal conductivity at low temperatures. The contribution of the silver powder to the heat capacity was then deducted by scaling the values from the literature [243] by mass in order

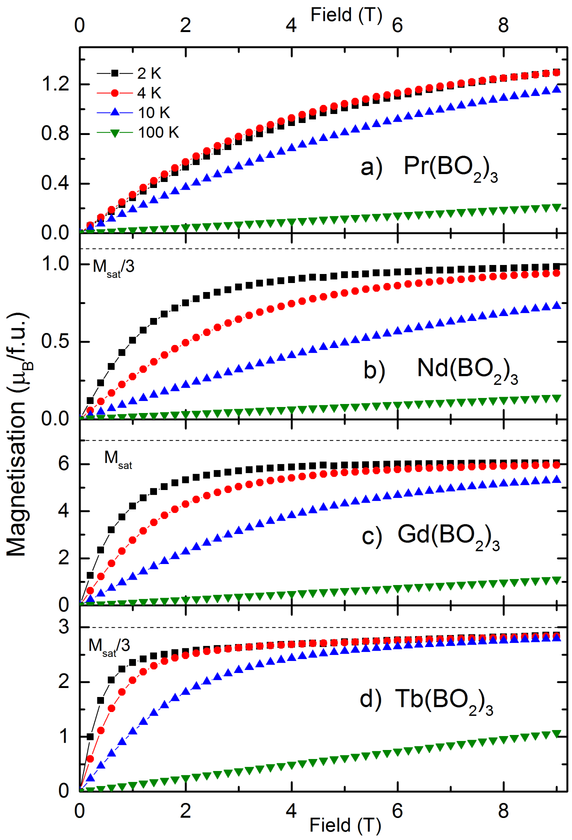

Figure 6.6 Isothermal magnetisation $M(H)$ curves at selected temperatures for *Ln*(BO_2)$_3$; *Ln* = Pr, Nd, Gd, Tb.

to obtain the heat capacity of the sample. The lattice contribution was subtracted using a Debye model (equation 2.37) with Debye temperatures in the range 250 - 325 K.

Figure 6.8 shows the magnetic component of the zero field heat capacity for *Ln*(BO_2)$_3$, *Ln* = Pr, Nd, Gd, Tb. A very broad feature is observed for Pr(BO_2)$_3$ at 5 K, consistent with the susceptibility measurements. There is no further ordering feature observed below 2 K. No ordering is seen for Nd(BO_2)$_3$ but the onset of a sharp transition is seen at 0.4 K. A sharp λ type transition at 1.1 K is seen for Gd(BO_2)$_3$. Tb(BO_2)$_3$ exhibits two sharp ordering features at 1.05 K and 1.95 K.

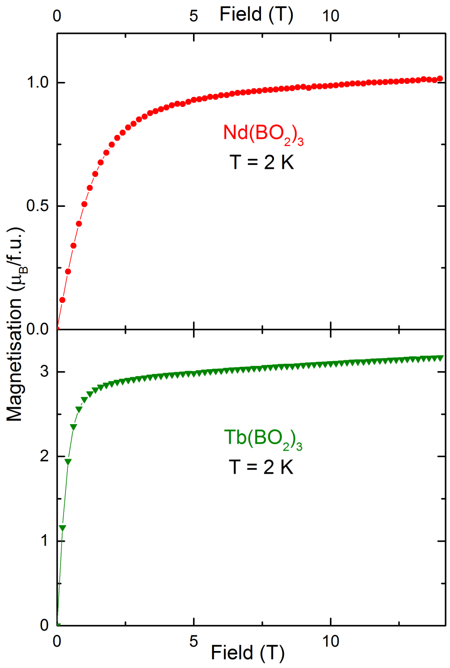

Figure 6.7 Isothermal magnetisation in a field of 14 T at 2 K for $Nd(BO_2)_3$ and $Tb(BO_2)_3$; in both cases the $M_{sat}/3$ plateau is found to persist.

6.5 Low temperature powder neutron diffraction

6.5.1 $Pr(BO_2)_3$

Low temperature PND measurements, $T \geq 1.5$ K, on $Pr(BO_2)_3$ were carried out on the D1B diffractometer at ILL, Grenoble (λ = 2.525 Å) using an Orange cryostat to investigate the existence of any magnetic ordering. Long scans were collected at 1.5 K and 30 K, below and above the feature at 5 K observed in the magnetic susceptibility and zero field heat capacity. The PND data shows no magnetic Bragg peaks or diffuse scattering down to 1.5 K, Figure 6.9. This leads to the conclusion that $Pr(BO_2)_3$ has a non-magnetic ground state as has been reported for complex Pr^{3+} oxides like $Pr_3Ga_5SiO_{14}$ [110] and $Pr_3A_2Sb_3O_{14}$ [119]. As reported elsewhere [110], the features in the bulk measurements for $Pr(BO_2)_3$ are consistent with van Vleck paramagnetism expected for such a ground state due to thermal population of low-lying excited states.

6.5.2 $Tb(BO_2)_3$

Ultra-low temperature PND measurements, $T \geq 0.4$ K, on $Tb(BO_2)_3$ were carried out on the WISH diffractometer at ISIS, Oxfordshire to investigate the nature of the two magnetic

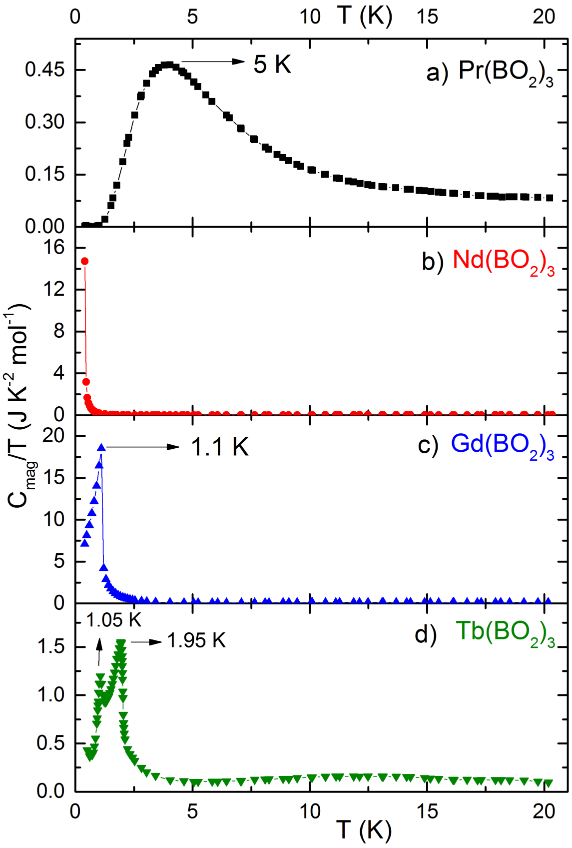

Figure 6.8 Magnetic heat capacity, $C_{mag}(T)$, in zero field for *Ln*(BO_2)$_3$; *Ln* = Pr, Nd, Gd, Tb.

ordering transitions at 1.05 K and 1.95 K respectively. Scans were collected in 0.1 K steps between 0.4 K and 2.0 K using a Heliox. Structural Bragg peaks corresponding to the copper can were observed at all temperatures and so, the data was analysed by taking a difference pattern of a scan at a particular temperature with the data at 2 K, where there are no magnetic Bragg peaks. Below 2 K, several magnetic Bragg peaks were observed. A constant term was added to all the data to remove the negative intensities. The intensity of the magnetic Bragg peaks evolves as a function of temperature on cooling. However, no changes in intensities are observed between 0.4 K and 0.9 K. The temperature dependence of the magnetic Bragg peaks for Tb(BO_2)$_3$ is shown in Figure 6.10 and the intensity of the most intense magnetic Bragg peak at $\approx d = 4.90$ Å is plotted as a function of temperature in Figure 6.11. It is seen that the intensity of all the magnetic Bragg peaks gradually increases as the sample is cooled from 1.9 K to 1.5 K, consistent with the onset of the magnetic ordering transition at 1.95 K in the zero field heat capacity data. On further cooling, the magnetic Bragg peak intensities decrease at 1.4 K and then again increase gradually until 0.9 K after which there is no change down to 0.4 K. It is likely that the increase in intensity corresponds to the magnetic ordering

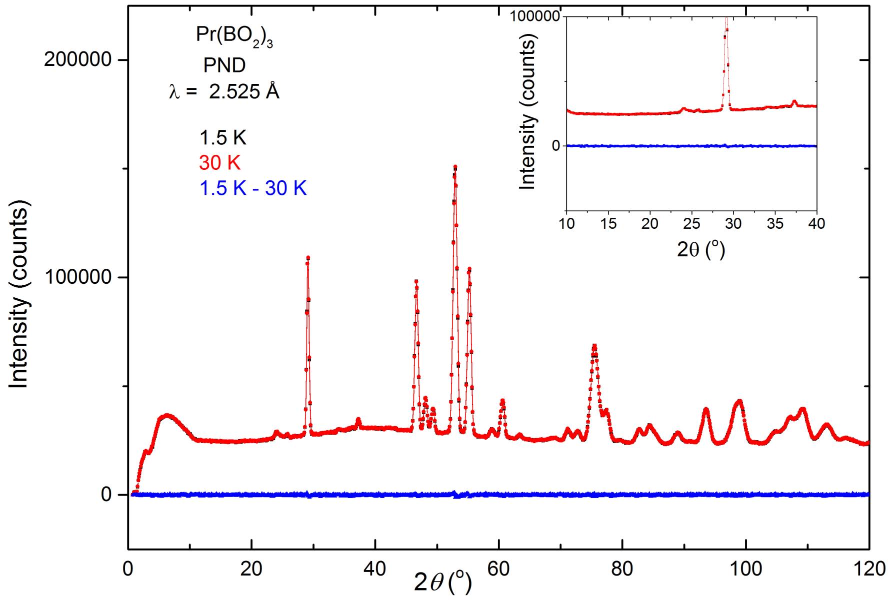

Figure 6.9 PND pattern for $Pr(BO_2)_3$ on D1B, ILL at 1.5 K and 30 K and the difference plot. Inset: a zoom-in of the same plot at low 2θ highlighting the complete absence of any magnetic Bragg peaks or diffuse scattering.

transition at 1.05 K but the exact nature of the magnetic ordering for either transition is unclear as shall be discussed below.

As discussed in Section 6.3, structural refinements at 100 K have shown the coexistence of the RT monoclinic phase along with a LT monoclinic structure in a ratio of approximately 3.75:1 by weight. Therefore one possible explanation for the two magnetic ordering transitions is that the two structural polymorphs order magnetically at two different temperatures. However it is unlikely that this is the case here because while additional Bragg peaks were observed for the LT phase in the structural refinements, specific magnetic Bragg peaks do not appear on cooling through the two transitions. Rather the intensities of all the magnetic Bragg peaks vary in a similar manner as a function of temperature. So, on the basis of the current data, it has to be assumed that both the structural phases contribute to the magnetic ordering.

Indexing of the magnetic propagation vector **k** from a difference pattern of the 1.5 K - 2 K data was attempted using the k search program in the Fullprof suite. The **k** vector was found to be incommensurate (δ, δ', δ'') for both structural phases. A Lebail refinement was attempted with the RT phase only as well as with both RT and LT phases (with different incommensurate propagation vectors). However, the modelling of the peaks was unsatisfactory. The accuracy of the indexed **k** vector so obtained is highly uncertain because it cannot be determined

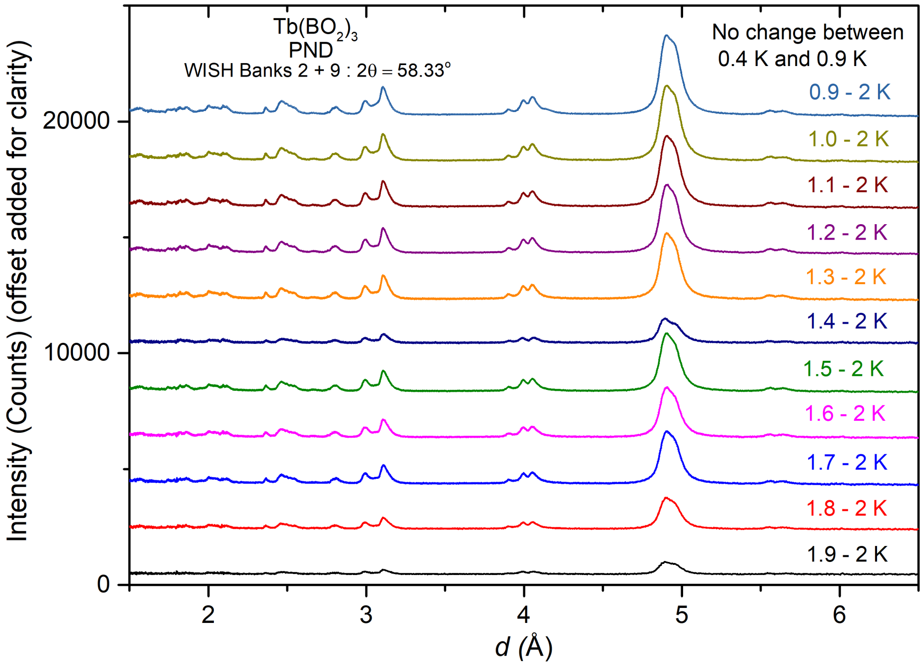

Figure 6.10 PND difference patterns between 0.4 and 2 K for Tb(BO_2)$_3$ on WISH, ISIS on Banks 2 + 9 with intensities offset for clarity; differences are taken with the 2 K data where no magnetic Bragg peaks are observed.

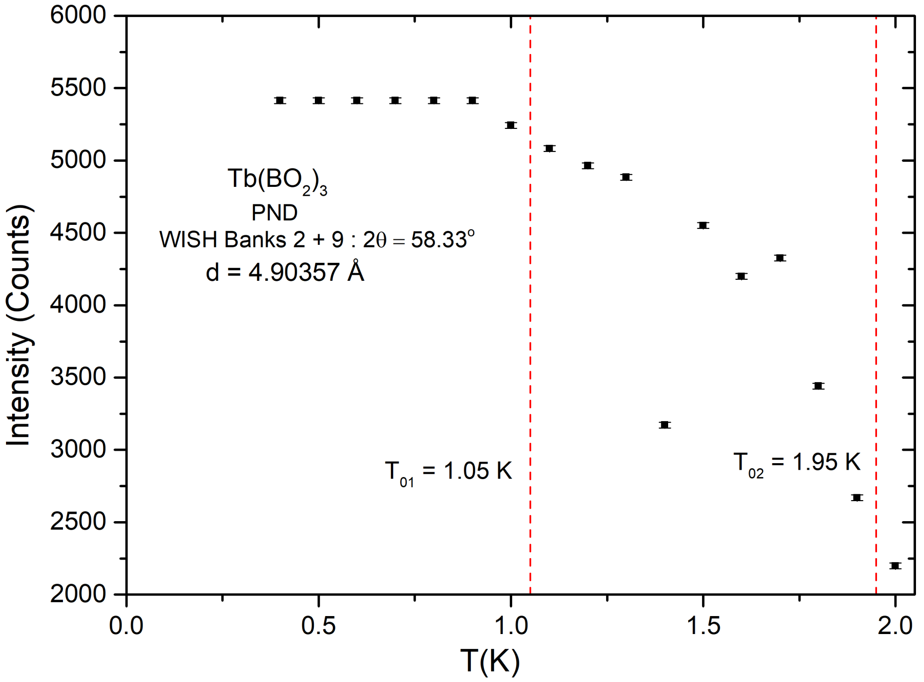

Figure 6.11 Intensity of the most intense magnetic Bragg peak at $\approx d = 4.90$ Å as a function of temperature for Tb(BO_2)$_3$ on WISH, ISIS on Banks 2 + 9; the two magnetic ordering transition temperatures are indicated in the same plot.

with absolute certainty whether magnetic peaks are observed from both structural phases or whether only one structural phase contributes to the magnetic ordering. Due to the low monoclinic symmetry, the incommensurate nature of the magnetic propagation vector and the coexistence of two structural phases, determination of the magnetic structure of $Tb(BO_2)_3$ has proven extremely challenging. Further analysis is required to resolve the low temperature PND data for $Tb(BO_2)_3$.

6.6 Discussion

Powder samples of $Ln(BO_2)_3$, Ln = Pr, Nd, Gd, Tb, have been synthesised. RT PXRD and PND refinements show that they crystallise in a monoclinic structure, consistent with previous reports. $Tb(BO_2)_3$ shows a structural transition at 150 K but contrary to previous reports, both the RT and LT structural phases coexist down to the lowest temperature. The bulk magnetic properties of $Ln(BO_2)_3$, Ln = Pr, Nd, Gd, Tb have been investigated for the first time.

The connectivity of the magnetic Ln^{3+} and the competition among different magnetic interactions play an important role in determining the magnetic behaviour of the monoclinic lanthanide metaborates. For complex lanthanide oxide systems, both exchange interactions (J_1) and dipolar interactions (D) need to be considered at low temperatures [45]. CEF effects also have a profound impact on the single-ion anisotropy and the magnetic properties for Ln^{3+} with non-zero values of orbital angular momentum [45]; in this case, Pr^{3+}, Nd^{3+} and Tb^{3+}. Nd^{3+} is a Kramer's ion and so, as reported for $Nd_3Mg_2Sb_3O_{14}$ [120] and $Nd_2Zr_2O_7$ [342], the single-ion ground state in $Nd(BO_2)_3$ is proposed to be a well-isolated doublet at low temperatures with effective $S = \frac{1}{2}$. Pr^{3+} and Tb^{3+} are non-Kramer's ions but the bulk magnetic measurements and neutron diffraction data indicate that the ground state is different. As reported for $Pr_3Ga_5SiO_{14}$ [110] and $Pr_3A_2Sb_3O_{14}$, A = Mg, Zn [119], in $Pr(BO_2)_3$, CEF effects lead to a non-magnetic ground state. In $Tb(BO_2)_3$, the low temperature physics is likely to be described by a ground state with with effective $S = \frac{1}{2}$, as proposed for $Tb_2Hf_2O_7$ [343] and $Tb_3A_2Sb_3O_{14}$, A = Mg, Zn [119].

Accurate modelling of all the relevant interactions require further inelastic neutron scattering experiments. However, an order of magnitude approximation can be obtained from the bulk magnetic measurements. The dipolar interaction energy can be estimated from the values of the effective magnetic moment and the nearest-neighbour $Ln-Ln$ distances using equation (1.42). The Curie-Weiss constant contains contributions from the nearest -neighbour exchange as well as other terms but an approximate value for the nearest-neighbour isotropic exchange energy can be obtained from the Curie-Weiss constant using equation (1.60) where the number of nearest-neighbour Ln^{3+} in $Ln(BO_2)_3$ is n = 2. For $Tb(BO_2)_3$, the dipolar interactions are calculated for both RT and LT phases as they coexist at temperatures $T \leq 150$ K. These values are given in Table 6.6. $Pr(BO_2)_3$ is excluded from this discussion as it has a non-magnetic ground state.

Table 6.6 Dipolar (D) and nearest-neighbour exchange (J_1) interactions for monoclinic $Ln(BO_2)_3$, Ln = Nd, Gd, Tb.

Ln	Nd	Gd	Tb RT phase	Tb LT phase
$D_{intra-chain}$ (K)	0.04	0.49	0.66	0.69
$D_{inter-chain}$ (K)	0.03	0.33	0.44	0.33
J_1 (K)	0.15	0.32	9.38	9.38

In highly anisotropic structures where the exchange interactions are primarily one-dimensional, the relative magnitudes of the J_1 and D interactions would determine whether the materials exhibit quasi one-dimensional behaviour. If the dipolar interactions dominate over J_1 and the inter-chain and intra-chain dipolar interactions are comparable, three-dimensional magnetic ordering is expected. If the intra-chain dipolar interactions are much greater than the inter-chain dipolar interactions or the J_1 interactions dominate over the dipolar interactions, quasi one-dimensional magnetic behaviour may still be observed. In case of $Ln(BO_2)_3$, the inter ($D_{inter-chain}$) and intra-chain ($D_{intra-chain}$) dipolar interactions are of comparable magnitude($D_{inter-chain}/D_{intra-chain} \approx 0.5 - 0.7$. Hence, considering only dipolar interactions, the magnetic Ln^{3+} would form a distorted hyper honeycomb lattice (Figure 6.1c) and be expected to show magnetic ordering in three-dimensions. On the other hand if $J_1 >> D$ the one-dimensional nature of the Ln^{3+} chains could be retained.

For $Gd(BO_2)_3$ the dipolar interactions are marginally greater than the J_1 exchange interactions. The ordering transition (T_N = 1.1 K) is very close to the Curie-Weiss temperature and the calculated frustration index is $f = 0.4$. This is typical for an antiferromagnet with no geometric frustration. The isothermal magnetisation indicates Heisenberg type Gd^{3+} spins. Thus it is proposed that the sharp λ type transition at 1.1 K in Figure 6.8 for $Gd(BO_2)_3$ corresponds to three-dimensional ordering of a Heisenberg antiferromagnet.

For Ln = Nd and Tb, the J_1 interactions are much greater than both $D_{intra-chain}$ and $D_{inter-chain}$ (for both RT and LT phases for $Tb(BO_2)_3$); hence the magnetic behaviour would expected to be quasi one-dimensional in nature. This is consistent with the bulk magnetic measurements; specifically the observation of a plateau at 1/3 of the saturation magnetisation at 2 K, for both $Nd(BO_2)_3$ and $Tb(BO_2)_3$ (Figure 6.6). It is proposed that this corresponds to a field-induced transition similar to that in other quasi one-dimensional Ising compounds like CoV_2O_6 [329] and $CoNb_2O_6$ [344]. However, unlike those systems, the plateau persists in a field of 14 T (Figure 6.7). Also unusually, the magnetisation plateaux are observed above the magnetic ordering transitions for both Ln = Nd and Tb. It is postulated that this is due to the existence of short-range magnetic correlations above the long-range ordering transitions. $Tb(BO_2)_3$ has two sharp transitions at 1.05 K and 1.95 K in zero field. This is reminiscent of another sign of the behaviour observed in quasi one-dimensional $CoNb_2O_6$ which has two transitions at 1.97 K and 2.97 K, corresponding to a superposition of two commensurate phases and an incommensurate magnetic structure respectively [325]. The existing PND data for $Tb(BO_2)_3$ shows that the two magnetic ordering transitions do not correspond to separate magnetic ordering of the structural phases. However, in order to draw further conclusions, the magnetic structure needs to be resolved. The ordering transitions lie well below the Curie-Weiss temperature, implying possible frustration in $Tb(BO_2)_3$.

For $Nd(BO_2)_3$ no magnetic ordering is seen down to 0.4 K although the sharp increase in C_{mag}/T below 0.45 K can be attributed to the onset of an ordering transition; measurements below 0.4 K are required to confirm this. The low temperature Curie-Weiss fit at lower temperatures for $Nd(BO_2)_3$ gives θ_{CW} = -0.2 K and no conclusions can be drawn regarding the frustration as the ordering transition is beyond the temperature limit of the heat capacity measurements. The weaker D and J_1 interactions are postulated to lead to magnetic ordering at lower temperatures as compared to $Tb(BO_2)_3$.

6.7 Magnetocaloric effect

The change in magnetic entropy, ΔS_m per mole, for the monoclinic $Ln(BO_2)_3$, is calculated from equation (1.64). From the isothermal magnetisation curves, it can be seen that $Ln(BO_2)_3$, Ln = Pr, Nd, Tb, exhibit substantial single-ion anisotropy and so would only be competitive magnetocalorics in the low field regime, $\mu_0 H \leq 2$ T, whereas in higher fields, $Gd(BO_2)_3$ will be a better magnetocaloric material. The ΔS_m values for $Ln(BO_2)_3$ at 2 K are compiled in Table 6.7 in magnetic fields where their performance as magnetocalorics is optimised. The values for the standard magnetocalorics, GGG and DGG, ass well as $GdBO_3$ and $DyBO_3$ from Chapter 5 are also tabulated for comparison in the relevant field regime.

It is seen that DGG and $DyBO_3$ surpass $Pr(BO_2)_3$, $Nd(BO_2)_3$ and $Tb(BO_2)_3$ as magnetocaloric materials. Hence these compounds do not offer any improvement for low temperature solid state magnetic refrigeration. In a field of 9 T, the change in magnetic entropy per mole for $Gd(BO_2)_3$ is comparable to GGG; however the borate framework being lighter, the change in magnetic entropy per unit mass is higher than GGG. Figure 6.12 shows

Table 6.7 MCE in monoclinic $Ln(BO_2)_3$, Ln = Pr, Nd, Gd, Tb, at T = 2 K.

Compound	Field (T)	ΔS_m ($\mathrm{J\,K^{-1}\,mol_{\mathit{Ln}}^{-1}}$)	ΔS_m ($\mathrm{J\,K^{-1}\,kg^{-1}}$)	ΔS_m ($\mathrm{mJ\,K^{-1}\,cc^{-1}}$)
$Gd(BO_2)_3$	9	13.4	46.9	227.1
$GdBO_3$	9	12.5	57.8	366.3
$Gd_3Ga_5O_{12}$ (GGG)	9	14.1	41.8	296.4
$Pr(BO_2)_3$	2	0.2	0.7	3.24
$Nd(BO_2)_3$	2	1.2	4.4	19.7
$Tb(BO_2)_3$		2.4	8.4	41.0
$DyBO_3$	2	3.1	13.9	92.5
$Dy_3Ga_5O_{12}$ (DGG)	2	3.8	11.0	80.6

ΔS_m per unit mass as a function of temperature in fields of 5 T and 9 T for $Gd(BO_2)_3$ and GGG; inset shows the variation in ΔS_m per unit mass as a function of magnetic field at T = 2 K. Therefore, it can be seen that $Gd(BO_2)_3$ can serve as an alternative to GGG in the liquid helium temperature regime. However the magnetocaloric performance of $Gd(BO_2)_3$ is inferior to that of $Gd(HCOO)_3$, the other quasi one-dimensional Ln^{3+} system, which has been reported to have a much higher MCE than GGG with a value of 49.4 $\mathrm{J\,K^{-1}\,mol_{\mathit{Ln}}^{-1}}$ at 2 K, 5 T [189, 201]. The MCE of $Gd(BO_2)_3$ is also inferior to that of $GdBO_3$ at 2 K, 9T, as seen from Table 6.7. One possible method for optimising the magnetocaloric efficiency in low magnetic fields could be the use of mixed lanthanide metaborates such as $Tb_xGd_{1-x}(BO_2)_3$. This approach has been used successfully in the case of the lanthanide formates [201].

6.8 Conclusion

Polycrystalline samples of $Ln(BO_2)_3$, Ln = Pr, Nd, Gd, Tb, have been prepared and the structure has been characterised using RT PXRD and PND. Structural Rietveld refinements show that they crystallise in a monoclinic structure containing one-dimensional chains of magnetic Ln^{3+}, consistent with previous reports. $Tb(BO_2)_3$ undergoes a structural transition at around 150 K and the room temperature monoclinic structure coexists with a low temperature monoclinic phase down to the lowest temperatures.

Bulk magnetic measurements have been carried out for the first time. The monoclinic $Ln(BO_2)_3$, Ln = Pr, Nd, Gd, Tb exhibit many interesting magnetic properties. $Pr(BO_2)_3$ has a non-magnetic ground state. $Gd(BO_2)_3$ undergoes antiferomagnetic ordering at 1.1 K and the magnetisation saturates at 6 μ_B/f.u, consistent with isotropic Gd^{3+} spins. The onset of

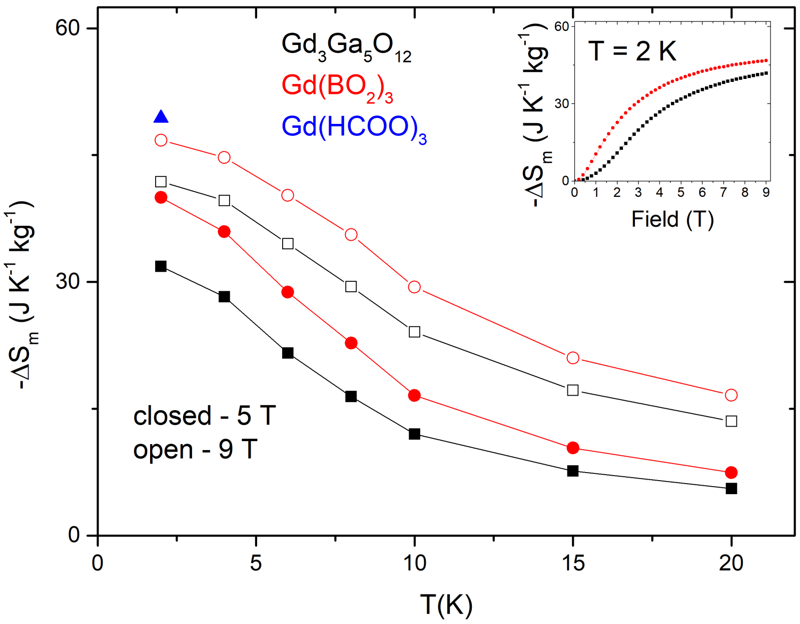

Figure 6.12 Change in magnetic entropy ΔS_m per unit mass for $Gd(BO_2)_3$ compared to GGG in magnetic fields of 5 T (closed symbols) and 9 T (open symbols); the ΔS_m value for $Gd(HCOO)_3$ at 2 K, 5 T is indicated on the same figure [189, 201]. The inset shows the variation in ΔS_m per unit mass as a function of magnetic field at $T = 2$ K.

magnetic ordering is seen in $Nd(BO_2)_3$ at 0.4 K while $Tb(BO_2)_3$ shows two sharp magnetic ordering features at 1.05 K and 1.95 K. The exact nature of the magnetic transitions and the contribution of the structural phases to the magnetic ordering in $Tb(BO_2)_3$ remains unknown. However, it can be concluded that the two transitions are not due to the two structural phases ordering separately. Both $Nd(BO_2)_3$ and $Tb(BO_2)_3$ show a $M_{sat}/3$ magnetisation plateau in fields up to 14 T at 2 K, consistent with quasi one-dimensional behaviour seen in other Ising compounds like CoV_2O_6 and $CoNb_2O_6$ [329, 344]. Calculation of the magnetocaloric effects shows that $Gd(BO_2)_3$ is an efficient magnetic refrigerant for $T \geq 2$ K. Further experiments such as more detailed PND measurements at $T < T_0$, inelastic neutron scattering and PND in field are required to precisely model the magnetic interactions, single-ion anisotropy and field-induced transitions in $Ln(BO_2)_3$. This would provide a fuller understanding of the magnetic behaviour of these materials.

Chapter 7

Conclusion

This thesis has explored the crystal structure and bulk magnetic properties of three families of complex lanthanide oxides: the lanthanide garnets, $Ln_3A_2X_3O_{12}$, the lanthanide orthoborates, LnBO$_3$, and the lanthanide metaborates, Ln(BO$_2$)$_3$. Polycrystalline samples of all the materials have been synthesised and the structure has been analysed using X-ray diffraction. In some cases, both X-ray and neutron diffraction have been used to obtain complementary structural information. The bulk magnetic properties have been characterised using magnetic susceptibility, isothermal magnetisation and heat capacity measurements: these have revealed a gamut of features such as long-range and short range ordering in zero field, field-induced transitions and magnetisation plateaux. For some materials, the magnetic ground state has been determined from low temperature neutron diffraction experiments.

Additionally, the magnetocaloric performance of all materials in the liquid helium temperature regime, $T \geq 2$ K, has been evaluated by calculating the change in magnetic entropy from the isothermal magnetisation curves. It has been shown that the magnetocaloric performance is related to the single-ion anisotropy of the magnetic Ln^{3+}: while the magnetocaloric performance of Heisenberg systems is optimised in high magnetic fields ≥ 5 T attainable using a superconducting magnet, materials with substantial single-ion anisotropy are more efficient magnetocalorics in fields ≤ 2 T, attainable using a commonly available permanent magnet. .

7.1 Lanthanide garnets

The lanthanide garnets, $Ln_3A_2X_3O_{12}$, crystallise in a cubic structure and contain three cation sites based on the coordination with oxygen: the dodecahedral magnetic Ln site, the octahedral A site and the tetrahedral X site. Their magnetic properties are of fundamental scientific interest because the magnetic Ln^{3+} form a highly frustrated three-dimensional network of corner-sharing triangles. Previous literature had mainly focused on lanthanide gallium garnets, $Ln_3\mathrm{Ga_5O_{12}}$, and lanthanide aluminium garnets, $Ln_3\mathrm{Al_5O_{12}}$, where the A and X sites were occupied by non-magnetic $\mathrm{Ga^{3+}}$ and $\mathrm{Al^{3+}}$ respectively. Most of the studies had been carried out on $\mathrm{Gd_3Ga_5O_{12}}$, a spin liquid candidate whose magnetic ground state has been the subject of much debate. $\mathrm{Gd_3Ga_5O_{12}}$ and $\mathrm{Dy_3Ga_5O_{12}}$ also served as the benchmark materials for magnetic refrigeration in the liquid helium temperature regime in the high field (> 5 T) and low field (< 2 T) regimes respectively.

In this thesis, a two part study has been carried out on a large family of lanthanide garnets with the dual aim of exploring the magnetic phase diagram and identifying more efficient magnetocaloric materials among the garnets.

The first part presents a systematic study of the structural and magnetic properties of the lanthanide garnets $Ln_3\mathrm{Ga_5O_{12}}$, $Ln_3\mathrm{Sc_2Ga_3O_{12}}$, $Ln_3\mathrm{Sc_2Al_3O_{12}}$, $Ln_3\mathrm{In_2Ga_3O_{12}}$, $Ln_3\mathrm{Te_2Li_3O_{12}}$ for Ln = Gd, Tb, Dy, Ho. It is observed that garnets with Ln = Gd show magnetic behaviour consistent with isotropic $\mathrm{Gd^{3+}}$ spins and no magnetic ordering is observed for $T \geq 0.4$ K. Magnetic ordering features are seen for garnets with Ln = Tb, Dy, Ho in the temperature range $0.4 < T < 2.5$ K, however the nature of the magnetic ordering varies for the different Ln as well as for different combinations of A and X. The changes in magnetic behaviour can be explained by tuning of the magnetic interactions and changes in the single-ion anisotropy. Among the Gd garnets, the maximum change in magnetic entropy per mole (15.45 $\mathrm{J\,K^{-1}\,mol_{Gd}^{-1}}$) is observed for $\mathrm{Gd_3Sc_2Ga_3O_{12}}$ at 2 K, in a field of 9 T. The performance of $\mathrm{Dy_3Ga_5O_{12}}$ as a magnetocaloric material is found to surpass the other garnets with Ln = Tb, Dy, Ho.

In the second part, the crystal structure and magnetic properties of $\mathrm{Cr^{3+}}$ and $\mathrm{Mn^{3+}}$ substituted lanthanide gallium garnets, $Ln_3\mathrm{CrGa_4O_{12}}$ and $Ln_3\mathrm{MnGa_4O_{12}}$, is presented for Ln = Gd, Tb, Dy, Ho. Both $\mathrm{Cr^{3+}}$ and $\mathrm{Mn^{3+}}$ substitution significantly reduce the frustration in $Ln_3\mathrm{Ga_5O_{12}}$ for Ln = Tb, Dy, Ho; the frustration is found to be relieved by a greater extent for $Ln_3\mathrm{MnGa_4O_{12}}$ as compared to $Ln_3\mathrm{CrGa_4O_{12}}$. The isothermal magnetisation measurements reveal that the substantial single-ion anisotropy in $Ln_3\mathrm{Ga_5O_{12}}$, Ln = Tb, Dy, Ho, as well as the isotropic nature of $\mathrm{Gd^{3+}}$ in $\mathrm{Gd_3Ga_5O_{12}}$ is retained on $\mathrm{Cr^{3+}}$ or $\mathrm{Mn^{3+}}$ substitution. The MCE of $\mathrm{Gd_3CrGa_4O_{12}}$ is 25% greater than $\mathrm{Gd_3Ga_5O_{12}}$ at 2 K, 9 T while the MCE of $Ln_3\mathrm{CrGa_{O12}}$ is enhanced by 20% for Ln = Dy and 120% for Ln = Ho compared to the unsubstituted $Ln_3\mathrm{Ga_5O_{12}}$ at 2 K, 2 T. Powder neutron diffraction on $\mathrm{Ho_3MnGa_4O_{12}}$ below the ordering transition at $T_N = 5.6$ K shows the formation of a long range ordered ordered state with $\mathbf{k}$ = (0,0,0) with concomitant ordering of $\mathrm{Ho^{3+}}$ and $\mathrm{Mn^{3+}}$ spins. The $\mathrm{Ho^{3+}}$ spins are aligned antiferromagnetically along the six crystallographic axes with no resultant moment while the $\mathrm{Mn^{3+}}$ spins are oriented along the body diagonals, such that there is a net moment along [111].

The magnetic structure can be visualised as ten-membered rings of corner-sharing triangles of Ho^{3+} spins with the Mn^{3+} spins ferromagnetically coupled to each individual Ho^{3+} spin in the triangle. The increase in the magnetic ordering temperature for both Ln_3CrGa_{O12} and Ln_3MnGa_{O12} indicates a possible universal mechanism for relieving the magnetic frustration in lanthanide garnets through selective chemical substitution.

7.2 Lanthanide orthoborates

Previous studies on lanthanide orthoborates, $LnBO_3$, had focused on their optical properties for their applications in phosphors as well as on resolving the crystal structure of the π-$LnBO_3$. In this thesis, the structural problem has been studied again and the magnetic properties of the π-$LnBO_3$ are presented for the first time. It is found that the π-$LnBO_3$, Ln = Eu, Gd, Tb, Dy, Ho, Er, Yb, crystallise in a layered monoclinic structure with the magnetic Ln^{3+} forming an edge-sharing triangular lattice, a prototype for two-dimensional frustration. The triangles are scalene, however all deviations from the ideal equilateral geometry are less than 1.5%. There is no evidence of disorder in the Ln^{3+} layers but significant peak broadening in neutron diffraction indicates that the borate layers are disordered. Such disorder had not been reported previously and development of a structural model incorporating this disorder remains an open problem.

Heat capacity measurements show ordering features at $T \leq 2$ K for $LnBO_3$, Ln = Gd, Tb, Dy, Er. No ordering is observed for $YbBO_3$ at $T \geq 0.4$ K while $HoBO_3$ is seen to have a non-magnetic state. $EuBO_3$ shows van Vleck paramagnetism. Isothermal magnetisation measurements indicate isotropic Gd^{3+} spins and strong single-ion anisotropy for Ln^{3+}, Ln = Tb, Dy, Ho, Er, Yb. For $T \geq 2$ K, $GdBO_3$ is found to be a competitive magnetocaloric material in fields ≥ 5 T while $DyBO_3$ is an efficient magnetocaloric in fields ≤ 2 T.

7.3 Lanthanide metaborates

Similar to the lanthanide orthoborates, the lanthanide metaborates, $Ln(BO_2)_3$, Ln = Pr, Nd, Gd, Tb had been studied for their optical properties. In this thesis, their magnetic properties have been investigated for the first time. They are found to crystallise in a monoclinic structure, consistent with previous reports, containing chains of magnetic Ln^{3+}. Of the metaborates studied, only $Tb(BO_2)_3$ undergoes a structural transition: below 150 K, the room temperature and low temperature monoclinic structures coexist down to the lowest measured temperatures.

$Pr(BO_2)_3$ is found to have a non-magnetic ground state. No magnetic ordering is observed down to 0.4 K for $Nd(BO_2)_3$. $Gd(BO_2)_3$ exhibits a sharp magnetic transition at 1.1 K, corresponding to three-dimensional magnetic ordering. The most interesting behaviour is shown by $Tb(BO_2)_3$ which shows two magnetic ordering features at 1.05 K and 1.95 K. However, resolving the magnetic structure from low temperature powder neutron diffraction data remains an open problem due to the coexistence of two structural phases and the incommensurate nature of the propagation vector(s). A magnetisation plateau at a third of the saturation magnetisation is seen at 2 K for both $Nd(BO_2)_3$ and $Tb(BO_2)_3$ which persists in an applied field of 14 T; this is proposed to be a signature of quasi one-dimensional behaviour.

7.4 Future outlook

The synthesis, structure, magnetic and magnetocaloric properties of the complex lanthanide oxides reported in this thesis opens up several areas of future research. The nature of the magnetic ground state, field-induced transitions as well as the underlying magnetic interactions and crystal electric fields (CEF) merit further investigation. This would enable one to map out the magnetic phase diagram for these materials for insight into their fundamental magnetic behaviour as well as for optimising their performance as magnetocaloric materials.

The impact of varying the single-ion anisotropy and chemical pressure on the magnetic ground state in the lanthanide garnets (Chapter 3) as well as introducing additional spins in the lattice (Chapter 4) can be investigated in more detail using neutron diffraction experiments at temperatures below the transition temperature. Determination of the crystal electric field levels using inelastic neutron scattering in the paramagnetic phase is essential to determine the nature of the spin anisotropy for each sample. The magnetic interactions can be studied by measuring the magnetic excitations (spin waves) using inelastic neutron scattering in the ordered phase. For garnets with Ln = Gd, bulk magnetic measurements below 0.4 K are required to determine the presence of any ordering transition. Neutron scattering experiments on Gd garnets are extremely challenging but use of 'hot' neutrons to limit the effect of absorption as well as complementary techniques like muon spectroscopy can lead to a greater understanding of the magnetic properties. In order to evaluate the magnetic interactions between the rare earth and transition metal spins in the chromium and manganese substituted lanthanide gallium garnets (Chapter 4), it is essential to understand the interactions between the Cr^{3+} or Mn^{3+} spins separately. This can be achieved using neutron scattering experiments on $Y_3CrGa_4O_{12}$ and $Y_3MnGa_4O_{12}$, where the only magnetic ions are Cr^{3+} and Mn^{3+} respectively.

Table 7.1 MCE at T = 2 K for the best magnetocaloric materials as determined in this thesis.

Compound	Field (T)	ΔS_m (J K^{-1} kg^{-1})	ΔS_m (mJ K^{-1} cc^{-1})
$Gd_3Ga_5O_{12}$ (GGG)	9	41.8	296.4
$Gd_3Sc_2Ga_3O_{12}$	9	48.1	309.5
$Gd_3Sc_2Al_3O_{12}$	9	52.8	304.5
$Gd_3CrGa_4O_{12}$	9	51.6	360.1
$GdBO_3$	9	57.8	366.3
$Gd(BO_2)_3$	9	46.9	227.1
$Dy_3Ga_5O_{12}$ (DGG)	2	11.0	80.6
$Dy_3CrGa_4O_{12}$	2	13.1	94.3
$DyBO_3$	2	13.9	92.5

The disorder in the borate layers of the lanthanide orthoborates needs to be modelled before in-depth neutron scattering studies can be carried out to study the magnetism. This could be resolved using single crystal XRD and ND total scattering experiments using pairwise distribution function (PDF) analysis to model the short-range correlations in the borate layers more accurately. The possibility of disorder arising from variations in sample preparation methods should also be tested by carrying out structural PND experiments on samples prepared through different synthetic routes, for example, quenching after heating during a solid-state reaction as well as sol-gel or hydrothermal synthesis. In case of the lanthanide metaborates, measurements below 0.4 K are required to determine the ordering transition for *Ln* = Nd while inelastic neutron scattering experiments are needed to estimate the crystal electric field levels and the single-ion anistropy. Magnetic PND in field would allow analysis of the one-third magnetisation plateau. The coexistence of the two structural phases for $Tb(BO_2)_3$, including the possibility of sample dependence, needs to be examined in further detail in order to resolve the nature of the magnetic ordering.

Investigation of the magnetocaloric effect of the complex lanthanide oxides reveals that in all cases, the Gd^{3+} based magnetocalorics (with isotropic spins) perform better in high fields $\geq$ 5 T, generated using a superconducting magnet, whereas Dy^{3+} based magnetocalorics (with strong single-ion anisotropy) are more efficient in fields $\leq$ 2 T, attainable using a permanent magnet. Therefore, in cases where cryogen-free operation is essential, Dy^{3+} magnetic refrigerants have to be used whereas a Gd^{3+} magnetic refrigerant is the material of choice where magnetocaloric performance (characterised by a high value of ΔS_m) needs to be maximised.

Table 7.1 shows the changes in magnetic entropy at T = 2 K (in the relevant field regimes) for the best magnetocaloric materials as determined from this thesis. Values are given in gravimetric and volumetric units as this is more relevant for practical applications. The MCE of the lanthanide orthoborates, $GdBO_3$ and $DyBO_3$ are highest in gravimetric units in 9 T and 2 T respectively, highlighting the importance of exploring polyanion frameworks containing Ln^{3+} as magnetic refrigerants. However, in volumetric units, the MCE of the chromium substituted gallium garnets, $Gd_3CrGa_4O_{12}$ and $Dy_3CrGa_4O_{12}$ are comparable to $GdBO_3$ and $DyBO_3$ respectively. Thus, introducing different chemical substituents into well-known magnetocaloric materials is also an effective strategy for enhancing the magnetocaloric performance. For future applications, the magnetocaloric performance of these materials should be assessed by designing salt pills and testing them in actual adiabatic demagnetisation refrigerators. This will help determine the actual cooling power, the minimum attainable temperature and establish them as competitive solid state magnetic refrigerants at low temperatures.

It is hoped that the results presented in this thesis will lead to further research on the properties and applications of these complex lanthanide oxides.

References

[1] S. Blundell, *Magnetism: a very short introduction* (Oxford University Press, Oxford, 2012).

[2] R. Moessner and A. P. Ramirez, Physics Today **59**, 24 (2006).

[3] S. Blundell, *Magnetism in Condensed Matter* (Oxford University Press, Oxford, 2001).

[4] C. Kittel, *Introduction to Solid State Physics* (Wiley India Private Limited, 2005).

[5] D. J. Griffiths, *Introduction to Electrodynamics*, 3rd ed. (Prentice Hall India Learning Private Limited, 2011).

[6] D. J. Griffiths, *Introduction to Quantum Mechanics*, 2nd ed. (Pearson Education, India, 2005).

[7] W. E. Lamb, Physical Review **85**, 259 (1952).

[8] G. A. Bain and J. F. Berry, Journal of Chemical Education **85**, 532 (2008).

[9] A. Orchard, *Magnetochemistry* (Oxford University Press, Oxford, 2007).

[10] H. Kramers, Proceedings of the Amsterstam Academy **33**, 959 (1930).

[11] H. Kramers, Physica **1**, 182 (1934).

[12] P. W. Anderson, Physical Review **79**, 350 (1950).

[13] J. B. Goodenough, Physical Review **100**, 564 (1955).

[14] J. B. Goodenough, Journal of Physics and Chemistry of Solids **6**, 287 (1958).

[15] J. Kanamori, Journal of Physics and Chemistry of Solids **10**, 87 (1959).

[16] J. J. Morton, *Magnetic properties of materials* (Oxford, 2012).

[17] A. P. Ramirez, Annual Review of Materials Science **24**, 453 (1994).

[18] E. Stryjewski and N. Giordano, Advances in Physics **26**, 487 (1977).

[19] S. Nagata, P. H. Keesom, and H. R. Harrison, Physical Review B **19**, 1633 (1979).

[20] V. Cannella and J. A. Mydosh, Physical Review B **6**, 4220 (1972).

[21] S. Süllow, G. J. Nieuwenhuys, A. A. Menovsky, J. A. Mydosh, S. A. M. Mentink, T. E. Mason, and W. J. L. Buyers, Physical Review Letters **78**, 354 (1997).

[22] A. Ito, H. Aruga, E. Torikai, M. Kikuchi, Y. Syono, and H. Takei, Physical Review Letters **57**, 483 (1986).

[23] K. Binder and A. P. Young, Reviews of Modern Physics **58**, 801 (1986).

[24] K. Fischer and J. Hertz, *Spin Glasses* (Cambridge University Press, Cambridge, 1991).

[25] J. A. Mydosh, *Spin glasses : an experimental introduction* (Taylor & Francis, London; Washington DC, 1993).

[26] J. A. Mydosh, Reports on Progress in Physics **78**, 052501 (2015).

[27] A. Samarakoon, T. J. Sato, T. Chen, G.-W. Chern, J. Yang, I. Klich, R. Sinclair, H. Zhou, and S.-H. Lee, Proceedings of the National Academy of Sciences of the United States of America **113**, 11806 (2016).

[28] A. M. Samarakoon, M. Takahashi, D. Zhang, J. Yang, N. Katayama, R. Sinclair, H. D. Zhou, S. O. Diallo, G. Ehlers, D. A. Tennant, S. Wakimoto, K. Yamada, G.-W. Chern, T. J. Sato, and S.-H. Lee, Scientific Reports **7**, 12053 (2017).

[29] I. Klich, S.-H. Lee, and K. Iida, Nature Communications **5**, 3497 (2014).

[30] J. Yang, A. Samarakoon, S. Dissanayake, H. Ueda, I. Klich, K. Iida, D. Pajerowski, N. P. Butch, Q. Huang, J. R. D. Copley, and S.-H. Lee, Proceedings of the National Academy of Sciences of the United States of America **112**, 11519 (2015).

[31] G. Toulouse, Commun. Phys. **2**, 115 (1977).

[32] J. Villain, Journal of Physics C: Solid State Physics **10**, 1717 (1977).

[33] P. Anderson, Journal of the Less Common Metals **62**, 291 (1978).

[34] G. H. Wannier, Physical Review **79**, 357 (1950).

[35] L. Balents, Nature **464**, 199 (2010).

[36] J. Villain, R. Bidaux, J.-P. Carton, and R. Conte, Journal de Physique **41**, 1263 (1980).

[37] E. F. Shender, Sov. Phys. JETP **56**, 178 (1982).

[38] D. Bergman, J. Alicea, E. Gull, S. Trebst, and L. Balents, Nature Physics **3**, 487 (2007).

[39] M. F. Collins and O. A. Petrenko, Canadian Journal of Physics **75**, 605 (1997).

[40] J. E. Greedan, Journal of Materials Chemistry **11**, 37 (2001).

[41] R. Moessner, Canadian Journal of Physics **79**, 1283 (2001).

[42] C. Lacroix, P. Mendels, and M. Frederic, *Introduction to Frustrated Magnetism: Materials, Experiments, Theory*, edited by C. Lacroix, P. Mendels, and F. Mila, Springer Series in Solid-State Sciences, Vol. 164 (Springer Berlin Heidelberg, 2011).

[43] H. T. Diep, *Frustrated Spin Systems*, 2nd ed. (World Scientific Publishing Co. Pte. Ltd, Singapore, 2013).

[44] M. Subramanian, G. Aravamudan, and G. Subba Rao, Progress in Solid State Chemistry **15**, 55 (1983).

[45] J. S. Gardner, M. J. P. Gingras, and J. E. Greedan, Reviews of Modern Physics **82**, 53 (2010).

[46] M. J. Whitaker and C. Greaves, Journal of Solid State Chemistry **215**, 171 (2014).

[47] P. W. Anderson, Physical Review **102**, 1008 (1956).

[48] J. Villain, Z Phys B. Cond. Mat **33**, 31 (1979).

[49] P. Bonville, J. A. Hodges, M. Ocio, J. P. Sanchez, P. Vulliet, S. Sosin, and D. Braithwaite, Journal of Physics: Condensed Matter **15**, 7777 (2003).

[50] B. D. Gaulin and J. S. Gardner, in *Introduction to Frustrated Magnetism: Materials, Experiments, Theory*, edited by C. Lacroix, P. Mendels, and F. Mila (Springer Berlin Heidelberg, 2011) pp. 177–206.

[51] M. J. Harris, S. T. Bramwell, D. F. McMorrow, T. Zeiske, and K. W. Godfrey, Physical Review Letters **79**, 2554 (1997).

[52] A. P. Ramirez, A. Hayashi, R. J. Cava, R. Siddharthan, and B. S. Shastry, Nature **399**, 333 (1999).

[53] L. Pauling, *The Nature of the Chemical Bond* (Cornell University Press, Ithaca, New York, 1945) pp. 301–304.

[54] S. T. Bramwell, Science **294**, 1495 (2001).

[55] M. J. P. Gingras, in *Introduction to Frustrated Magnetism: Materials, Experiments, Theory*, edited by C. Lacroix, P. Mendels, and F. Mila (Springer Berlin Heidelberg, 2011) pp. 293–329.

[56] M. J. P. Gingras and P. A. McClarty, Reports on Progress in Physics **77**, 056501 (2014).

[57] X. Ke, B. G. Ueland, D. V. West, M. L. Dahlberg, R. J. Cava, and P. Schiffer, Physical Review B **76**, 214413 (2007).

[58] G. Prando, P. Carretta, S. R. Giblin, J. Lago, S. Pin, and P. Ghigna, Journal of Physics: Conference Series **145**, 012033 (2009).

[59] H. D. Zhou, J. G. Cheng, A. M. Hallas, C. R. Wiebe, G. Li, L. Balicas, J. S. Zhou, J. B. Goodenough, J. S. Gardner, and E. S. Choi, Physical Review Letters **108**, 207206 (2012).

[60] C. L. Henley, Annual Review of Condensed Matter Physics **1**, 179 (2010).

[61] S. Petit, E. Lhotel, B. Canals, M. Ciomaga Hatnean, J. Ollivier, H. Mutka, E. Ressouche, A. Wildes, M. R. Lees, and G. Balakrishnan, Nature Physics **12**, 746 (2016).

[62] C. Castelnovo, R. Moessner, and S. L. Sondhi, Nature **451**, 42 (2008).

[63] T. Fennell, P. P. Deen, A. R. Wildes, K. Schmalzl, D. Prabhakaran, A. T. Boothroyd, R. J. Aldus, D. F. McMorrow, and S. T. Bramwell, Science **326**, 415 (2009).

[64] D. J. P. Morris, D. A. Tennant, S. A. Grigera, B. Klemke, C. Castelnovo, R. Moessner, C. Czternasty, M. Meissner, K. C. Rule, J.-U. Hoffmann, K. Kiefer, S. Gerischer, D. Slobinsky, and R. S. Perry, Science **326**, 411 (2009).

[65] S. T. Bramwell, S. R. Giblin, S. Calder, R. Aldus, D. Prabhakaran, and T. Fennell, Nature **461**, 956 (2009).

[66] R. F. Wang, C. Nisoli, R. S. Freitas, J. Li, W. McConville, B. J. Cooley, M. S. Lund, N. Samarth, C. Leighton, V. H. Crespi, and P. Schiffer, Nature **439**, 303 (2006).

[67] S. Ladak, D. E. Read, G. K. Perkins, L. F. Cohen, and W. R. Branford, Nature Physics **6**, 359 (2010).

[68] S. Zhang, I. Gilbert, C. Nisoli, G.-W. Chern, M. J. Erickson, L. O'Brien, C. Leighton, P. E. Lammert, V. H. Crespi, and P. Schiffer, Nature **500**, 553 (2013).

[69] P. Anderson, Materials Research Bulletin **8**, 153 (1973).

[70] P. A. Lee, Science **321**, 1306 (2008).

[71] L. Savary and L. Balents, Reports on Progress in Physics **80**, 016502 (2017).

[72] Y. Zhou, K. Kanoda, and T.-K. Ng, Reviews of Modern Physics **89**, 025003 (2017).

[73] M. Hermele, M. P. A. Fisher, and L. Balents, Physical Review B **69**, 064404 (2004).

[74] H. R. Molavian, M. J. P. Gingras, and B. Canals, Physical Review Letters **98**, 157204 (2007).

[75] E. Lhotel, C. Paulsen, P. D. de Réotier, A. Yaouanc, C. Marin, and S. Vanishri, Physical Review B **86**, 020410 (2012).

[76] P. Bonville, I. Mirebeau, A. Gukasov, S. Petit, and J. Robert, Physical Review B **84**, 184409 (2011).

[77] B. D. Gaulin, J. S. Gardner, P. A. McClarty, and M. J. P. Gingras, Physical Review B **84**, 140402 (2011).

[78] T. Fennell, M. Kenzelmann, B. Roessli, M. K. Haas, and R. J. Cava, Physical Review Letters **109**, 017201 (2012).

[79] K. Fritsch, K. A. Ross, Y. Qiu, J. R. D. Copley, T. Guidi, R. I. Bewley, H. A. Dabkowska, and B. D. Gaulin, Physical Review B **87**, 094410 (2013).

[80] S. Guitteny, J. Robert, P. Bonville, J. Ollivier, C. Decorse, P. Steffens, M. Boehm, H. Mutka, I. Mirebeau, and S. Petit, Physical Review Letters **111**, 087201 (2013).

[81] H. Takatsu, S. Onoda, S. Kittaka, A. Kasahara, Y. Kono, T. Sakakibara, Y. Kato, B. Fåk, J. Ollivier, J. Lynn, T. Taniguchi, M. Wakita, and H. Kadowaki, Physical Review Letters **116**, 217201 (2016).

[82] T. Taniguchi, H. Kadowaki, H. Takatsu, B. Fåk, J. Ollivier, T. Yamazaki, T. J. Sato, H. Yoshizawa, Y. Shimura, T. Sakakibara, T. Hong, K. Goto, L. R. Yaraskavitch, and J. B. Kycia, Physical Review B **87**, 060408 (2013).

[83] K. A. Ross, L. Savary, B. D. Gaulin, and L. Balents, Physical Review X **1**, 021002 (2011).

[84] L.-J. Chang, S. Onoda, Y. Su, Y.-J. Kao, K.-D. Tsuei, Y. Yasui, K. Kakurai, and M. R. Lees, Nature Communications **3**, 992 (2012).

[85] L. Pan, S. K. Kim, A. Ghosh, C. M. Morris, K. A. Ross, E. Kermarrec, B. D. Gaulin, S. M. Koohpayeh, O. Tchernyshyov, and N. P. Armitage, Nature Communications **5**, 4970 (2014).

[86] L. Pan, N. J. Laurita, K. A. Ross, B. D. Gaulin, and N. P. Armitage, Nature Physics **12**, 361 (2015).

[87] Y. Tokiwa, T. Yamashita, M. Udagawa, S. Kittaka, T. Sakakibara, D. Terazawa, Y. Shimoyama, T. Terashima, Y. Yasui, T. Shibauchi, and Y. Matsuda, Nature Communications **7**, 10807 (2016).

[88] R. M. D'Ortenzio, H. A. Dabkowska, S. R. Dunsiger, B. D. Gaulin, M. J. P. Gingras, T. Goko, J. B. Kycia, L. Liu, T. Medina, T. J. Munsie, D. Pomaranski, K. A. Ross, Y. J. Uemura, T. J. Williams, and G. M. Luke, Physical Review B **88**, 134428 (2013).

[89] L.-J. Chang, M. R. Lees, I. Watanabe, A. D. Hillier, Y. Yasui, and S. Onoda, Physical Review B **89**, 184416 (2014).

[90] E. Lhotel, S. R. Giblin, M. R. Lees, G. Balakrishnan, L. J. Chang, and Y. Yasui, Physical Review B **89**, 224419 (2014).

[91] J. Gaudet, K. A. Ross, E. Kermarrec, N. P. Butch, G. Ehlers, H. A. Dabkowska, and B. D. Gaulin, Physical Review B **93**, 064406 (2016).

[92] A. Yaouanc, P. Dalmas de Réotier, L. Keller, B. Roessli, and A. Forget, Journal of Physics: Condensed Matter **28**, 426002 (2016).

[93] K. Kimura, S. Nakatsuji, J.-J. Wen, C. Broholm, M. B. Stone, E. Nishibori, and H. Sawa, Nature Communications **4**, 1934 (2013).

[94] S. Petit, E. Lhotel, S. Guitteny, O. Florea, J. Robert, P. Bonville, I. Mirebeau, J. Ollivier, H. Mutka, E. Ressouche, C. Decorse, M. Ciomaga Hatnean, and G. Balakrishnan, Physical Review B **94**, 165153 (2016).

[95] P. Bonville, S. Guitteny, A. Gukasov, I. Mirebeau, S. Petit, C. Decorse, M. C. Hatnean, and G. Balakrishnan, Physical Review B **94**, 134428 (2016).

[96] N. Martin, P. Bonville, E. Lhotel, S. Guitteny, A. Wildes, C. Decorse, M. Ciomaga Hatnean, G. Balakrishnan, I. Mirebeau, and S. Petit, Physical Review X **7**, 041028 (2017).

[97] L. Savary, K. A. Ross, B. D. Gaulin, J. P. C. Ruff, and L. Balents, Physical Review Letters **109**, 167201 (2012).

[98] M. E. Zhitomirsky, M. V. Gvozdikova, P. C. W. Holdsworth, and R. Moessner, Physical Review Letters **109**, 077204 (2012).

[99] K. Ross, Y. Qiu, J. Copley, H. Dabkowska, and B. Gaulin, Physical Review Letters **112**, 057201 (2014).

[100] S. Petit, J. Robert, S. Guitteny, P. Bonville, C. Decorse, J. Ollivier, H. Mutka, M. J. P. Gingras, and I. Mirebeau, Physical Review B **90**, 060410 (2014).

[101] M. E. Zhitomirsky, P. C. W. Holdsworth, and R. Moessner, Physical Review B **89**, 140403 (2014).

[102] M. E. Brooks-Bartlett, S. T. Banks, L. D. C. Jaubert, A. Harman-Clarke, and P. C. W. Holdsworth, Physical Review X **4**, 011007 (2014).

[103] E. Lefrançois, V. Cathelin, E. Lhotel, J. Robert, P. Lejay, C. V. Colin, B. Canals, F. Damay, J. Ollivier, B. Fåk, L. C. Chapon, R. Ballou, and V. Simonet, Nature Communications **8**, 209 (2017).

[104] C. Waldtmann, H.-U. Everts, B. Bernu, C. Lhuillier, P. Sindzingre, P. Lecheminant, and L. Pierre, The European Physical Journal B **2**, 501 (1998).

[105] M. Mambrini and F. Mila, The European Physical Journal B **17**, 651 (2000).

[106] M. B. Hastings, Physical Review B **63**, 014413 (2000).

[107] P. Bordet, I. Gelard, K. Marty, A. Ibanez, J. Robert, V. Simonet, B. Canals, R. Ballou, and P. Lejay, Journal of Physics: Condensed Matter **18**, 5147 (2006).

[108] R. J. Cava, K. L. Holman, T. McQueen, E. J. Welsh, D. V. West, and A. J. Williams, in *Introduction to Frustrated Magnetism: Materials, Experiments, Theory* (Springer Berlin Heidelberg, 2011) pp. 131–154.

[109] L. L. Lumata, T. Besara, P. L. Kuhns, A. P. Reyes, H. D. Zhou, C. R. Wiebe, L. Balicas, Y. J. Jo, J. S. Brooks, Y. Takano, M. J. Case, Y. Qiu, J. R. D. Copley, J. S. Gardner, K. Y. Choi, N. S. Dalal, and M. J. R. Hoch, Physical Review B **81**, 224416 (2010).

[110] A. Zorko, F. Bert, P. Mendels, K. Marty, and P. Bordet, Physical Review Letters **104**, 057202 (2010).

[111] H. D. Zhou, B. W. Vogt, J. A. Janik, Y.-J. Jo, L. Balicas, Y. Qiu, J. R. D. Copley, J. S. Gardner, and C. R. Wiebe, Physical Review Letters **99**, 236401 (2007).

[112] V. Simonet, R. Ballou, J. Robert, B. Canals, F. Hippert, P. Bordet, P. Lejay, P. Fouquet, J. Ollivier, and D. Braithwaite, Physical Review Letters **100**, 237204 (2008).

[113] Q. J. Li, Z. Y. Zhao, H. D. Zhou, W. P. Ke, X. M. Wang, C. Fan, X. G. Liu, L. M. Chen, X. Zhao, and X. F. Sun, Physical Review B **85**, 174438 (2012).

[114] K. Li, Y. Hu, Y. Wang, T. Kamiyama, B. Wang, Z. Li, and J. Lin, Journal of Solid State Chemistry **217**, 80 (2014).

[115] W. Fu and D. IJdo, Journal of Solid State Chemistry **213**, 165 (2014).

[116] Z. Dun, J. Trinh, K. Li, M. Lee, K. Chen, R. Baumbach, Y. Hu, Y. Wang, E. Choi, B. Shastry, A. Ramirez, and H. Zhou, Physical Review Letters **116**, 157201 (2016).

[117] M. B. Sanders, K. M. Baroudi, J. W. Krizan, O. A. Mukadam, and R. J. Cava, Physica Status Solidi B **253**, 2056 (2016).

[118] M. B. Sanders, J. W. Krizan, and R. J. Cava, J. Mater. Chem. C **4**, 541 (2016).

[119] Z. L. Dun, J. Trinh, M. Lee, E. S. Choi, K. Li, Y. F. Hu, Y. X. Wang, N. Blanc, A. P. Ramirez, and H. D. Zhou, Physical Review B **95**, 104439 (2017).

[120] A. Scheie, M. Sanders, J. Krizan, Y. Qiu, R. J. Cava, and C. Broholm, Physical Review B **93**, 180407 (2016).

[121] A. Bertin, P. Dalmas de Réotier, B. Fåk, C. Marin, A. Yaouanc, A. Forget, D. Sheptyakov, B. Frick, C. Ritter, A. Amato, C. Baines, and P. J. C. King, Physical Review B **92**, 144423 (2015).

[122] J. A. M. Paddison, H. S. Ong, J. O. Hamp, P. Mukherjee, X. Bai, M. G. Tucker, N. P. Butch, C. Castelnovo, M. Mourigal, and S. E. Dutton, Nature Communications **7**, 13842 (2016).

[123] B. Canals, I.-A. Chioar, V.-D. Nguyen, M. Hehn, D. Lacour, F. Montaigne, A. Locatelli, T. O. Menteş, B. S. Burgos, and N. Rougemaille, Nature Communications **7**, 11446 (2016).

[124] H. Karunadasa, Q. Huang, B. G. Ueland, J. W. Lynn, P. Schiffer, K. A. Regan, and R. J. Cava, Physical Review B **71**, 144414 (2005).

[125] F. Damay, C. Martin, V. Hardy, A. Maignan, G. André, K. Knight, S. R. Giblin, and L. C. Chapon, Physical Review B **81**, 214405 (2010).

[126] F. Damay, C. Martin, V. Hardy, A. Maignan, C. Stock, and S. Petit, Physical Review B **84**, 020402 (2011).

[127] O. A. Petrenko, Low Temperature Physics **40**, 106 (2014).

[128] O. Young, G. Balakrishnan, M. R. Lees, and O. A. Petrenko, Physical Review B **90**, 094421 (2014).

[129] H.-F. Li, C. Zhang, A. Senyshyn, A. Wildes, K. Schmalzl, W. Schmidt, M. Boehm, E. Ressouche, B. Hou, P. Meuffels, G. Roth, and T. Brückel, Frontiers in Physics **2**, 42 (2014).

[130] T. H. Cheffings, M. R. Lees, G. Balakrishnan, and O. A. Petrenko, Journal of Physics: Condensed Matter **25**, 256001 (2013).

[131] O. A. Petrenko, O. Young, D. Brunt, G. Balakrishnan, P. Manuel, D. D. Khalyavin, and C. Ritter, Physical Review B **95**, 104442 (2017).

[132] N. Gauthier, B. Prévost, A. Amato, C. Baines, V. Pomjakushin, A. D. Bianchi, R. J. Cava, and M. Kenzelmann, Journal of Physics: Conference Series **828**, 012014 (2017).

[133] N. Gauthier, A. Fennell, B. Prévost, A. Désilets-Benoit, H. A. Dabkowska, O. Zaharko, M. Frontzek, R. Sibille, A. D. Bianchi, and M. Kenzelmann, Physical Review B **95**, 184436 (2017).

[134] O. A. Petrenko, G. Balakrishnan, N. R. Wilson, S. de Brion, E. Suard, and L. C. Chapon, Physical Review B **78**, 184410 (2008).

[135] T. J. Hayes, G. Balakrishnan, P. P. Deen, P. Manuel, L. C. Chapon, and O. A. Petrenko, Physical Review B **84**, 174435 (2011).

[136] D. L. Quintero-Castro, B. Lake, M. Reehuis, A. Niazi, H. Ryll, A. T. M. N. Islam, T. Fennell, S. A. J. Kimber, B. Klemke, J. Ollivier, V. G. Sakai, P. P. Deen, and H. Mutka, Physical Review B **86**, 064203 (2012).

[137] S. Ghosh, H. D. Zhou, L. Balicas, S. Hill, J. S. Gardner, Y. Qiu, and C. R. Wiebe, Journal of Physics: Condensed Matter **23**, 164203 (2011).

[138] O. Young, L. C. Chapon, and O. A. Petrenko, Journal of Physics: Conference Series **391**, 012081 (2012).

[139] O. Young, A. R. Wildes, P. Manuel, B. Ouladdiaf, D. D. Khalyavin, G. Balakrishnan, and O. A. Petrenko, Physical Review B **88**, 024411 (2013).

[140] W. I. Kinney and W. P. Wolf, Journal of Applied Physics **50**, 2115 (1979).

[141] S. Hov, H. Bratsberg, and A. Skjeltorp, Journal of Magnetism and Magnetic Materials **15-18**, 455 (1980).

[142] N. Woo, D. M. Silevitch, C. Ferri, S. Ghosh, and T. F. Rosenbaum, Journal of Physics: Condensed Matter **27**, 296001 (2015).

[143] P. Schiffer, A. P. Ramirez, D. A. Huse, P. L. Gammel, U. Yaron, D. J. Bishop, and A. J. Valentino, Physical Review Letters **74**, 2379 (1995).

[144] O. Petrenko, C. Ritter, M. Yethiraj, and D. Paul, Physica B: Condensed Matter **241-243**, 727 (1997).

[145] O. A. Petrenko, C. Ritter, M. Yethiraj, and D. McK Paul, Physical Review Letters **80**, 4570 (1998).

[146] S. R. Dunsiger, J. S. Gardner, J. A. Chakhalian, A. L. Cornelius, M. Jaime, R. F. Kiefl, R. Movshovich, W. A. MacFarlane, R. I. Miller, J. E. Sonier, and B. D. Gaulin, Physical Review Letters **85**, 3504 (2000).

[147] I. M. Marshall, S. J. Blundell, F. L. Pratt, A. Husmann, C. A. Steer, A. I. Coldea, W. Hayes, and R. C. C. Ward, Journal of Physics: Condensed Matter **14**, L157 (2002).

[148] S. Ghosh, T. F. Rosenbaum, and G. Aeppli, Physical Review Letters **101**, 157205 (2008).

[149] P. P. Deen, O. A. Petrenko, G. Balakrishnan, B. D. Rainford, C. Ritter, L. Capogna, H. Mutka, and T. Fennell, Physical Review B **82**, 174408 (2010).

[150] J. A. M. Paddison, H. Jacobsen, O. A. Petrenko, M. T. Fernandez-Diaz, P. P. Deen, and A. L. Goodwin, Science **350**, 179 (2015).

[151] P. Schiffer, A. P. Ramirez, D. A. Huse, and A. J. Valentino, Physical Review Letters **73**, 2500 (1994).

[152] Y. K. Tsui, C. A. Burns, J. Snyder, and P. Schiffer, Physical Review Letters **82**, 3532 (1999).

[153] P. P. Deen, O. Florea, E. Lhotel, and H. Jacobsen, Physical Review B **91**, 014419 (2015).

[154] N. D'Ambrumenil, O. A. Petrenko, H. Mutka, and P. P. Deen, Physical Review Letters **114**, 227203 (2015).

[155] A. Rousseau, J.-M. Parent, and J. A. Quilliam, Physical Review B **96**, 060411 (2017).

[156] C. Liu, S. M. Wu, J. E. Pearson, J. S. Jiang, N. D'Ambrumenil, and A. Bhattacharya, (2017), arXiv:1710.04269 .

[157] Y. Li, H. Liao, Z. Zhang, S. Li, F. Jin, L. Ling, L. Zhang, Y. Zou, L. Pi, Z. Yang, J. Wang, Z. Wu, and Q. Zhang, Scientific Reports **5**, 16419 (2015).

[158] Y. Li, D. Adroja, D. Voneshen, R. I. Bewley, Q. Zhang, A. A. Tsirlin, and P. Gegenwart, Nature Communications **8**, 15814 (2017).

[159] Y. Shen, Y.-D. Li, H. Wo, Y. Li, S. Shen, B. Pan, Q. Wang, H. C. Walker, P. Steffens, M. Boehm, Y. Hao, D. L. Quintero-Castro, L. W. Harriger, M. D. Frontzek, L. Hao, S. Meng, Q. Zhang, G. Chen, and J. Zhao, Nature **540**, 559 (2016).

[160] Y. Li, D. Adroja, P. K. Biswas, P. J. Baker, Q. Zhang, J. Liu, A. A. Tsirlin, P. Gegenwart, and Q. Zhang, Physical Review Letters **117**, 097201 (2016).

[161] Y.-D. Li and G. Chen, Physical Review B **96**, 075105 (2017).

[162] Y.-D. Li, Y.-M. Lu, and G. Chen, Physical Review B **96**, 054445 (2017).

[163] Y. Xu, J. Zhang, Y. Li, Y. Yu, X. Hong, Q. Zhang, and S. Li, Physical Review Letters **117**, 267202 (2016).

[164] Y. Li, G. Chen, W. Tong, L. Pi, J. Liu, Z. Yang, X. Wang, and Q. Zhang, Physical Review Letters **115**, 167203 (2015).

[165] Y.-D. Li, X. Wang, and G. Chen, Physical Review B **94**, 035107 (2016).

[166] J. A. Paddison, M. Daum, Z. Dun, G. Ehlers, Y. Liu, M. Stone, H. Zhou, and M. Mourigal, Nature Physics **13**, 117 (2016).

[167] Z. Zhu, P. Maksimov, S. R. White, and A. Chernyshev, Physical Review Letters **119**, 157201 (2017).

[168] Q. Luo, S. Hu, B. Xi, J. Zhao, and X. Wang, Physical Review B **95**, 165110 (2017).

[169] X. Zhang, F. Mahmood, M. Daum, Z. Dun, J. A. M. Paddison, N. J. Laurita, T. Hong, H. Zhou, N. P. Armitage, and M. Mourigal, (2017), arXiv:1708.07503 .

[170] F. Pobell, *Matter and Methods at Low Temperatures* (Springer Berlin Heidelberg, Berlin, Heidelberg, 2007).

[171] A. Cho, Science **326**, 778 LP (2009).

[172] J. Glanz, Science **279**, 2045 (1998).

[173] A. M. Tishin and Y. I. Spichkin, *The Magnetocaloric effect and its Applications* (Institute of Physics Publishing, Bristol, 2003).

[174] A. Smith, The European Physical Journal H **38**, 507 (2013).

[175] E. Brück, Journal of Physics D: Applied Physics **38**, R381 (2005).

[176] V. K. Pecharsky and K. A. Gschneidner Jr, Journal of Magnetism and Magnetic Materials **200**, 44 (1999).

[177] K. A. Gschneider Jr., V. K. Pecharsky, and A. O. Tsokol, Reports on Progress in Physics **68**, 1479 (2005).

[178] P. Wikus, E. Canavan, S. T. Heine, K. Matsumoto, and T. Numazawa, Cryogenics **62**, 150 (2014).

[179] P. Debye, Annals of Physics **386**, 1154 (1926).

[180] W. F. Giauque, Journal of the American Chemical Society **49**, 1864 (1927).

[181] W. F. Giauque and D. P. MacDougall, Physical Review **43**, 768 (1933).

[182] M. E. Zhitomirsky, Physical Review B **67**, 104421 (2003).

[183] J. Barclay and W. Steyert, Cryogenics **22**, 73 (1982).

[184] M. D. Kuz'min and A. M. Tishin, Journal of Physics D: Applied Physics **24**, 2039 (1991).

[185] A. C. Sackville Hamilton, G. I. Lampronti, S. E. Rowley, and S. E. Dutton, Journal of Physics: Condensed Matter **26**, 116001 (2014).

[186] R. A. Fisher, G. E. Brodale, E. W. Hornung, and W. F. Giauque, The Journal of Chemical Physics **59**, 4652 (1973).

[187] E. W. Hornung, R. A. Fisher, G. E. Brodale, and W. F. Giauque, The Journal of Chemical Physics **61**, 282 (1974).

[188] B. Daudin, A. Lacaze, and B. Salce, Cryogenics **22**, 439 (1982).

[189] G. Lorusso, J. W. Sharples, E. Palacios, O. Roubeau, E. K. Brechin, R. Sessoli, A. Rossin, F. Tuna, E. J. L. McInnes, D. Collison, and M. Evangelisti, Advanced Materials **25**, 4653 (2013).

[190] Y.-C. Chen, L. Qin, Z.-S. Meng, D.-F. Yang, C. Wu, Z. Fu, Y.-Z. Zheng, J.-L. Liu, R. Tarasenko, M. Orendáč, J. Prokleška, V. Sechovský, and M.-L. Tong, J. Mater. Chem. A **2**, 9851 (2014).

[191] E. Palacios, J. A. Rodríguez-Velamazán, M. Evangelisti, G. J. McIntyre, G. Lorusso, D. Visser, L. J. de Jongh, and L. A. Boatner, Physical Review B **90**, 214423 (2014).

[192] Y. Yang, Q.-C. Zhang, Y.-Y. Pan, L.-S. Long, and L.-S. Zheng, Chem. Commun. **51**, 7317 (2015).

[193] Y.-C. Chen, J. Prokleška, W.-J. Xu, J.-L. Liu, J. Liu, W.-X. Zhang, J.-H. Jia, V. Sechovský, and M.-L. Tong, J. Mater. Chem. C **3**, 12206 (2015).

[194] M. Xia, S. Shen, J. Lu, Y. Sun, and R. Li, Chemistry - A European Journal (2018), 10.1002/chem.201705669.

[195] R. Li, T. Numazawa, T. Hashimoto, A. Tomokiyo, T. Goto, and S. Todo, in *Advances in Cryogenic Engineering Materials* (Springer US, Boston, MA, 1986) pp. 287–294.

[196] M. Ball, M. J. M. Leask, W. P. Wolf, and A. F. G. Wyatt, Journal of Applied Physics **34**, 1104 (1963).

[197] J. Filippi, J. Lasjaunias, A. Ravex, F. Tchéou, and J. Rossat-Mignod, Solid State Communications **23**, 613 (1977).

[198] J. Filippi, F. Tcheou, and J. Rossat-Mignod, Solid State Communications **33**, 827 (1980).

[199] A. Tomokiyo, H. Yayama, T. Hashimoto, T. Aomine, M. Nishida, and S. Sakaguchi, Cryogenics **25**, 271 (1985).

[200] T. Numazawa, K. Kamiya, T. Okano, and K. Matsumoto, Physica B: Condensed Matter **329-333**, 1656 (2003).

[201] P. J. Saines, J. A. M. Paddison, P. M. M. Thygesen, and M. G. Tucker, Mater. Horiz. **2**, 528 (2015).

[202] P. Timbie, G. Bernstein, and P. Richards, Cryogenics **30**, 271 (1990).

[203] C. Hagmann, D. Benford, and P. Richards, Cryogenics **34**, 213 (1994).

[204] D. Jang, T. Gruner, A. Steppke, K. Mitsumoto, C. Geibel, and M. Brando, Nature Communications **6**, 8680 (2015).

[205] Y. Tokiwa, B. Piening, H. S. Jeevan, S. L. Budko, P. C. Canfield, and P. Gegenwart, Science Advances **2**, e1600835 (2016).

[206] S. Kobayashi, S. Mitsuda, M. Ishikawa, K. Miyatani, and K. Kohn, Physical Review B **60**, 3331 (1999).

[207] R. Coldea, D. A. Tennant, E. M. Wheeler, E. Wawrzynska, D. Prabhakaran, M. Telling, K. Habicht, P. Smeibidl, and K. Kiefer, Science **327**, 177 (2010).

[208] L. E. Smart and E. A. Moore, in *Solid State Chemistry An Introduction* (CRC Press, Taylor and Francis Group, Boca Raton, Florida, 2012) Chap. 3, pp. 138–141.

[209] M. Glazer and G. Burns, *Space Groups for Solid State Scientists* (Academic Press, Elsevier Science Publishing Co Inc, United States, 2013).

[210] D. Sivia, in *Elementary Scattering Theory* (Oxford University Press, Oxford, 2011) pp. 63–91.

[211] R. Pynn, *Neutron Scattering: a primer* (Los Alamos Science, 1990) p. 2.

[212] L. E. Smart and E. A. Moore, in *Solid State Chemistry An Introduction* (CRC Press, Taylor and Francis Group, Boca Raton, Florida, 2012) Chap. 2, pp. 75–100.

[213] "Generation of X-rays," .

[214] G. E. Bacon, in *Neutron Diffraction (Second Edition)* (Clarendon Press, Oxford, 1962) pp. 1–16.

[215] A. W. Hewat, Materials Science Forum **9**, 69 (1986).

[216] E. Suard and A. Hewat, Neutron News **12**, 30 (2001).

[217] I. P. O. Campo, J. F. Clergeau, S. Martínez, M. Olmos, O. Fabelo, and J, Journal of Physics: Conference Series **549**, 12003 (2014).

[218] T. C. H. Convert, P. F. Henry, H. E. Fischer, J. Torregrossa, and Pierre, Measurement Science and Technology **19**, 34001 (2008).

[219] L. C. Chapon, P. Manuel, P. G. Radaelli, C. Benson, L. Perrott, S. Ansell, N. J. Rhodes, D. Raspino, D. Duxbury, E. Spill, and J. Norris, Neutron News **22**, 22 (2011).

[220] G. E. Bacon, in *Neutron Diffraction (Second Edition)* (Clarendon Press, Oxford, 1962) pp. 18–53.

[221] F. S. Varley, Neutron News **3** (1992).

[222] H. M. Rietveld, Journal of Applied Crystallography **2**, 65 (1969).

[223] L. B. McCusker, R. B. Von Dreele, D. E. Cox, D. Louër, and P. Scardi, Journal of Applied Crystallography **32**, 36 (1999).

[224] L. W. Finger, D. E. Cox, and A. P. Jephcoat, Journal of Applied Crystallography **27**, 892 (1994).

[225] J. Rodriguez-Carvajal, *Introduction to the Program FULLPROF: Refinement of Crystal and Magnetic Structures from Powder and Single Crystal Data* (2017).

[226] A. Le Bail, Powder Diffraction **20**, 316 (2005).

[227] J. Rodríguez-Carvajal, Physica B: Condensed Matter **192**, 55 (1993).

[228] T. Roisnel and J. Rodriguez-Carvajal, in *Materials Science Forum, Proceedings of the Seventh European Powder Diffraction Conference (EPDIC 7)*, edited by R. Delhez and E. Mittenmeijer (2000) pp. 118–123.

[229] L. W. Alvarez and F. Bloch, Physical Review **57**, 111 (1940).

[230] Y. Gell and D. B. Lichtenberg, Il Nuovo Cimento A Series 10 **61**, 27 (1969).

[231] G. E. Bacon, in *Neutron Diffraction (Second Edition)* (Clarendon Press, Oxford, 1962) pp. 145–159.

[232] V. O. Garlea and B. C. Chakoumakos, in *Neutron Scattering - Magnetic and Quantum Phenomena, Volume 48* (Academic Press, Elsevier Science Publishing Co Inc, United States, 2015) 1st ed., Chap. 4, pp. 203–290.

[233] E. Ressouche, École thématique de la Société Française de la Neutronique **13**, 02001 (2014).

[234] Y. A. Izyumov, V. E. Naish, and R. P. Ozerov, in *Neutron Diffraction of Magnetic Materials* (Springer US, Boston, MA, 1991) pp. 137–222.

[235] A. Wills, Physica B: Condensed Matter **276-278**, 680 (2000).

[236] M. McElfresh, *Fundamentals of Magnetism and Magnetic Measurements Featuring Quantum Design's Magnetic Property Measurement System* (Quantum Design US, 1994).

[237] J. Clarke, Scientific American , 36 (1994).

[238] *Physical Property Measurement System AC Measurement System (ACMS II) Option User's Manual* (Quantum Design US, 2015).

[239] E. S. R. Gopal, in *Specific Heats at Low Temperatures* (Springer US, Boston, MA, 1966) pp. 20–54.

[240] E. S. R. Gopal, in *Specific Heats at Low Temperatures* (Springer US, Boston, MA, 1966) pp. 84–111.

[241] G. A. Slack and D. W. Oliver, Physical Review B **4**, 592 (1971).

[242] M. J. Weber, *Handbook of optical materials* (CRC Press, Taylor and Francis Group, Boca Raton, Florida, 2003) p. 512.

[243] D. Smith and F. Fickett, Journal of Research of the National Institute of Standards and Technology **100**, 119 (1995).

[244] *Physical Property Measurement System Dynacool User's Manual* (Quantum Design US, 2014).

[245] *Physical Property Measurement System Heat Capacity Option User's Manual* (Quantum Design US, 2015).

[246] M. E. Fisher, Philosophical Magazine **7**, 1731 (1962).

[247] A. M. Hallas, A. M. Arevalo-Lopez, A. Z. Sharma, T. Munsie, J. P. Attfield, C. R. Wiebe, and G. M. Luke, Physical Review B **91**, 104417 (2015).

[248] A. M. Hallas, J. G. Cheng, A. M. Arevalo-Lopez, H. J. Silverstein, Y. Su, P. M. Sarte, H. D. Zhou, E. S. Choi, J. P. Attfield, G. M. Luke, and C. R. Wiebe, Physical Review Letters **113**, 267205 (2014).

[249] Z. L. Dun, M. Lee, E. S. Choi, A. M. Hallas, C. R. Wiebe, J. S. Gardner, E. Arrighi, R. S. Freitas, A. M. Arevalo-Lopez, J. P. Attfield, H. D. Zhou, and J. G. Cheng, Physical Review B **89**, 064401 (2014).

[250] J. R. Stewart, J. S. Gardner, Y. Qiu, and G. Ehlers, Physical Review B **78**, 132410 (2008).

[251] C. Reshmi, S. Savitha Pillai, K. Suresh, and M. R. Varma, Journal of Magnetism and Magnetic Materials **324**, 1962 (2012).

[252] F. Maglia, V. Buscaglia, S. Gennari, P. Ghigna, M. Dapiaggi, A. Speghini, and M. Bettinelli, The Journal of Physical Chemistry B **110**, 6561 (2006).

[253] J. A. Quilliam, S. Meng, H. A. Craig, L. R. Corruccini, G. Balakrishnan, O. A. Petrenko, A. Gomez, S. W. Kycia, M. J. P. Gingras, and J. B. Kycia, Physical Review B **87**, 174421 (2013).

[254] O. Florea, E. Lhotel, H. Jacobsen, C. S. Knee, and P. P. Deen, Physical Review B **96**, 220413 (2017).

[255] J. Hamman and P. Manneville, Journal de Physique **34**, 615 (1973).

[256] K. Kamazawa, D. Louca, R. Morinaga, T. J. Sato, Q. Huang, J. R. D. Copley, and Y. Qiu, Physical Review B **78**, 064412 (2008).

[257] J. Hammann and M. Ocio, Journal de Physique **38**, 463 (1977).

[258] J. Hammann and M. Ocio, Physica B+C **86-88**, 1153 (1977).

[259] H. Capel, Physica **31**, 1152 (1965).

[260] J. Filippi, J. Lasjaunias, B. Hébral, J. Rossat-Mignod, and F. Tchéou, Journal of Magnetism and Magnetic Materials **15-18**, 527 (1980).

[261] H. D. Zhou, C. R. Wiebe, L. Balicas, Y. J. Yo, Y. Qiu, J. R. D. Copley, and J. S. Gardner, Physical Review B **78**, 140406 (2008).

[262] J. M. Hastings, L. M. Corliss, and C. G. Windsor, Physical Review **138**, A176 (1965).

[263] J. Hammann, Acta Crystallographica Section B Structural Crystallography and Crystal Chemistry **25**, 1853 (1969).

[264] J. Felsteiner and S. K. Misra, Physical Review B **24**, 2627 (1981).

[265] A. H. Cooke, T. L. Thorp, and M. R. Wells, Proceedings of the Physical Society **92**, 400 (1967).

[266] R. P. Applegate, Y. Zong, and L. Corruccini, Journal of Physics and Chemistry of Solids **68**, 1756 (2007).

[267] R. D. Shannon, Acta Crystallographica Section A **32**, 751 (1976).

[268] B. Reid, D. McMorrow, P. Mitchell, O. Prakash, and A. Murani, Physica B: Condensed Matter **174**, 51 (1991).

[269] S. T. Bramwell, M. N. Field, M. J. Harris, and I. P. Parkin, Journal of Physics: Condensed Matter **12**, 483 (2000).

[270] S. Nagata, H. Sasaki, K. Suzuki, J. Kiuchi, and N. Wada, Journal of Physics and Chemistry of Solids **62**, 1123 (2001).

[271] O. A. Petrenko and D. McK. Paul, Physical Review B **63**, 024409 (2000).

[272] T. Yavors'kii, M. Enjalran, and M. J. P. Gingras, Physical Review Letters **97**, 267203 (2006).

[273] S. E. Dutton, E. D. Hanson, C. L. Broholm, J. S. Slusky, and R. J. Cava, Journal of Physics: Condensed Matter **23**, 386001 (2011).

[274] L.-q. Yan, F. Maciá, Z.-w. Jiang, J. Shen, L.-h. He, and F.-w. Wang, Journal of Physics: Condensed Matter **20**, 255203 (2008).

[275] M. C. Kemei, S. L. Moffitt, D. P. Shoemaker, and R. Seshadri, Journal of Physics: Condensed Matter **24**, 046003 (2012).

[276] D. Rodic, M. Mitric, R. Tellgren, H. Rundlof, and A. Kremenovic, Journal of Magnetism and Magnetic Materials **191**, 137 (1999).

[277] M. Lahoubi, M. Guillot, A. Marchand, F. Tcheou, and E. Roudault, IEEE Transactions on Magnetics **20**, 1518 (1984).

[278] M. Lahoubi, W. Younsi, M.-L. Soltani, and B. Ouladdiaf, Journal of Physics: Conference Series **200**, 082018 (2010).

[279] M. Guillot, A. Marchand, F. Tchéou, and P. Feldmann, Journal of Applied Physics **53**, 2719 (1982).

[280] R. D. McMichael, J. J. Ritter, and R. D. Shull, Journal of Applied Physics **73**, 6946 (1993).

[281] V. Provenzano, J. Li, T. King, E. Canavan, P. Shirron, M. DiPirro, and R. D. Shull, Journal of Magnetism and Magnetic Materials **266**, 185 (2003).

[282] K. Matsumoto, A. Matsuzaki, K. Kamiya, and T. Numazawa, Japanese Journal of Applied Physics **48**, 113002 (2009).

[283] A. J. Neer, J. Milam-Guerrero, J. E. So, B. C. Melot, K. A. Ross, Z. Hulvey, C. M. Brown, A. A. Sokol, and D. O. Scanlon, Physical Review B **95**, 144419 (2017).

[284] M. Giot, L. C. Chapon, J. Androulakis, M. A. Green, P. G. Radaelli, and A. Lappas, Physical Review Letters **99**, 247211 (2007).

[285] S. E. Dutton, P. D. Battle, F. Grandjean, G. J. Long, and K. Oh-Ishi, Inorganic Chemistry **47**, 11212 (2008).

[286] P. Mendels, A. Olariu, F. Bert, D. Bono, L. Limot, G. Collin, B. Ueland, P. Schiffer, R. J. Cava, N. Blanchard, F. Duc, and J. C. Trombe, Journal of Physics: Condensed Matter **19**, 145224 (2007).

[287] C. M. N. Kumar, Y. Xiao, H. S. Nair, J. Voigt, B. Schmitz, T. Chatterji, N. H. Jalarvo, and T. Brückel, Journal of Physics: Condensed Matter **28**, 476001 (2016).

[288] O. V. Kovalev, H. T. Stokes, and D. M. Hatch, *Representations of the crystallographic space groups : irreducible representations, induced representations and corepresentations* (Gordon and Breach Science Publishers, Yverdon, Switzerland, 1993).

[289] A. Muñoz, J. A. Alonso, M. J. Martínez-Lope, M. T. Casáis, J. L. Martínez, and M. T. Fernández-Díaz, Physical Review B **62**, 9498 (2000).

[290] A. Muñoz, J. A. Alonso, M. J. Martínez-Lope, M. T. Casáis, J. L. Martínez, and M. T. Fernández-Díaz, Chemistry of Materials **13**, 1497 (2001).

[291] F. Yen, C. R. Dela Cruz, B. Lorenz, Y. Y. Sun, Y. Q. Wang, M. M. Gospodinov, and C. W. Chu, Physical Review B - Condensed Matter and Materials Physics **71**, 180407 (2005).

[292] O. P. Vajk, M. Kenzelmann, J. W. Lynn, S. B. Kim, and S. W. Cheong, Journal of Applied Physics **99**, 08E301 (2006).

[293] N. P. Raju, J. E. Greedan, J. S. Pedersen, C. Simon, A. Maignan, A. M. Niraimathi, E. Gmelin, and M. A. Subramanian, Journal of Applied Physics **79**, 6173 (1996).

[294] J. E. Greedan, N. P. Raju, A. Maignan, C. Simon, J. S. Pedersen, A. M. Niraimathi, E. Gmelin, and M. A. Subramanian, Physical Review B **54**, 7189 (1996).

[295] L. Shen, C. Greaves, R. Riyat, T. C. Hansen, and E. Blackburn, Physical Review B **96**, 094438 (2017).

[296] A. Midya, N. Khan, D. Bhoi, and P. Mandal, Applied Physics Letters **103**, 2011 (2013).

[297] A. Midya, N. Khan, D. Bhoi, and P. Mandal, Physica B: Condensed Matter **448**, 43 (2014).

[298] K. Dey, A. Indra, S. Majumdar, and S. Giri, J. Mater. Chem. C **5**, 1646 (2017).

[299] Y. Q. Cai, Y. Y. Jiao, Q. Cui, J. W. Cai, Y. Li, B. S. Wang, M. T. Fernández-Díaz, M. A. McGuire, J.-Q. Yan, J. A. Alonso, and J.-G. Cheng, Physical Review Materials **1**, 064408 (2017).

[300] M. B. Sanders, F. A. Cevallos, and R. J. Cava, Materials Research Express **4**, 036102 (2017).

[301] E. M. Levin, R. S. Roth, and J. B. Martin, American Mineralogist **46**, 1030 (1961).

[302] S. Lemanceau, G. Bertrand-Chadeyron, R. Mahiou, M. El-Ghozzi, J. Cousseins, P. Conflant, and R. Vannier, Journal of Solid State Chemistry **148**, 229 (1999).

[303] A. Goryunova, *Beitrag zur Kristallchemie und Kristallsynthese binärer Seltenerdborate vom Typ SEB3O6 und SEBO3*, Ph.D. thesis, University of Cologne (2003).

[304] Y. Wang, T. Endo, L. He, and C. Wu, Journal of Crystal Growth **268**, 568 (2004).

[305] R. Velchuri, B. V. Kumar, V. R. Devi, G. Prasad, D. J. Prakash, and M. Vithal, Materials Research Bulletin **46**, 1219 (2011).

[306] A. Szczeszak, T. Grzyb, S. Lis, and R. J. Wiglusz, Dalton Transactions **41**, 5824 (2012).

[307] Y. Laureiro, M. M. Veiga, F. Fernandez, R. Puche, A. Jerez, and C. Pico, Journal of the Less Common Metals **157**, 335 (1990).

[308] Y. Laureiro, M. Veiga, F. Fernández, R. Saez-Puche, A. Jerez, and C. Pico, Journal of the Less Common Metals **167**, 387 (1991).

[309] R. E. Newnham, M. J. Redman, and R. P. Santoro, Journal of the American Ceramic Society **46**, 253 (1963).

[310] W. F. Bradley, D. L. Graf, and R. S. Roth, Acta Crystallographica **20**, 283 (1966).

[311] G. Chadeyron, M. El-Ghozzi, R. Mahiou, A. Arbus, and J. Cousseins, Journal of Solid State Chemistry **128**, 261 (1997).

[312] J. Lin, D. Sheptyakov, Y. Wang, and P. Allenspach, Chemistry of Materials **16**, 2418 (2004).

[313] A. Pitscheider, R. Kaindl, O. Oeckler, and H. Huppertz, Journal of Solid State Chemistry **184**, 149 (2011).

[314] A. I. Smirnov, L. E. Svistov, L. A. Prozorova, A. Zheludev, M. D. Lumsden, E. Ressouche, O. A. Petrenko, K. Nishikawa, S. Kimura, M. Hagiwara, K. Kindo, A. Y. Shapiro, and L. N. Demianets, Physical Review Letters **102**, 037202 (2009).

[315] R. S. Fishman and S. Okamoto, Physical Review B **81**, 020402 (2010).

[316] L. C. Chapon, P. Manuel, F. Damay, P. Toledano, V. Hardy, and C. Martin, Physical Review B **83**, 024409 (2011).

[317] S. E. Dutton, E. Climent-Pascual, P. W. Stephens, J. P. Hodges, A. Huq, C. L. Broholm, and R. J. Cava, Journal of Physics: Condensed Matter **23**, 246005 (2011).

[318] H. Huppertz, B. von der Eltz, R.-D. Hoffmann, and H. Piotrowski, Journal of Solid State Chemistry **166**, 203 (2002).

[319] Y. Takikawa, S. Ebisu, and S. Nagata, Journal of Physics and Chemistry of Solids **71**, 1592 (2010).

[320] K. A. Ross, T. Proffen, H. A. Dabkowska, J. A. Quilliam, L. R. Yaraskavitch, J. B. Kycia, and B. D. Gaulin, Physical Review B **86**, 174424 (2012).

[321] S. T. Bramwell, M. J. Harris, B. C. den Hertog, M. J. P. Gingras, J. S. Gardner, D. F. McMorrow, A. R. Wildes, A. L. Cornelius, J. D. M. Champion, R. G. Melko, and T. Fennell, Physical Review Letters **87**, 047205 (2001).

[322] J.-J. Wen, W. Tian, V. O. Garlea, S. M. Koohpayeh, T. M. McQueen, H.-F. Li, J.-Q. Yan, J. A. Rodriguez-Rivera, D. Vaknin, and C. L. Broholm, Physical Review B **91**, 054424 (2015).

[323] S. Calder, X. Ke, F. Bert, A. Amato, C. Baines, C. Carboni, R. J. Cava, A. Daoud-Aladine, P. Deen, T. Fennell, A. D. Hillier, H. Karunadasa, J. W. Taylor, P. Mendels, P. Schiffer, and S. T. Bramwell, Physical Review B **81**, 064425 (2010).

[324] S. Agrestini, C. L. Fleck, L. C. Chapon, C. Mazzoli, A. Bombardi, M. R. Lees, and O. A. Petrenko, Physical Review Letters **106**, 197204 (2011).

[325] P. W. C. Sarvezuk, E. J. Kinast, C. V. Colin, M. A. Gusmão, J. B. M. da Cunha, and O. Isnard, Journal of Applied Physics **109**, 07E160 (2011).

[326] N. D. Mermin and H. Wagner, Physical Review Letters **17**, 1133 (1966).

[327] M. Hase, I. Terasaki, and K. Uchinokura, Physical Review Letters **70**, 3651 (1993).

[328] S. E. Dutton, M. Kumar, M. Mourigal, Z. G. Soos, J.-J. Wen, C. L. Broholm, N. H. Andersen, Q. Huang, M. Zbiri, R. Toft-Petersen, and R. J. Cava, Physical Review Letters **108**, 187206 (2012).

[329] S. A. J. Kimber, H. Mutka, T. Chatterji, T. Hofmann, P. F. Henry, H. N. Bordallo, D. N. Argyriou, and J. P. Attfield, Physical Review B **84**, 104425 (2011).

[330] D. R. Harcombe, P. G. Welch, P. Manuel, P. J. Saines, and A. L. Goodwin, Physical Review B **94**, 174429 (2016).

[331] A. Mayolet, W. Zhang, P. Martin, B. Chassigneux, and J. C. Krupa, Journal of The Electrochemical Society **143**, 330 (1996).

[332] F. Meng, X. Zhang, W. Li, T. Xie, and H. J. Seo, Journal of Physics and Chemistry of Solids **73**, 564 (2012).

[333] X. Zhang, F. Meng, W. Li, S. I. Kim, Y. M. Yu, and H. J. Seo, Journal of Alloys and Compounds **578**, 72 (2013).

[334] J. Weidelt, Zeitschrift for anorganische und allgemeine Chemie **374**, 26 (1970).

[335] A. Goriounova, P. Held, P. Becker, and L. Bohatý, Acta Crystallographica Section E Structure Reports Online **59**, i83 (2003).

[336] H. Emme, T. Nikelski, T. Schleid, R. Pöttgen, M. H. Möller, and H. Huppertz, Zeitschrift für Naturforschung B **59**, 202 (2004).

[337] V. Pakhomov, G. Sil'nitskaya, A. Medvedev, and B. Dzhurinskij, Izvestiya Akademii Nauk SSSR, Neorganicheskie Materialy **8**, 1259 (1972).

[338] G. Abdullaev, K. S. Mamedov, and G. Dzhafarov, Kristallografiya **20**, 265 (1975).

[339] P. Becker and R. Fröhlich, Crystal Research and Technology **43**, 1240 (2008).

[340] M. C. Hatnean, M. R. Lees, O. A. Petrenko, D. S. Keeble, G. Balakrishnan, M. J. Gutmann, V. V. Klekovkina, and B. Z. Malkin, Physical Review B **91**, 174416 (2015).

[341] V. K. Anand, A. K. Bera, J. Xu, T. Herrmannsdörfer, C. Ritter, and B. Lake, Physical Review B **92**, 184418 (2015).

[342] E. Lhotel, S. Petit, S. Guitteny, O. Florea, M. Ciomaga Hatnean, C. Colin, E. Ressouche, M. R. Lees, and G. Balakrishnan, Physical Review Letters **115**, 197202 (2015).

[343] R. Sibille, E. Lhotel, M. Ciomaga Hatnean, G. J. Nilsen, G. Ehlers, A. Cervellino, E. Ressouche, M. Frontzek, O. Zaharko, V. Pomjakushin, U. Stuhr, H. C. Walker, D. T. Adroja, H. Luetkens, C. Baines, A. Amato, G. Balakrishnan, T. Fennell, and M. Kenzelmann, Nature Communications **8**, 892 (2017).

[344] I. Maartense, I. Yaeger, and B. Wanklyn, Solid State Communications **21**, 93 (1977).

Appendix A

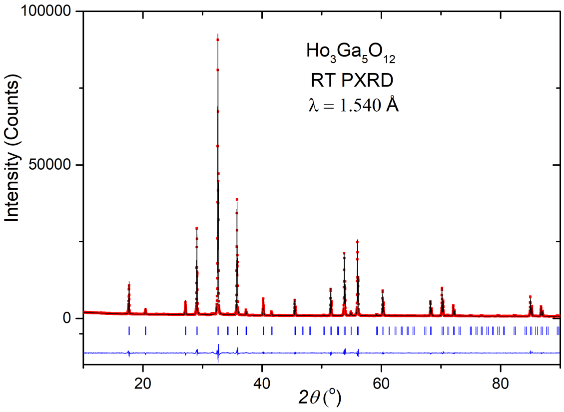

Figure A.1 Room temperature PXRD pattern for $Ho_3Ga_5O_{12}$: Red dots - Experimental data, Black line - Modelled data, Blue line - Difference pattern, Blue ticks - Bragg positions.

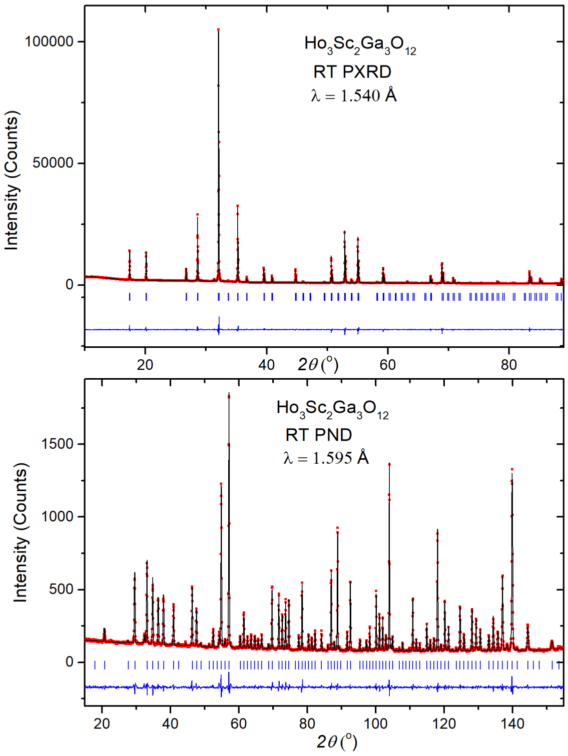

Figure A.2 Room temperature PXRD and PND pattern for $Ho_3Sc_2Ga_3O_{12}$: Red dots - Experimental data, Black line - Modelled data, Blue line - Difference pattern, Blue ticks - Bragg positions.

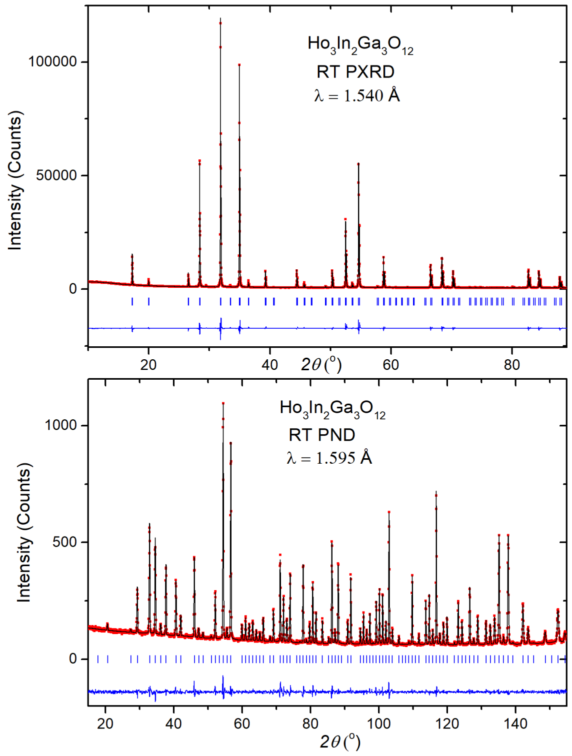

Figure A.3 Room temperature PXRD and PND pattern for $Ho_3In_2Ga_3O_{12}$: Red dots - Experimental data, Black line - Modelled data, Blue line - Difference pattern, Blue ticks - Bragg positions.

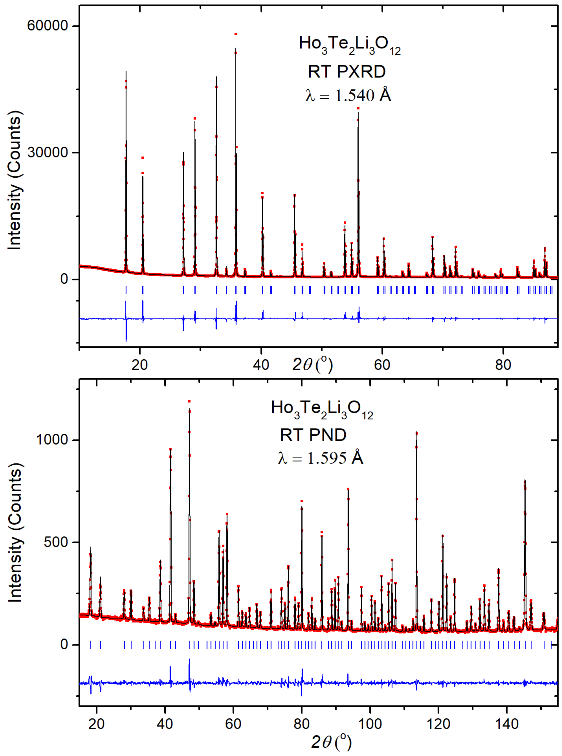

Figure A.4 Room temperature PXRD and PND pattern for $Ho_3Te_2Li_3O_{12}$: Red dots - Experimental data, Black line - Modelled data, Blue line - Difference pattern, Blue ticks - Bragg positions.

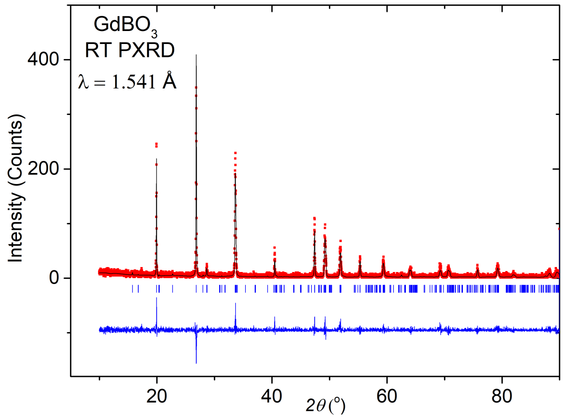

Figure A.5 Room temperature PXRD pattern for $GdBO_3$: Red dots - Experimental data, Black line - Modelled data, Blue line - Difference pattern, Blue ticks - Bragg positions.

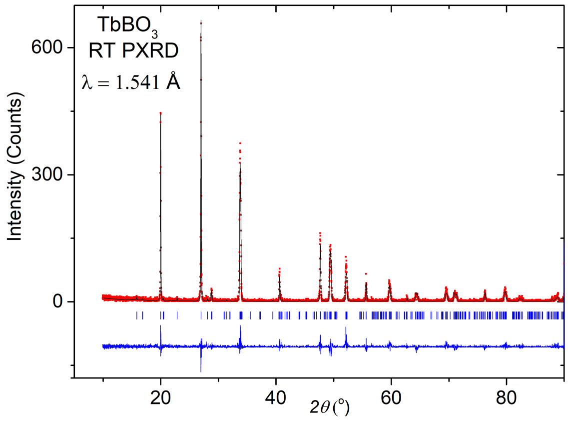

Figure A.6 Room temperature PXRD pattern for $TbBO_3$: Red dots - Experimental data, Black line - Modelled data, Blue ticks - Bragg positions, Blue line - Difference pattern.

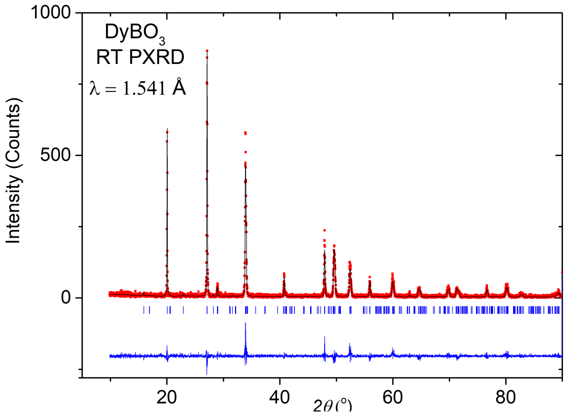

Figure A.7 Room temperature PXRD pattern for $DyBO_3$: Red dots - Experimental data, Black line - Modelled data, Blue line - Difference pattern, Blue ticks - Bragg positions.

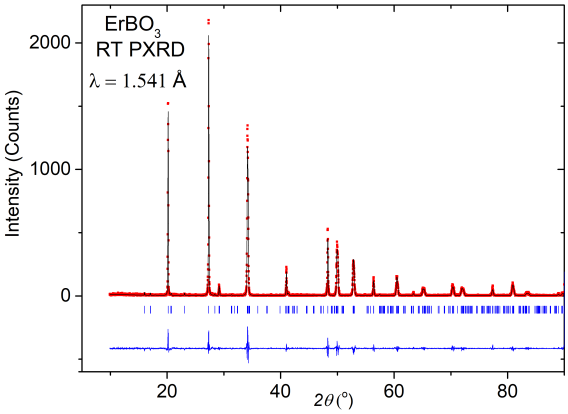

Figure A.8 Room temperature PXRD pattern for $ErBO_3$: Red dots - Experimental data, Black line - Modelled data, Blue line - Difference pattern, Blue ticks - Bragg positions.

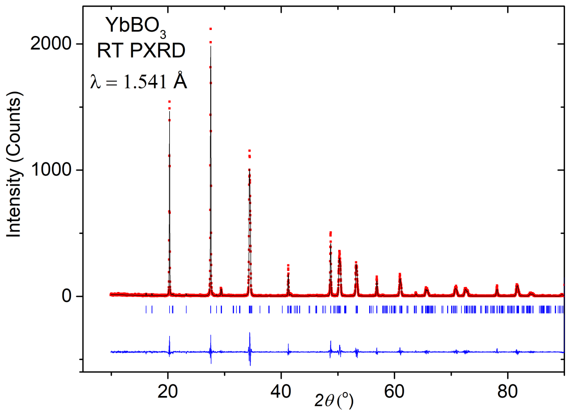

Figure A.9 Room temperature PXRD pattern for $YbBO_3$: Red dots - Experimental data, Black line - Modelled data, Blue line - Difference pattern, Blue ticks - Bragg positions.

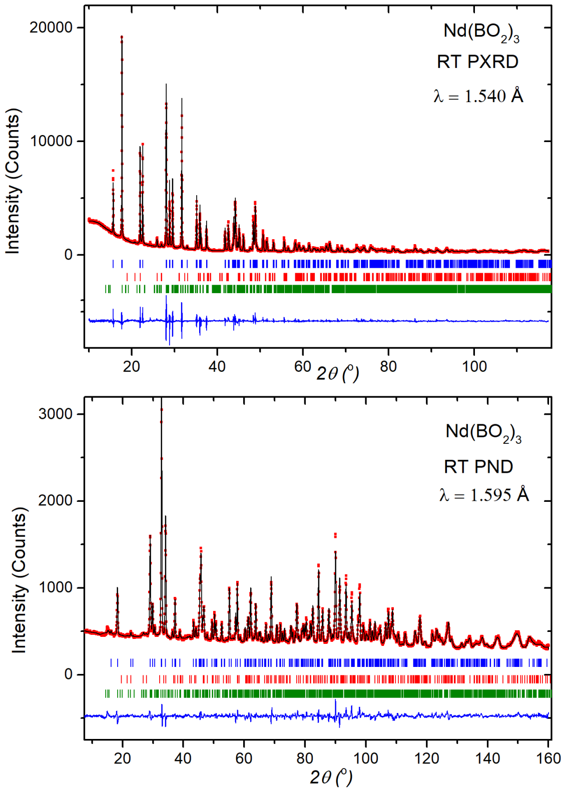

Figure A.10 Room temperature PXRD and PND pattern for $Nd(BO_2)_3$: Red dots - Experimental data, Black line - Modelled data, Blue line - Difference pattern, Blue ticks - Bragg positions; for $Nd(BO_2)_3$, Red ticks - Bragg positions for $NdBO_3$, Green ticks - Bragg positions for H_3BO_3.

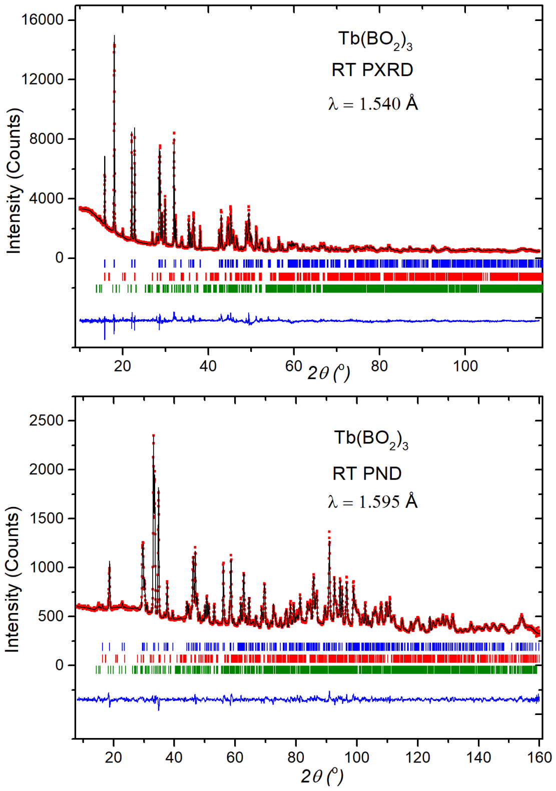

Figure A.11 Room temperature PXRD and PND pattern for Tb(BO$_2$)$_3$: Red dots - Experimental data, Black line - Modelled data, Blue line - Difference pattern, Blue ticks - Bragg positions; for Tb(BO$_2$)$_3$, Red ticks - Bragg positions for TbBO$_3$, Green ticks - Bragg positions for H$_3$BO$_3$.

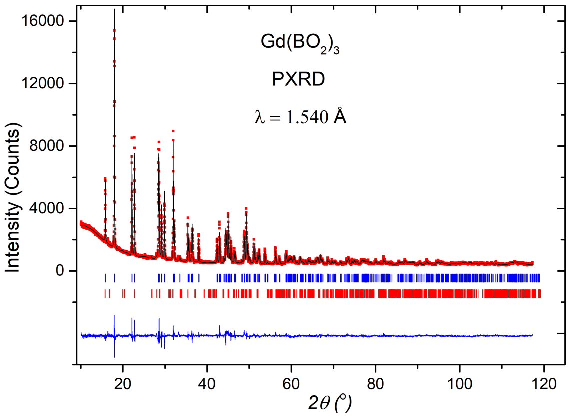

Figure A.12 Room temperature PXRD pattern for Gd(BO$_2$)$_3$: Red dots - Experimental data, Black line - Modelled data, Blue line - Difference pattern, Blue ticks - Bragg positions; for Gd(BO$_2$)$_3$, Red ticks - Bragg positions for GdBO$_3$.